STRUCTURAL DYNAMICS OF H^+/DRUG ANTIPORT IN AN ARCHAEAL MATE TRANSPORTER

By

Kevin Lindsay Jagessar

Dissertation

Submitted to the Faculty of the

Graduate School of Vanderbilt University

in partial fulfillment of the requirements

for the degree of

DOCTOR OF PHILOSOPHY

in

Chemical and Physical Biology

May 8th, 2020

Approved:

Albert Beth, Ph.D.

Charles Cobb, Ph.D.

Jens Meiler, Ph.D.

Benjamin Spiller, Ph.D.

To my parents,

Paul and Caroline

TABLE OF CONTENTS

Page

APPENDIX

LIST OF TABLES

TABLE Page

LIST OF FIGURES

FIGURE Page

LIST OF ABBREVIATIONS

ABC	ATP binding cassette
AtDTX14	eukaryotic MATE from *Arabidopsis thaliana*
CasMATE	eukaryotic MATE from *Camelina sativa*
CFX	ciprofloxacin
CL	cardiolipin
CW	continuous wave
β-DDM	n-Dodecyl β-D-maltoside
DEER	double electron-electron resonance
DinF	DNA damage inducible protein F family
DinF-Bh	DinF MATE from *Bacillus halodurans*
DXR	doxorubicin
EPR	electron paramagnetic resonance
ClbM	DinF MATE from *Escherichia coli*
EL	extracellular loop
Et	ethidium
GPCRs	G-protein coupled receptors
hCG	human chorionic gonadotropin
HDX-MS	hydrogen-deuterium exchange mass spectrometry
hMATE	human MATE transporter
IF	inward facing
IL	intracellular loop
LCP	lipidic cubic phase
MATE	multidrug and toxin extrusion
MD	molecular dynamics
MDR	multidrug resistance
MFS	major facilitator superfamily

MIC	minimum inhibitory concentration
MIRAS	multiple wavelength isomorphous replacement with anomalous scattering
mMATE	mouse MATE transporter
MOP	multidrug/oligosaccharidyl-lipid/polysaccharide superfamily
mRNA	messenger RNA
MTSSL	(1-oxyl-2,2,5,5-tetramethylpyrroline-3-methyl)methanethiosulfonate
MVF	mouse virulence factor family
β-NG	n-nonyl-β-glucopyranoside
NtMATE	tobacco plant MATE transporter
NFX	norfloxacin
NiEDDA	Ni(II)ethylenediamide diacetic acid
NorM-Ng	NorM from *Neisseria. gonorrhea*
NorM-Ps	NorM from *Pseudomonas stutzeri*
NorM-Vc	NorM from *Vibrio cholerae*
NorM-Vp	NorM from *Vibrio parahaemolyticus*
OAT	organic anion transporter
OCT	organic cation transporter
OF	outward facing
OLF	oligosaccharidyl-lipid flippase
PACE	proteobacterial antimicrobial compound efflux
PC	phosphatidylcholine
PE	phosphatidylethanolamine
PfMATE	DinF MATE from *Pyrococcus furiosus*
PST	prokaryotic polysaccharide transporter
R6G	Rhodamine 6G
RbMATE	rabbit MATE transporter
RND	resistance, nodulation and division
SAD	single-wavelength anomalous dispersion

SbMATE	sorghum plant MATE transporter
SMR	small multidrug resistance
SNP	single nucleotide polymorphism
TM	transmembrane
TPP	tetraphenylphosphonium
VcmN	DinF MATE from Vibrio cholerae
WT	wild-type

CHAPTER I

Structure and function of MATE transporters

Active transport across membranes is essential for life (1). Numerous transporter families have evolved as a result to handle a variety of processes that includes the import of essential nutrients, reuptake of signaling molecules, and the export of metabolic waste. Multidrug (MDR) transporters function in the removal of structurally and chemically diverse molecules, including antibiotics and antiseptics, and serve to circumvent drug toxicity (2–5). Despite a high energetic cost, export of the drug from inside the cell by MDR transporters is the primary defense mechanism (2, 6, 7). This mechanism allows the cell sufficient time to adapt other resistance mechanisms to modify or degrade the drug or to modify the target of the drug (8). In prokaryotes and eukaryotes, these mechanisms have facilitated resistance to commonly used antibiotics and anticancer agents (6, 9, 10). With a dearth of new treatments, the widespread distribution of these transporters presents a serious clinical challenge for successful pharmacological treatment of bacterial infections and cancers (3, 11–15). In cancer cells, drug efflux allows for adaptive mechanisms that result in cell plasticity and phenotype switching, which contributes to resistance to chemotherapy drugs (16, 17). Drug tolerant cells can subsequently drive cancer relapse if treatment is discontinued.

MDR transporters are grouped into two main categories: primary active transporters and secondary active transporters. Primary active transporters or ATP binding cassette (ABC) transporters are defined by their direct utilization of chemical energy through ATP hydrolysis to power conformational changes for substrate transport (18, 19). Secondary active transporters, on the other hand, employ electrochemical gradients, maintained by primary active processes, to promote transport (19, 20). While specific ion and substrate dependence varies among secondary active transporters, the mechanism of transport can be classified into three general categories:

uniport, symport, and antiport (20). Uniporters allow diffusion of specific chemical substrates through the membrane, relying on the chemical gradient of substrate to impose directionality. In contrast, symporters and antiporters couple the energetically favorable translocation of ions to energetically uphill transport of substrates against their concentration gradients (19, 21). Symporters and antiporters are defined by the directionality of ion and substrate transfer with antiport comprising opposite directionality (22, 23) and symport encompassing unidirectional mechanisms (24).

There are currently six secondary active membrane transporter families identified, classified according to sequence homology and topology (25). The major facilitator superfamily (MFS), small multidrug resistance (SMR) family, the resistance, nodulation and division (RND) family, the multidrug and toxic compound extrusion (MATE) family, and more recently described, the proteobacterial antimicrobial compound efflux (PACE) and the AbgT family utilize electrochemical gradients to drive transport of substrates against their concentration gradients out of the cell. MATE transporters were first identified in 1998 and since then much has been described regarding structure and function (23, 25).

Phylogeny of MATE transporters

MATE transporters were originally classified as MFS transporters (26). However, their topology was revealed to be distinct from members of the MFS and so were classified as a new transporter family (26, 27). MATE transporters are classified into the multidrug/oligosaccharidyl-lipid/polysaccharide (MOP) flippase superfamily (28). Besides the MATE transporters, this superfamily also includes the prokaryotic polysaccharide transporter (PST) family, the oligosaccharidyl-lipid flippase (OLF) family, and the mouse virulence factor family (MVF). Of the members of this superfamily, the MATE transporters are most numerous and are found across all kingdoms of life (28). Multiple orthologues of the PST transporters are found in archaea and bacteria, while the MVF proteins are found only in bacteria. In contrast the OLF proteins are found only in eukaryotes, specifically in the endoplasmic reticulum. Phylogenetic analyses suggest a relative degree of relatedness of the four families and demonstrates that the MATE, MVF, and PST families are more interrelated than to the OLF family (Fig. 1.1) (28). This suggests that primordial proteins related to the PST family might be the common ancestor from which the other families diverged.

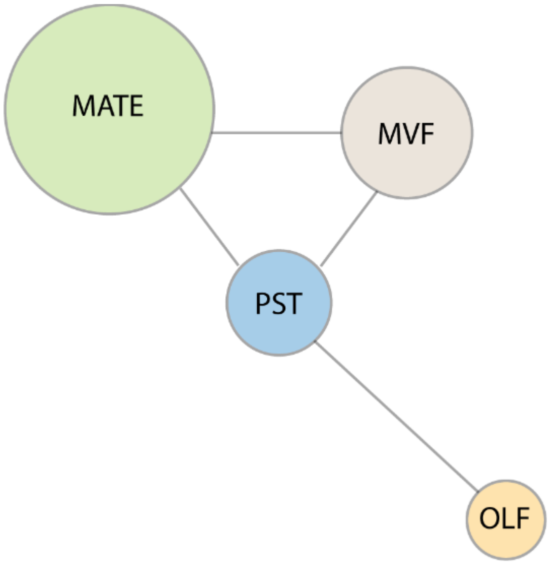

Figure 1.1: **Schematic depiction of the relative relatedness of members of the MOP superfamily**. Phylogenetic analyses suggest that primordial proteins related to the PST family are the common ancestor of members of this superfamily (28).

The MATE transporters are further categorized into three phylogenetic branches based on amino acid sequence similarity (26): the NorM and DNA damage-inducible protein F (DinF) subfamilies (typically found in archaea and bacteria) that are Na^+ and/or H^+-coupled, and the Eukaryotic subfamily that is putatively H^+-coupled. The first MATE transporter that was characterized was NorM from the bacterium *Vibrio parahaemolyticus*, a Na^+/drug antiporter that confers resistance to toxic dyes, fluoroquinolones, and aminoglycosides (29, 30). Since then many other MATE efflux pumps have been identified in many pathogenic bacteria including *Acinetobacter baumannii* (31), *Brucella melitensis* (32), *Clostridium difficile* (33), *Haemophilus influenza* (34), *Neisseria gonorrhoeae* (35, 36), *Neisseria meningitides* (35), *Pseudomonas* *aeruginosa* (37), *Staphylococcus aureus* (38, 39), and *Vibrio cholerae* (40–42) with multiple paralogues of the MATE transporters found within a single organism.

While endogenous substrates generally have not been identified for bacterial MATE transporters, except for *Escherichia coli* ClbM which has been implicated in precolibactin toxin transport (43), the known substrates of these transporters are a wide range of cationic and aromatic compounds whose efflux is coupled to a Na^+ and/or H^+ gradient (25). These compounds include dyes such as ethidium bromide (Et) and doxorubicin (DXR), and antibiotic fluoroquinolones such as ciprofloxacin (CFX) and norfloxacin (NFX), β-lactam antibiotics such as penicillin, and aminoglycoside antibiotics such as kanamycin and erythromycin. As substrates of the MATEs, these antibiotics are exported from the cell thus lowering the concentration of the drug to where it is below the minimum inhibitory concentration (MIC) toward the bacterium and rendering the antibiotic ineffective. As previously mentioned, this has allowed bacteria to evolve additional mechanisms to degrade or modify the drug, thus contributing to the phenomenon of multi drug resistance, a serious and rapidly growing public health crisis. Of greater concern is that the MATE transporter MepA from *S. aureus* has already been shown to confer resistance against a new generation of glycylcycline antibiotics that have shown promising activity against methicillin and vancomycin resistant strains (39).

Eukaryotic MATE transporters in plants

In plants, the MATE family constitutes one of the largest transporter families with 67 identified paralogues in *Solanum lycopersicum* (tomato), 58 in *Arabidopsis thaliana*, 49 in *Zea mays* (maize), and 48 in *Solanum tuberosum* (potato) (44, 45). Genetic studies have suggested that tandem and segmental duplications have contributed to the expansion and evolution of this family of transporters (44). MATE transporters in plants have been implicated in myriad processes including aluminum tolerance in acidic soils and protection of roots from inhibitory compounds (46–48), iron homeostasis (49, 50), alkanoid and flavonoid transport including anthocyanin accumulation (51–55), siacylic acid-dependent disease resistance signaling (56), hormone signaling (57, 58), and detoxification of lipophilic compounds (59). Moreover, MATE expression is tissue specific, carrying out specific but overlapping functions in the leaves, flowers, fruits, seeds, stems and shoots, and roots. Accumulation of endogenous alkaloids such as nicotine in the leaves of the tobacco plant *Nicotiana tabacum* is associated with the expression of NtMATE1, NtMATE2, and Nt-JAT1 genes (60, 61). Aluminum tolerance in *Sorghum bicolor* is associated with the efflux of citrate from the roots by SbMATE into the rhizosphere, which results in the formation of non-toxic complexes with aluminum (62). Similar MATE genes are found to be upregulated in *Arabidopsis thaliana* (46), *Triticum* (wheat) (63), *Hordeum vulgare* (barley) (64), and *Zea mays* (maize) (47), to name a few, in response to aluminum stress.

MATE transporters in humans and animals

In humans, MATE transporter orthologues (hMATEs) are differentially expressed in the luminal surface of renal tubular cells of the kidney and the bile canaliculi of the liver (65). mRNA analysis has shown that hMATE1 is expressed in the kidney and the liver and to a lesser extent in the adrenal glands, testis, and skeletal muscle. In contrast, hMATE2 and its splicing variant hMATE2-K are expressed solely in the kidney (66, 67). In the kidney, the hMATE1 and hMATE2-K transporters are localized on the brush border membrane of proximal epithelial cells and colocalize with the organic cation transporter OCT2 and the organic anion transporters OAT1 and OAT3, which are found on the basolateral membrane (66). The expression levels of these transporters are higher than that of any other renal drug transporters in the cortex of the kidney and are responsible for the terminal step of organic cation/anion excretion from the kidney (66–68).

hMATE1, hMATE2 and hMATE2-K efflux structurally diverse, low molecular weight organic cations coupled to an inwardly-directed proton gradient that is sustained by the membrane Na^+/H^+ exchanger and the V-type proton ATP-ase. (69–73). While the co-localization and overlapping specificities of hMATEs in the kidneys suggest a redundant system, their substrate specificities are not identical. Human MATEs in the kidney have been reported to transport drugs such as metformin (a widely prescribed anti-diabetic medication) (74, 75), atenolol (a β-blocker used to treat hypertension) (76), acyclovir (antiviral agent), and chloroquine (antiprotozoal agent) (77). These proteins also transport antibiotics and chemotherapeutics such as cisplatin and oxaliplatin (70, 78). However, potent inhibitory effects are observed by cimetidine, levofloxacin, and pyrimethamine, to name a few (79, 80).

Pyrimethamine, an anti-parasitic treatment sold under the trade name Daraprim, has been shown to be a potent and specific inhibitor of the MATE transporter (81). Experiments with wild-type (WT) male mice found that 80 min after pyrimethamine administration the total concentration in the kidney and plasma was 51.1 µM and 5.5 µM, respectively. The unbound pyrimethamine in the kidney and the plasma was determined to be 1.3 µM and 0.45 µM, respectively (81). This demonstrated that the concentration of unbound pyrimethamine in the kidney was much higher than the K_i for mouse MATE1 (mMATE1) (0.14 µM), while the unbound pyrimethamine in the plasma was much lower than the K_i for mouse OCT1 and OCT2 (3.6 and 6.0 µM) (82). This suggested that pyrimethamine inhibited mMATE1 but not OCT1 or OCT2 with which mMATE1 is co-localized in the kidney. For hMATE1 and hMATE2-K pyrimethamine is far more potent an inhibitor, with reported K_i values of 93 nM and 59 nM, respectively (83).

As the last site of organic cation secretion, the MATE transporters in the kidney represent a site of drug-drug interactions and mediate drug toxicity. For example, hMATE1 but not hMATE2-K transports cisplatin from epithelial cells and therefore, cisplatin will accumulate and induce tubular toxicity to a greater extent than oxaliplatin, which is a substrate for both transporters and thus can be more easily exported from the cells (84). Mutation of hMATE1 or inhibition by the antiemetic ondansetron can greatly potentiate cisplatin nephrotoxicity. Indeed mMATE1 -/- mice were more prone to cisplatin induced nephrotoxicity and had increased cisplatin plasma and renal concentrations compared to WT mice (85). Similarly, coadministration of cimetidine significantly increases exposure to dofetilide, metformin, procainamide or levofloxacin (78, 86–89). Fluoroquinolones such as levofloxacin and ciprofloxacin in turn have inhibitory effects on the clearance of drugs such as procainamide, which is used to treat cardiac arrythmia (90).

Functional single nucleotide polymorphisms (SNPs) of hMATE1 and hMATE2-K are associated with the enhanced activity of metformin. Studies in mMATE1 -/- mice had a 2-fold increase in the systemic exposure to metformin compared to WT mice as a result of reduced renal clearance (91). Concomitantly, the null mice also had increased liver concentration of metformin compared to the WT mice and displayed symptoms consistent with lactic acidosis, a rare side effect of metformin (92). Type 2 diabetes patients with a SNP within the *IDE/HHEX* gene region (*HHEX_23-AA*, i.e. adenine at that position in both *HHEX_23* copies) (93–95) proved to be slow eliminators of metformin and responded better to the drug (96, 97). However, while inhibition of MATEs by pyrimethamine increased the blood concentration of metformin, it did not enhance its hypoglycemic effect (98).

Other transport processes involving endogenous substrates have been investigated for the MATE transporters. Export of testosterone, thought to occur by passive diffusion owing to its hydrophobicity, was shown to be facilitated by MATE2 in pig Leydig cells. Testosterone produced by human chorionic gonadotropin (hCG) treatment in pig Leydig cells accumulated in the presence of the MATE inhibitors cimetidine or pyrimethamine in a concentration-dependent manner compared to control cells (99). This implicated MATE2 in steroidogenesis in the pig Leydig cells. Pyrimethamine has been shown to increase serum creatinine levels, suggesting a role for MATE transporters in creatinine transport (100, 101). Support for this hypothesis came from studies of mMATE -/- mice in which serum creatinine levels were increased compared to WT mice (91), thus implicating the rodent MATE transporter in apical efflux of creatinine into the urine. Similar experiments have also implicated MATEs in the transport of thiamine (vitamin B) (81), where inhibition of mMATE1 in mice by pyrimethamine significantly increased plasma concentration of thiamine.

Though knockout animal strains have been established to determine the physiological importance of MATE transporters and other renal tubular transporters, there is still considerable interspecies differences in transporter biochemistry, expression, and localization making extrapolation to humans difficult. While the characteristics of hMATE1 and rodent MATE1 are similar, hMATE2-K and rodent MATE2 exhibit low sequence identity (38%) and different expression patterns (70). Additionally, while both hMATE1 and rodent MATE1 are localized in the kidney and liver, rodent MATE1 is also localized in brain glia-like cells and capillaries, pancreatic duct cells, urinary bladder epithelium, alpha cells of the islets of Langerhans, Leydig cells, and Ito cells storing vitamin A (70, 102). *In vitro* assays to determine the effect of a compound on transport by tubular transporters such as the MATEs are universally accepted as routine procedures. Though pharmacological and biochemical analyses of hMATEs have been conducted to determine basic transport properties, potential ligands, and pharmacokinetics (72, 90, 103–105), the molecular mechanisms underlying organic cation recognition and transport by hMATEs are not well understood.

The U.S Food and Drug Administration in its 2017 draft guidance on drug-drug interaction concluded that inhibition of hMATE1 and hMATE2-K should be studied for all new investigational drugs and substrate studies are required if 25% of total drug clearance is due to renal secretion (65). Since a structural biology approach has long been employed to understand protein function, extensive efforts have been made to determine the structures of MATE transporters to illuminate the mechanisms of ligand recognition and binding and subsequent transport. Several MATE transporter structures have been reported in the literature with archaeal, eubacterial, and eukaryotic origins.

Protein	Subfamily	Organism	PDB ID	Resolution (Å)	Ligand
NorM-VC	NorM	*Vibrio cholerae*	3MKT	3.65	
			3MKU	4.20	Rb+
NorM-NG	NorM	*Neisseria gonorrhoeae*	4HUK	3.60	TPP, monobody
			4HUL	3.80	Cs+, monobody
			4HUM	3.50	ethidium, monobody
			4HUN	3.60	R6G, monobody
			5C6P	3.00	verapamil, monobody
PfMATE	DinF	*Pyrococcus furiosus*	3VVN	2.40	
			3VVO	2.50	
			3VVP	2.90	Br-norfloxacin
			3WBN	2.45	Cyclic peptide MaL6
			3VVR	3.00	Cyclic peptide MaD5
			3VVS	2.60	Cyclic peptide MaD3S
			3W4T	2.10	
			6FHZ	2.80	
			6GWH	2.80	
			6HFB	3.50	Cs+
			4MLB	2.35	
DinF-BH	DinF	*Bacillus halodurans*	4LZ6	3.20	
			4LZ9	3.70	R6G
			5C6N	3.00	
			5C6O	3.00	verapamil
VcmN	DinF	*Vibrio cholerae*	6IDP	2.20	
			6IDR	2.50	
			6IDS	2.80	
ClbM	DinF	*Escherichia coli*	4Z3N	2.70	
			4Z3P	3.30	Rb+
AtDTX14	eMATE	*Arabidopsis thaliana*	5Y50	2.60	
CasMATE	eMATE	*Camelina sativa*	5XJJ	2.90	

Table 1.1: **Reported structures of the MATE transporters**.

Structures of MATE transporters

A variety of crystallization methods and strategies have been employed to obtain crystals of MATE transporters. These involve using detergents and lipids as membrane mimetics, monobodies engineered against the protein molecule, and a range of buffer conditions to facilitate crystallization. Thus far, 29 crystal structures of 8 MATE transporters have been published from 7 organisms across the NorM, DinF, and eukaryotic subfamilies (Table 1.1). A sequence alignment of these 8 transporters reveals conserved elements that have been implicated in ion and substrate binding and conformational change (Fig. 1.2).

MATE transporters typically consist of ~400-500 amino acids and are composed of 12 transmembrane helices (TM). TMs 1-6 and TMs 7-12 constitute the N-terminal and C-terminal domains, respectively, hereafter referred to as the N- and C-lobes. The N-terminal segment of TM1 and the C-terminal segment of TM12 are oriented to the intracellular side of the lipid bilayer. The N- and C-lobes are related by an intramolecular two-fold pseudosymmetry and are connected by an intracellular loop of ~15 amino acid residues.

While a structure of a mammalian MATE transporter has yet to be reported, hydropathy analyses have suggested that human, rat, and rabbit MATE1 (rbMATE1), which are 570, 566, and 568 amino acid residues, respectively, are composed of 13 TMs, thus orienting the C-terminal segment of the transporter to the extracellular side of the bilayer (70). This structure and orientation was confirmed by immunocytochemistry experiments in which the accessibility of the C-terminus of rbMATE1 was tested in permeabilized and non-permeabilized cells (106). The results showed that the C-terminus was accessible in both permeable and non-permeable cells, while mMATE1, which is predicted to have 12 TMs and thus the C-terminus is oriented to the intracellular side of the membrane, was only accessible in permeabilized cells (106). Given that structures currently available demonstrate that 12 TMs constitute the core of the functional transporter, the importance of TM 13 to transport is unclear.

Figure 1.2: Sequence alignment of MATE homologs from the NorM, DinF and eukaryotic subfamilies

Alternating access

The prevalent framework to define conformational cycling in transporters reflects alternating access of an ion/substrate binding site or sites that is exposed to opposite sides of the membrane by conformational changes. Mitchell postulated that membrane transport should be defined in terms of a moving barrier (107) wherein the substrate binding site is at a fixed point within the transporter, but a barrier between that site and the aqueous phases on either side of the transporter can undergo conformational changes so that the binding site is accessible only from one side of the membrane at a time (Fig. 1.3). In the case of the MATE transporters, an antiport model would involve cation binding to the transporter when it is open to the extracellular side of the membrane, or in an outward facing (OF) state. Ion is then transported across the membrane in an energetically downhill process determined by an electrochemical gradient (Fig. 1.3-1). The transporter orients so that it opens to the intracellular side of the membrane in an inward facing conformation (IF) (Fig 1.3-2). Before reorientation of the transporter, substrate binds and subsequently is transported in the opposite direction (Fig. 1.3-3), even against a concentration gradient provided the electrochemical gradient is not dissipated (108).

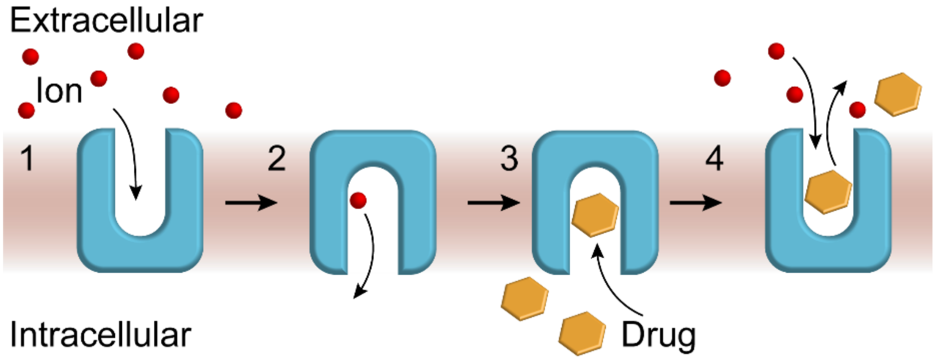

Figure 1.3: **Schematic of alternating access in antiport**. Ion binding (**1**) upon exposure of the binding site to the periplasm or extracellular environment (OF) reorients the transporter so that the binding site is exposed to the intracellular environment (IF). Ion release (**2**) is coupled to substrate capture from the cytoplasm (**3**), upon which the transporter reorients to the OF conformation where ion binding/substrate release could occur (**4**).

The OF to IF conformational change is likely to transition through intermediate states. States in which the binding site is accessible from both sides of the membrane would violate fundamental tenets of alternating access. In such a conformation, the transporter would allow uncoupled flux of substrates and would be equivalent to a channel through the membrane that is selective for the substrate. This would also result in dissipation of the cation gradient. Therefore, transport by alternating access must include an occluded intermediate in which the substrate and cation binding sites are not accessible from either side of the membrane.

Below is a comprehensive review of the reported crystal structures of the MATE transporters and the major findings from the respective articles. The reported structures (Table 1.1) are framed in the context of an alternating access model to establish mechanistic relevance to ion and substrate coupled antiport.

The NorM subfamily of MATE transporters

The NorM subfamily of MATE transporters was the first MATE transporter subfamily that was functionally and structurally characterized. The first functional data was reported for NorM from *Vibrio parahaemolyticus* (NorM-Vp) and its homolog from *E. coli* YdhE (29). It was established via transport assays that NorM-Vp transported ethidium in a sodium-dependent manner (30), and mutation of conserved residues Asp 32 in the N-lobe, and Glu 251 and Asp 367 in the C-lobe abrogated transport (109). Structures of transporters from the NorM subfamily were later reported from *Vibrio cholerae* and *Neisseria gonorrhea* (110, 111) and provided structural information regarding conformational states and ligand binding sites.

NorM-Vc

The first structures reported of the MATE transporters were of NorM from *Vibrio cholerae* (NorM-Vc), a sodium coupled MATE transporter from the NorM subfamily. Structures were determined via X-ray diffraction of protein crystals obtained in n-nonyl-β-glucopyranoside (β-NG) and 3α-hydroxy-7α, 12α-bis[(β-D-maltopyranosyl)ethoxyl)] cholane (FA-231), with and without rubidium (Rb$^+$). The structures with and without rubidium were solved to 3.65 Å and 4.2 Å, respectively (Fig. 1.4A, B).

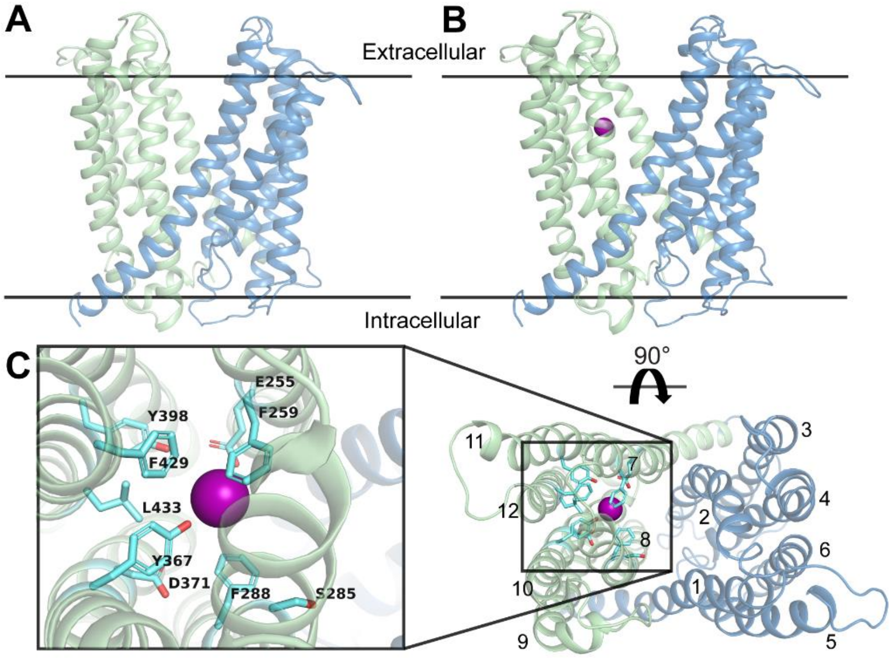

Figure 1.4: **NorM-Vc crystal structures reveal OF conformation**. Apo (**A**) [PDB ID: 3MKT] and cation bound (**B**) [PDB ID: 3MKU] structures adopt the same conformations. The N-lobe and C-lobes are colored blue and green respectively. Rb$^+$ is bound to the C-lobe (**C**) and is coordinated by residues on TMs 7, 8 and 10 (inset) in a cation-π interaction. Side chains of residues are depicted as sticks and are colored in cyan.

The structures adopt an outward facing (OF) conformation regardless of the presence cation (Figs. 1.4A, B). Cation, in this case Rb$^+$ (or Cs$^+$), electron dense Na$^+$ congeners more easily visualized by X-ray diffraction, were found bound to the C-lobe (Fig. 1.4C, not shown, respectively) and coordinated by a number of residues across the C-terminal TMs (Fig. 1.4C, inset), most notably Glu 255 on TM7 and Asp 371 on TM9. These residues are conserved among the NorM transporters (Fig. 1.2) and were found to abrogate transport when mutated in NorM-Vp (109). Indeed, X-ray diffraction of crystals of NorM-Vc D371A and NorM-Vc D371N soaked in RbCl or CsCl did not contain residual densities corresponding to Rb$^+$ or Cs$^+$, suggesting that these mutations abolish cation binding (110). The effect of D371A and D371N mutations on substrate binding of DXR or R6G measured by fluorescence polarization (1.00 ± 0.08 µM and 2.09 ± 0.01 µM, respectively, in wild type), was not reported (110).

No density corresponding to cation was observed in the region of Asp 36 (Asp 32 in NorM-Vp) and it was unclear whether substitution mutations of Asp 36 were made and tested in binding experiments and/or with the Et efflux assay. Thus, the role of Asp 36 in the transport mechanism remained undetermined.

NorM-Ng

Following the NorM-Vc structures, structures of a NorM subfamily transporter from *Neisseria gonorrhea* (NorM-Ng) were reported (111). The structures were determined from crystals of NorM-Ng bound to a monobody that was previously identified from a phage display library. This monobody was reported to facilitate crystallization using the hanging drop vapor diffusion method. Notably, all crystallization conditions lacked sodium. Crystals of NorM-Ng with Cs^+ and with tetraphenyl phosphonium (TPP), ethidium (Et), and R6G were obtained and the structures were determined by molecular replacement using NorM-Vc (PDB ID: 3MKT) as a search model and multiple wavelength isomorphous replacement with anomalous scattering (MIRAS) phasing and solved to 3.81 Å, 3.59 Å, 3.49 Å, and 3.59 Å, respectively (Figs. 1.5A-D). Another structure of NorM-Ng was later reported with verapamil, an inhibitor of MATE transporters, bound to the molecule of NorM-Ng (Fig. 1.5E). This structure was obtained by molecular replacement and MIRAS phasing as before, but to a resolution of 3.0 Å.

The structures, much like those of NorM-Vc, adopt an OF conformation regardless of the ligand bound. This conformation was also adopted by the transporter in the presence of verapamil. Cation was found bound to the C-lobe as in NorM-Vc and was coordinated by the conserved Glu 261 on TM7 and a cation-π interaction involving the side chain of Tyr 294 (Fig. 5A, inset). Indeed, substitution mutations of these residues attenuated NorM-Ng mediated R6G efflux and resistance to TPP, R6G, and Et in drug resistance assays compared to NorM-Ng WT. Drug substrates on the other hand are coordinated by charge-dipole interactions with Ser 61, Gln 284, Ser 288, and electrostatic interactions with the conserved Asp 41 (Fig. 1.2) on TM1, and Asp 355 and Asp 356 (Figs. 1.5B-D, insets). Alanine mutations of Asp 41, Gln 284, Asp 355, and Asp 356 compromised resistance to TPP, R6G, and Et and attenuated NorM-Ng mediated R6G efflux, underscoring the importance of these residues for transport.

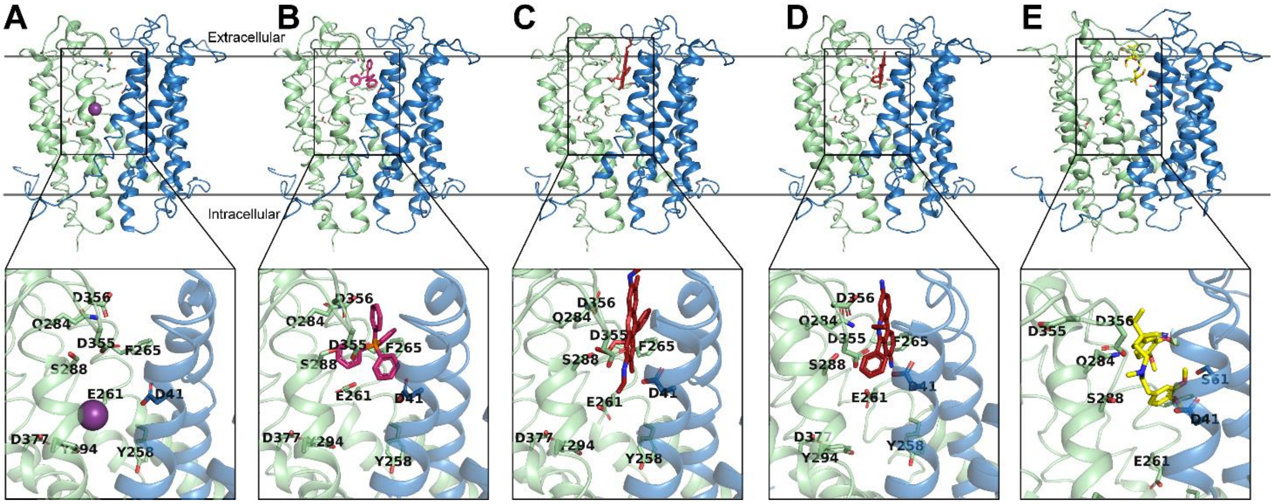

Figure 1.5: **NorM-Ng crystal structures**. Structures reveal cation bound (**A**) [PDB ID: 4HUL], TPP bound (**B**) [PDB ID: 4HUK], R6G bound (**C**) [PDB ID: 4HUN], Et bound (**D**) [PDB ID: 4HUM], and inhibitor bound (**E**) [PDB ID: 5C6P] structures adopt the same conformations, regardless of the presence of ligand. Residues hypothesized to coordinate ligand binding are highlighted in the insets and are depicted as sticks.

While the binding site of verapamil overlaps with that of the other substrates, it interacts via H-bonds with Ser 61 and Gln 284 (Fig. 1.5E, inset). Though verapamil is only mildly toxic under the experimental conditions used for the resistance assay, resistance to verapamil by S61A and Q284A mutants (in addition to D41A, D355A, D356A mutants) was attenuated compared to WT (112). Given that S61A did not compromise resistance to TPP, R6G, or Et, these data imply that verapamil and TPP, R6G, and Et have distinct but over lapping binding sites that may underlie the poly-specificity of multi-drug transporters.

Alignment of the reported structures of NorM-Ng (not shown) reveals no significant structural deviations of TMs, regardless of whether the transporter is bound to cation or drug. In the verapamil bound structure, the EL3-4 and EL9-10 loops do demonstrate rearrangement compared to the cation bound structure, however, any mechanistic relevance remains to be determined.

DinF subfamily of MATE transporters

The DNA damage inducible protein F (DinF) MATE subfamily are conserved across archaea and eubacteria. The first DinF MATE structure reported was from the hyperthermophile *Pyrococcus furiosus,* followed by DinF-Bh from *Bacillus halodurans*, ClbM from *E. coli*, and VcmN from *V. cholerae*. This subfamily includes members that are Na^+- and/or H^+-coupled. The structures reported from this subfamily are structurally diverse and have served to further our understanding of antiport by the MATE transporters within the framework of alternating access.

DinF-Bh

DinF-Bh is a H^+-coupled MATE antiporter from *B. halodurans*. Several structures of the transporter were reported with and without ligands, including verapamil, as well as a protonation mimic (D40N) (113). Crystallization experiments were performed using the hanging drop vapor diffusion method and crystals were obtained in solutions containing NaCl and β-dodecyl maltoside (β-DDM). The structures were determined by molecular replacement and MIRAS and solved to a resolution of 3.20 Å for the Apo structure (PDB ID: 4LZ6), 3.70 Å for the R6G bound structure (PDB ID: 4LZ9) and 3.0 Å for the verapamil bound structure (PDB ID: 5C6O) and the protonation mimetic DinF-Bh D40N (PDB ID: 5C6N).

Interestingly, the transporter adopts a different conformation than what was previously reported for NorM-Ng and NorM-Vc. Unlike NorM-Ng and NorM-Vc where the central cavity is open to the extracellular side between TM1 and TM2 in the N-lobe and TM7 and TM8 in the C-lobe, in the DinF-Bh apo- and R6G bound structures TM7 and TM8 are shifted towards TM1 and TM2 in the N-lobe, away from TMs 9-12 (Fig. 1.6A). The intracellular side of the transporter, like in the NorM-Ng and NorM-Vc structures, remains highly ordered, obstructing access to the central cavity. Interestingly, all the structures of DinF-Bh that have been reported have adopted this conformation. A substitution mutation of Asp 40, a highly conserved residue in the NorM and DinF subfamilies (Fig. 1.2), to generate a protonation mimic DinF-Bh D40N, adopted the same conformation as the Apo and substrate bound structures (Fig. 1.6B). While this has been postulated to be an OF conformation, it may represent a structural intermediate in the transport cycle, possibly an occluded state.

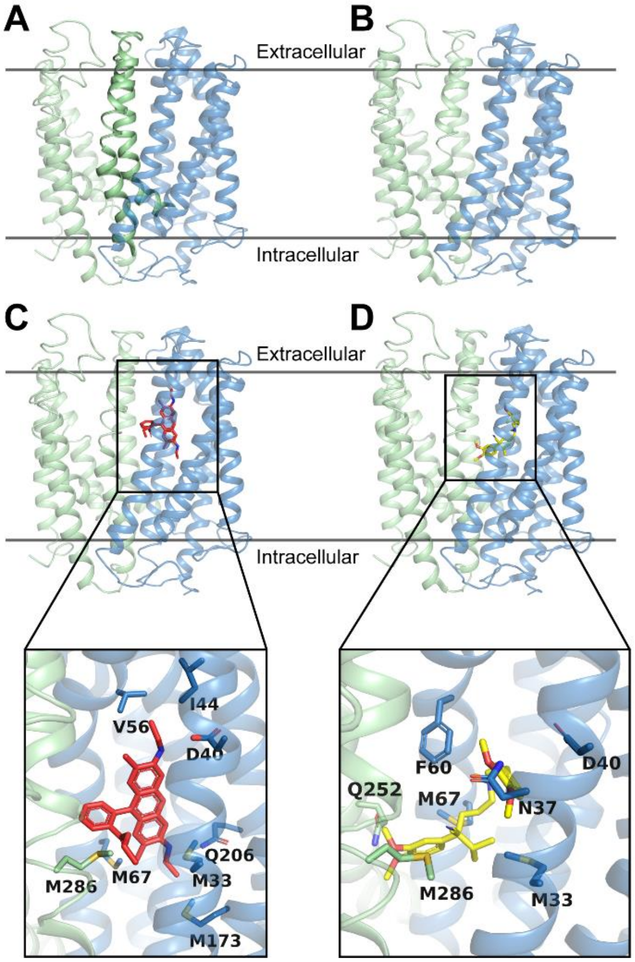

Figure 1.6: **Structures of Din-Bh adopt a different conformation than that seen for other MATE transporters**. TMs 7 and 8 are closer to the N-lobe and are highlighted on the Apo structure (PDB ID: 4LZ6) (**A**). No structural changes are observed in a D40N mutant of DinF-Bh (PDB ID: 5C6N) (**B**). Binding of R6G (PDB ID: 4LZ9) (**C**) and verapamil, an inhibitor (PDB ID: 5C6O) (**D**), is coordinated by residues on TMs 1 and 2 in the N-lobe and TMs 7 and 8 in the C-lobe (insets).

The N-lobe and TMs 7 and 8 of the C-lobe constitute a cavity to which R6G and verapamil bind (Fig. 1.6C, D). R6G binding is coordinated via hydrophobic interactions with the side chains of Met 33, Ile 44, Val 56, Met 67, and Met 173, and charge-dipole and charge-charge interactions with the side chains of Asp 40, Tyr 139, Gln 206, and Met 286 (Fig. 1.6C, inset). Alanine mutations of these residues attenuate the ability of the transporter to confer resistance to toxic concentrations of R6G in drug resistance assays. Verapamil binding is coordinated by Met 33, Tyr 36, Met 67, and Met 286 via Van der Waals interactions, and Asn 37 and Gln 252 via H-bonds (Fig. 1.6D, inset). Alanine mutations of these residues, except for M67A, attenuate the ability of DinF to enhance cell survival in drug resistance assays with verapamil.

Similar to NorM-Ng, the binding sites of R6G and verapamil overlap, which underlies the reduced affinity for R6G with increasing concentrations of verapamil. However, the verapamil molecule is far removed from the conserved Asp 40 that is involved in R6G binding. This is significant as it was shown that at pH 4.0, binding of R6G is reduced, indicating that R6G release is proton dependent. Additionally, R6G binding to the D40N protonation mimetic mirrored the binding at pH 4.0, defining a specific role for Asp 40 in the efflux mechanism. It was therefore postulated that H^+ release substrate by breaking the charge-charge interaction between substrate and Asp 40. Asp 40 then H-bonds to Asp 184, a conserved residue in the DinF MATE transporters (Fig. 1.2). Thus, a different coupling mechanism must be involved to release verapamil from DinF-Bh in the transport cycle.

PfMATE

PfMATE is a H^+-coupled MATE transporter from the hyperthermophile *P. furiosus*. Unlike the crystal structures of other MATE transporters, this transporter has been crystallized in different conformations with different ligands, providing insight into the structural rearrangements that may occur for transport. The first set of structures captured the transporter in two conformations. These structures were determined by single-wavelength anomalous dispersion (SAD) phasing and molecular replacement from crystals obtained via lipidic cubic phase (LCP) with liquefied monoolein at high and low pH conditions, with the MATE substrate NFX, and with inhibitors (114, 115). The high and low pH crystals were obtained in reservoir solutions containing 28-30% PEG400, 50 mM MES/NaOH, 20 mM $CaCl_2$, 100 mM NaSCN; pH 6.0-8.0. The structures at high and low pH were solved to 2.4 Å (PDB ID: 3VVN) and 2.5 Å (PDB ID: 3VVO), respectively. The structures with ligands were obtained from crystals in reservoir solutions containing 26–28% PEG550MME, 100 mM Tris-HCl, 100 mM Li_2SO_4; pH 8.0 These structures were also solved to high resolution, in the range of 2.4 - 3.0 Å (114).

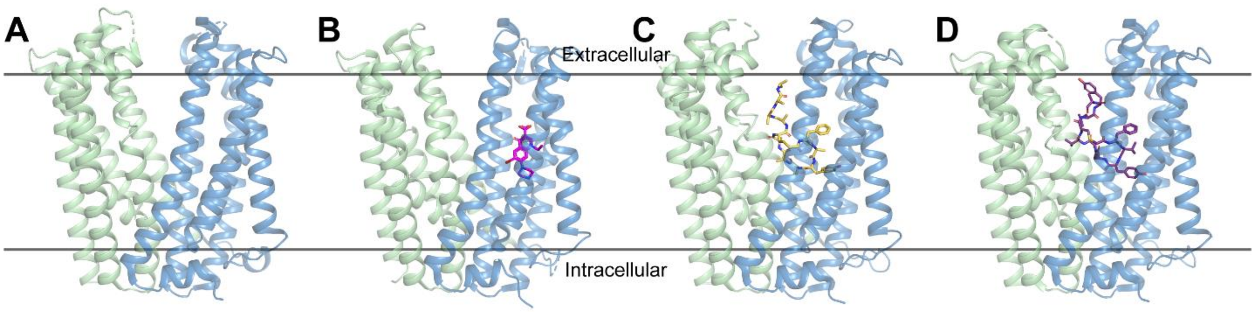

Figure 1.7: **PfMATE crystal structures with and without substrate adopt the same structural conformation**. As a putative H$^+$-coupled antiporter, PfMATE structures were determined at pH 8.0 (**A**) [PDB ID: 3VVN]; with NFX bound (**B**) [PDB ID: 3VVP]; and bound to peptide inhibitors MaD5 (**C**) [PDB ID: 3VVR] and MaD3S (**D**) [PDB ID: 3VVS]. The N- and C-lobes are depicted in blue and green, respectively. The binding sites of MaD5 and MaD3S partially overlap with that of NFX, illustrating the mechanism of inhibition. A third inhibitor of PfMATE, MaL6, was not as potent an inhibitor and is not depicted.

The structures obtained at high pH and with NFX and inhibitors adopt the same conformation (Figs. 1.7A – D). This conformation is inconsistent with that of DinF-Bh, where TM7 and TM8 are proximal to TM1 and TM2 in the N-lobe. Rather, the structures of PfMATE with ligands (Fig. 1.7B – D) and without ligands (Fig. 1.7A) are consistent with the helical orientations of NorM-Vc and NorM-Ng (Figs. 1.4 and 1.5). However, the structure obtained at low pH (Fig. 1.8A) adopts a unique conformation not seen in the NorM transporters (Figs. 1.4 and 1.5) nor in DinF-Bh (Fig. 1.6). At low pH, TM1 is bent at Gly 30 which is thought to be facilitated by the

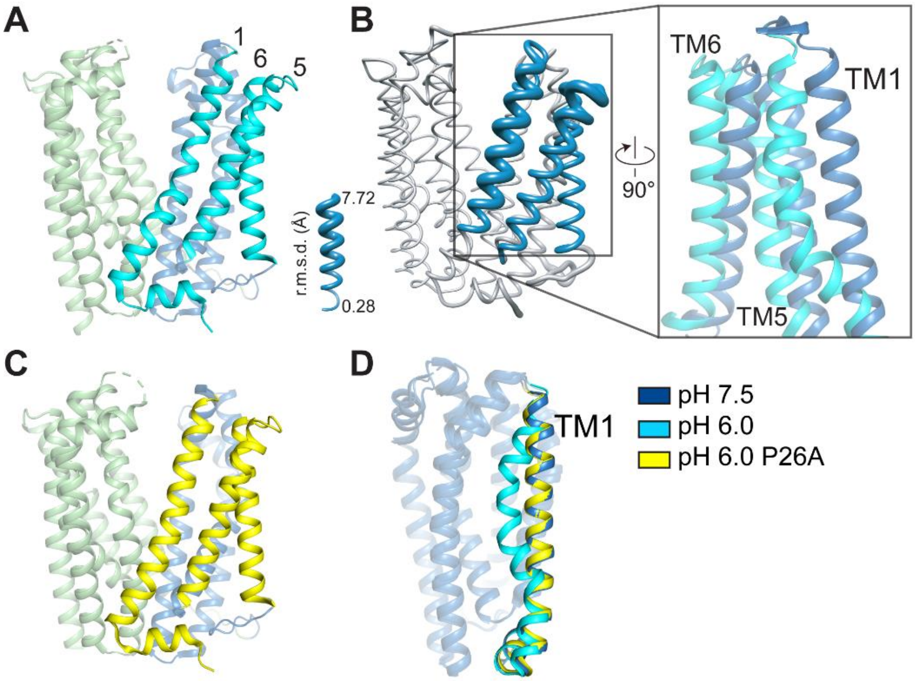

Figure 1.8: **The N-lobe of PfMATE undergoes conformational change at low pH that is mediated by Pro 26**. PfMATE WT structure at low pH (PDB 1D: 3VVO) demonstrates that TMs1, 5, and 6 (in cyan) are bent (**A**). RMSD derived from the alignment of the high pH (PDB ID: 3VVN) and low pH (PDB ID: 3VVO) structures is depicted on a ribbon representation of the high pH structure (**B**). Structural alignment of the high and low pH structures reveals that TMs 1, 5, and 6 bending is the only significant structural change (**B**, **inset**). For clarity, TMs 2, 3, and 4 are not depicted. A P26A mutant of PfMATE crystallized at low pH (PDB ID: 3W4T) does not demonstrate TMs 1, 5, and 6 bending (in yellow) (**C**) A comparison of TM1 conformations across the structures (**D**) demonstrates that TM1 of P26A approximates the conformation of TM1 of PfMATE WT at high pH. For clarity, TMs of the C-lobe are not depicted in (**D**).

conserved Pro 26 (Fig. 1.2). Indeed, a structure of PfMATE P26A from crystals obtained at low pH does not demonstrate TM1 bending (Fig. 1.8C, D). In addition to TM1 bending, structural alignment of the high and low pH structures reveals that TMs 5 and 6 are bent away from the membrane normal (Fig. 1.8B, inset). A comparison of the side chains of the N-lobes from the high and low pH structures (Figs. 1.9A and 1.9B, respectively) reveals that at low pH the conserved Asp 41 side chain changes conformation in association with TM1 bending and results in rearrangement of an H-bond network that involves, among others, the conserved residues Asp 184 and Thr 202 in TM5 and TM6, respectively. Drug resistance assays with norfloxacin and transport assays with Et revealed that D41A and D184A mutants abolish resistance and efflux activities of PfMATE.

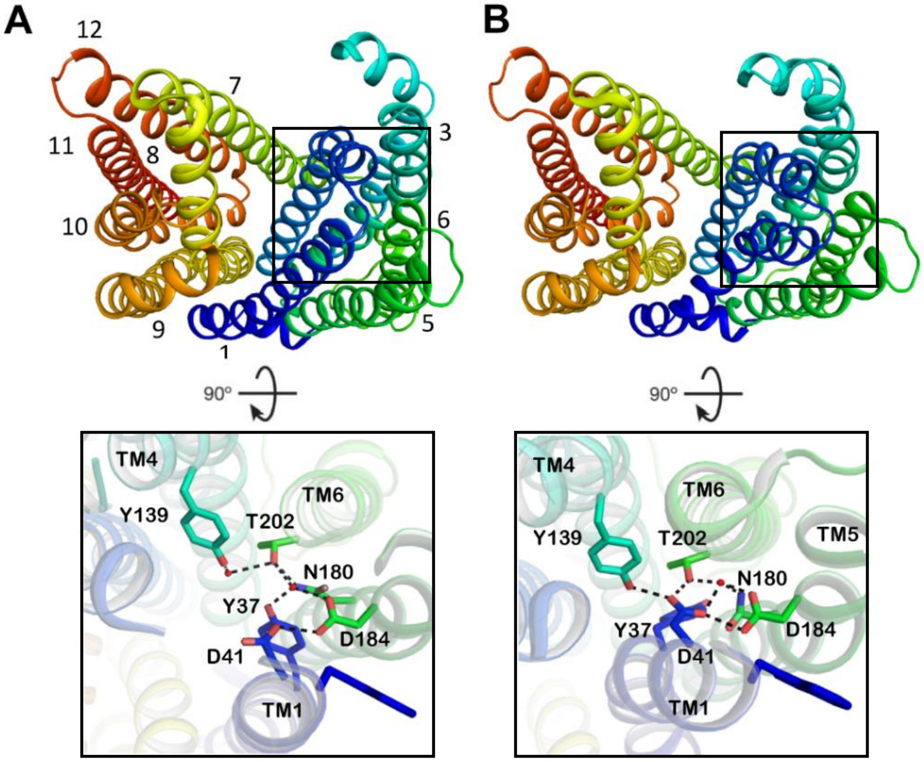

Figure 1.9: **H-bond network in the N-lobe of PfMATE.** Side chains of residues in the N-lobe of PfMATE that constitute an H-bond network are depicted as sticks in the high pH **(A)** and low pH **(B)** structures. In the straight conformation of TM1, Asp 41 interacts via H-bonds with Asp 184 (**A**). However, upon protonation, Asp 41 changes orientation and forms H-bonds with Tyr 139 and Thr 202 (**B**). The resulting conformation change is associated with TM1 bending and TM5 and TM6 movement away from the membrane normal. This collapses the drug binding cavity in the N-lobe and is thought to lead to substrate extrusion.

NFX is found deep within the N-lobe (Fig. 1.7B) and binding is mediated by residues Gln 34, Tyr 37, Asn 153, Met 173, Ser 177, Thr 202, Ser 205, Met 206, Thr 209 and Ile 21. Notably some of these residues are involved in the H-bond network in the N-lobe (Fig. 1.9). Alanine substitution mutations of Met 173, Asn 180, and Met 206 were shown to attenuate PfMATE mediated resistance to NFX and abolished Et and H^+ transport (114).

The structures of PfMATE in complex with cyclic peptide inhibitors, MaD3S, MaD5 (Fig. 1.7C and 1.7 D, respectively), and MaL6 (not shown), were also determined (114). Structural analysis suggests that Mad3S and MaD5, the more potent inhibitors of drug efflux in transport and resistance assays, bind to the central cleft and substrate binding site of PfMATE in the OF conformation (Fig. 1.7C, D). Binding is mediated by Gln 34, Asn 38, Asn 154, Met 206, and Gln 253. The reported biochemical studies of substitution mutants with these inhibitors are limited but do indicate that a M206W mutant of PfMATE recovers H^+ transport but not Et transport in the presence of these inhibitors (114, 116).

Notably absent among the crystal structures of the MATEs was an inward facing (IF) structure. The current dogma of membrane transport proposes alternating access of the substrate binding site to the extracellular and intracellular sides of the membrane (108). While many laboratories studying MATE transporters have postulated such a conformation must exist in the transport cycle, such a conformation had proven elusive. However, an IF structure of PfMATE was recently reported together with OF structures. The IF structure (PDB ID: 6FHZ) was determined from crystals obtained via LCP in a 0.1 M citrate buffer at pH 5.0 with 0.1 M NaCl. Notably, affinity chromatography purified PfMATE was incubated with *P. furiosus* lipids before additional purification and preparation for crystallization trials that yielded crystals of IF PfMATE. The OF structures were determined from crystals obtained via LCP (PDB ID: 6GWH) in a 0.1M citrate buffer at pH 5.0 with 0.1M NaCl and the sitting drop vapor diffusion method (PDB ID: 4MLB, 6FHB) with reservoir solutions containing PEG2000 monomethyl ether in ADA-HCl buffer at pH 6.5.

Compared to the previously published OF structures of PfMATE, the IF structure reveals extensive structural repacking of TMs. On the extracellular side the N-lobe and C-lobe TMs converge, while on the intracellular side, TMs 2 and 3 in the N-lobe and TMs 8 and 9 in the C-lobe diverge and open the intracellular gate (Fig. 1.10B). TM7 in the C-lobe bends slightly toward the N-lobe (Fig. 1.10A, right panel) while TM1 undergoes partial unwinding and pivots about Gly

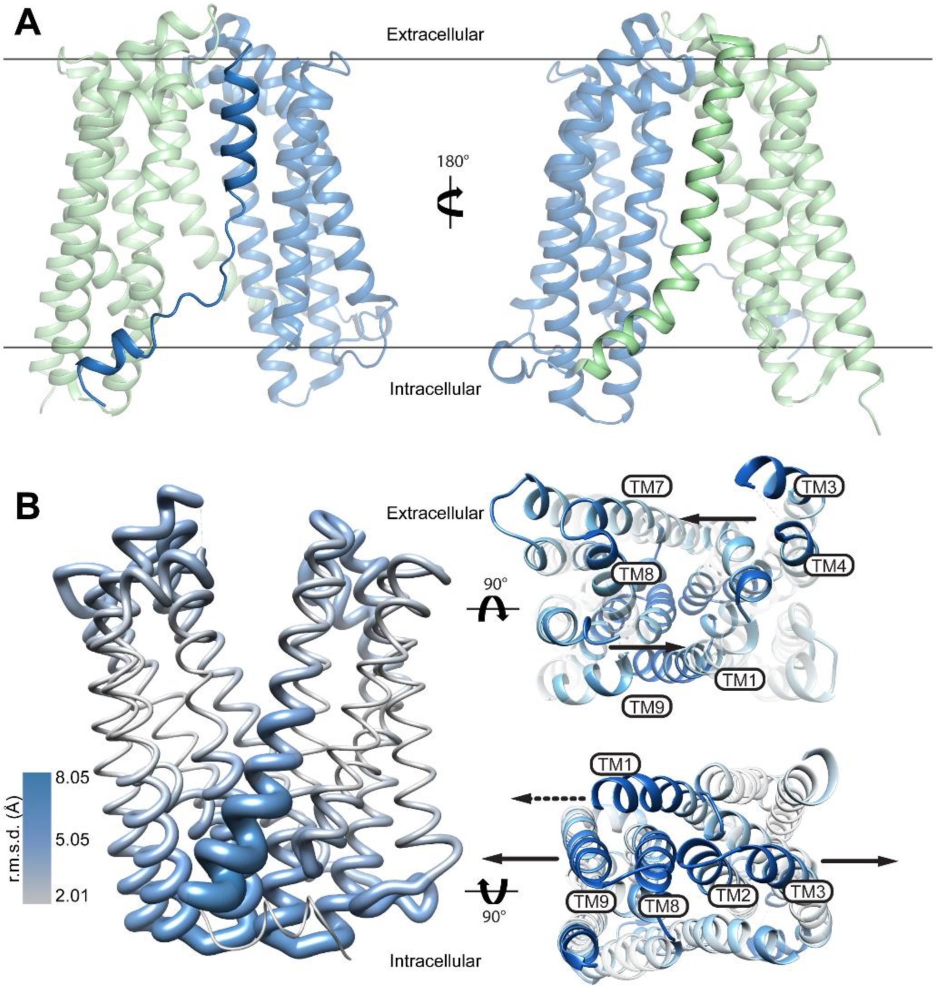

Figure 10: Crystal structure of PfMATE in an IF conformation (PDB ID: 6FHZ) (**A**). N- and C-lobes are colored blue and green, respectively.TM1 (highlighted) is associated with the C-lobe at low pH and is only partly helical, suggesting a great degree of flexibility (**A**, **left panel**). TM7 is associated with the N-lobe and is bent toward the N-lobe (**A**, right panel). (**B**) Comparison of OF and IF crystal structures of PfMATE. The RMSD was derived from the alignment of the OF (PDB ID: 3VVN) and IF (PDB ID: 6FHZ) structures and depicted on a ribbon representation of the OF structure. Viewed from the extracellular and intracellular sides of the transporter, arrows indicate the direction of predicted movement of TMs in the OF to IF transition. The dashed arrow in the intracellular view points to TM1 unwinding.

30 27° in the Y/Z plane and 42° in the X/Z plane (Fig. 1.10A, left panel). As noted, the IF structure was determined from protein incubated with native *P. furiosus* lipids while crystals obtained in the absence of *P. furiosus* lipids adopted the OF conformation (Fig. 1.11A, left panel). Furthermore, as the crystals corresponding to both structures were obtained at low pH this implies that the IF

structure is associated with native lipids. Indeed, Zakrzewska et al. also assert that lipids may be a substrate for PfMATE, further evidenced by the observation of densities corresponding to monoolein in the previous crystal structures reported by Tanaka et al., albeit at high pH.

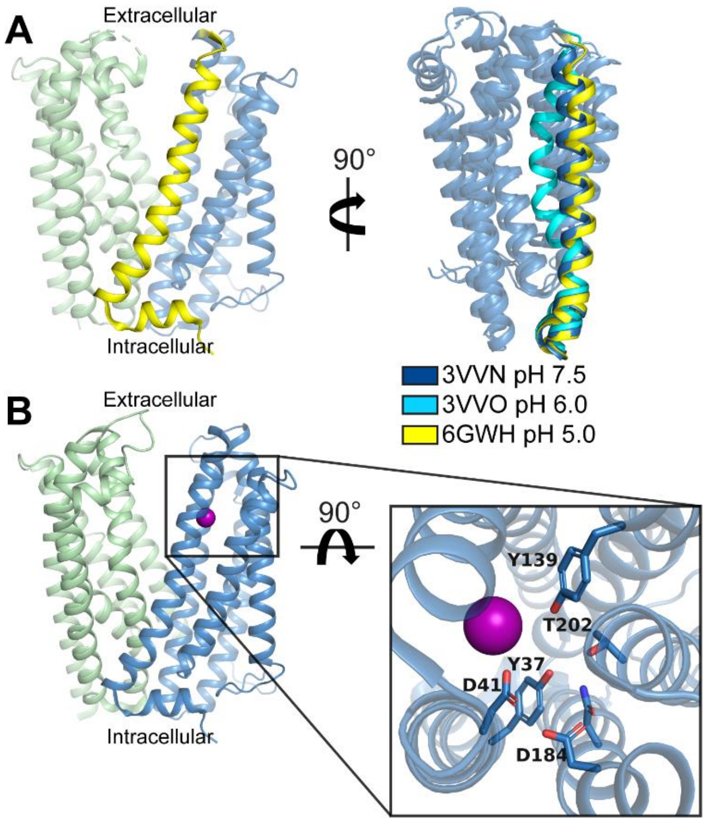

Figure 1.11: **OF structures determined by Zakrzewska et al. at low pH depict TM1 in a straight conformation**. Structures determined from crystals obtained by LCP (PDB ID: 6GWH) (**A**) or sitting drop vapor diffusion (PDB ID: 6FHB) (**B**) with precipitant solutions at low pH adopt the same conformation. 6GWH was aligned to 3VVN (neutral pH) and 3VVO (pH 6.0). The N-lobe is shown in **A** (right panel) with TM1 highlighted. For clarity, TMs of the C-lobe are not depicted. Residual density corresponding to Cs^+ is depicted in the N-lobe (blue) of PfMATE (**B**). The Cs^+ ion is coordinated by conserved residues in the N-lobe (**B**, **inset**).

Interestingly, the OF conformations obtained at low pH diverged with the previous OF structures. Notably, TM1 is not bent in the OF structures reported by Zakrzewska et al. irrespective of the crystallization media (Fig. 1.11A, right panel). Collectively, these findings would imply that formation of the IF state is independent of protonation. The authors also reported a previously unobserved anomalous difference electron density assigned to Cs^+, a sodium congener, adjacent to Asp 41 in one of the OF structures (Fig. 1.11B, inset). Therefore, while the IF structure of PfMATE has provided much insight, it has inspired questions regarding the identity of the coupling ion. Though Tanaka and colleagues demonstrated H^+-dependent transport (114), MD simulations reported here and elsewhere support the role of Na^+ as the coupling ion for PfMATE (117, 118). Therefore, further investigation must be conducted to elucidate the role of H^+ and Na^+ and substrates in the OF to IF structural changes and their relevance to multidrug transport.

ClbM

One of the more significant contributions to the investigation of the MATE transporters was a report on the structures of the ClbM MATE transporter from *E. coli*. The *clbM* gene which encodes the ClbM transporter is located on the *pks* gene island, which is implicated in colibactin biosynthesis. Colibactin is a genotoxin that has been implicated in double stranded-DNA breaks and neoplastic changes (119–121) and has been shown to promote the development of colorectal cancer (CRC) in azoxymethane-treated *Il10*$^{-/-}$ mice (122). ClbM facilitates the export of the prodrug scaffold of precolibactin to the periplasmic space of *E. coli*, thus mediating colibactin toxicity. The ClbM transporter was therefore the first bacterial MATE transporter with a defined biological function that was structurally characterized.

Two structures of ClbM were reported, with and without cation (PDB ID: 4Z3P and 4Z3N, respectively). These structures were reported as part of a larger study that established that ClbM is essential in mediating the genotoxic effects of colibactin in mice and zebrafish (123). Crystallization experiments were performed using LCP with monoolein and 30% PEG 500 DME, 100 mM Li2SO4, 400 mM NaCl and 100 mM sodium cacodylate, pH 6.8 precipitant solution (123). The structures were determined by molecular replacement using PfMATE (3VVN) as a search model and solved to a resolution of 2.7 Å for the apo structure and 3.3 Å for the cation-bound structure (Fig. 1.12A, B).

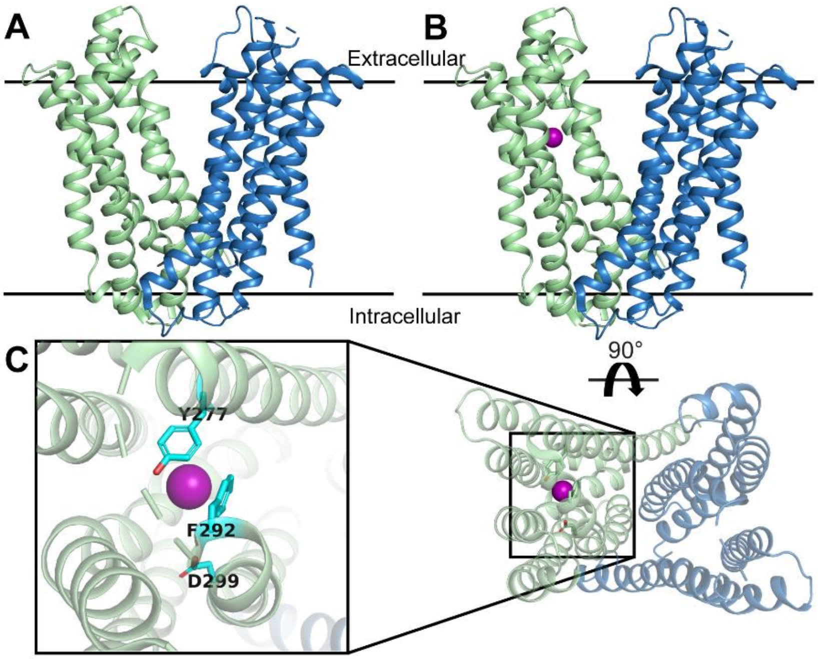

Figure 1.12: **Crystal structures of ClbM reveal Apo (A)** [PDB ID: 4Z3N] **and cation bound (B)** [PDB ID: 4Z3P] **structures adopt the same conformations**. The N-lobe and C-lobes are colored blue and green respectively. Rb^+ is bound to the C-lobe (**C**) and is coordinated by residues on TMs 7 and 8 (inset) in a cation-π interaction. Side chains of residues are depicted as sticks and are colored in cyan.

The structures of ClbM adopt an OF conformation with similar topology to other MATE transporters (Fig. 1.12A, B), however, IL6-7 is not resolved in these structures unlike the structures for all other reported MATE transporters. Notably, the bent conformation of TM1 in PfMATE is not observed in the structures of ClbM, however, the pH at which the ClbM crystals were obtained is higher than the pH at which the bent form of PfMATE was obtained. The volume of the internal cavity of ClbM is much larger than reported for other MATE structures, ostensibly to accommodate the precolibactin molecule.

ClbM is reportedly a member of the DinF subfamily based on sequence similarity to PfMATE. Indeed, the N-lobe of ClbM contains conserved residues such as Asp 53, Asn 194, Asp 199 which are homologous to Asp 41, Asn 180, Asp 184 in PfMATE (Fig. 1.9). These residues participate in an H-bond network that is a determinant of PfMATE function (114). However, in

ClbM, Rb^+, a sodium analog, is found bound in the C-lobe suggesting that ClbM may be Na^+-coupled (Fig. 1.12B). Mousa et al. also demonstrate in a later study that ClbM is able to efflux Et and R6G with a Na^+, K^+, or Rb^+ gradient (43). Interestingly, R6G efflux, but not Et efflux, was induced at low pH and was attenuated at higher pH (43). This result suggests that ClbM is cation promiscuous.

The Rb^+ atom in the cation-bound structure of ClbM is found bound in the C-lobe, which is inconsistent with previous reports of PfMATE and DinF, where coupling ion is thought to be coordinated by conserved residues in the N-lobe (112, 113, 117, 118). Rather, Rb^+ binding in the C-lobe of ClbM is reminiscent of NorM-Ng and NorM-Vc. However, the Rb^+ atom is coordinated solely by cation-π interactions involving the side chains of Y277 and F292 on TMs 7 and 8, respectively (Fig. 1.12C, inset). Alanine mutations of these residues, as well as of the N-lobe residues involved in the H-bond network, failed to substantially attenuate the efflux activity of ClbM. These data led Mousa et al. to conclude that ClbM can couple to both Na^+ and H^+ gradients to achieve substrate efflux.

VcmN

The structure of TM1 reported for PfMATE by Tanaka et al. (114) at low pH inspired much debate as such a conformation was not observed in prior or subsequent studies of other MATE transporters. Furthermore, TM1 of PfMATE was observed in the same conformation regardless of the crystallization conditions employed by Zakzrewska et al. (117). However, three structures of the DinF MATE transporter VcmN from *V. cholerae* were reported under different pH conditions in two conformations mirroring the structures reported by Tanaka et al. (114). Crystallization experiments were performed using LCP with monoolein and precipitant solutions at pH 7.5 – 8.0 and pH 5.0 (124, 125). The structures were determined by molecular replacement using PfMATE (3VVN) as a search model and solved to a resolution of 2.2 Å for the pH 7.5 structure, 2.5 Å for the pH 5.0 structure and 2.8 Å for the VcmN D35N structure (Fig. 1.13).

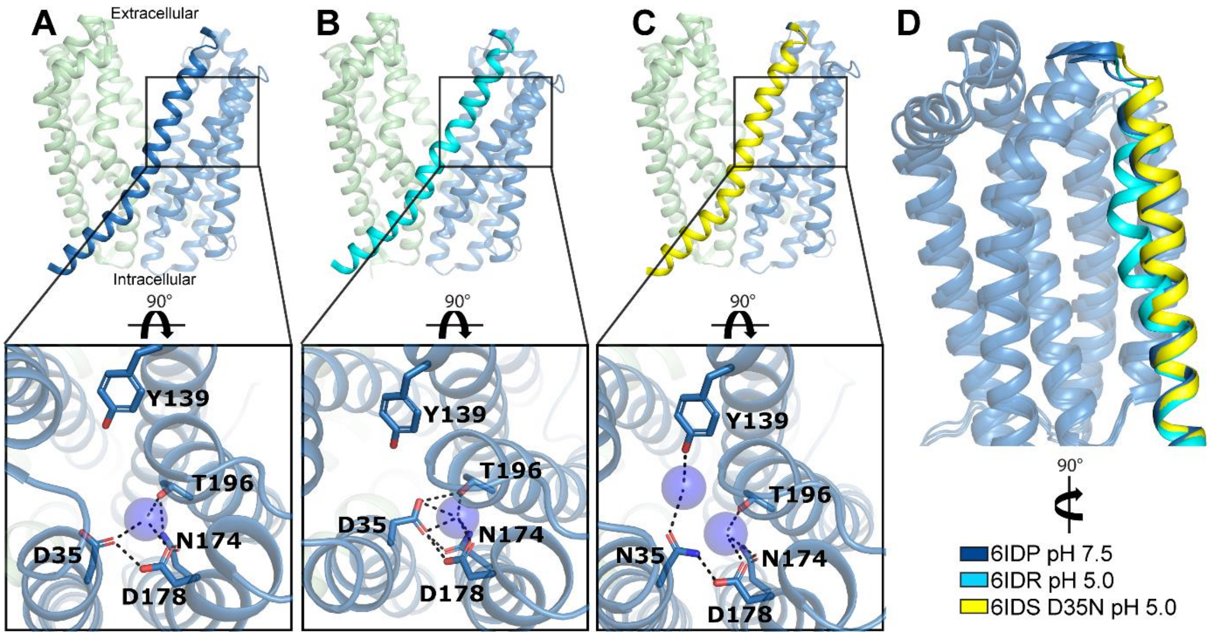

Figure 1.13: **Structures of VcmN reveal that the transporter undergoes TM1 bending at low pH**. TM1 is highlighted in structures at neutral pH (PDB ID: 6IDP) (**A**), at low pH (PDB ID: 6IDR) (**B**), and in VcmN D35N at low pH (PDB ID: 6IDS) (**C**) in blue N- and C-lobes are colored blue and green respectively. The insets depict the side chains that participate in an H-bond network in the N-lobe that is mediated by water (shown as a blue sphere). An alignment of the three crystal structures reveals that at low pH, TM1 is bent (**D**) similar to PfMATE.

All the structures of VcmN reported by Kusakizako et al. (125) adopt an OF conformation (Fig. 1.13). However, an alignment of these crystal structures reveals structural differences in the N-lobe in TM1 and TMs 5 and 6, reminiscent of PfMATE. TM1 of VcmN was bent at the conserved Pro 20 and Gly 24 in the structure determined from crystals obtained at low pH. A putative water mediated H-bond network in the N-lobe (Fig. 1.13A, inset), similar to that shown for PfMATE, involving Asp 35 on TM1, Asp 178 on TM5, and Thr 196 on TM6 is substantially rearranged with TM1 bending. In the bent conformation of TM1 the side chain of Asp 35 points into the N-lobe cavity where it recruits Asn 174, Asp 178, and Thr 196 in a new H-bond network (Fig. 1.13B, inset). That this bending occurs at low pH suggests a mechanism similar to PfMATE wherein protonation of the conserved aspartate on TM1 results in TM1 bending, rearrangement of the H-bond network, and movement of TMs 5 and 6 away from the membrane normal. This would collapse the N-lobe cavity and result in release of substrate. However, the structure of TM1 in the VcmN D35N mutant, a protonation mimic, adopts a conformation more closely resembling the pH 7.5 structure in which TM1 is straight. A closer inspection reveals that this mutant forms an H-bond network that is distinct from the low pH structure whereby Asn 35 engages Tyr 133 in a water mediated H-bond network but not Thr 196 (Fig. 1.13C, inset). However, the authors reason that VcmN D35N could represent a protonation intermediate that occurs before TM1 bending and the rearrangement of the H-bond network in Fig. 1.13B.

Kusakizako et al. also demonstrated in Et efflux assays that the transport activity of the VcmN D35N mutant is attenuated. This is consistent with previous reports of PfMATE and DinF-Bh, underscoring the importance of this conserved Asp and the H-bond network in the N-lobe to transport activity. While Et efflux assays here using spheroblasts demonstrate that transport is H^+-dependent, it is not indicated whether a sodium dependence was investigated. As the structural and biochemical evidence for H^+- and/or Na^+-dependent transport mounts, it would behoove researchers to investigate the structural and biochemical consequences of coupling multiple cations to substrate binding and transport by the archaeal and bacterial MATE transporters of the NorM and DinF subfamilies.

Eukaryotic subfamily of MATE transporters

Structural investigation of MATE transporters has been dominated by members of the NorM and DinF subfamilies. While extremely significant given the role of the bacterial MATE transporters in multidrug transport and resistance, the study of eukaryotic MATE transporters, especially of plants and animals, have shown that they are key determinants in regulating homeostasis and toxicity in the tissues in which they are expressed and their activity can affect the overall health and survival of an organism. As discussed previously, multiple paralogues of MATE transporters are found in plants where they are localized in different tissues fulfilling a variety of roles, from attenuating heavy metal toxicity in soil to hormone signaling in leaves and shoots. In humans, many investigations have demonstrated the importance of MATEs in mediating the pharmacokinetics of drugs and toxicity in the kidney and liver where the MATEs are predominantly expressed.

Given the amino acid sequence analysis and available biochemical data, it is thought that the mechanism and structures of eukaryotic MATE transporters differ from those of NorM and DinF transporters (70, 106). Conserved residues in the N-lobe that constitute the H-bond network and are critical for function in the NorM and DinF MATE transporters are conspicuously absent in eukaryotic MATEs (Fig. 1.2). The conserved aspartate on TM1 has repeatedly been demonstrated to be critical for transport in NorM and DinF subfamily members, however, in the eukaryotic MATEs this residue is replaced with a serine. However, the proline residue that is thought to facilitate TM bending upon cation binding in the N-lobe in the DinF MATEs is conserved across all the MATE subfamilies; therefore, other mechanisms must exist to effect conformational change in the N-lobe, if indeed TM1 bending is relevant to ion-coupled substrate transport.

Recently, the structures of MATEs from *Camelina sativa* (CasMATE) and *Arabidopsis thaliana* (AtDTX14) were reported, as the first eukaryotic MATE structures. The implications of the structural features of these transporters and their relevance are discussed below.

CasMATE

C. sativa is a member of the Brassicaceae family and has emerged as a viable industrial oil seed crop (126). It is adaptable to different environmental conditions and has low requirement for water and nutrients, early maturity, and resistance to common cruciferous pests and pathogens (127, 128). In plants, MATE transporters have been associated with several of these advantageous traits (46–48, 56–58, 129). Amino acid sequence analysis of the CasMATE transporter from *C. sativa* reveals that it is more closely related to the NorM subfamily than the DinF subfamily. Conserved aspartate residues on TM1 and TM5 in the N-lobe of the NorM and DinF transporters are conspicuously absent in CasMATE and other eukaryotic MATE transporters

(Fig. 1.2). However, residues Glu 255 and Asp 371 in the C-lobe of NorM that are implicated in cation binding are conserved among the NorM and Eukaryotic MATE subfamilies and are homologous to Glu 265 and Asp 383 in CasMATE (Fig. 1.2). This may imply a mechanism of cation binding in the plant MATE transporters similar to that of NorM transporters.

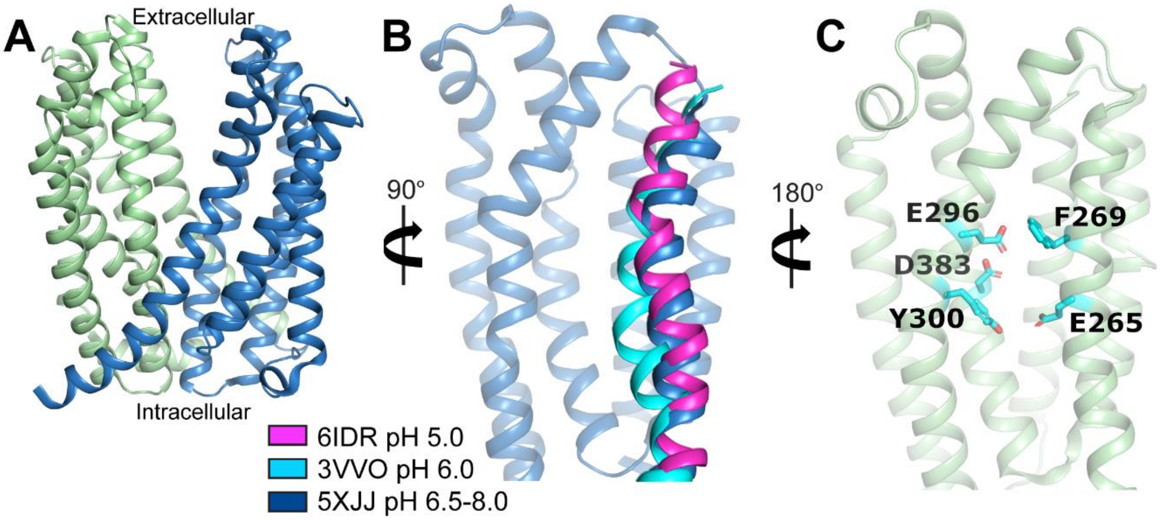

Figure 1.14: **CasMATE structure reflects elements of NorM and DinF MATE subfamilies**. CasMATE adopts an OF conformation (PDB ID: 5XJJ) (**A**). A structural alignment with PfMATE (cyan) and VcmN (magenta) structures determined at low pH reveals TM1 of the N-lobe of CasMATE adopts a bent conformation at low pH (**B**). A view of the C-lobe cavity also reveals that CasMATE contains residues that are conserved among the NorM subfamily thought to be involved in ion/substrate transport (**C**).

A structure of CasMATE was the first reported from the eukaryotic MATE subfamily (Fig. 1.14). A truncated construct of CasMATE was expressed and purified and used in crystallization trials. Crystals were obtained via LCP with monoolein in precipitant solutions at pH 8.0, pH 7.5, and 6.5. The structure was determined via X-ray diffraction and molecular replacement using PfMATE (3VVN) as a search model and solved to a resolution of 2.9 Å (PDB ID: 5XJJ).

CasMATE has similar topology to other MATE transporters with 12 TMs arranged into two 6 TM bundles that constitute the N-lobe and the C-lobe connected by a 12 amino acid intracellular loop (Fig. 1.14A). The transporter adopts an OF conformation like that seen for the majority of the structures reported thus far. The TMs of the N-lobe and the C-lobe each constitute binding cavities for ligand binding; however, the N-lobe cavity is narrower than the C-lobe cavity by virtue of bulky amino acid side chains on TMs 2 and 6 oriented into the cavity (130). Interestingly, TM1 of CasMATE is bent in a similar manner as VcmN and PfMATE at low pH, which was shown to reduce the volume of the N-lobe cavity to effect substrate extrusion (Fig. 1.14B) (114). Additionally, in the C-lobe, TM12 contains an extended length of residues at the C-terminus that adopts a helical structure and runs parallel to the lipid bilayer at the interface of the membrane and the cytoplasm. In the C-lobe, conserved residues Glu 265 and Asp 383 along with Tyr 300, are clustered in a similar manner to NorM transporters, implying a similar mechanism of cation coordination. However, no cation is observed in the structure and it is unclear whether the authors attempted to soak crystals in CsCl or RbCl for further crystallographic analysis. Additionally, no functional assays to establish proton/cation dependence or substrate transport are reported. Therefore, while the structure is informative to establish a structural model for the eukaryotic MATE subfamily, further investigation is required to address fundamental questions regarding substrate/ion dependent transport.

AtDTX14

AtDTX14 MATE transporter is one of 58 MATE paralogues expressed in *A. thaliana*. The remarkably large number of MATE transporters encoded in the genome of *A. thaliana* underscores their physiological importance in plants. AtDTX14 shares ~32% sequence similarity to hMATE1. A P36A mutant of AtDTX14 was expressed and purified and was crystallized by LCP with monoolein in 100 mM Na-citrate, pH 5.0–5.3, 100 mM $MgSO_4$, 50–100 mM NaK-tartrate-tetrahydrate and 20–24% PEG550MME precipitant solution. The X-ray diffraction data was phased by molecular replacement using the NorM-Vc structure (3MKT) as the search model and the structure was subsequently solved to 2.6 Å (PDB ID: 5Y50).

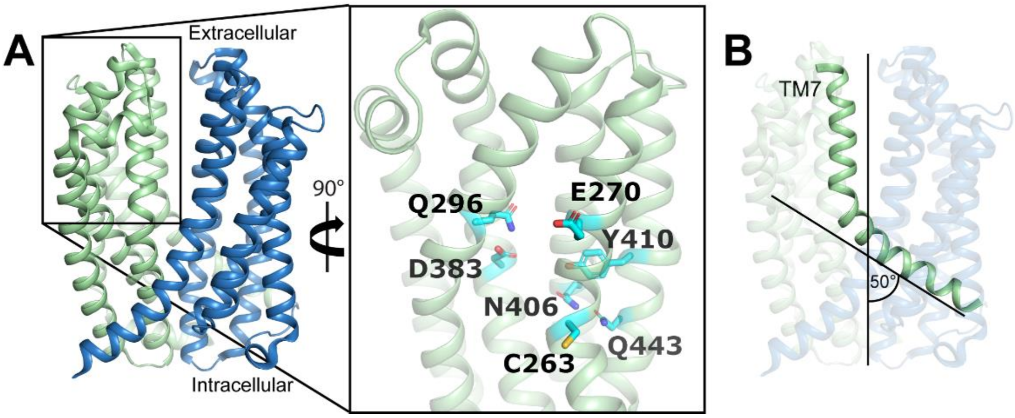

Figure 1.15: **Structure of AtDTX14 MATE adopts an OF conformation**. AtDTX14 N- and C-lobes depicted in blue and green, respectively, are closer to each other than in other MATE transporters (PDB ID: 5Y50) (**A**). The C-lobe of the transporter (inset) is composed of residues, depicted as sticks, that constitute an H-bond network. These residues are homologous to C-lobe residues in the NorM subfamily. Protonation of this network may facilitate the N- and C-lobe orientation by bending the N-terminus of TM7 50° towards the membrane normal (**B**) with concomitant straightening of the C-terminus end of TM7.

As with CasMATE, the structure of AtDTX14 is in an OF conformation, however, the TMs on the extracellular side of AtDTX14 are more closely packed and results in a narrower extracellular cleft (Fig. 1.15A). TM12 also adopts a similar conformation with an additional helical region at the C-terminus. Unlike CasMATE, TM1 of AtDTX14 is straight, however, no inferences can be made regarding the conformational differences of TM1 given that Pro 36 is mutated and such a mutation was shown to abolish TM1 bending in PfMATE (Fig. 1.8D). However, unlike PfMATE where the P26A mutation also renders the transporter inactive in drug resistance assays, AtDTX14 P36A is able to convey resistance to NFX in its host *E. coli* strain, though resistance is attenuated compared to WT. As the residues that constitute the H-bond network in the N-lobe of NorM and DinF transporters are not conserved in the eukaryotic MATEs, the authors suggest that the AtDTX14 P36A resistance data implies that the transport mechanism is independent of TM1 conformational change. However, the attenuated resistance suggests compromised activity and would implicate TM1 in the transport mechanism.

Notably, in the structure of AtDTX14, TM7 is bent approximately 50° about Cys 263 (Fig. 1.15A, inset; 15B). In this hinge region are conserved residues Glu 265 on TM7 and Asp 383 on TM10, reminiscent of CasMATE and the NorM transporters. Additional residues Gln 296 on TM8, Asn 406 and Tyr 410 on TM11, and Gln 443 on TM12 participate in an H-bond network in the C-lobe with Glu 265 and Asp 383 (Fig. 1.15B). Therefore, given that this structure was determined from a crystal obtained at low pH it is possible that this structure may represent a protonated transport intermediate. Indeed, NFX resistance of *E. coli* expressing Q296A, D383A, or Q443A mutants of AtDTX14 is compromised. It is unclear, however, whether mutants of Glu 265 or Gln 296 were also tested. Without such functional studies, further experimentation must be done in order to delineate the mechanism of ion/substrate dependent transport.

Implications of structural studies of MATE transporters

Crystallography has proven indispensable for determining the three-dimensional structure of transporters and has allowed us to reconcile previous biochemical studies and pursue further investigations into functional details regarding substrate/ion transport and the concomitant conformational changes. However, transporters are dynamic assemblies that constantly sample multiple conformations and favor different conformational equilibria during the transport cycle. Given that most MATE transporters crystallized thus far reflect structures occupying an OF conformation, defining the mechanistic details of ion coupled antiport are difficult. Many of the proposed transport models do hypothesize transition states where ion and substrate are preferentially bound to an occluded or IF conformation. A recent structure of PfMATE in an IF conformation described above, helped to define the structural elements involved in the OF to IF conformation change. However, the conditions under which the IF structure was obtained in addition to the other reported OF structures by Zakrzewska et al. (117) confounds the previous findings of Tanaka et al. (114) concerning ion-dependence and casts doubt on the functional consequence of TM1 bending in the conformational cycle..

Crystallization of membrane proteins within the confines of the crystal lattice obscures dynamic modes essential for the OF to IF conformation by stabilizing energetically favorable conformers in the ensemble. Confounding the mechanistic interpretation of the data are inconsistencies concerning structural elements such as TM1 bending and the effect of the coupling ion and substrate on conformational change. Additionally, amino acid sequence analyses have identified several conserved residues that have been shown to be critical for drug resistance and ion flux (Fig. 1.2). However, how these residues are involved in ion-coupled conformational dynamics of the MATE transporters have only recently been illuminated.

Investigating conformational dynamics of MATE transporters

The native environment of multidrug transporters such as the MATEs is the lipid bilayer which differs in its physicochemical properties from detergent micelles. The use of monoolein in LCP has proven more amenable for MATE protein crystallography (114, 117, 123, 124, 130, 131) and other high impact target proteins such as G-protein coupled receptors (GPCRs) (132, 133). However, the addition of precipitant solutions to monoolein for LCP results in a bicontinuous cubic phase which consists of interpenetrating but non-contacting water channels separated by a highly curved lipid bilayer that can alter protein dynamics and conformational sampling (134–136). Recent studies have shown that the biophysical properties of the membrane and lipid-protein interactions play an integral role in modulating the structure (137), stability (138), function (139), oligomeric state (140), and conformational dynamics (141) of transporters.

Unrestrained by the confines of the crystal lattice, proteins can sample multiple conformations that can be probed in a time dependent manner to determine their extent and amplitude in a native-like environment. Investigation of the conformational dynamics of MATE transporters has been limited with only a few studies reported to date. Investigations have been carried out using hydrogen-deuterium exchange mass spectrometry (HDX-MS) and double electron-electron resonance (DEER) spectroscopy of NorM from *Pseudomonas stutzeri* (NorM-Ps) and NorM-Vc, respectively.

HDX-MS of NorM-Ps

HDX-MS monitors the exchange rates of the backbone amide hydrogens with surrounding heavy water molecules. Differences in deuterium incorporation at specific segments of the protein under different biochemical conditions can be used to map structural changes and detect ligand binding sites (142, 143). HDX-MS studies of NorM-Ps, a proton coupled MATE transporter, sought to define the conformation of the transporter in β-DDM detergent micelles and identify structural changes that occur in the presence of the substrate DAPI. As no structure of NorM-Ps has been reported, the authors generated a homology model based on NorM-Vc (PDB ID: 3MKU). Eisinger et al. (144) report that at neutral pH (pH 7.5) NorM-Ps has higher incorporation of deuterium at its intracellular side versus its extracellular side. This would imply that NorM-Ps adopts an IF conformation in detergent at neutral pH. This result is in stark contrast to the crystallographic data for other MATE transporters where the majority of the structures occupy an OF conformation, irrespective of the biochemical conditions. In the presence of DAPI, NorM-Ps displays a decrease in deuterium incorporation in segments of TM7 and TM10 where the conserved residues Glu 257 and Asp 373, respectfully, are located. Consistent with antiport models which posit that substrate stabilizes an OF structure (19, 145), in the presence of DAPI there was a concomitant increase in deuterium incorporation in the extracellular halves of TM1, TM2, and TM8.

Mutants D38N and D373N of NorM-Ps were previously shown to abrogate DAPI efflux from everted vesicles (146). The latter mutant also demonstrated reduced binding affinity for DAPI. Therefore, these mutants were used in HDX-MS experiments to further delineate the transport mechanism. For NorM-Ps D38N, DAPI binding occluded the previously defined DAPI binding site resulting in decreased deuterium uptake similar to WT. However, the uptake of deuterium at the periplasmic side of the transporter was reduced with deuterium incorporation occurring only on the extracellular half of TM1. This implicates Asp 38 in the IF to OF conformational change of NorM-Ps. Consistent with its compromised binding of DAPI, deuterium incorporation was not affected in the NorM-Ps D373N mutant with DAPI present.

The study reported by Eisinger et al. (144) established the effect of substrate on driving conformational change of the transporter. While the results of HDX cannot be used to draw conclusions regarding the structure of the transporter when substrate is bound, the study represents a significant advancement from static structures to dynamics.

DEER of NorM-Vc

DEER, or pulsed electron paramagnetic resonance (EPR), was applied in two studies of NorM-Vc. DEER instrumentation and analysis have been reviewed extensively and will not be discussed in great depth here. Briefly, a paramagnetic nitroxide spin label is introduced at a cysteine residue engineered into the primary sequence of a protein in which native cysteines have been removed. The dynamics of the spin label report mobility and solvent accessibility to membrane and water-soluble reagents. The introduction of two spin labels into the protein complements accessibility and mobility with the ability to measure distances between spin label pairs, up to 80 Å (147). The spin echo decay of one label is modulated by the intramolecular dipolar interaction with the other label on the same protein molecule. This results in an oscillating echo decay, the periodicity of which reflects the average distance between the spins in the conformational ensemble of the protein (148).

Steed et al. (149) applied DEER to the study of NorM-Vc using ruboxyl, a spin-labeled derivative of daunorubicin, a substrate of NorM transporters. Norm-Vc bound ruboxyl with the same affinity as daunorubicin and demonstrated concentration dependent spin mobility changes indicating binding. Sodium failed to displace or inhibit ruboxyl binding, however, doxorubicin, another known substrate of NorM-Vc was shown to compete with ruboxyl binding, as indicated

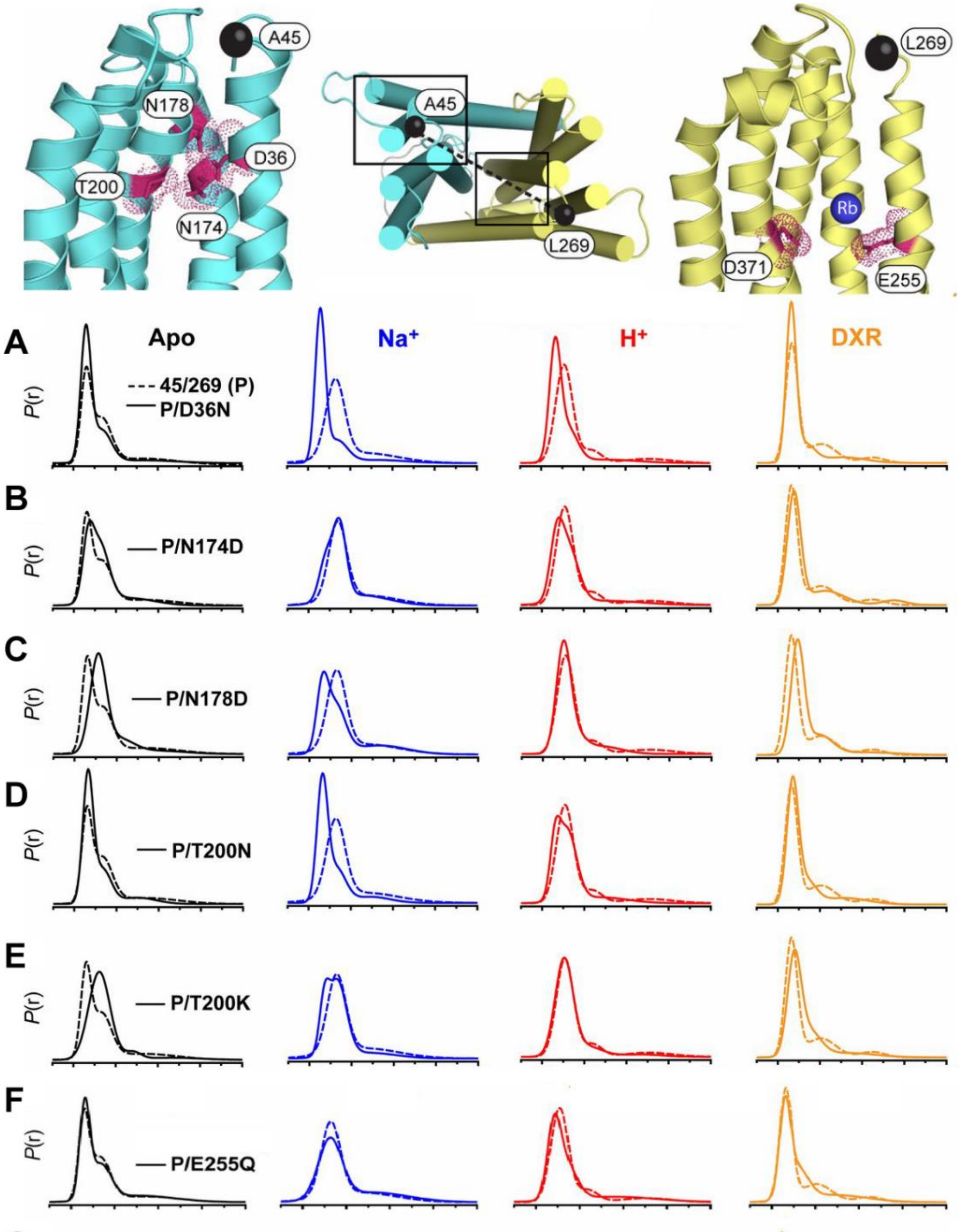

Figure 1.16: **Conformational dynamics of N-lobe and C-lobe background mutants of NorM-Vc**. Polar residues lining a cavity within the N-lobe of NorM-Vc targeted for mutagenesis are shown as sticks outlined by a space-filling representation. The location of conserved E255 and D371 within the C-lobe is shown highlighting interactions with a bound Rb^+. The location of spin labels for the A45C/L269C pair is shown as black spheres connected by a dashed line. (**A**–**G**) *P*(*r*) of each mutant (solid line) is compared with the *P*(*r*) of the parent construct (P, dashed line) for each biochemical condition.

by increased spin mobility originating from the ruboxyl molecules. To determine the site of high affinity ruboxyl binding, single spin labels were introduced into NorM-Vc and DEER experiments were carried out with ruboxyl. Distance distributions from the DEER experiments placed the position of the nitroxide moiety of the bound ruboxyl in the periplasmic cleft near TM7 of the transporter, although, given the flexibility of the linkage between the drug and the nitroxide, the orientation of the ruboxyl molecule could not be established. However, this is consistent with the location occupied by substrates in the crystal structures of NorM-Ng.

The effect of sodium was unsurprising, given later investigations that further illuminated the principles of ion/substrate interaction in NorM-Vc (150, 151). Claxton et al. used spin label pairs in NorM-Vc to define the conformational changes that occur with sodium and the drug doxorubicin and, significantly, at low pH to mimic protonation (151). Multicomponent distance distributions determined from DEER measurements of the Apo state of NorM-Vc were modulated in a Na^+- or DXR-dependent manner. These effects were greater for spin label pairs sampling distances across the periplasmic cleft between the N- and C-lobes. Sodium was shown to increase the longer distance populations of these pairs suggesting stabilization of an OF state. Interestingly, low pH induced a decrease in distance, contrary to the effect of Na^+. The pattern of mobility changes for single spin labels on TM1 in response to Na^+ or H^+ suggest rotation or more intriguingly, TM1 bending, which could reflect the structural changes reported for TM1 in PfMATE at low pH. Conversely, DXR stabilized the population of shorter distances, most profoundly between TM1 and TM7.

This TM1/TM7 pair was used as a reporter to determine the role of conserved residues in the N-lobe and the C-lobe as arbiters of conformational changes that underlie transport (Fig. 1.16) (151). A NorM D36N mutant enhanced population of the short distance component of the TM1/TM7 pair but failed to elicit conformational changes in response to Na^+ or H^+ to longer distances (Fig. 1.16A). A similar result was demonstrated for NorM-Vc T200N (Fig. 1.16D). Interestingly, a T200K mutant to mimic an ion bound state by introducing a permanent positive charge induced a shift to a longer distance in the Apo state, which overlaps with the H$^+$-bound state (Fig. 1.16E, black traces). Indeed, this mutant did not demonstrate H$^+$-induced conformational change (Fig. 1.16E, red traces). This effect was also observed for N178D (Fig. 1.16C), which is semi conserved in the NorM and DinF subfamilies. In the latter, this residue is an aspartate. In the C-lobe, mutations of conserved residues Glu 255 and Asp 371 (E255Q and D371N, respectively) did not preclude Na$^+$- and H$^+$-driven conformational change. However, DXR-induced conformational changes were attenuated, consistent with a reduction in DXR binding affinity for these mutants. The authors concluded that the results implicated protonation/deprotonation of E255 and D371 in mediating DXR binding and its conformational intermediate. Moreover, the study conclusively demonstrates the Na$^+$/H$^+$ dependence of NorM-Vc for drug transport.

Significance of further investigations of MATE transporters

As the first H$^+$-coupled DinF MATE transporter crystallized, not only with multiple ligands but in an OF and an IF conformation, many structural elements of a transport mechanism have been reported for PfMATE. However, the bent TM1 structure reported by Tanaka et al. (114) has been roundly criticized as being irreproducible thus challenging the role of this conformation in the transport cycle (113, 117, 118). Though NFX was reported to be bound to the N-lobe of the transporter, residual densities corresponding to monoolein, thought to be mimicking substrate, were observed in the central cleft between the N- and C-lobes and within the cavities of each lobe in the Apo pH 8.0 structure (114). In the C-lobe, the monoolein molecule is close to Gln 253 on TM7, which is homologous to the conserved Glu residue on TM7 seen in the NorM and Eukaryotic MATE subfamilies. In the low pH structure reported by Tanaka and colleagues, the monoolein molecule is displaced from within the N- and C- lobe cavities and is positioned in the central cleft, albeit still in close proximity to Gln 253 on TM7. These results are intriguing since Zakrzewska et al. (117) reported structures of PfMATE in an IF conformation determined from crystals of purified protein incubated in native *P. furiosus* lipids. Moreover, the identity of the coupling ion of PfMATE has also been questioned. Ficici et al. (118) demonstrated that the atomic B-factor of an electron density signal in the N-lobe of PfMATE at Asp 41, previously identified by Tanaka et al. as a water molecule that is a component of the H-bond network (Fig. 1.9), may actually correspond to Na^+. Furthermore, the IF and OF structures reported by Zakrzewska and colleagues were both determined from crystals obtained at pH 5.0, suggesting that the reported structures are independent of proton.

These observations demand further examination of the PfMATE structures and their context within the transport cycle. Additionally, how intermediate states are connected through dynamic fluctuations in structure is an important consideration of ion-coupled transport. Claxton et al. used DEER spectroscopy to identify the consequences of ligand binding on the structural characteristics of NorM-Vc, demonstrating the feasibility of this approach to study the conformational dynamics of the MATE transporters. Such spectroscopic approaches can be used to identify the structural characteristics of intermediate states of PfMATE as well as capture the dynamics associated with specific transporter conformations.

The body of work presented here describes the investigation of the conformational cycle of PfMATE in the transport of substrate using EPR spectroscopy, a technique sensitive to both local and global conformational changes in protein structure. We first seek to define the ion dependence of PfMATE drug transport using a combination of molecular biology and biochemical approaches. Subsequently, we report the conformational changes associated with ions and substrates using DEER and the sequence determinants of these conformational changes. The results correlate conformational changes with transport activity and offer a novel perspective of the mechanistic details of coupled transport in PfMATE.

CHAPTER II

The N-lobe of PfMATE mediates proton coupling required for drug resistance

Crystal structures of the MATE transporters with various bound substrates have identified unique interaction motifs implying divergent transport mechanisms between MATE subfamilies (111–114, 152). TPP, Et, and R6G were found to bind a negatively charged central cavity formed by acidic and polar residues from the N-lobe and C-lobe near the membrane-water interface in the Na^+-coupled transporter NorM from *N. gonorrhea* (NorM-Ng) (111). Ligand-dependent conformational changes were predicted to facilitate an allosteric coupling transport mechanism (111, 153). In contrast, R6G was found buried within the hydrophobic TM core of H^+-coupled DinF from *B. halodurans* (DinF-Bh) in which the majority of contacts are made with N-lobe residues, including a conserved Asp in TM1 that mediates the only charge-charge interaction with the substrate (113). Disruption of this interaction by substitution (D40N) or protonation of the Asp impaired R6G binding, suggesting an overlapping H^+/R6G binding site. Consequently, H^+ binding was implicated in drug release by directly competing with the substrate binding site (113).

Despite these fundamental differences between MATE subfamilies, mechanistic diversity within the DinF subfamily has been the subject of controversy. Crystallographic analyses of the archaeon *P. furiosus* (PfMATE) not only identified a distinct drug NFX binding site deep within the N-lobe, but also a bent conformation of TM1 associated with rearrangement of a hydrogen-bond network putatively induced by protonation of the conserved Asp 41 (114). A similar conformation of TM1 has yet to be reported for DinF-Bh. Thus, in combination with complementary functional

---

This chapter is adapted from the article "The N-lobe of the archaeal MATE transporter PfMATE mediates proton coupling required for drug resistance."

Kevin L. Jagessar contributed to methodology development and was responsible for investigation, data collection and curation, formal analysis, and writing and editing of the article.

analysis, the structures of PfMATE supported a transport model distinct from DinF-Bh, invoking a critical role of the N-lobe in facilitating H^+-dependent conformational changes in TM1 that collapse the norfloxacin binding cavity. Similar structural changes have been described recently for another bacterial MATE of the DinF subfamily, arguing that the bent conformation of TM1 is a conserved obligatory intermediate in the transport cycle (125).

Here, we explore the function of conserved residues previously implicated in H^+ and drug binding within the DinF subfamily to define mechanistic features of the N-lobe that support drug resistance in PfMATE. Our multi-faceted approach incorporates a cell growth assay tailored to uncover PfMATE-mediated resistance to toxic concentrations of R6G in combination with steady-state drug binding and structural analysis. We show that, unlike DinF-Bh, high affinity binding of R6G to PfMATE does not require the charged sidechain contributed by a strictly conserved TM1 Asp. However, R6G resistance is compromised by substitution of N-lobe residues that disrupt formation of a H^+-stabilized structural intermediate. The results highlight a role of the N-lobe in mediating ion coupling to transport through allostery yet support the notion of unique drug binding sites and divergent transport mechanisms within the same subfamily of MATE transporters.

Results

R6G resistance assay: approach and design

Expression of PfMATE promotes cell growth in the presence of the fluoroquinolone antibiotic norfloxacin (114), but resistance to R6G toxicity has not been demonstrated previously. To characterize PfMATE-mediated R6G resistance in vivo, we adapted a cell growth assay previously used to probe the survival of *E. coli* expressing the Na^+/H^+-dependent homolog NorM from *V. cholerae* (NorM-Vc) when subjected to toxic concentrations of DXR (149, 151). This assay was shown to discriminate between variants of NorM-Vc that support or compromise cell growth, facilitating the correlation of apparent drug resistance to ion/drug-dependent conformational dynamics associated with the transport mechanism (151). Similarly, expression of functional PfMATE is expected to increase cell survival in the presence of toxic substrates.

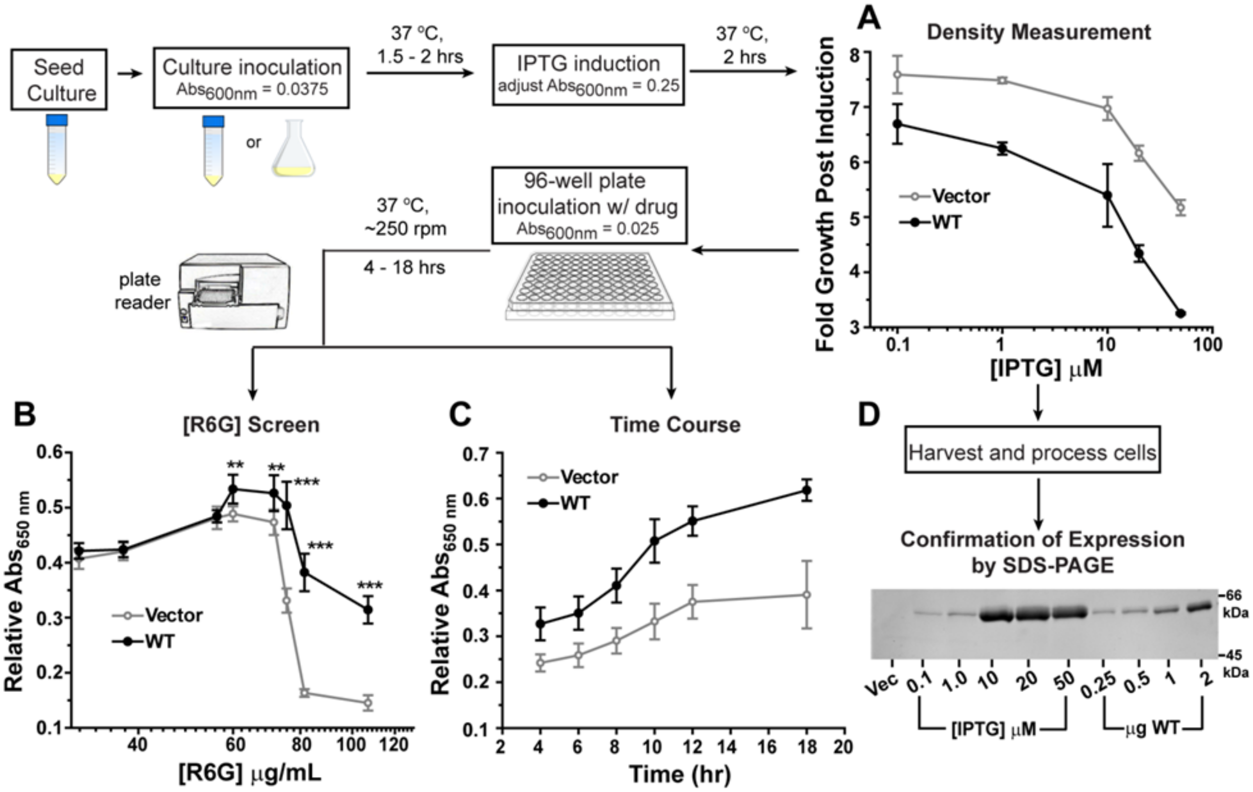

Figure 2.1: **Flow diagram of the R6G resistance assay**. (**A**) Comparison of growth for cells harboring vector (gray line) and WT PfMATE (black line) after 2 hrs induction with different IPTG concentrations. (**B**) Expression of WT PfMATE increases cell survival at elevated R6G concentrations relative to the vector control. Each data point represents the average of two independent experiments. For each experiment, the data was measured in triplicate from separate wells on the plate after 10 hrs at 37 °C. The Abs_{650nm} in the presence of R6G was normalized to the 0 μg/mL R6G well. The standard deviation (SD) is shown for each data point. P-values were determined by an unpaired *t*- test. For (**), P-values range from 0.004-0.009; for (***), P-values are < 0.0001. (**C**) Cells expressing WT PfMATE demonstrate better growth than the vector control at all time points. The Abs_{650nm} in the presence of R6G was normalized to the 0 μg/mL R6G well. The R6G concentration was 75 μg/mL. The data points are shown with the standard deviation, and each data point was generated from an *n*=3-6 independent experiments as described for (**B**). (**D**) The relative expression of WT PfMATE as a function of IPTG concentration was visualized by SDS-PAGE and staining with InVision His tag stain. Purified PfMATE WT used as a standard is shown for comparison.

The experimental paradigm is illustrated as a flow diagram in Fig. 2.1 and additional details are provided in the Experimental Procedures. Briefly, a small seed culture grown overnight from freshly transformed BL21 (DE3) cells was used to inoculate a larger volume of growth medium with a target absorbance at 600 nm (Abs_{600nm}) of 0.0375. The cells were allowed to grow for up to two hours at 37 °C, then diluted to Abs_{600nm} ~0.25 and induced with IPTG. Following a two-hour incubation period for protein production, the cells were seeded into a 96-well plate containing growth medium and the substrate R6G. Cell growth was monitored by the Abs_{650nm}, which was measured by a plate reader over a defined period of time. This wavelength (650 nm) was chosen to minimize the contribution of R6G to the overall absorbance at high (>30 µg/mL) R6G concentrations (Fig. S1). The plate format allowed screening of numerous conditions as a function of time, such as IPTG and drug concentrations. Importantly, cell growth in the absence of drug was incorporated as a control for cell health and viability over the course of the assay, as described below. Therefore, the Abs_{650nm} in the absence of drug was used as a normalization factor to obtain a relative Abs_{650nm}.

R6G resistance assay: identification of PfMATE expression parameters

Standardization of this assay for screening activity of PfMATE required careful consideration of key protein expression parameters. Cell growth post induction is strongly dependent on the IPTG concentration. In general, cells expressing PfMATE WT grew less than cells harboring vector alone (pET-19b) at all IPTG concentrations tested (Fig. 2.1A). This pattern of cell growth was inversely correlated with WT expression levels as visualized by SDS-PAGE analysis, especially in the range of 10-50 µM IPTG which induced robust expression (Fig. 2.1D). Furthermore, cells expressing WT displayed reduced growth relative to the vector in the absence of drug over the course of the assay (Fig. S2A). These observations suggested that WT expression is metabolically challenging and/or toxic to the cell. We thus reasoned that high-level WT expression may reduce cell capacity to proliferate under additional toxic stress and obfuscate

PfMATE-mediated drug resistance. In support of this conclusion, we observed an increase in the growth of cells expressing WT at elevated R6G concentrations (≥ 60 µg/mL) relative to vector alone upon induction with 1 µM IPTG (Fig. 2.1B and Fig. S2B). Enhanced cell survival was seen over the entire time course of the assay at 75 µg/mL R6G after normalizing to growth in the absence of drug (Fig. 2.1C). The ratio of Abs_{650nm} indicated that expression of WT increased cell growth by 53 ± 9% on average (n = 6) relative to vector at the 10 hr time point where the normalized growth curve began to plateau. In contrast, cell growth was greatly impaired at the identical R6G concentration following induction with 10 µM IPTG (Fig. S3).

In addition to the IPTG concentration, potentiation of cell survival was contingent on a full complement of multidrug transporters. Previous applications of this assay with NorM-Vc utilized an *E. coli* strain devoid of seven endogenous multidrug transporters (BL21 (DE3)-Δ7: macAB, yojHI, acrAB, acrEF, emrAB, emrKY and mdtEF) (151, 154). However, PfMATE-mediated resistance to R6G toxicity was neither observed in this background, nor in the BL21 (DE3)-Δ3 strain (deletion of macAB, yojHI and acrAB) relative to vector alone under similar expression conditions (Fig. S4). This result suggested that the elevated R6G resistance conferred by expression of WT PfMATE involved concerted activity of intrinsic transporters.

Amino acid substitutions in the N-lobe of PfMATE compromise resistance to R6G

Previous crystallographic, computational, and functional studies of PfMATE suggested a critical role of the N-lobe in binding of target substrates and coupling to the H^+ gradient to drive transport (114, 155). In conjunction with a highly conserved Pro (Pro 26 in PfMATE) in TM1, a hydrogen bond network composed of residues that line a cavity in the N-lobe was proposed to mediate a H^+-dependent conformational change in TM1 that facilitates substrate extrusion. Sequence alignment and phylogenetic analysis indicated that these residues are highly conserved (156, 157) (Fig. S5). Consistent with this result, substitution of these residues impaired resistance to norfloxacin and transport of ethidium (114). We tested a subset of these variants to ascertain the contribution of these residues to R6G resistance (Fig. 2.2A).

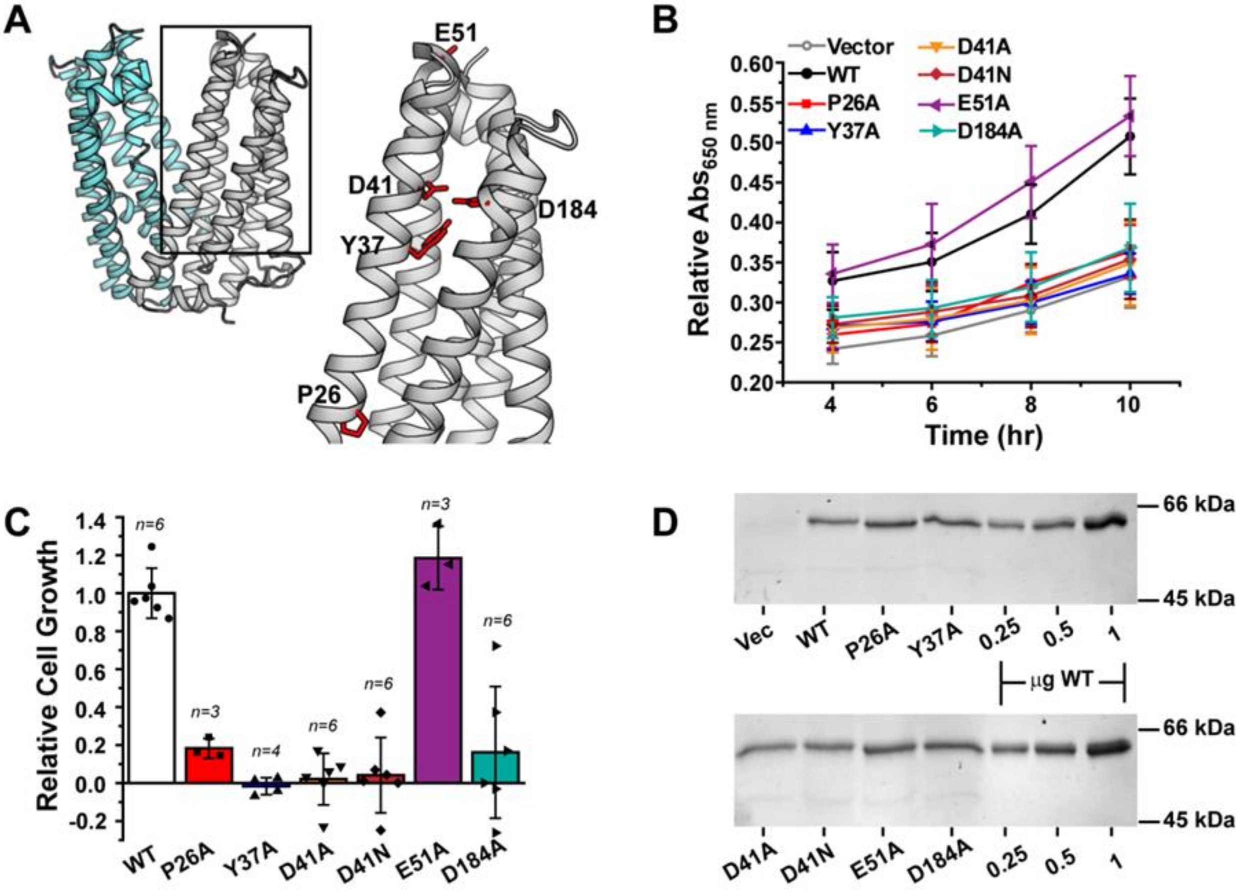

Figure 2.2: **R6G resistance profiles for NTD residue substitutions**. (**A**) Structure of PfMATE (PDB 3VVN) highlighting the location of residues chosen for site directed mutagenesis in the N-lobe (gray). The C-lobe is shown in cyan. (**B**) Time course of cell growth for the variants relative to both the vector and WT at 37 °C in the presence of 75 μg/mL R6G. The curves were generated from at least three independent experiments as described in the methods and the Fig. 1 legend. The Abs_{650nm} in the presence of R6G was normalized to the 0 μg/mL R6G well. The standard deviation is shown for each data point. (**C**) The data in panel (**B**) at the 10 hr time point was transformed into a cell growth profile relative to WT PfMATE after subtracting the contribution of the vector control. The bar plot highlights the average and standard deviation for the indicated number of measurements. One-way ANOVA indicated that the population means are significantly different at the 0.05 level, F (6, 27) = 28.82, p = 1.57×10^{-10}. (**D**) SDS-PAGE followed by InVision His tag staining confirmed similar levels of expression for each construct. The last three lanes on each gel image is purified PfMATE WT used as a standard.

Site directed mutagenesis of N-lobe residues (P26A, Y37A, D41A/N and D184A) significantly impaired cell growth relative to WT in the presence of 75 µg/mL R6G, and instead clustered with the vector control (Fig. 2.2B and Fig. S2C-D). In contrast, substitution of a nearby non-conserved surface Glu in TM2 (E51A), designed as a control, demonstrated a similar pattern of growth as the WT. Capturing the pattern of PfMATE-mediated R6G resistance, a growth profile of the variants relative to WT (Fig. 2.2C) indicated that substitution of functionally-required residues reduced cell growth by ~80% or more. Importantly, the apparent loss of functional activity could not be attributed to reduced expression levels of the variants (Fig. 2.2D and Fig. S6), and size exclusion chromatography analysis of the purified variants were consistent with folded transporter (Fig. S7).

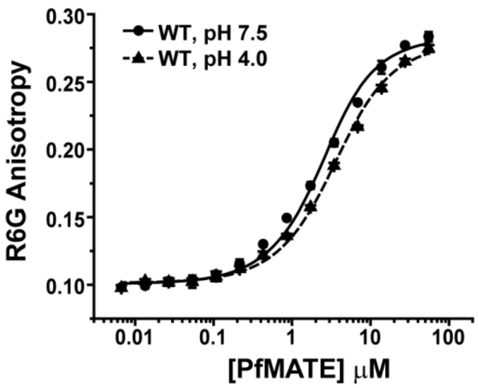

Figure 2.3: **Binding curves of R6G to WT PfMATE**. Changes in the fluorescence anisotropy of R6G were plotted as a function of protein concentration in β-DDM buffer at the indicated pH and 23 °C. The data points represent the average and standard deviation of three binding experiments, and the solid and dashed lines are nonlinear least squares fits of the curves to obtain the K_D (Table 2.1).

Construct	K_D (± SD*) (µM)	*n*
Wild-Type, pH 7.5	1.59 (0.09)	6
, pH 4.0	2.67 (0.17)	3
P26A, pH 7.5	1.74 (0.07)	3
Y37A, pH 7.5	1.29 (0.26)	3
D41A, pH 7.5	2.06 (0.22)	3
D41N, pH 7.5	1.98 (0.02)	3
E51A, pH 7.5	2.24 (0.10)	3
D184A, pH 7.5	1.98 (0.06)	3

* Standard deviation

Table 2.1. **R6G binding affinity to PfMATE mutants**

N-lobe variants retain high affinity R6G binding

We explored the mechanistic basis of compromised R6G resistance by two approaches. First, we investigated the role of targeted residues in R6G binding. Formation of a complex between R6G and PfMATE purified in β-dodecyl maltoside (β-DDM) micelles was monitored by R6G fluorescence anisotropy. Binding of drug to PfMATE was associated with an increase in anisotropy, similar to the change in fluorescence polarization that was observed upon binding to DinF-Bh (113). Titration of R6G with increasing concentrations of PfMATE generated a binding isotherm that was fit with a single site binding model to determine the K_D (Fig. 2.3). The binding curve collected at pH 7.5 indicated that R6G was bound to WT PfMATE with high affinity. A subtle right shift in the curve was observed at pH 4.0, corresponding to a less than two-fold increase in K_D (Table 1). Notably, introduction of the N-lobe variants, including D41A/N, only marginally perturbed R6G affinity at pH 7.5 relative to the WT. Binding analysis of the E51A variant reported the largest deviation from WT, yet it retained WT-like resistance activity (Fig. 2.2C). These results therefore suggested that compromised resistance is unlikely to be the consequence of impaired substrate binding.

N-lobe variants disrupt H^+-driven conformational changes

Employed as an environmentally sensitive probe, the pattern of Trp fluorescence in transporters has been shown previously to be an effective spectroscopic tool to monitor conformational changes (158–160). PfMATE contains five endogenous Trp residues, two of which are found in the N-lobe. One of these, Trp 216, is located > 20 Å away from the N-lobe cavity and near the intracellular side of TM6. The other Trp residue, Trp 44, is located near the C-terminus of TM1 in close proximity to the network of hydrogen-bonded sidechains that has been proposed to facilitate TM1 bending (Fig. 2.4A). Thus, we exploited intrinsic Trp fluorescence as a surrogate reporter of conformational changes induced by H^+.

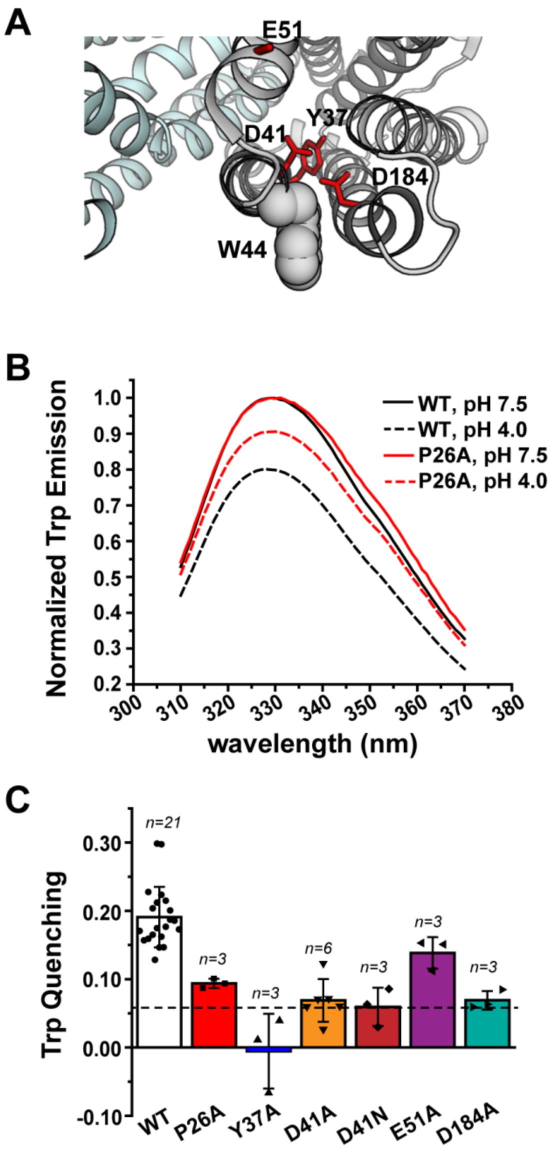

Figure 2.4: NTD amino acid substitutions disrupt the pattern of H$^+$-dependent Trp quenching. (**A**) Structure of PfMATE (PDB 3VVN) illustrating the location of Trp 44 (shown in space filling representation) relative to the NTD variants. (**B**) Trp fluorescence is quenched for WT PfMATE at pH 4.0 (black dashed trace), which is reduced by introduction of P26A (red dashed trace). The P26A spectra are shown as a representative dataset. Spectra were acquired at 23 °C in β-DDM buffer. (**C**) Profile of Trp quenching for the NTD variants. The bar plot highlights the average and standard deviation for the indicated number of measurements. One-way ANOVA indicated that the population means are significantly different at the 0.05 level, F (6, 35) = 20.29, p = 4.53 x 10^{-10}. The horizontal dashed line indicates the quenching observed for the W44C variant. The color code is the same as in Fig. 2.2.

Fluorescence spectra of WT PfMATE in β-DDM micelles reported a ~20% reduction in Trp emission intensity at pH 4.0 relative to pH 7.5 (Fig. 2.4B), which we attributed to increased solvent exposure of buried Trp sidechain(s) at low pH. Mutation of Trp 44 reduced the fluorescence quenching to ~6% although R6G binding and resistance activity remained relatively unaffected (data not shown), suggesting that Trp 44 contributed to the majority of the signal change in WT PfMATE.

With the exception of E51A, pH-dependent Trp quenching was attenuated substantially in the N-lobe variants (Fig. 2.4B, C). The quenching observed for D41A, D41N, and D184A was reduced to similar levels as the W44C variant. Although quenching was less attenuated for P26A and mostly limited for Y37A, the observed reduction in Trp quenching was consistent with impaired formation of a distinct conformation. Remarkably, the overall quenching profile shown in Fig. 2.4C echoed the R6G resistance profile shown in Fig. 2.2C. Thus, the pattern of quenching strongly implied that substitution of relevant residues in the N-lobe disrupted H^+-dependent structural transitions likely associated with the transport cycle.

Discussion

A fundamental property of MATE transporters is the ability to bind and export a broad range of chemically diverse substrates. In addition to H^+-dependent ethidium efflux, PfMATE has been described previously to promote bacterial growth in the presence of the fluoroquinolone antibiotic NFX (114). In support of a role in multidrug transport, the results presented here establish that PfMATE also confers enhanced resistance against toxic concentrations of the antimicrobial R6G. Furthermore, R6G resistance is compromised by mutation of residues predicted to be required for transport.

Importantly, PfMATE-mediated resistance to R6G toxicity was observed in *E. coli* under specific expression conditions. Manipulation of the IPTG concentration used for induction was required to balance the metabolic challenge of transporter expression in the host with the conferred advantage of exporting a toxic substrate present at high concentrations in the growth medium. Moreover, the lack of R6G resistance in hypersensitive *E. coli* strains supports the notion of coordinated drug efflux mediated by multiple transporters sharing overlapping substrate specificities (161). In this context, PfMATE likely bolsters R6G resistance by integrating with other R6G transport systems, such as the tripartite AcrAB-TolC assembly (162, 163), which was deleted in the BL21 (DE3)-Δ3 and -Δ7 strains (154). According to this model, complete removal of the hydrophobic substrate engenders PfMATE-mediated extrusion into the periplasm followed by export across the outer membrane by the AcrAB-TolC complex. Thus, the data suggests that heterologous expression of PfMATE in *E. coli* cannot fully compensate for the loss of major multidrug transporters under the conditions described here.

Combining the cell growth assay with site directed mutagenesis indicated that R6G resistance is dependent on the integrity of a conserved network of polar sidechains lining a cavity in the N-lobe. Among these residues, a strictly conserved TM1 Asp has been proposed to form part of the R6G binding site in the homolog DinF-Bh (113). Accordingly, R6G binding affinity was reduced by more than 30-fold in a DinF-Bh variant predicted to mimic protonation of the carboxylate moiety (D40N). This result was interpreted as evidence for a mutually exclusive H+/drug binding site, the hallmark of a direct competition mechanism. However, substantial perturbation of R6G binding affinity was not observed with homologous variants in PfMATE (D41A/N). Furthermore, the marginal reduction in binding affinity at low pH implies that PfMATE-R6G interactions are not mediated directly by charged sidechains that undergo protonation/deprotonation events. These results strongly suggest that R6G is stabilized by distinct binding motifs in PfMATE and DinF-Bh. That is, the H^+ and R6G binding sites appear to be nonoverlapping in PfMATE.

In contrast to the binding analysis, substitution of functionally required N-lobe residues altered the pattern of H^+-dependent Trp quenching relative to the WT, which we interpret as impaired formation of a unique structural intermediate. Previous crystallographic and computational studies have demonstrated that the conserved residues of the N-lobe cavity investigated here contribute to an ion binding site (114, 118, 155). As a reflection of the predicted involvement of these residues in the structural dynamics of TM1, the observed pattern of Trp quenching in the N-lobe variants highlights the role of conserved sidechains in shaping H^+-driven conformational changes in PfMATE. Y37A, D41A, D41N and D184A likely disrupt rearrangement of the hydrogen bond network induced by H^+ binding, effectively inhibiting conformational changes. Although not directly involved in H^+ binding, Pro 26 in conjunction with Gly 30 was hypothesized to form a hinge in TM1 (114). By extension, P26A may impair TM1 bending in response to H^+ binding within the N-lobe cavity.

Based on the apparent correlation between Trp quenching of N-lobe variants (Fig. 2.4C) and the cell growth profile (Fig. 2.2C), we propose that this residue network is critical to mediate coupling of ion gradients through conformational changes that allosterically modulate substrate binding affinity to trigger substrate release. This conclusion is supported by spectroscopic analysis of NorM-Vc that revealed the significance of a similar network of residues within the N-lobe cavity in determining ion-driven conformational dynamics central to drug resistance (Fig. 1.16) (151). Experiments that further define the nature and magnitude of ligand-dependent conformational changes and the relationship to R6G binding and resistance in PfMATE are ongoing.

Together, the functional and biochemical analysis of PfMATE emphasizes both common and diverging mechanistic principles of ion-coupled substrate transport in the MATE family. The evidence presented here supports an emerging transport model that envisions ion coupling mediated by specific residues in the N-lobe to induce conformational changes that culminate in substrate extrusion. However, differences in binding sites for shared substrates of MATE homologs may reflect evolution of transport mechanisms. Subsequent studies with other substrates and transporters are warranted to further uncover shared and unique determinants of MATE transport mechanisms.

Experimental Procedures

Site-Directed Mutagenesis

Wild-type PfMATE was cloned into the pET-19b vector encoding an N-terminal 10-His tag under control of an inducible T7 promoter. Mutations were generated using a single-step PCR in which the entire plasmid was replicated from a single mutagenic primer. The template plasmid was subsequently digested by DpnI. Plasmids were propagated using XL-1 Blue or DH5α cells and were sequenced using both T7 forward and reverse primers to confirm mutagenesis and the absence of aberrant changes in the protein coding region.

Expression and Purification of PfMATE

C43 (DE3) cells were freshly transformed with pET-19b encoding WT or mutant PfMATE. A single colony was used to inoculate a 40 mL LB medium which was grown overnight (~15 h) at 34 °C and was subsequently used to inoculate 2 L of minimal medium A. Cultures were incubated at 37 °C with shaking until reaching an $\text{Abs}_{600\text{nm}}$ of ~0.8, at which time the expression of PfMATE was induced by the addition of 1 mM IPTG. The cultures were incubated overnight (~15 h) at 20 °C and then harvested. Cell pellets were resuspended in 20 mL of lysis buffer (20 mM Tris-HCl pH 8.0, 20 mM NaCl, 30 mM imidazole, and 10% (v/v) glycerol), including 10 mM DTT, and lysed by five passes through an Avestin C3 homogenizer. Cell debris was removed by centrifugation at 9,000 x g for 10 min. Membranes were isolated from the supernatant by centrifugation at 200,000 x g for 1.5 h. Membrane pellets were resuspended in lysis buffer containing 1.5 % (w/v) β-dodecyl maltoside (β-DDM) and 0.5 mM DTT and incubated on ice while being stirred for 1 hour. Insoluble material was cleared by centrifugation at 200,000 x g for 30 min. The cleared extract was bound to 1.0 mL (bed volume) Ni-NTA Superflow resin (Qiagen) at 4 °C for 2 h. After washing with 10 bed volumes of buffer containing 30 mM imidazole, PfMATE was eluted with buffer containing 300 mM imidazole. Elution fractions (4 mL total) were combined and then concentrated to 2.0 mL in a 100,000 MWCO filter concentrator (Millipore) and injected in 1 mL samples onto a Superdex

200 Increase 10/300 GL column (GE Healthcare) equilibrated with 50 mM Tris/MES pH 7.5, 0.05 % β-DDM. Peak fractions of purified PfMATE were combined and concentrated using a 100,000 MWCO filter concentrator and the final concentration was determined by A280 measurement (ε = 46870 M−1·cm−1).

R6G binding assay

Stock solutions of rhodamine 6G (Acros) were made in ultrapure water. Drug concentrations for assays were determined by spectrophotometer measurement at 524 nm (ε = 116,000 M−1·cm−1) of samples diluted in ethanol. R6G (2.1 uM) was mixed with increasing concentrations of PfMATE WT or variants in 50 mM Tris/MES pH 7.5, 0.05 % β-DDM buffer in a total volume of 25 µL in a 384-well black fluorescence microplate (Greiner Bio-One) and incubated at room temperature for >5 min. R6G fluorescence anisotropy was measured using a BioTek Synergy H4 microplate reader with a 480 nm excitation filter (20 nm band pass) and a 570 nm emission filter (10 nm band pass). Binding isotherms were measured in triplicate and R6G binding affinity was determined by non-linear least squares analysis in the program Origin (OriginLab). The average K_D and standard deviation for each mutant are reported in Table 2.1.

Tryptophan Fluorescence

Purified PfMATE in 50 mM Tris/MES pH 7.5, 0.05 % β-DDM buffer was adjusted to pH 4.0 using an empirically determined volume of 1 M citric acid. Samples at pH 7.5 were adjusted with an equivalent volume of buffer to maintain an equal concentration of protein between pH conditions. Samples were placed in a 1 cm quartz fluorometer cell (Starna Cells, Inc) and tryptophan fluorescence was measured using a T-format fluorometer (Photon Technology International) with excitation and emission slit widths of 4 nm and 1 nm, respectively. The fluorescence spectrum was acquired from 310 to 370 nm following excitation at 295 nm. Spectra were normalized to the peak intensity (329 nm) of the pH 7.5 sample to determine the extent of

H+-dependent quenching. Experiments were repeated at least in triplicate and the mean and standard deviation of fluorescence quenching was determined. To assess statistically the impact of substitutions on Trp quenching, a one-way ANOVA conducted in Origin determined that the population means are significantly different at the 0.05 level.

R6G Resistance Assay

Resistance to R6G toxicity was carried out as previously described with several modifications. *Escherichia coli* BL21 (DE3) cells were transformed with empty pET-19b vector, pET19b encoding PfMATE WT, or variants. A dense overnight culture from a single colony was used to inoculate 12 mL of LB broth (Fisher Scientific) containing 0.1 mg/mL ampicillin (Gold Biotechnology) to a starting Abs_{600nm} of 0.0375. Cultures were grown for an additional 1.5 - 2 h at 37 °C, and then diluted to Abs_{600nm} of 0.25. Expression of the encoded construct was induced with 1-50 µM IPTG (Gold Biotechnology). Expression was allowed to continue at 37 °C for 2 h, after which the Abs_{600nm} of the cultures was adjusted to 0.5. The cells were then used to inoculate (1:20 dilution, starting Abs 600 nm = 0.025) a sterile 96-well microplate (Greiner Bio-one) containing 50% LB broth, 0.1 mg/mL ampicillin, and R6G. IPTG was not included on the microplates. Microplates were incubated at 37 °C with shaking at ~250 rpm for at least 10 h, and cell growth was monitored by Abs_{650nm} on a BioTek Synergy H4 microplate reader. Data points were collected every 2 h. The Abs_{650nm} in the presence of R6G was normalized to the 0 µg/mL R6G well to obtain a relative Abs_{650nm}, which accounts for growth behavior of the vector, WT and variants in the absence of drug (Fig. S2). Screening of [IPTG] indicated that 1 µM IPTG resulted in optimal resistance, which was used for all subsequent experiments. Due to the narrow dynamic range to observe enhanced R6G resistance (Fig. 2.1B), each experiment included a vector and WT control. P-values in Fig. 2.1B were determined by an unpaired *t*-test (GraphPad), indicating that the population means of cell growth for WT and vector are significantly different at the indicated R6G concentrations. The time course of cell growth for WT and variants relative to vector was determined at 75 µg/mL R6G. The relative activity of each variant was determined by subtracting the Abs_{650nm} of the vector followed by normalization to the corrected Abs_{650nm} of the WT at the 10 h time point. Each data point was acquired from triplicate measurements in three distinct wells on the plate, and the experiment was repeated at least three times to obtain the mean and standard deviation. To assess statistically the impact of the substitutions on relative cell growth, a one-way ANOVA conducted in Origin determined that the population means are significantly different at the 0.05 level.

To confirm PfMATE expression, 50mL of cells harboring vector, WT and PfMATE variants were induced with 1 µM IPTG for 2 h at 37 °C and harvested by centrifugation. Cells were resuspended in 1 mL of lysis buffer [20 mM Tris-HCl, 20 mM NaCl, and 10% (v/v) glycerol (pH 8.0)] with 2.0 mM PMSF and lysed by sonication (60 - 1 sec pulses with 10 sec resting intervals). Cell lysates were centrifuged at 3,400 x g for 8 min to remove cell debris. The supernatant was subsequently ultracentrifuged for 30 min at 70,000 x g to obtain the membrane fraction. PfMATE was extracted from a normalized amount of membrane mass in 200 µL lysis buffer supplemented with 2% (w/v) β-DDM for 1 h at 4 °C, after which the samples were ultracentrifuged at 90,000 x g to clear insoluble material. The supernatant was then mixed with 40 µL (bed volume) of Ni-NTA Superflow resin (Qiagen) for 1 h at 4 °C in the presence of 20 mM imidazole. The resin was then applied to a micro spin column (BioRad Bio-spin) and the resin was washed with eight bed volumes of buffer containing 30 mM imidazole. The protein was eluted with 50 uL of buffer containing 300 mM imidazole and equal-volume samples for SDS-PAGE were prepared from the eluates. Following electrophoresis on a 12.5% acrylamide gel, the protein was visualized by InVision His-tag gel stain (Novex).

CHAPTER III

Sequence and structural determinants of alternating access in PfMATE

Until very recently, the canon of MATE structures has been limited to outward-facing (OF) conformations, regardless of bound ligand, obfuscating any mechanistic interpretation. In the context of antiport, alternating access models postulate the isomerization of a transporter between an OF state, to which ions bind, and an inward-facing (IF) state, to which substrate binds and/or ions are released to the intracellular side (21). In the OF MATE structures, the putative central substrate binding cavities are shielded from the cytoplasm by highly ordered and packed protein regions, suggesting that transition to an IF conformation requires extensive structural rearrangements. A view of these rearrangements was recently captured from an IF crystal structure of PfMATE (117). This structure, determined in the presence of native *P. furiosus* lipids, showed a change in the orientation of the central cavity that exposes its lumen to the intracellular side. Compared to the OF structure, TMs (2-6) and (8-12) in the two lobes undergo relative rigid body movement that disrupts helical packing and leads to the formation of new contacts. As highlighted in Fig. 3.1, a rupture of the interface between the two lobes repacks the intracellular side of the transporter resulting in a cavity open to the cytoplasm.

Although the OF and IF structures of PfMATE suggest a blueprint of alternating access (Fig. 3.1), critical elements of the transport mechanism remain unresolved. Substrate/ion antiport entails differential stability of the OF and IF conformations when either ligand is bound, yet Zakrzewska et al. (117) found that the OF state also crystallizes at low pH (pH 5.0 - 6.5), albeit in

---

This chapter is adapted from the article “Sequence and structural determinants of ligand-dependent alternating access of a MATE transporter”.

Kevin L. Jagessar was responsible for investigation, data collection and curation, formal analysis, and writing and editing of the article.

the absence of native lipids. This observation led the authors to question the role of protons in driving isomerization between OF and IF conformations. Further confounding the mechanistic interpretation of the IF and OF structures in the context of the transport cycle is the observation that structures of substrate- and ion-bound NorM-Ng as well as PfMATE at pH 8.0 and 6.0 were outward-facing, with bending of TM1 in the latter at lower pH proposed to mediate proton coupling (113, 114, 118). Finally, the residues and structural elements that couple ion gradients to conformational changes are not defined, although a network of conserved charged residues in the N-lobe of PfMATE was indirectly implicated (164).

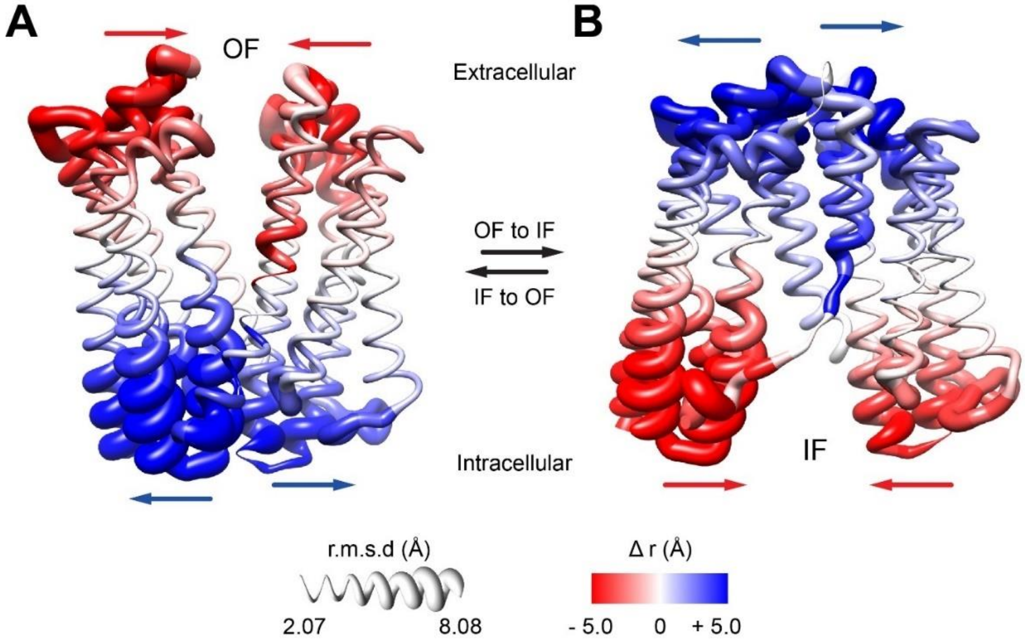

Figure. 3.1: Model of PfMATE alternating access inferred from the crystal structures. The Cα r.m.s. deviations (r.m.s.d.) were derived from the alignment of the OF (PDB ID: 3VVN) and IF (PDB ID: 6FHZ) structures and mapped onto ribbon representations of the OF (**A**) and IF (**B**) structures. Ribbon thickness is proportional to increasing r.m.s.d. Viewed from the side of the transporter, arrows show the direction of inferred movement from comparison of the OF and IF structures. Lateral movement (Δr), toward (red) or away from (blue) the center of mass of the protein, which is aligned with the membrane normal, is overlaid on the OF and IF r.m.s.d. depictions.

Prior to publication of the IF structure, we initiated a systematic Double Electron-Electron Resonance (DEER) (147, 148, 165–167) investigation of PfMATE to map proton- and substrate-dependent conformational changes in a lipid bilayer-like environment and to identify sequence motifs of ion and substrate coupling. For this purpose, an extensive network of spin label pairs was introduced at the extracellular and intracellular sides to interrogate ligand-dependent movements of TM helices. Here, we report that patterns of experimental distance distributions from DEER analysis reveal that an IF conformation is populated at pH 4.0 whereas pH 7.5 and substrate binding favor an OF conformation, demonstrating that protonation drives alternating access. Although these conformational changes were exclusively observed in lipid bilayers, native *P. furiosus* lipids were not required. Systematic mutagenesis of conserved residues uncovered an essential role for residue Glu 163 in driving the pH-dependent isomerization of PfMATE. Together these findings can be integrated into a model of ligand-dependent alternating access that provide a mechanistic context for the IF and OF crystal structures.

Results

Coupled ion/substrate antiport entails the population of at least two conformational states, OF and IF, that are differentially stabilized by ligands (19, 145). To avoid shorting the ion gradient, isomerization between the two states only occurs if one of the ligands is bound to the transporter. Therefore, to uncover the ligand dependence of PfMATE, which putatively couples proton translocation to the cytoplasm to substrate extrusion to the periplasm, DEER distances distributions were determined at pH 4.0 to mimic a protonated state, at pH 7.5 to favor deprotonation, and in the presence of R6G at pH 7.5 to populate a substrate-bound state.

Structural and functional integrity of PfMATE mutants

The functional profiles of the PfMATE mutants were analyzed by a recently described three-assay protocol (164). First, we tested if the expression of the unlabeled double cysteine mutants in *E. coli* conferred resistance to toxic concentrations of the antimicrobial R6G. This assay is a surrogate reporter of drug efflux by PfMATE. Similar to the WT, cells harboring the double cysteine mutants of PfMATE survived exposure to R6G concentrations that are lethal to cells transformed with empty vector (Fig. S8). Two pairs (W44C/D120C and W44C/E134C) displayed resistance that was 20% of WT suggesting compromised activity as a consequence of the mutations. However, these mutants were not critical for our spectroscopic interpretation.

Second, we used fluorescence anisotropy to quantitatively measure the affinity of PfMATE spin-labeled mutants to R6G *in vitro.* The apparent K_D indicated that spin-labeled mutants in detergent micelles bind the substrate with similar affinity as the WT (Table S1).

Finally, the integrity of the proton conformational "switch" was assessed by monitoring pH-dependent Trp quenching. We have shown previously that protonation of WT-PfMATE leads to a reduction in Trp fluorescence, arising primarily from changes in the environment of Trp 44. The structural basis of this quenching was attributed to localized structural rearrangements of TM1 (164). Robust Trp quenching for the spin-labeled mutants at pH 4.0 (Fig. S9) suggest that the underlying conformational change is similar to WT. As expected, mutants involving Trp 44 displayed attenuated quenching in response to low pH. Taken together, these data indicated that the cysteine mutations and subsequent spin labeling did not result in detectable structural or functional perturbations, although the effects of spin labeling on the transport function cannot be determined from these assays.

Lipids are required for PfMATE conformational changes

Previous DEER investigations of the MATE homolog NorM-Vc showed Na^+ and H^+-dependent conformational changes in β-dodecyl maltoside (DDM) micelles (151). However, lowering the pH or addition of Na^+ failed to induce substantial distance changes in DDM-solubilized PfMATE. Spin label pairs monitoring the intracellular and extracellular sides had similar distributions at pH 4.0 and 7.5 (Fig. 3.2, left panels), indicating the absence of large-scale conformational changes. In contrast, PfMATE reconstituted into nanodiscs composed of *E. coli* polar lipids and egg phosphotidylcholine (see Methods) displayed evidence of large-scale distance changes upon protonation (Fig. 3.2, right panels). The strict lipid dependence of the pH-induced conformational changes is in agreement with the reported requirement of *P. furiosus* lipids for crystallization of the IF conformation (117). However, the DEER distance changes were observed with non-native lipid components. Neither R6G binding at pH 7.5 nor addition of 50 mM Na^+ at pH 7.5 elicited distance changes (Fig. S10), pointing to protonation as the primary trigger of PfMATE isomerization in lipid bilayers.

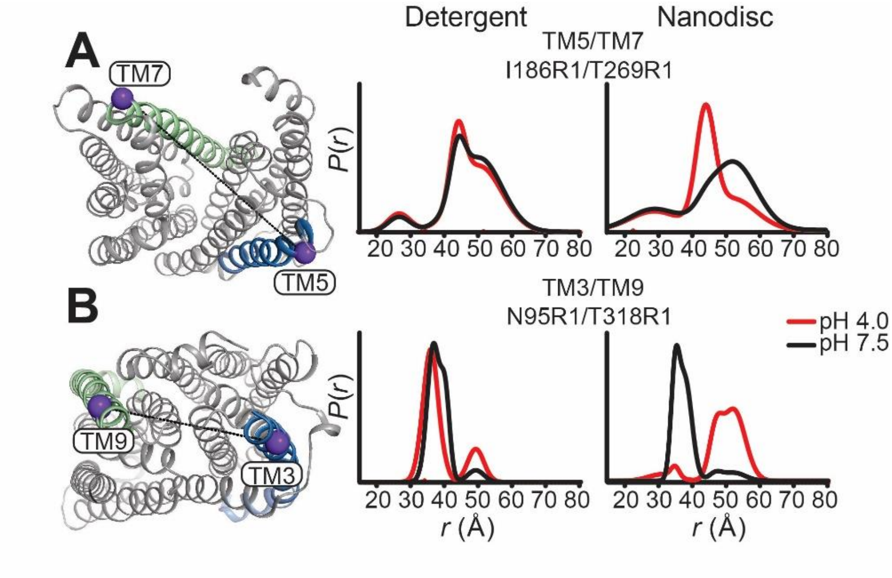

Figure 3.2: Ligand-dependent conformational dynamics of PfMATE requires a lipid environment. (**A**) Representative spin label pairs sampling distances between TM5 and TM7 on the extracellular side and (**B**) TM3 and TM9 on the intracellular side of PfMATE. R1 refers to the spin label side chain (see Methods). The spin label locations are highlighted on the OF structure by purple spheres connected by a line. The helices targeted in the N-lobe and C-lobe are highlighted in blue and green, respectively. Distance distributions, representing the probability of a distance *P*(*r*) versus the distance (*r*) between spin labels, are shown in black traces at pH 7.5 and red traces at pH 4.0 in DDM micelles (left panel) and lipid nanodiscs (right panel).

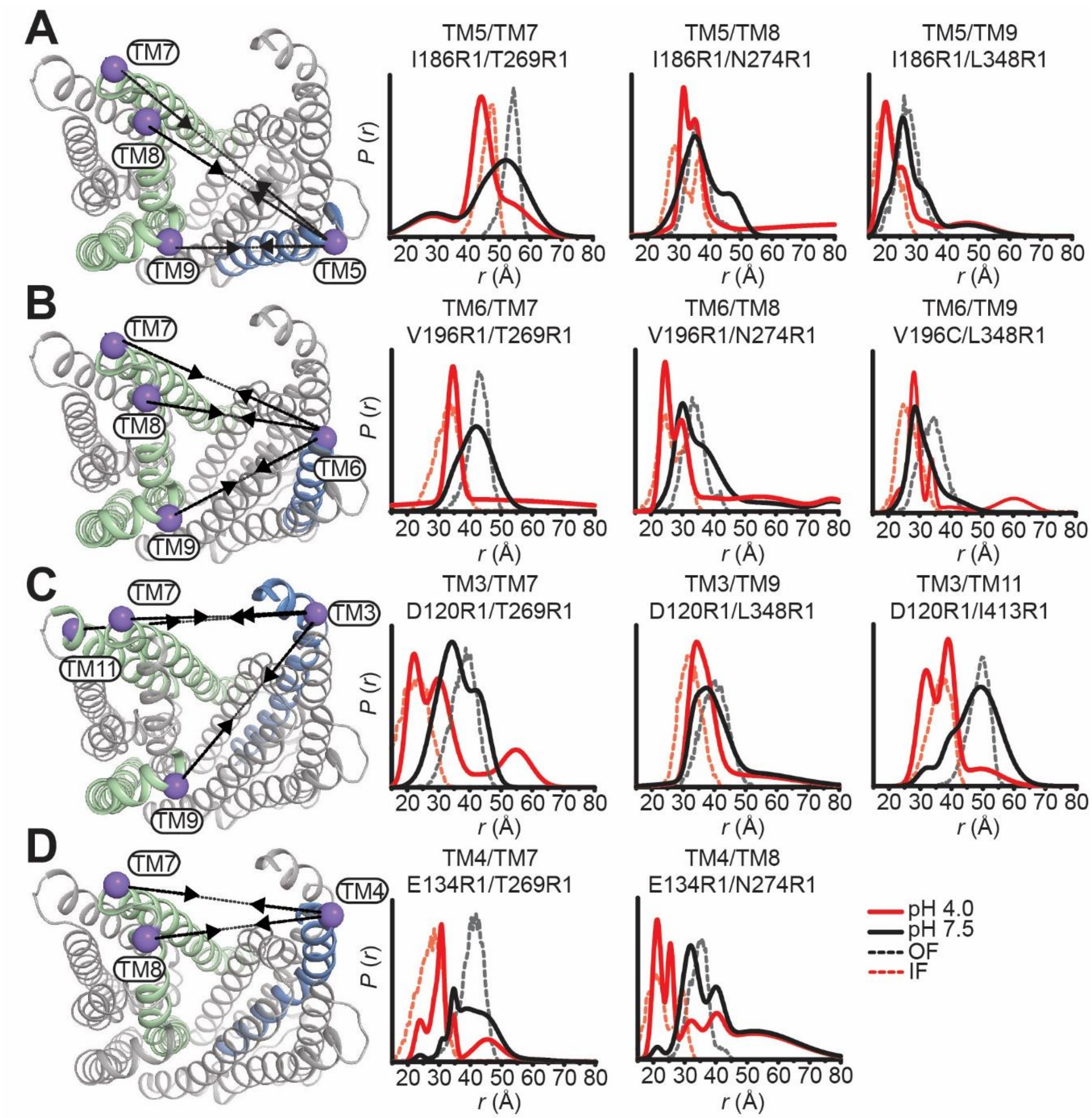

Figure 3.3: Protonation closes the extracellular side of PfMATE. Spin label pairs across the N- and C-lobes for DEER distance measurements are depicted on the extracellular side of the OF structure (**A** – **D**). Experimentally determined distributions (solid lines) are plotted with the predicted distance distributions derived from the OF (black, dashed traces) and the IF (red, dashed traces) crystal structures. Measurements from TMs 7, 8, and 9 in the C-lobe to TMs 5 and 6 (**A** and **B**) in the N-lobe report decreased distances at pH 4.0 consistent with movement of these helices toward each other. Commensurate distance changes at pH 4.0 measured from TMs 3 and 4 in the N-lobe to the C-lobe (**C** and **D**) indicate closure of the extracellular side. Experimentally determined distance changes are summarized on the OF structure depiction. Increases or decreases in distance are denoted with ◄--- ---► or ---► ◄---, respectively.

Protonation induces closing of the extracellular side

To determine the extent and amplitude of the pH-dependent conformational changes, two sets of spin-labeled pairs were designed to survey the extracellular side of PfMATE. One set of pairs monitored distances between helices from the N-lobe to helices in the C-lobe (Figs. 3.3-3.4). The other set consisted of labels monitoring distances between helices within each lobe (Fig. S11).

In contrast to limited intradomain distance changes (Fig. S11), a strikingly simple overall pattern emerged from the shifts in the distributions between the N- and C-lobe to shorter distances upon lowering the pH from 7.5 to 4.0 (Fig. 3.3, solid black and red traces, respectively). This pattern is highlighted by the relative movements that close the central cavity between TMs 7, 8 and 9 in the C-lobe and TMs 3, 4, 5 and 6 in the N-lobe (arrows in Figure 3.3). These observed distance changes are congruent with a relative movement between the N- and C-lobes toward each other. Unlike most TMs in the N-lobe, distance changes between TM1 and TMs 7 or 8 were more limited, suggesting movement of TM1 that is coupled to rearrangements of these helices in the C-lobe (Fig. 3.4).

To determine if these distance changes are consistent in magnitude and direction with those expected based on the OF and IF structures, distance distributions predicted from these structures (see Methods, dashed distributions in Figures 3.3 and 3.4) were compared with the experimental distributions. Except for TM1, we found that distributions calculated from the IF structure (6FHZ) generally overlapped with the pH 4.0 distributions whereas those calculated from the OF structure (3VVN) corresponded to the pH 7.5 distributions. This remarkable agreement between predictions and experiments linked the structural rearrangements observed in the IF structure to protonation. This result is also consistent with the expectation of antiport models that the driving ions stabilize the IF conformation (107, 108).

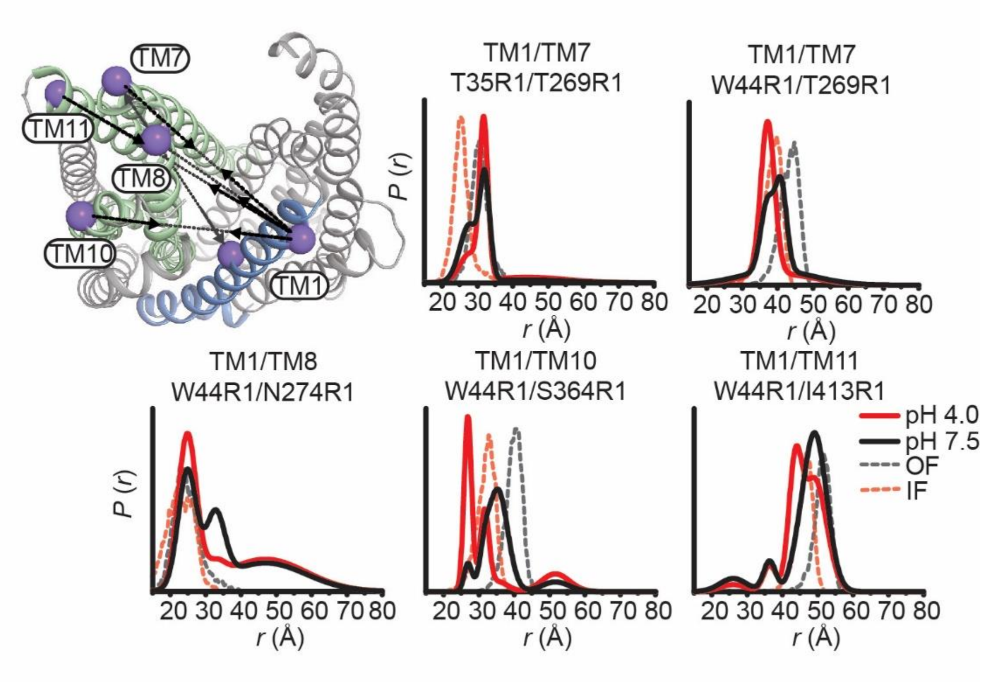

Figure 3.4: Relative movement of TM1 on the extracellular side of PfMATE is limited. The labeled positions on TM1 (purple spheres) to positions in the C-lobe for DEER measurements at pH 7.5 and pH 4.0 are depicted on the extracellular side of the OF structure. Distance distributions at pH 4.0 for TM1 are incongruent with predicted distributions based on the IF structure. Experimentally determined distance changes are denoted on the OF structure by ←--- ---→ (increase) or ---→ ←--- (decrease).

Notably, TM1 distance distributions to TMs 7 and 8 showed disagreements with the predicted distributions in both magnitude and direction (Fig. 3.4). A complex pattern of H^+-dependent distance changes is reported by two spin label pairs (T35R1/T269R1 and W44R1/T269R1) monitoring relative movements between different points on TM1 and TM7 (Fig. 3.4, upper panels). This pattern may reflect twisting of TM1, which may underpin the pH-dependent Trp quenching (Fig. S9) (164). Moreover, distance changes for TM1 were opposite to those predicted by the pH 6.0 OF crystal structure depicting a bent conformation of TM1 (114) (Fig. S12). Although its mechanistic role is controversial (113, 117), this conformation of TM1 was also captured in a crystal structure of a H^+-coupled MATE from *V. cholerae* (168). These observations, in conjunction with the DEER data and Trp quenching, suggest that twisting/bending of TM1 may be required for the population of the IF state.

Protonation induces opening of the intracellular side

Coupled to the closing of the large central cavity on the extracellular side, protonation induced large amplitude movement of TM helices on the intracellular side (Fig. 3.5). Distributions between the N- and C- lobes shift to larger average distances at pH 4.0 relative to pH 7.5, in stark contrast to the extracellular side where distances predominantly decrease. The pattern of distance changes identified TMs 3 and 9 as focal points of conformational changes with an increase in distance between these two helices on the order of 17 Å (Fig. 3.5A). TM3 moves away from TMs 1, 9 and 11 while TM9 moves away from TMs 6, 7 and 11 (Fig. 3.5A, B, respectively). Consequently, these movements facilitate the rupture of the tightly packed N- and C-lobe interface and the formation of an opening to the cytoplasm.

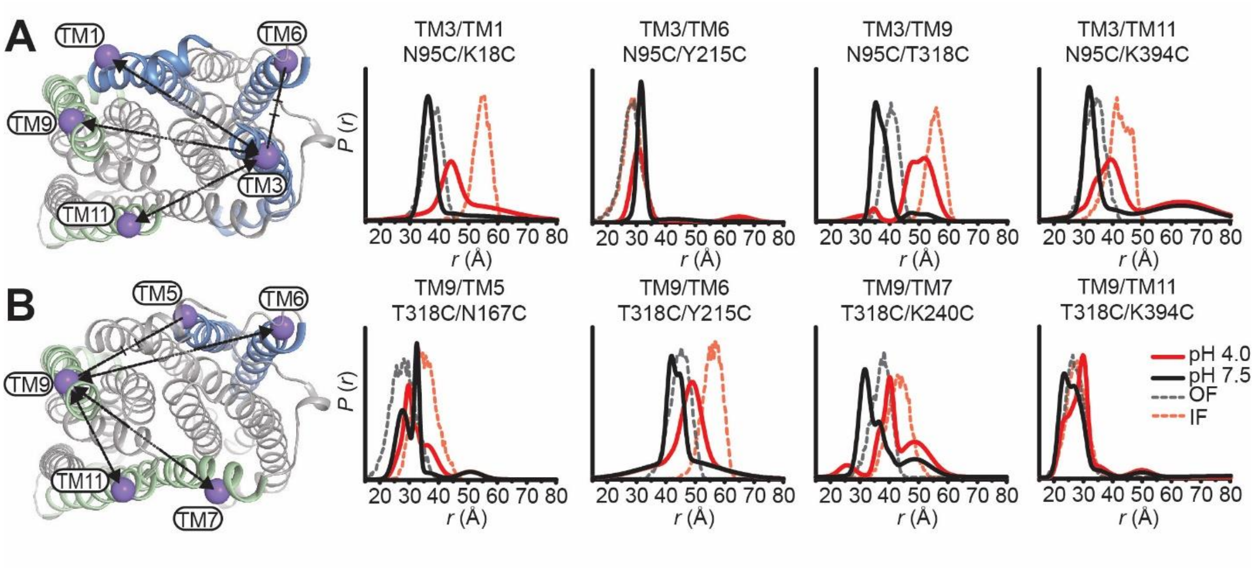

Figure 3.5: Relative movement of TM3 and TM9 on the intracellular side induced by protonation. Labeled positions for DEER measurements at pH 7.5 and pH 4.0 on TM3 and TM9 (**A** and **B**, respectively) to other TMs in the N- and C-lobes are depicted on the intracellular side of the OF structure. Experimentally determined distance changes are denoted on the OF structure by ←--- ---→ (increase), ---→ ←--- (decrease), or -----|⊢----- (no change). Protonation favors an increase in distance between the N- and C-lobes as predicted by the IF structure. The data identify TM3 and TM9 as foci of conformational changes, with an ~ 15 Å increase in distance between these two helices at pH 4.0.

Except for TM1, we found a remarkable correspondence between the helices identified from pH-induced distance changes and those implicated in the opening of the intracellular side from comparison of the crystal structures (Figs. 3.5, 3.6B; dashed lines). Moreover, predicted and experimental distance distributions partially overlap and the directions of the distance changes are identical, demonstrating that the intracellular side of the low pH conformation observed by DEER has similar features to the IF crystal structure.

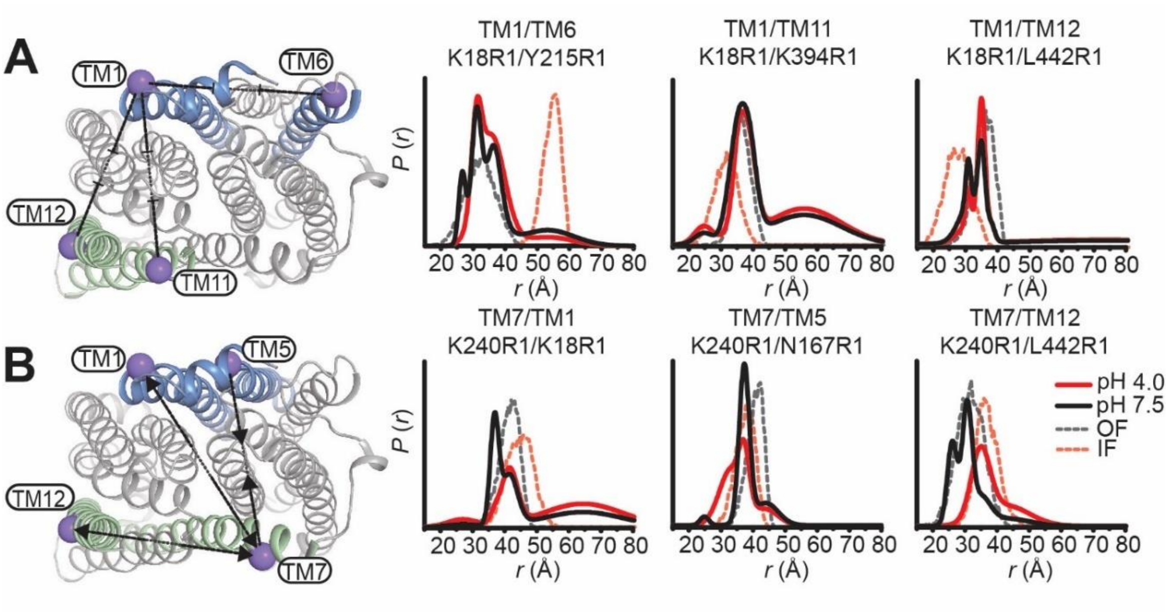

Figure 3.6: H$^+$-dependent conformational changes of TM1 and TM7 are limited on the intracellular side. Positions for DEER measurements from TM1 and TM7 to helices in the N- and C-lobes are indicated on the OF structure. Experimentally determined distance changes are denoted on the OF structure by ←--- ---→ (increase), ---→ ←--- (decrease), or ----| |---- (no change). Relative distance changes involving TM1 are incongruent with the distances predicted from the IF structure (**A**). Measurement of TM7 labeled pairs (**B**) report changes in distance at pH 4.0 that suggest movement away from the C-lobe (TM7-TM12) and toward the N-lobe (TM7-TM5).

However, prominent discrepancies between predicted and experimental distributions are noted for the intracellular side of TM1, which in the IF structure unwinds leading to distance changes relative to TMs 3, 6, 11 and 12 (Figs. 3.5A, 3.6A). In contrast, the experimental distance change between TM1 and TM3 was smaller than predicted (Fig. 3.5A), and distance distributions were almost superimposable at low and high pH between TM1 and TMs 6, 11 and 12 (Fig. 3.6A, red and black lines, respectively). Together, these observations suggest that the intracellular side of TM1 remained intact under our conditions and does not recapitulate the conformational changes predicted by the IF crystal structure.

Identification of residues involved in the protonation switch

An antiport mechanism requires the energetically downhill translocation of either Na^+ or H^+ to drive the uphill transport of the substrate or drug. Whereas the NorM and DinF subfamily putatively couple to different ions, there has been evidence supporting a critical role for a conserved acidic residue on the extracellular side of TM1, Asp 41 in PfMATE, that engages a number of amino acids in a network of H-bonds in the N-lobe (164) (Fig. 3.7A). Protonation of Asp 41 was predicted to induce rearrangement of this network (114).

To investigate if protonation of acidic residue(s) underpins the pH-dependence of PfMATE alternating access, we determined the pK of the OF to IF transition. For this purpose, we measured the pH dependence of the distance change for the N95R1/T318R1 intracellular pair, which monitors relative movement of TM3 and TM9 (Fig. 3.7B). Global analysis of the distributions (see Methods) yielded a titration curve depicting the populations of IF and OF (Fig. 3.7B) as a function of pH. A p*K* of approximately 5.1 was obtained from a non-linear least squares fit, consistent with the protonation/deprotonation of acidic residue(s) as the driver of PfMATE isomerization.

To pinpoint this residue or cluster of residues, we carried out mutagenesis of amino acids, including Asp 41, that have been identified by previous studies as functionally critical and/or are highly conserved in MATE subfamilies (114, 118, 164) (Fig. 3.7A, Fig. S13A). OF/IF isomerization in these backgrounds was monitored by the TM1/TM10 extracellular pair W44R1/S364R1 (Fig. 3.7C) and the TM3/TM9 intracellular pair N95R1/T318R1 (Fig. 3.7D). We found that substitutions of conserved residues D41A and D184A in the N-lobe cluster did not abrogate structural changes reported by the two pairs (Fig. 3.7C, D; Fig. S13B, C) although these substitutions compromised drug resistance and impaired pH-induced Trp quenching (164) (Figs. S8, S9; Figs. 2.2, 2.4). Remarkably, Y37A was the only substitution in the N-lobe cluster that strongly disrupted coupled conformational changes (Fig. 3.7C, D). In the OF crystal structure, this residue interacts with Asp 41 and Asp 184 in an H-bond network (Fig. 3.7A) yet is unlikely to undergo protonation in the pH range identified above.

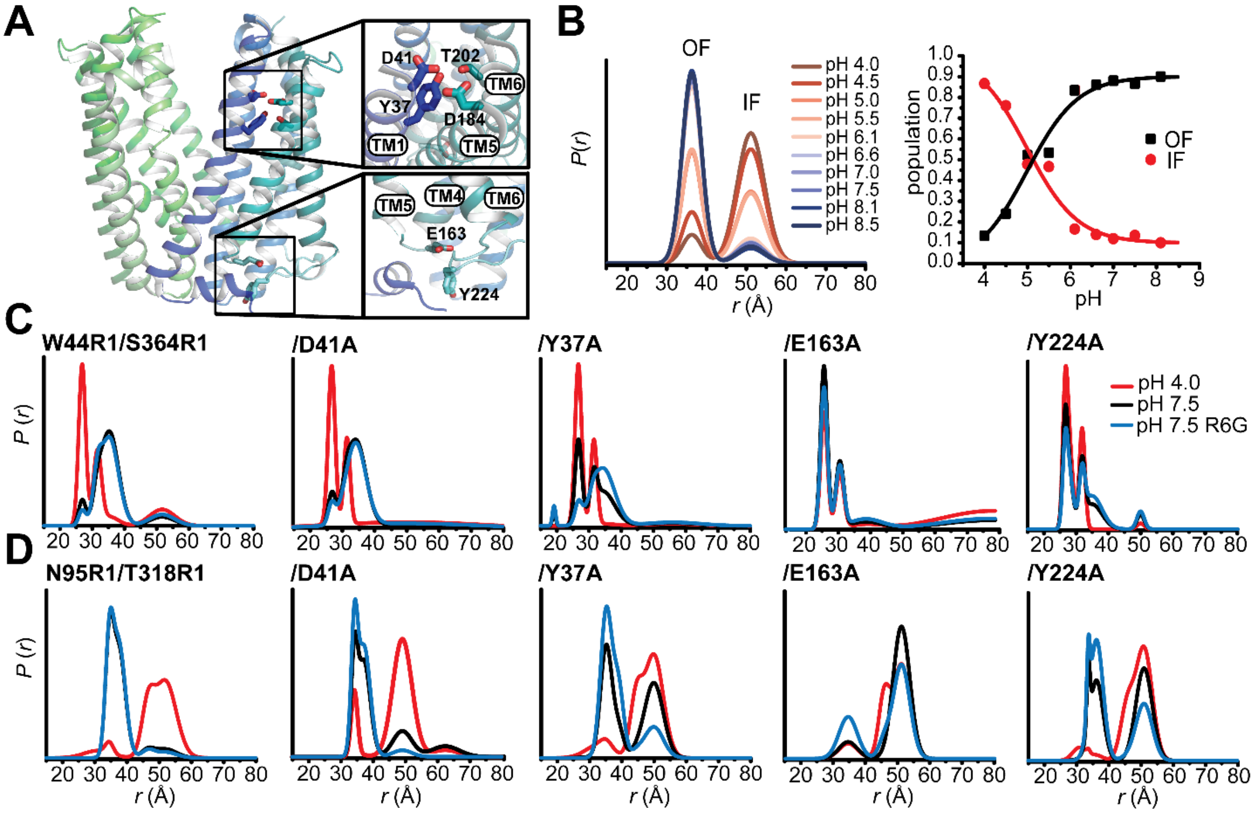

Figure 3.7: E163 is critical for the relative stability of the OF and IF conformations. Conserved residues previously identified in the N-lobe as crucial for PfMATE function are shown as sticks in the OF structure in the top inset (**A**). Glu 163 on IL4-5 and Tyr 224 on IL6-7 are depicted in the lower inset. Distance distributions acquired from titration of the intracellular reporter pair N95R1/T318R1 from pH 4.0 to 8.5 were fit assuming a two-component Gaussian distance distribution (**B**, left panel) to quantify the variation in population as a function of pH (**B**, right panel). A pK of 5.1 was obtained from a non-linear least squares fit of the populations for the OF and IF peaks (**B**, black and red curves, respectively). Distance distributions of extracellular (W44R1/S364R1) and intracellular (N95R1/T318R1) reporter pairs (**C** and **D**, respectively, Fig. S13) in acidic residue mutant backgrounds at pH 4.0, pH 7.5, and with R6G at pH 7.5 (blue traces). While D41A does not inhibit isomerization, Y37A, E163A, and Y224A abrogates the H$^+$-dependent alternating access and destabilizes the OF conformation at pH 7.5.

However, none of the mutations of residues in the N-lobe cluster fully mimicked the effects of alanine substitution of E163, located on an intracellular loop between TM4 and 5 (IL4-5) (Fig. 3.7A). This substitution concomitantly inactivated PfMATE in R6G resistance (Fig. S8) and abrogated conformational changes on both sides of the transporter (Fig. 3.7C, D). Moreover, distance distributions for this mutant shifted towards the protonated form at pH 7.5, suggesting that this glutamate is critical for the relative stability of the IF and OF conformations. To reinforce the importance of the negatively-charged sidechain, we mutated Tyr 224, which is found on the cytoplasmic loop between TM6 and 7 (IL6-7) and is in close proximity in the OF structure to Glu 163 and potentially engages it in an H-bond or pi-charge interaction (Fig. 3.7A). Distance distributions for Y224A were shifted to favor the IF conformation at pH 7.5 on both sides of the transporter (Fig. 3.7C, D), supporting the notion that interactions of Tyr 224 with Glu 163 modulates the relative stability of the IF and OF conformations. Thus, while a conserved network of polar and charged residues in the N-lobe is implicated in proton translocation, our data suggest that Glu 163 is the protonation master switch that regulates the H^+-dependent transition between IF and OF conformations.

Substrate binding stabilizes the OF conformation

As noted above, distance distributions of spin label pairs in the WT background in the presence and absence of R6G were superimposable at pH 7.5, suggesting that R6G binds to the OF conformation. To assess the energetic consequences of substrate binding, we took advantage of the Y37A, E163A, and Y224A mutations which reduce the relative stability of the OF intermediate. We found that in the Y37A background, binding of R6G shifted the populations of the W44R1/S364R1 and N95R1/T318R1 reporter pairs toward the OF conformation at pH 7.5 (Fig. 3.7C, D), indicating that substrate binding stabilizes the OF conformation as would be expected for an antiporter. However, in the Glu 163A and Tyr 224A backgrounds, we found that binding of R6G shifted the populations of the intracellular N95R1/T318R1 reporter pair but not of the extracellular W44R1/S364R1 pair (Fig. 3.7D, C), possibly resulting in an occluded conformation and further underscoring the importance of Glu 163 in OF/IF switching.

Discussion

The extensive DEER analysis reported above illuminates principles of PfMATE alternating access, fills in critical gaps in the mechanism of substrate- and ion-coupling and sets the stage for understanding how lipids modulate the conformational cycle of the transporter. In general, the remarkable agreement between experimental and predicted distance distributions, the latter calculated with modeling simplified spin labels (169), establishes that the DEER-detected, protonation-driven conformational changes in lipid nanodiscs describe, in outline, the OF to IF alternating access deduced from the crystal structures. Large amplitude distance changes, detected on both sides of PfMATE, reflect the pH-induced closing and opening of the extracellular and intracellular sides respectively. Although our results are consonant with a strict lipid dependence of PfMATE isomerization, the DEER analysis indicates that native lipids are not absolutely required to achieve an IF conformation. However, it is conceivable that endogenous lipids, predominantly consisting of diphytanyl acyl chains, may shape the energetics of alternating access in a native cellular environment.

Notable deviations between predicted and experimental distributions were observed for TM1. Inter- and intra-lobe distance changes involving TM1 were mostly limited and of lesser magnitude than expected. Furthermore, we find no evidence for the loss of α-helical structure seen in the IF model. This discrepancy may be rationalized through inspection of packing interactions imposed by crystal contacts between protomers where the N-terminus of one PfMATE appears to mediate interactions with a neighboring PfMATE molecule. We speculate that these constraints drive a non-native conformation of TM1 in the structure.

PfMATE isomerization is driven by protonation

Protonation, experimentally achieved by lowering the pH, is sufficient to support transition from OF to IF states in the presence of non-native lipids. Binding of R6G did not engender large conformational changes in a WT background. That the substrate stabilizes the OF conformation was deduced from distance measurements in mutant backgrounds that shift the equilibrium towards the IF conformation.

The original structures by Tanaka et al. (114) purportedly identified a proton binding site in a cluster of conserved residues in the N-lobe. However, subsequent molecular dynamics simulations, in conjunction with reexamination of the crystallographic data, suggested that Na^+ is bound at this site (118). Although our findings do not weigh in specifically on this question, they conclusively demonstrate that Na^+ binding does not drive the transition from OF to IF (Fig. S10). Thus, the ligand dependence captured by the DEER analysis establishes that alternating access of PfMATE is proton-coupled.

E163 is the master protonation switch

Reinforcing this conclusion is the finding that alanine substitution of a single acidic residue, Glu 163, found on an intracellular loop between TM4 and 5 abrogates the proton-dependence of alternating access and destabilizes the OF conformation resulting in an IF conformation at pH 7.5. Specifically, disruption of the interaction between Glu 163 and Tyr 224 leads to a shift in distance populations indicating that the stability of the OF intermediate is reduced (Fig. 3.7C, D). Although Tyr 224 is not widely conserved, analysis of 500 homologs of PfMATE indicates that Glu is present at position 163 in 45% of the sequences (156, 170). Collectively, these results suggest that specific interactions between IL4-5 and IL6-7 underpin the stability of the OF conformation, which may have implications across the MATE family. We propose that the large IL6-7 loop may function as a “belt” that regulates the conformational landscape. Upon disruption of the IL4-5/IL6-7 interaction via Glu 163 protonation, IL6-7 could move away from the N-lobe, allowing TM3 to tilt relative to the membrane normal on the intracellular side thus promoting isomerization to the IF state. This is reminiscent of the mechanism proposed for the MOP transporter MurJ (171) wherein bending of the intracellular portion of TM7 by 90° is associated with movement of IL6-7, which is hypothesized to release the tension in the loop and allow opening of the intracellular gate.

Previous investigations into residues involved in ion-coupling focused on the N-lobe cluster, such as D41, and to a lesser extent on residues in the C-lobe implicated in binding of Na^+ congeners in the crystal structures of NorM transporters (36, 109, 144, 146, 149–151, 172, 173). Our previously published work and the data reported here support the involvement of the N-lobe residues in PfMATE function as reflected in compromised drug resistance and reduced Trp quenching, which has been interpreted as impairing the formation of a structural intermediate required for the transport cycle (164). However, our data here indicate that alanine substitutions of these residues do not completely abrogate the H^+-dependent OF/IF isomerization (Fig. S13).

To resolve the apparent discrepancy, it is instructive to contrast the direct detection of conformational changes with resistance assays which do not report exclusively on transporter isomerization. Combined with the blunt nature of mutagenesis, the reduced resistance of the mutants could result from convoluted effects of local structural distortion, interference with ligand binding, and/or changes in transport kinetics. The latter is particularly confounding because the ability of a transporter to confer resistance depends on a delicate balance between the passive diffusion rate of hydrophobic/amphipathic drugs through the membrane bilayer and the rate of extrusion by the transporter. Thus, increasing the dimensionality of the analysis by combining direct detection of conformational dynamics with functional assays provides unique insight into the role of sequence and structural motifs in the transport mechanism.

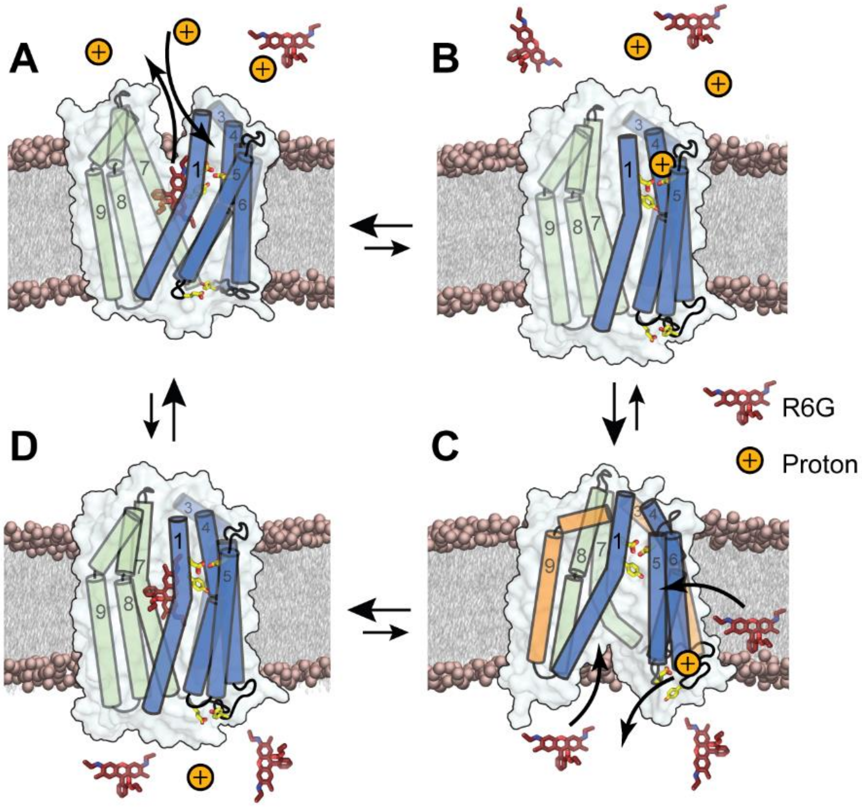

Figure 3.8: Proposed model of antiport for PfMATE. N- and C-lobe helices are depicted as cylinders and are colored blue and green, respectively. For clarity not all helices are shown. Side chains of Y37, D41 and D184 on the extracellular side, and E163 and Y224 on the intracellular side are represented as sticks. In the resting state, substrate is bound to the transporter and stabilizes the OF conformation (**A**), (Fig. S10, black, blue traces; appendices). Upon protonation of residues in the N-lobe cluster, substrate is released and the transporter could isomerize to an occluded conformation (**B**). Proton translocates from the extracellular side to the intracellular side, where E163 undergoes protonation thereby disrupting the IL4-5/IL6-7 interaction and opening the intracellular side through movements of TM3 and TM9 (orange cylinders, **C**), (Figs. 3.5, 3.6 red traces). The IF conformation binds drug, either from the cytoplasm or from the inner leaflet of the membrane bilayer (**C**), upon which the transporter isomerizes to a drug bound occluded conformation (**D**), (Fig. 3.7**C**, **D**) which in turn isomerizes spontaneously to the OF resting state (**A**).

Model of PfMATE ligand dependent alternating access

Framed in the context of the available structures, our results lead to an antiport model of PfMATE that reveals how protons and substrate differentially modulate the stability of the IF and OF conformations, identifies residues critical for protonation, and suggests a putative path for proton translocation (Fig. 3.8). In this model, the stable resting state is OF (Fig. 3.8A) whereas the IF (Fig. 3.8C) is of relatively high energy. Binding of R6G stabilizes the OF whereas protonation drives the isomerization to the IF state (Fig. 3.8, B to C), as would be expected if the proton motive force powers alternating access.

We propose that the high energy IF state is destabilized by the terminal step of proton dissociation from E163. To ensure coupled antiport, proton dissociation must occur simultaneously with binding of substrate (Fig. 3.8C). The data presented here does not weigh in on whether the proton/substrate competition is direct or indirect. However, we have previously suggested that H^+ and substrate occupy distinct binding sites (164). Following proton release to the intracellular side, the transporter, bound to substrate, spontaneously isomerizes to the OF conformation (Fig. 3.8, D to A).

Although primarily cast in terms of explicit OF/IF conformations, the model does not exclude the possibility of the population of membrane accessible but solution-occluded conformations (Fig. 3.8B, D) as we have proposed for the major facilitator superfamily transporter LmrP and has been presumed for MurJ (171, 174). Such a conformation may serve to enable substrate binding from the inner leaflet of the bilayer while excluding protons. This conformation should be of similar energy to the OF state in light of the marginal stabilization of the OF by the substrate R6G. The occupation of a substrate-bound doubly occluded state (Fig. 3.8C) may be inferred from the analysis of W44C/S364R1 and N95C/T318R1 where alanine substitution of critical residues (Glu 163 and Tyr 224) supported closing of the intracellular side but not concomitant opening of the extracellular side (Fig. 3.7C, D).

A combination of approaches, including sequence analysis, spectroscopic studies, and molecular dynamics simulations, have underscored the significance of a conserved residue network in the N-lobe cavity to the transport mechanism (114, 118, 151, 164). This cavity likely serves as the ion entry point (175), but the ion translocation pathway to the intracellular side has not been defined experimentally. Further examination of the PfMATE sequence through alignments and conservation analysis (ConSurf server (170, 176) outlines a putative pathway from the N-lobe cavity to the master switch, E163. This pathway is lined by a cascade of polar and charged sidechains, which may be capable of water-mediated proton transfer. The integrated approach described here will enable testing the roles of these residues in the alternating access mechanism of PfMATE.

Experimental Procedures

Site-Directed Mutagenesis

Wild-type PfMATE was cloned into pET19b vector encoding an N-terminal 10-His tag under control of an inducible T7 promoter and was used as the template to introduce double cysteine pairs and background mutations via site-directed mutagenesis with complementary oligonucleotide primers. Substitution mutations were generated using a single-step PCR in which the entire template plasmid was replicated from a single mutagenic primer. PfMATE mutants were sequenced using both T7 forward and reverse primers to confirm mutagenesis and the absence of aberrant changes. Mutants are identified by the native residue and primary sequence position followed by the mutant residue.

Expression, Purification, and Labeling of PfMATE

Escherichia coli C43 (DE3) cells were freshly transformed with pET19b vector encoding wild-type or mutant PfMATE. A transformant colony was used to inoculate Luria-Bertani (LB) media (LabExpress, Ann Arbor, MI) containing 0.1 mg/mL ampicillin (Gold Biotechnology, St. Louis, MI) which was grown overnight (~15 h) at 34 °C and was subsequently used to inoculate 3 L of minimal medium A at a 1:50 dilution. Cultures were incubated while being shaken at 37 °C until they reached an absorbance at 600 nm ($\mathrm{Abs}_{600\mathrm{nm}}$) of ~0.8, at which time the expression of PfMATE was induced by the addition of 1mM IPTG (Gold Biotechnology, St. Louis, MI). The cultures were incubated overnight (~15 h) at 20 °C and then harvested by centrifugation. Cell pellets were resuspended in 20 mL of resuspension buffer [20 mM Tris-HCl, pH 7.5, 20 mM NaCl, 30 mM imidazole, and 10% (v/v) glycerol], including 10 mM DTT, and lysed by five passes through an Avestin C3 homogenizer. Cell debris was removed by centrifugation at 9,000 x g for 10 min. Membranes were isolated from the supernatant by centrifugation at 200,000 x g for 1.5 h.

Membrane pellets were solubilized in resuspension buffer containing 20 mM β-DDM (Anatrace, Maumee, OH) and 0.5 mM DTT and incubated on ice with stirring for 1 hour. Insoluble material was cleared by centrifugation at 200,000 x g for 30 min. The cleared extract was bound to 1.0 mL (bed volume) Ni-NTA Superflow resin (Qiagen, Germantown, MD) at 4 °C for 2 h. After washing with 10 bed volumes of buffer containing 30 mM imidazole, PfMATE was eluted with buffer containing 300 mM imidazole.

Double cysteine mutants were labeled with two rounds of 20-fold molar excess 1-oxyl-2,2,5,5-tetramethylpyrroline-3-methyl methanethiosulfonate (Enzo Life Sciences, Farmingdale, NY) per cysteine at room temperature in the dark over a 4-hour period, after which the sample was placed on ice at 4 °C overnight (~15 h) to yield the spin label side chain R1. Unreacted spin label was removed by size exclusion chromatography over a Superdex200 Increase 10/300 GL column (GE Healthcare, Pittsburg, PA) into 50 mM Tris/MES, pH 7.5, 1 mM β-DDM, and 10% (v/v) glycerol buffer. Peak fractions of purified PfMATE were combined and concentrated using an Amicon Ultra 100,000 MWCO filter concentrator (Millipore, Burlington, MA) and the final concentration was determined by A_{280} measurement ($\varepsilon = 46870\ M^{-1}\cdot cm^{-1}$) for use in subsequent studies.

Reconstitution of PfMATE into Nanodiscs

E. coli polar lipids and PC (L-α phosphatidylcholine) (Avanti Polar Lipids, Alabaster, USA) were combined in a 3:2 w/w ratio, dissolved in chloroform, evaporated to dryness on a rotary evaporator and desiccated overnight under vacuum in the dark. The lipids were hydrated in 50 mM Tris/MES pH 7.5 buffer to a final concentration of 20 mM, homogenized by freezing and thawing for 10 cycles, and stored in small aliquots at −80 °C. MSP1D1E3 was expressed and purified as previously described and dialyzed into 50mM Tris/MES pH 7.5 buffer (177). MSP1D1E3 was concentrated using a 10,000 MWCO filter concentrator and the final protein concentration was determined by A_{280} measurement (ε = 29,910 $M^{-1}\cdot cm^{-1}$).

For reconstitution into nanodiscs, spin-labeled double cysteine mutants in β-DDM micelles were mixed with *E. coli* polar lipids/PC lipid mixture, MSP1D1E3 and sodium cholate in the following molar ratios: lipid:MSP1D1E3, 50:1; MSP1D1E3:PfMATE, 10:1; cholate:lipid, 3:1. Reconstitution reactions were mixed at 4 °C for 1 hour. The detergent was removed from the reaction by addition of 0.1 g/ml Biobeads (Bio-Rad, Hercules, CA) and incubation at 4 °C for 1 hour. This was followed by another addition of 0.1 g/ml Biobeads with 1-hour incubation, after which 0.2 mg/ml Biobeads were added and mixed overnight. The next day, 0.2 mg/ml Biobeads were added and mixed for one hour (165). The reaction was filtered using a 0.45 µm filter to remove Biobeads. Full nanodiscs were separated from empty nanodiscs by size exclusion chromatography into 50 mM Tris/MES, pH 7.5 and 10% (v/v) glycerol buffer. The PfMATE-containing nanodiscs were concentrated using Amicon ultra 100,000 MWCO filter concentrator, then characterized using SDS-PAGE to verify reconstitution and estimate reconstitution efficiency. The concentration of spin-labeled mutants in nanodiscs was determined as described previously by comparing the intensity of the integrated CW-EPR spectrum to that of the same mutant in detergent micelles (178).

CW-EPR and DEER Spectroscopy

CW-EPR spectra of spin-labeled PfMATE samples were collected at room temperature on a Bruker EMX spectrometer operating at X-band frequency (9.5 GHz) using 10 mW incident power and a modulation amplitude of 1.6 G. DEER spectroscopy was performed on an Elexsys E580 EPR spectrometer operating at Q-band frequency (33.9 GHz) with the dead-time free four-pulse sequence at 83 K (147). The pulse lengths were 10-14 ns (π/2) and 20 ns (π) for the probe pulses and 40 ns for the pump pulse. The frequency separation was 63 MHz. To ascertain the role of H^+, samples were titrated to pH 4.0 with an empirically determined amount of 1 M citric acid and confirmed by pH microelectrode measurement. The substrate-bound state was generated by addition of 1 mM R6G at high and low pH. Samples for DEER analysis were cryoprotected with 24% (v/v) glycerol and flash-frozen in liquid nitrogen.

Primary DEER decays were analyzed using home-written software operating in the Matlab (MathWorks, Natick, MA) environment as previously described (177, 179). Briefly, the software carries out global analysis of the DEER decays obtained under different conditions for the same spin-labeled pair. The distance distribution is assumed to consist of a sum of Gaussians, the number and population of which are determined based on a statistical criterion. A noticeable change in the intermolecular background was observed in nanodiscs at pH 4.0 giving rise to a steep decay relative to pH 7.5. This change in background was reversible by returning to pH 7.5. Negative stain electron microscopy analysis of a related MATE transporter suggests that this pH-dependent change in background is associated with reversible clustering of individual nanodisc particles. We also analyzed DEER decays individually and found that the resulting distributions are in agreement with those obtained from global analysis. The differences were primarily in the number of Gaussian components required for the fit. Because our analysis assumes two conformations, IF and OF, the differences in the shape of the distance components is not material to our conclusion.

Distance distributions on the PfMATE crystal structures [Protein Data Bank (PDB) ID code 3VVN, 6FHZ] were predicted *in silico* using 1 ns molecular-dynamics simulations with dummy spin labels (MDDS) with default parameters using the DEER Spin-Pair Distributor at the CHARMM-GUI website (169, 180).

R6G Resistance Assay

Resistance to R6G toxicity conferred by unlabeled double cysteine mutants was carried out as previously described (164). *Escherichia coli* BL21 (DE3) were transformed with empty pET19b vector, pET19b encoding PfMATE wild-type, or mutant PfMATE. A dense overnight culture from a single transformant was used to inoculate 10 mL of LB broth containing 0.1 mg/mL ampicillin to a starting Abs_{600nm} of 0.0375. Cultures were grown to Abs_{600nm} of 0.3 at 37 °C and expression of the encoded construct was induced with 1.0 μM IPTG (Gold Biotechnology). Expression was allowed to continue at 37 °C for 2 h, after which the Abs_{600nm} of the cultures was adjusted to 0.5. The cells were then used to inoculate (1:20 dilution, starting Abs_{600nm} = 0.025) a sterile 96-well microplate (Greiner Bio-one, Monroe, NC) containing 50% LB broth, 0.1 mg/mL ampicillin, and 60-72 μg/mL R6G. Microplates were incubated at 37 °C with shaking at 200 rpm for 6-10 h, after which the cell density (Abs_{650nm}) was measured on a BioTek Synergy H4 microplate reader and normalized to the wild-type construct. Each data point was performed in triplicate, and the experiment was repeated to obtain the mean and standard error of the mean (S.E.M). To statistically determine the impact of substitutions on R6G resistance, a one-way ANOVA in the program Origin (OriginLab, Northampton, MA) determined that the difference between population means was statistically significant at the 0.05 level.

Fluorescence Anisotropy

R6G was solubilized in water and dilutions in ethanol were prepared and measured spectrophotometrically at 524 nm ($\varepsilon = 116{,}000\ M^{-1}\cdot cm^{-1}$) to determine the concentration. Dilutions of purified PfMATE in 50 mM Tris/MES pH 7.5, 10% glycerol (v/v),1mM β-DDM buffer were mixed with a constant concentration of R6G (2.0 uM) in a total volume of 25 μL in a 384-well black fluorescence microplate (Greiner Bio-One, Monroe, NC) and incubated at room temperature for >5 min. R6G fluorescence anisotropy was measured using a BioTek Synergy H4 microplate reader with a 480 nm excitation filter (20 nm band pass) and a 570 nm emission filter (10 nm band pass) (181). Each point was measured in triplicate and R6G binding affinity was determined by a non-linear least squares analysis of each individual curve in Origin. The average K_D and standard deviation (S.D.) for each mutant are reported.

Tryptophan Fluorescence Quenching

Purified PfMATE in 50 mM Tris/MES pH 7.5, 10% glycerol (v/v), 1mM β-DDM buffer was adjusted to pH 4.0 using an empirically determined volume of 1 M citric acid. Samples at pH 7.5 were adjusted with an equivalent volume of buffer to maintain an equal concentration of protein between pH conditions. Samples were placed in a quartz fluorometer cell (Starna Cells Inc, Atascadero, CA ; cat #: 16.40F-Q-10/Z15) and tryptophan fluorescence quenching was monitored using a T-format fluorometer from Photon Technology International at 23 °C. The excitation wavelength was (λ_{ex}) 295 nm and tryptophan fluorescence was monitored between (λ_{em}) 310 nm and 370 nm. The fluorescence intensity at 329 nm was recorded from the spectra to determine the difference in fluorescence intensity between pH 7.5 and pH 4.0 samples (164). Experiments were repeated in triplicate and the mean and S.E.M of fluorescence quenching was determined. A one-way ANOVA in Origin to assess the impact of substitutions on Trp quenching revealed that there was a statistically significant difference between population means at the 0.05 level.

CHAPTER IV

Sodium drives the population of a unique intermediate in PfMATE

Promiscuity for the ionic species coupled to MATE-mediated substrate transport is an emerging theme from a number of studies illustrating that the MATE transport cycle may be dependent on more than one ion (43, 150, 151). As a result, defining the molecular basis of cation selectivity in MATE transporters has proven challenging. Though many structures of MATE transporters have been reported, they give little insight into the structural and chemical basis for ion selectivity since crystal structures are too low resolution to explicitly identify ions. Given that the number of electrons in Na^+ and water are the same they are virtually indistinguishable in X-ray diffraction data. Thus, ion binding sites have been informed by using heavy atom congeners that likely do not capture endogenous sites for Na^+. Compounding this challenge is that ion specificity of the MATEs (and other multidrug transporters) has typically been analyzed by cell-based resistance experiments which are difficult to control for ions and may not reflect effects exclusively due to MATE activity.

Interestingly the *E. coli* ClbM transporter from the DinF subfamily, which is most homologous to PfMATE, was shown in biochemical experiments to couple to protons as well as to several other ions to achieve transport, including Na^+, Cs^+, and Rb^+ (43). The structure of ClbM reported residual densities modeled as ions in the C-lobe occupying a previously unobserved binding site. It was postulated that a break in TM11 could facilitate the accommodation of the larger diameter atomic orbitals of Cs^+, and Rb^+. However, this structural feature is not conserved in the MATE family. MD simulations reveal that the conserved Asp 299 at the middle of the transmembrane region of TM7 in the C-lobe of ClbM is more likely to be protonated rather than bound to a Na^+ (182). In contrast, Na^+ was stably bound in simulations to semi-conserved residues Asp 53 and Asn 195 on TMs 1 and 5 in the N-lobe of ClbM.

The initial structures of PfMATE were determined from crystals obtained at neutral and low pH in precipitant solutions containing Na^+ (114). The low pH protonated structure reported a structural change in TM1, which was bent around Gly 30, and in TMs 5 and 6, which were tilted 10° away from the membrane normal compared to the neutral pH Apo structure. These structural changes were interpreted as a rearrangement of a water-mediated H-bond network in the N-lobe involving the side chains of Asp 41, Asn 180, corresponding to Asp 53 and Asn 195 in ClbM, as well as Asp 184, and Thr 202 (Fig. 1.9). Quantum mechanical and molecular mechanical (QM/MM) MD simulations suggested that in the Apo structure only Asp 41 is protonated, however, in the low pH structure both Asp 41 and Asp 184 are predicted to be protonated (155), thus forming the basis for the proposed structural changes. However, a later MD study suggested that the residual electron density in the N-lobe in proximity to Asp 41, Asn 180, Asp 184, and Thr 202 was more consistent with a Na^+ ion rather than a water molecule based on the corresponding atomic B-factors, coordination number and geometry of this site (118). The simulations allowed Ficici et al. to conclude that the OF structure of PfMATE is indeed Na^+ bound, however, with a proton shared between Asp 41 and Asp 184 to form a carboxyl-carboxylate pair (118). Furthermore, their data implied selectivity for Na^+ over H+ in the N-lobe of PfMATE.

Fueling the debate about the identity of the coupling ion in PfMATE was the reported IF structure by Zakrzewska et al. which contained residual density identified as Na^+ in the N-lobe of the transporter in close proximity to Asp 41 (117). This observation was interpreted as evidence for Na^+ involvement in driving conformational change. In contrast, we have shown that protonation of residues in the N-lobe of PfMATE likely leads to localized structural rearrangement of TM1 detectable by a reduction in Trp fluorescence (164). Furthermore, we have attributed the IF state of PfMATE exclusively to H^+-dependent conformational changes and identified key sidechains that mediate this conformational change. Nevertheless, the *in silico* and crystallographic evidence implicates a role for Na^+ in the transport mechanism of PfMATE.

Prior to publication of the MD investigations and the IF structure, we sought to delineate this aspect of ion coupling in PfMATE and determine a role for Na^+ in the conformational cycle. For this purpose, we leveraged an extensive network of spin label pairs described previously to interrogate Na^+-dependent movement of TMs in PfMATE. While we reiterate the H^+-dependence of the IF conformation, we also report a unique Na^+-dependent intermediate that involves the conserved residues in the N-lobe, thus providing additional evidence for dual-ion specificity in PfMATE.

Results

Substrate/ion antiport requires the population of at least two conformational states in which the substrate binding site is alternately exposed to the intracellular (IF) or the extracellular environments (OF) (21). Previous investigation of the proton driven conformational change in PfMATE using DEER spectroscopy identified distance changes on the extracellular and intracellular sides of the transporter in the transition to the IF state (164). Specifically, we observed decreases in distances on the extracellular side of the transporter across the central cleft between the N- and C-lobes. Concomitantly, there were increases in distance on the intracellular side of the transporter that identified TM3 and TM9 movements as structural determinants of the IF conformation. We previously reported also that Na^+ appeared to have little or no effect on PfMATE structure at pH 7.5 (Fig. S10). Ficici et al. determined that Na^+ occupation of its binding site in the N-lobe was predicated on an H-bond between Asp 41 and Asp 184 (118). Therefore, we investigated if Na^+ driven conformational changes in PfMATE displays pH dependence using the established library of spin label pairs probing distances on the extracellular and intracellular sides of the transporter.

Ligand dependence of PfMATE is unaltered by sodium

The structural and functional profiles of PfMATE in the presence of Na^+ were analyzed by several approaches that have been previously described (164). We quantified R6G binding affinity to PfMATE by monitoring R6G fluorescence anisotropy in detergent buffer supplemented with 50mM NaCl. The apparent K_D indicated that sodium did not significantly affect binding to R6G at either pH 7.5 or pH 4.0 (Fig. S14A).

PfMATE demonstrates pH-dependent Trp quenching, a consequence of local structural arrangements in the environment of Trp 44 on TM1 (164). This has been used as a surrogate reporter of the functional integrity of the transporter. However, Trp fluorescence was not quenched at pH 7.5 upon the addition of sodium (Fig. S14B). Furthermore, the addition of 50mM NaCl did not affect pH dependent Trp quenching, indicating that quenching is determined by protonation.

The structural and functional integrity of PfMATE mutants were also assayed in this manner. Spin-labeled double cysteine mutants of PfMATE for DEER analysis bind substrate with similar affinity as WT and demonstrate robust Trp quenching at pH 4.0 similar to WT (Fig. S9, Table S1). Additionally, PfMATE mutants were tested to determine their ability to confer resistance to toxic concentrations of R6G. This assay is a surrogate reporter of PfMATE transport. Expression of unlabeled PfMATE mutants conferred resistance to concentrations of R6G that are toxic to cells transformed with empty vector. These results suggest that the cysteine mutations and subsequent labeling did not result in any significant functional or structural perturbations (183). However, the ion specificity of PfMATE transport function cannot be deduced from these assays, particularly with regard to the R6G resistance assay.

Na^+ mediated conformational changes are pH-dependent

DEER investigation of PfMATE previously demonstrated that formation of an IF conformation at low pH was only observed upon PfMATE reconstitution into nanodiscs composed of *E. coli* polar lipids and egg phosphatidylcholine (PC). Therefore, to investigate the role of sodium in PfMATE conformational cycle, we carried out DEER experiments with and without sodium at high and low pH in nanodiscs. Spin label pairs monitoring the intracellular and extracellular sides of the transporter demonstrate that 50mM Na^+ failed to elicit distance changes at pH 7.5 (Figs. 4.1–4.3). Distance distributions with Na^+ at pH 7.5 overlap with distance distributions without Na^+ under Apo conditions (purple and black traces, respectively). In contrast, at low pH, Na^+ (cyan traces) elicits a shift in distinct distance components of select spin label pairs (N274R1/E134R1, N274R1/I186R1 and N274R1/413R1). As a consequence, the distance distributions of these pairs at pH 4.0 in the presence of Na+ bear unique features from the distributions observed in the absence of Na^+ or at low pH (Apo pH 7.5, black trace; Apo pH 4.0, red trace). The pH dependence of Na^+ conformational change is in keeping with MD simulations which determined that the sodium ion is stably bound when the side chains of Asp 41 and Asp 184 are engaged in an H-bond.

Extracellular conformational change with Na^+ at low pH is limited

The pH dependent conformation changes reported for PfMATE identified large scale distance changes between the N- and C-lobes of the transporter. The pattern of distance changes was highlighted by decreases in distance between TMs 7 and 8 in the C-lobe to TMs 4, 5, and 6 in the N-lobe that were consistent with movement of the lobes towards each other to close the central cavity from the extracellular milieu (Fig. 4.1A, B; red traces). At low pH Na^+ elicited few conformational changes on the extracellular side of the transporter (Fig. 4.1, cyan traces). However, the pattern of distance changes emerging from DEER measurements identified TM8 as the focal point of Na+-dependent rearrangements (Fig. 4.1B, C). The distance distributions are characterized by a shift in equilibrium between populations that define the IF conformation. The conformational state of PfMATE with Na^+ at pH4 is congruent with TM8 movement away from TMs 4 and 5 in the N-lobe (Fig. 4.1B) and towards TM11 in the C-lobe (Fig. 4.1C).

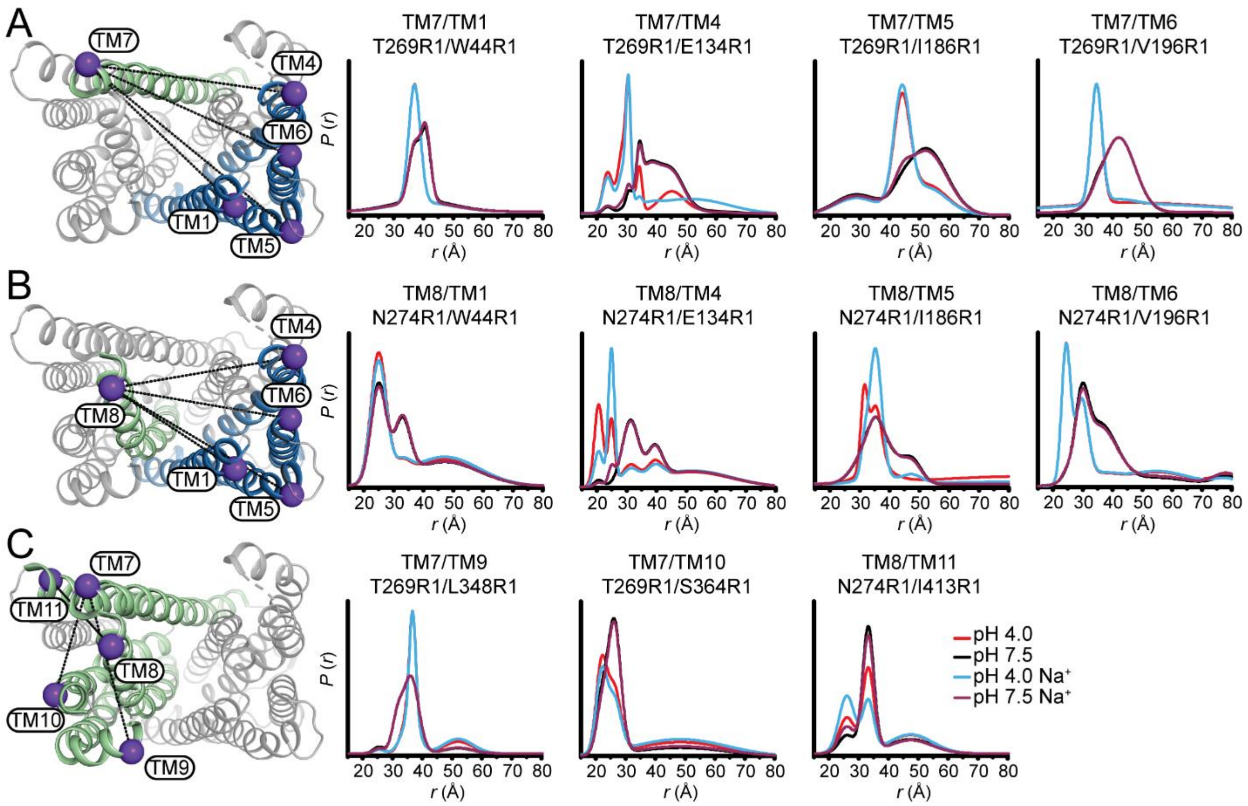

Figure 4.1. **Relative movement of TM7 and TM8 on the extracellular side of PfMATE in response to Na$^+$**. Spin labeled positions on TMs in the N-lobe (blue TMs) and C-lobe (green TMs) are highlighted on the OF structure by purple spheres. Experimentally determined distributions are plotted. TM7 movement at pH4 with 50 mM NaCl is limited (**A**). TM8 is a focal point for conformational change on the extracellular side as it moves away from TMs 4 and 5 in N-lobe (**B**) and towards TM11 in the C-lobe (**C**).

Importantly, these distance distributions with Na$^+$ at pH 4.0 are in disagreement with the predicted distributions from the OF pH 6.0 and pH 5.0 structures and the IF structure at pH 5.0 (114, 117). Additionally, there are no significant distance changes with Na$^+$ at low pH observed for TM1. The pattern of pH-dependent distance changes in TM1 was associated with possible twisting of TM1 that may underpin Trp quenching at low pH. That Na$^+$ does not elicit Trp quenching at low pH is consistent with the Na$^+$ pH 4.0 DEER data for TM1.

Intracellular conformational change with Na+ at low pH reveals a unique structural intermediate

In contrast to the extracellular side of the transporter, Na+-induced distance changes between TM helices on the intracellular side were more extensive. DEER measurements at low pH identified TMs 3 and 9 as the focal points of conformational changes with an increase in distance of 17 Å between these two TMs (Fig. 4.2A; red trace). However, the addition of 50 mM NaCl at pH 4.0 resulted in a shift in the distribution that resulted in a decrease in the average distance between probes on TM3 and TM9 (Fig. 4.2A; cyan trace). This stabilized a unique structural intermediate that is distinct from the pH 7.5 state but is sampled in the pH 4.0 state. Though rotation of TMs 3 and 9 cannot be ruled out as determinants of these changes in *P* (*r*), no changes in spin label mobility are reported by continuous wave EPR spectra (Appendix II), which report variations in the local environment of the spin label (184).

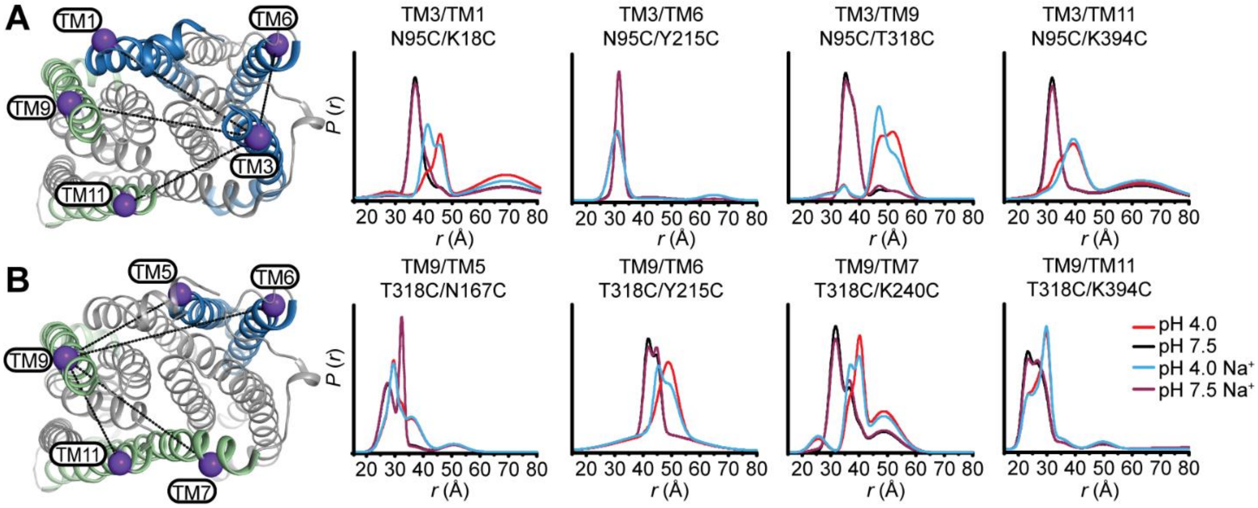

Figure 4.2: **Relative movement of TM3 and TM9 on the intracellular side induced by Na$^+$**. Labeled positions for DEER measurements on TM3 and TM9 (**A** and **B**, respectively) to other TMs in the N- and C-lobes are depicted on the intracellular side of the OF structure. While protonation favors an increase in distance between the N- and C-lobes, Na$^+$ pH 4.0 induces a unique conformational intermediate with average distances between spin labels that are greater than distances at pH 7.5 but shorter than distances measured at pH 4.0 by DEER.

Na^+ dependent distance changes are also reported for TM3 and TM9 when measured to other TMs at pH 4.0 (Fig. 4.2A, B), consistent with the purported role of TM3 and TM9 in intracellular gating (183). Shifts in distance populations between TM3 and TM1 (Fig. 4.2A), between TM9 and TM6, and TM9 and TM7 (Fig. 4.2B) are observed as a consequence of Na^+ addition at pH 4.0 (Fig. 4.2A, B; cyan traces). These shifts resulted in a unique structural intermediate with average distances between spin labels that are greater than the average distance at pH 7.5 but shorter than the average distance measured at pH 4.0 by DEER. Consequently, these movements would seem to enhance a particular component of the IF state that may facilitate a partial closing of the intracellular gate of the transporter.

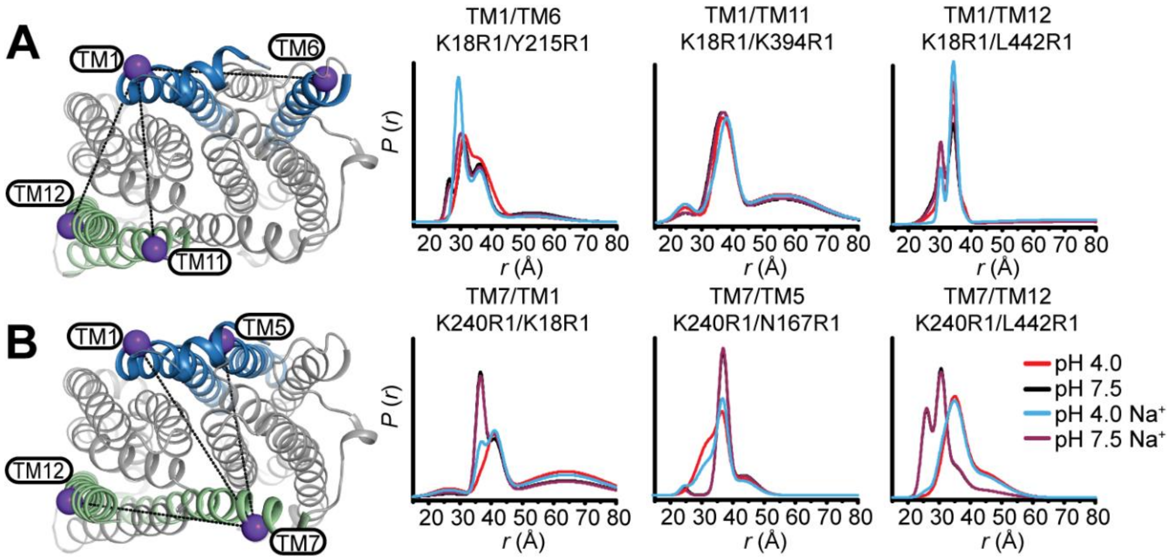

Figure 4.3: **Na^+ binding at low pH stabilizes a conformational intermediate overlapping with the OF conformation of TM1 and TM7**. Positions for DEER measurements from TM1 and TM7 to helices in the N- and C-lobes are indicated on the OF structure. Relative distance changes involving TM1 (**A**) and TM7 (**B**) with Na^+ at low pH are congruent with the OF conformation.

Supporting this interpretation, DEER measurements from TM1 to TM6 (Fig. 4.3A) and from TM1 to TM7 (Fig. 4.3B) with Na^+ at pH 4.0 reveal stabilization of a conformational intermediate overlapping with the pH 7.5 conformation (Fig. 4.3A, B; black and cyan traces).

Furthermore, CW EPR analysis reveals no spectral changes that would indicate spin mobility changes that could be correlated with global structural rearrangements (Appendix II). Importantly, the conformational changes observed from TM1 to TMs 6, 11, and 12 suggest that TM1 remains intact under these experimental conditions and is incongruent with the conformational changes implied by the IF crystal structure in which TM1 is unwound.

Identification of residues mediating Na$^+$-dependent conformational changes

Structures of NorM-Vc and ClbM have implied the binding sites for Na$^+$ are located in the N-lobe and the C-lobe of the MATE transporters. Mutagenesis of conserved residues in conjunction with functional assays has also supported these findings, identifying key residues that may be involved in ligand binding and transport. Recent *in silico* approaches with molecular dynamics simulations also support the involvement of conserved residues in the N- and C-lobes for ion and substrate binding and transport. Our previous study using DEER to investigate the H$^+$-dependent conformational changes in PfMATE exploited the sensitivity of the N95R1/T318R1 intracellular pair as a reporter of the OF/IF isomerization to identify residues involved in stabilization of intermediates. Therefore, we introduced substitution mutations of conserved N-lobe residues (Fig. 4.4A, top inset) into N95R1/T318R1 to monitor changes in the Na$^+$/H$^+$-dependent conformational equilibrium. These residues included Pro 26, Asp 41, and Thr 202 (Fig. 4.4A, top inset) as well as Glu 163 and Tyr 224 (Fig. 4.4A, lower inset) which were uncovered as determinants of IF/OF conformational switching.

The IF population characteristic of the N95R1/T318R1 reporter consists of two components with centers at ~45 Å and 52 Å that are at equilibrium at pH 4.0. (Fig. 4.4B, red trace). Na$^+$ induces a leftward shift in the distance distribution at pH 4.0 that enhances the 45 Å distance component of the IF intermediate and reduces the population of the longest distance component at 52 Å. This change in population was attenuated by P26A, D41A, and T202N mutations.

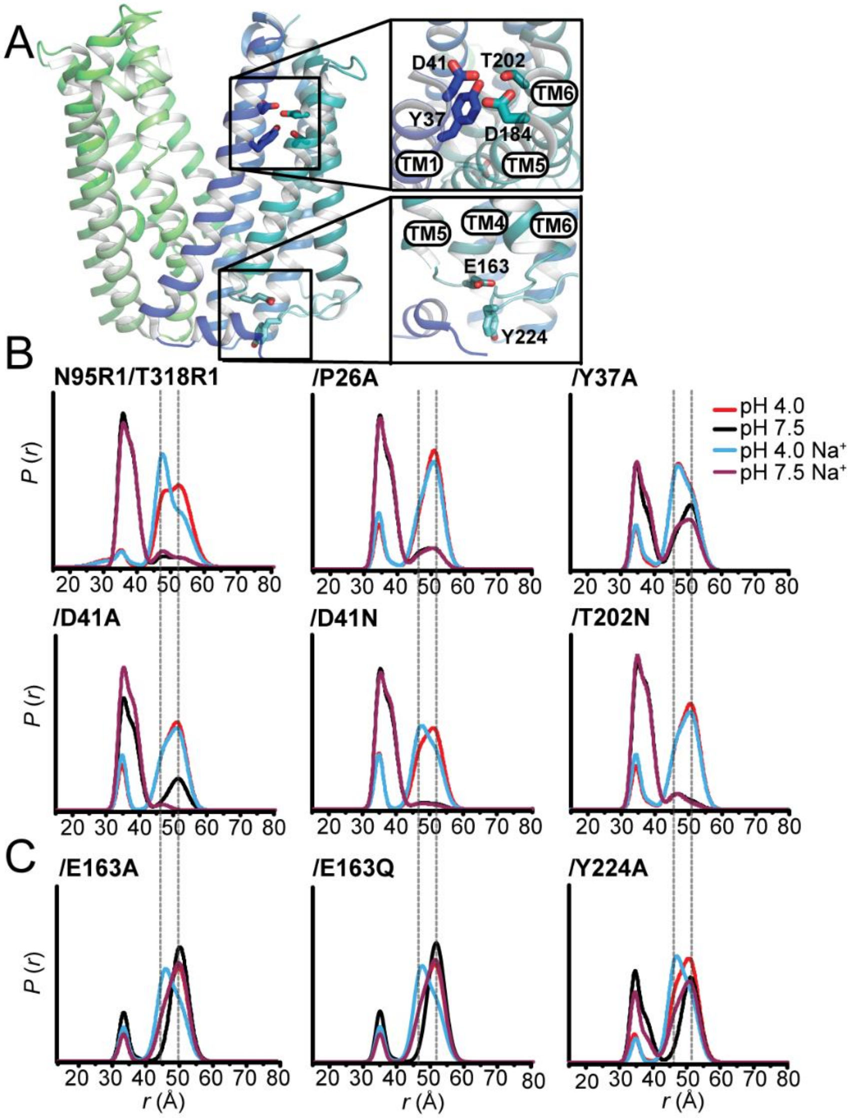

Figure 4.4. **N-lobe residues mediate the Na⁺ low pH conformation**. Conserved residues previously identified in the N-lobe as crucial for PfMATE function are shown as sticks in the OF structure in the top inset (**A**). E163 on IL4-5 and Y224 on IL6-7 are depicted in the lower inset. Distance distributions of the intracellular reporter pair N95R1/T318R1 (**B** and **C**, **Fig. S3**) in acidic residue mutant backgrounds at pH 4.0 and pH 7.5 with and without 50mM Na⁺. While P26A, D41A, and T202N inhibit the Na⁺ pH 4.0 structural intermediate, Y37A stabilizes this conformation. E163A and Y224A, previously shown to destabilize the OF conformation at pH 7.5, do not inhibit the Na⁺ pH 4.0 structural intermediate.

Notably, these mutations attenuated PfMATE-mediated resistance to toxic concentrations of R6G (Fig. S8) (164) but do not abrogate the pH-dependent conformational change (Fig. 4.4B, cyan and red traces). Interestingly, the D41N mutation retains sensitivity to Na^+ at low pH (Fig. 4.4B), though is also impaired in resistance assays with R6G. Notably, the Y37A mutation, which was shown to partially stabilize the IF conformation (Fig. 4.4B, black trace) (183), stabilized the Na^+ dependent intermediate as well at pH 4.0 (Fig. 4.4B, red trace). Indeed, the *P* (*r*) for Y37A in the presence of Na^+ at low pH was superimposable with respect to the low pH condition (Fig 4.4B, cyan and red traces).

Ligand dependence captured by DEER measurements has established that alternating access of PfMATE is H^+-coupled. This conclusion was reinforced by shifts in distance populations to a protonated state at pH 7.5 upon disruption of the interaction between Glu 163 on IL4-5 and Tyr 224 on IL6-7 due to alanine substitution mutations (183). However, E163A, E163Q, or Y224A mutants failed to abrogate the Na^+-dependent conformational shift at low pH (Fig. 4.4C). Consonant with the notion that E163A, E163Q, and Y224A mutations effect a conformational change at pH 7.5 that mimics a protonated state, Na^+ addition at pH 7.5 was observed to elicit a leftward shift in the distance distribution that overlaps with the Na^+ low pH population (Fig. 4.4B, C; purple traces). Mutations of Gln 253 and Glu 331 on TM7 and TM9 (Fig. S16A), which were identified as binding sites for Cl^- and H^+ (117, 118), respectively, did not affect H^+-dependent nor Na^+-dependent conformational change (Fig. S16B). Collectively, the dependence of ion-driven distance changes on conserved residues in the N-lobe suggests that Na^+ and H^+ form specific interactions with the side chains of these residues that determine the conformation of the Na^+ driven intermediate.

Discussion

The DEER analysis reported here illuminates important aspects of ion coupling in the conformational landscape of the transport cycle of PfMATE and establishes that Na^+ binding drives formation of a unique structural intermediate. This intermediate is defined in part by a distinct conformation of TM8 on the extracellular side, and of TMs 1, 3, and 9 on the intracellular side. The formation of this intermediate is dependent on protonation which stabilizes the IF conformation. That mutagenesis of conserved N-lobe residues impairs Na^+-driven structural rearrangements implies that Na^+ can bind to the IF structure, coordinated by residues in the N-lobe (Fig. 4.4B). This is inconsistent with a previous *in silico* approach which postulated that the OF substrate free PfMATE structure (PDB ID: 3VVN) represents a Na^+-bound state where Asp 41 and Asp 184 form a carboxyl-carboxylate interaction with a shared proton (118).

Sidechains of Asp 41 or Asp 184 are not essential for H^+-dependent stabilization of the IF state (183). In the absence of the Asp 41 sidechain, transition to the Na^+-driven intermediate is attenuated (Fig. 4.4B), suggesting that Asp 41 (and perhaps Asp 184) is involved in coordinating Na^+.

We have previously shown that the DEER data obtained at low pH is in good agreement with the predicted distance distributions from the IF crystal structure (180, 183). However, the IF structure was determined from crystals obtained in precipitant solutions at low pH containing NaCl and residual density in the N-lobe was putatively identified as Na^+ in the IF structure. This is incongruous with the DEER measurements reported here in which Na^+ addition to the IF structure at low pH induces a unique conformational intermediate that is distinct from the OF and IF conformations at pH 7.5 and pH 4.0, respectively. Collectively, the DEER analysis rules out the possibility that Na^+ could be permanently bound to the structure. MD simulations demonstrate that protonation of Asp 41 and Asp 184, leads to the dissociation of Na^+ (118). Consistent with the DEER data, the protonated transporter could transition to an IF conformation where Na^+ could bind (Fig. 4.1, 4.2; red traces). Indeed, we demonstrate that this is the case, however, Na^+ would be assumed to drive the transporter back to an OF conformation, which is inconsistent with the structural intermediate described herein (Fig. 4.1, 4.2; cyan traces). Nevertheless, the DEER data presented here convincingly show a Na^+-dependent conformational change in the IF low pH state.

Mutation of conserved N-lobe residues attenuates PfMATE-mediated R6G resistance (164), but these mutants are still able to achieve H^+-dependent OF/IF conformational switching.

Correlating the R6G resistance data for the N-lobe residues (Fig. S8) (183) which mediate the Na^+-bound low pH intermediate measured by DEER (Fig. 4.4A, B), it is possible to hypothesize the relevance of this intermediate to a functional transport cycle. The Na^+ low pH state of the transporter may represent an IF occluded structure with a thin intracellular gate due to the conformational shift between TM3 and TM9 (Fig. 4.2A) which results in a partial closing of the intracellular side. While such a conformation has not been captured by crystallography or other means among MATE transporters, an IF occluded structure was reported for the lipid flippase MurJ of the MOP superfamily (171). Population of this intermediate may represent a component in the transport cycle as the transporter transitions from the IF to OF conformation. Mutation of conserved N-lobe residues, while permitting OF to IF switching, may be unable to populate this IF occluded structure, thus trapping the transporter in the IF conformation in a H^+-dependent manner.

However, this interpretation does not rationalize the negligible effect of Na^+ on substrate binding. To firmly establish the role of Na^+ in the functional transport cycle will require in vitro transport assays. Additional experiments with R6G and Na^+ utilizing the N95R1/T318R1 reporter pair with Y37A, E163A, and Y224A mutations can also be carried out using DEER to exploit the sensitivity of these mutants to R6G binding. Together with the Na^+ low pH intermediate defined here, these approaches could prove crucial to uncovering the role of Na^+ in substrate recognition and extrusion in the transport cycle.

Experimental Procedures

Site-Directed Mutagenesis

Wild-type PfMATE was cloned into pET19b vector encoding an N-terminal 10-His tag under control of an inducible T7 promoter and was used as the template to introduce double cysteine pairs and background mutations via site-directed mutagenesis with complementary oligonucleotide primers. Substitution mutations were generated using a single-step PCR in which the entire template plasmid was replicated from a single mutagenic primer. PfMATE mutants were sequenced using both T7 forward and reverse primers to confirm mutagenesis and the absence of aberrant changes. Mutants are identified by the native residue and primary sequence position followed by the mutant residue.

Expression, Purification, and Labeling of PfMATE

Escherichia coli C43 (DE3) cells were freshly transformed with pET19b vector encoding wild-type or mutant PfMATE. A transformant colony was used to inoculate Luria-Bertani (LB) media (LabExpress, Ann Arbor, MI) containing 0.1 mg/mL ampicillin (Gold Biotechnology, St. Louis, MI) which was grown overnight (~15 h) at 34 °C and was subsequently used to inoculate 3 L of minimal medium A at a 1:50 dilution. Cultures were incubated while being shaken at 37 °C until they reached an absorbance at 600 nm (Abs_{600nm}) of ~0.8, at which time the expression of PfMATE was induced by the addition of 1mM IPTG (Gold Biotechnology, St. Louis, MI). The cultures were incubated overnight (~15 h) at 20 °C and then harvested by centrifugation. Cell pellets were resuspended in 20 mL of resuspension buffer [20 mM Tris-HCl, pH 7.5, 20 mM NaCl, 30 mM imidazole, and 10% (v/v) glycerol], including 10 mM DTT, and lysed by five passes through an Avestin C3 homogenizer. Cell debris was removed by centrifugation at 9,000 x g for 10 min. Membranes were isolated from the supernatant by centrifugation at 200,000 x g for 1.5 h.

Membrane pellets were solubilized in resuspension buffer containing 20 mM β-DDM (Anatrace, Maumee, OH) and 0.5 mM DTT and incubated on ice with stirring for 1 hour. Insoluble material was cleared by centrifugation at 200,000 x g for 30 min. The cleared extract was bound to 1.0 mL (bed volume) Ni-NTA Superflow resin (Qiagen, Germantown, MD) at 4 °C for 2 h. After washing with 10 bed volumes of buffer containing 30 mM imidazole, PfMATE was eluted with buffer containing 300 mM imidazole.

Double cysteine mutants were labeled with two rounds of 20-fold molar excess 1-oxyl-2,2,5,5-tetramethylpyrroline-3-methyl methanethiosulfonate (Enzo Life Sciences, Farmingdale, NY) per cysteine at room temperature in the dark over a 4 hour period, after which the sample was placed on ice at 4 °C overnight (~15 h) to yield the spin label side chain R1. Unreacted spin label was removed by size exclusion chromatography over a Superdex200 Increase 10/300 GL column (GE Healthcare, Pittsburg, PA) into 50 mM Tris/MES, pH 7.5, 1 mM β-DDM, and 10% (v/v) glycerol buffer. Peak fractions of purified PfMATE were combined and concentrated using an Amicon Ultra 100,000 MWCO filter concentrator (Millipore, Burlington, MA) and the final concentration was determined by A_{280} measurement (ε = 46870 $M^{-1}\cdot cm^{-1}$) for use in subsequent studies.

Reconstitution of PfMATE into Nanodiscs

E. coli polar lipids and PC (L-α phosphatidylcholine) (Avanti Polar Lipids, Alabaster, USA) were combined in a 3:2 w/w ratio, dissolved in chloroform, evaporated to dryness on a rotary evaporator and desiccated overnight under vacuum in the dark. The lipids were hydrated in 50 mM Tris/MES pH 7.5 buffer to a final concentration of 20 mM, homogenized by freezing and thawing for 10 cycles, and stored in small aliquots at −80 °C. MSP1D1E3 was expressed and purified as previously described and dialyzed into 50mM Tris/MES pH 7.5 buffer (177). MSP1D1E3 was concentrated using a 10,000 MWCO filter concentrator and the final protein concentration was determined by A_{280} measurement (ε = 29,910 $M^{-1}\cdot cm^{-1}$).

For reconstitution into nanodiscs, spin-labeled double cysteine mutants in β-DDM micelles were mixed with *E. coli* polar lipids/PC lipid mixture, MSP1D1E3 and sodium cholate in the following molar ratios: lipid:MSP1D1E3, 50:1; MSP1D1E3:PfMATE, 10:1; cholate:lipid, 3:1. Reconstitution reactions were mixed at 4 °C for 1 hour. The detergent was removed from the reaction by addition of 0.1 g/ml Biobeads (Bio-Rad, Hercules, CA) and incubation at 4 °C for 1 hour. This was followed by another addition of 0.1 g/ml Biobeads with 1-hour incubation, after which 0.2 mg/ml Biobeads were added and mixed overnight. The next day, 0.2 mg/ml Biobeads were added and mixed for one hour (165). The reaction was filtered using a 0.45 µm filter to remove Biobeads. Full nanodiscs were separated from empty nanodiscs by size exclusion chromatography into 50 mM Tris/MES, pH 7.5 and 10% (v/v) glycerol buffer. The PfMATE-containing nanodiscs were concentrated using Amicon ultra 100,000 MWCO filter concentrator, then characterized using SDS-PAGE to verify reconstitution and estimate reconstitution efficiency. The concentration of spin-labeled mutants in nanodiscs was determined as described previously by comparing the intensity of the integrated CW-EPR spectrum to that of the same mutant in detergent micelles (178).

CW-EPR and DEER Spectroscopy

CW-EPR spectra of spin-labeled PfMATE samples were collected at room temperature on a Bruker EMX spectrometer operating at X-band frequency (9.5 GHz) using 10 mW incident power and a modulation amplitude of 1.6 G. DEER spectroscopy was performed on an Elexsys E580 EPR spectrometer operating at Q-band frequency (33.9 GHz) with the dead-time free four-pulse sequence at 83 K (147). The pulse lengths were 10-14 ns (π/2) and 20 ns (π) for the probe pulses and 40 ns for the pump pulse. The frequency separation was 63 MHz. To ascertain the role of H^+, samples were titrated to pH 4.0 with an empirically determined amount of 1 M citric acid and confirmed by pH microelectrode measurement. The substrate-bound state was generated by addition of 1 mM R6G at high and low pH. Samples for DEER analysis were cryoprotected with 24% (v/v) glycerol and flash-frozen in liquid nitrogen.

Primary DEER decays were analyzed using home-written software operating in the Matlab (MathWorks, Natick, MA) environment as previously described (177, 179). Briefly, the software carries out global analysis of the DEER decays obtained under different conditions for the same spin-labeled pair. The distance distribution is assumed to consist of a sum of Gaussians, the number and population of which are determined based on a statistical criterion.

Fluorescence Anisotropy

R6G was solubilized in water and dilutions in ethanol were prepared and measured spectrophotometrically at 524 nm (ε = 116,000 $M^{-1}\cdot cm^{-1}$) to determine the concentration. Dilutions of purified PfMATE in 50 mM Tris/MES pH 7.5, 10% glycerol (v/v), 1 mM β-DDM buffer were mixed with a constant concentration of R6G (2.0 uM) in a total volume of 25 µL in a 384-well black fluorescence microplate (Greiner Bio-One, Monroe, NC) and incubated at room temperature for >5 min. R6G fluorescence anisotropy was measured using a BioTek Synergy H4 microplate reader with a 480 nm excitation filter (20 nm band pass) and a 570 nm emission filter (10 nm band pass) (181). Each point was measured in triplicate and R6G binding affinity was determined by a non-linear least squares analysis of each individual curve in Origin. The average K_D and standard deviation (S.D.) for each mutant are reported.

Tryptophan Fluorescence Quenching

Purified PfMATE in 50 mM Tris/MES pH 7.5, 10% glycerol (v/v), 1 mM β-DDM buffer was adjusted to pH 4.0 using an empirically determined volume of citric acid. Samples at pH 7.5 were adjusted with an equivalent volume of buffer to maintain an equal concentration of protein between pH conditions. Samples were placed in a quartz fluorometer cell (Starna Cells Inc, Atascadero, CA; cat #: 16.40F-Q-10/Z15) and tryptophan fluorescence quenching was monitored using a T-format fluorometer from Photon Technology International at 23 °C. The excitation wavelength was (λ_{ex}) 295 nm and tryptophan fluorescence was monitored between (λ_{em}) 310 nm and 370 nm. The fluorescence intensity at 329 nm was recorded from the spectra to determine the difference in fluorescence intensity between pH 7.5 and pH 4.0 samples (164).

CHAPTER V

Perspectives on future Investigations

Synopsis

Despite the physiological significance of MATE transporters in multidrug resistance, a dearth of mechanistic knowledge relating efflux activity to a conformational cycle has precluded a rigorous understanding of substrate transport. At the outset of this investigative work, OF structures of NorM from *V. cholerae* and *N. gonorrhoeae*, DinF-Bh from *B.* halodurans, and PfMATE from *P. furiosus* had been reported. These structures adopted the same conformation regardless of bound ligand, except for PfMATE, which at low pH demonstrated TM1 bending in the N-lobe of the transporter. Since then, structures of the colibactin transporter ClbM from *E. coli*, VcmN from *V. cholerae,* and the eukaryotic MATE transporters AtDTX14 from *A. thaliana* and CasMATE from *C. sativa* have been reported, capturing similar OF conformations. In the context of a putative alternating access transport cycle, the mechanism by which these structures adopt other obligatory intermediate states remained unclear. The functional and spectroscopic analysis of PfMATE presented herein represents a significant advancement in our knowledge of proton-coupled MATE transporters, establishing PfMATE as the most characterized MATE transporter to date.

Initial DEER analysis of spin-labeled PfMATE in detergent micelles revealed no significant conformational changes under low pH conditions. Given that PfMATE was crystallized via LCP and densities corresponding to monoolein were identified in the N- and C-lobe cavities, we speculated that DEER experiments in a lipid environment might engender the conformational changes expected based on the low pH crystal structure. Therefore, we determined optimal conditions for PfMATE reconstitution into nanodiscs consisting of *E. coli* polar lipids and egg PC. Nanodisc-reconstituted spin-labeled PfMATE demonstrated extensive structural rearrangements at low pH that were incongruent with the low pH structure by Tanaka et al. Instead, the large-scale distance changes between spin labels suggested stabilization of an IF conformation.

Concurrent with our investigation, a structure of PfMATE in an IF conformation was determined, ostensibly facilitated by native *P. furiosus* lipids. While our exhaustive DEER data set is mostly consistent with this structure, our work is distinguished by resolving confounding aspects of ligand dependent alternating access, specifically the role of protons, and identification of a protonation switch involved in the mechanism of OF/IF conformational change. Although endogenous *P. furiosus* lipids were proposed to be required for transition to the IF state, the DEER analysis indicates that non-native lipids will also stabilize this conformation. Furthermore, investigation of ion promiscuity suggests the presence of a unique Na^+/H^+-dependent intermediate that may be involved in the transport cycle.

PfMATE was previously demonstrated to efflux ethidium from spheroblasts and mediate resistance to NFX. However, we were unable to reproduce either result in our investigations. A substantial effort went toward adapting and benchmarking assays for defining PfMATE function and ion and substrate interactions. These assays established the conserved residues in the N-lobe as determinants for H^+-dependent conformational changes via Trp fluorescence quenching, which was correlated to R6G efflux in a cell-based resistance assay. These assays also allowed us to identify other residues involved in PfMATE function, including Glu 163. Incorporating substitution mutations of Glu 163 into DEER experiments we have established this residue as the protonation switch in PfMATE for mediating OF/IF transitioning.

The outcome of this investigation highlights the contribution of combining systematic DEER analysis with mutagenic and functional analysis of conserved residues. By uncovering the interplay between substrate and ion in the energetics of ligand-dependent transitions between conformational states, these data fill in critical gaps that the crystal structures leave unaddressed and set the stage to ascertain further details of alternating access in PfMATE.

Lipid dependence of PfMATE alternating access

There is an overwhelming body of evidence that suggests that the properties of biological membranes, such as dielectric constant, lateral pressure and curvature, and membrane thickness, can affect folding (140, 185), impart stability (138, 186, 187) and modulate the function and physiological roles (139, 188) of membrane proteins. Earlier work on rhodopsin suggested that the bilayer may modulate GPCR function (189, 190) and structural studies suggested specific interactions with phosphatidylethanolamine (PE) (191). More recently, it was shown that lipids, specifically phosphatidylglycerol (PG), act as allosteric modulators of β2-adrenergic receptor function and the lipid phosphatidylinositol 4,5-bisphosphate (PIP_2) controls signaling events in dopamine mediated neurotransmission associated with physiological and behavioral consequences (192).

Previously, an investigation was undertaken to determine the nature of lipid dependence for the H^+-coupled multidrug transporter LmrP from *Lactococcus lactis* using DEER spectroscopy (141). By measuring changes in equilibrium in nanodisc reconstituted LmrP between the OF and IF conformations of spin-labeled pairs with different lipid compositions, Martens et al. demonstrated a correlation between the degree of methylation of the ethanolamine headgroup and the population of the OF conformation (141). Specifically, methylation of the PE headgroup led to stabilization of the OF conformation, suggesting that direct H-bonds between the headgroup and the transporter play a role in OF/IF conformational change.

The role of lipids in PfMATE alternating access has come to the forefront due to the strict requirement of lipids on transition to the H^+-stabilized IF conformation. As noted, the IF structure of PfMATE was determined from crystals of purified protein incubated with native *P. furiosus* lipids (117) and monoolein densities were defined in the N- and C- lobe cavities of the OF pH 7.5 structure but were absent in the OF low pH structure (114). Consequently, lipids appear to be potent modulators of the transport mechanism. Computational studies of PfMATE in the OF low pH conformation have suggested that lipid headgroups play an important role in protonation of the conserved Asp 184 in the N-lobe, which is predicted to support conformational changes of TM1 (155). It is possible that lipid headgroups interact with the conserved cluster of residues in the N-lobe to potentiate conformational changes and stabilize distinct structural intermediates.

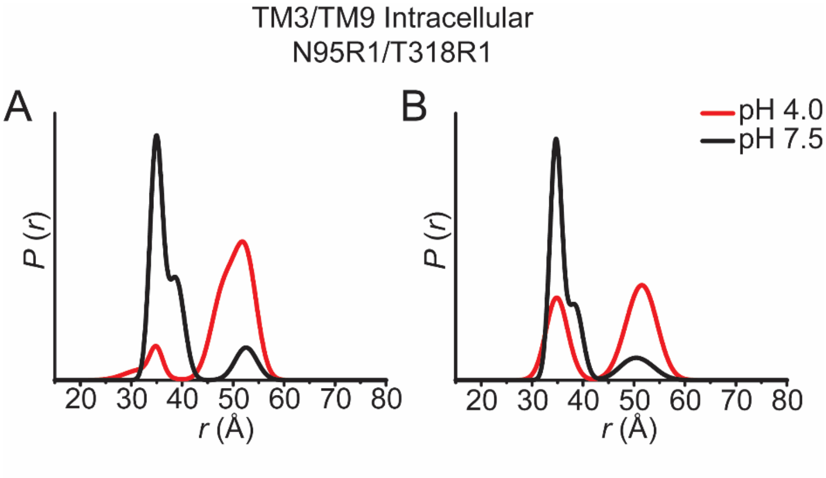

Fig 5.1: **PE shifts the conformational equilibrium of PfMATE**. Nanodiscs with synthetic lipids (40% PE, 40% PC, 14% PG, 6% cardiolipin) yielded a conformational equilibrium that strongly favored formation of the IF at low pH (~90% occupation) (**A**). These distributions recapitulated the data obtained in nanodiscs consisting of *E. coli* polar lipids and egg PC (3:2). Removal of PE (i.e., 80% PC, 14% PG, 6% cardiolipin composition) reduced occupation of the IF conformation to ~60% (**B**).

We have demonstrated PfMATE H^+-dependent conformational change in nanodiscs consisting of *E. coli* polar lipids and PC, disputing the requirement for native lipids posited by Zakrzewska et al. (117). The lipid mixture used for nanodisc reconstitution contains *E. coli* polar lipids, which consists of 67% PE, 23% phosphatidylglycerol (PG), and 10% cardiolipin (CL), and PC in a 3:2 ratio. Therefore, we can utilize the strategy employed for LmrP to investigate the dependence on the lipid headgroups in PfMATE. Specifically, the effect of lipid composition on conformational change can be determined by DEER using the reporter pairs N95R1/318R1 and W44C/S364R1 to measure the changes in the population of the OF and IF conformational states. Indeed, preliminary data with the N95R1/318R1 reconstituted into nanodisc in which PE was replaced with PC (80% PC, 14% PG, 6% CL) indicated that the H^+-dependent conformational change was attenuated (Fig. 5.1). Like LmrP, this result would seem to suggest that the interaction of the lipid head group with the transporter stabilizes the OF conformation, thus attenuating the rightward shift in the distance distribution to the IF conformation (Fig. 5.1B).

To determine the lipid interaction with the transporter, substitution mutations of conserved N-lobe residues such as Pro 26, Asp 41, and Asp 184 in the reporter pairs may be used in DEER experiments with the PE-deficient nanodiscs. Substitution mutations of additional residues shown to be involved in OF/IF switching such as Tyr 37, Glu 163, and Tyr 224 should also be analyzed in this manner. A pH titration experiment (refer to Fig. 3.7B) could also be done to define shifts in the p*K* of the OF/IF transition. Importantly, the effect of native lipids should also be investigated with these mutants of PfMATE. These experiments could identify critical sequence and structural determinants that support the conformational cycle and shape the energy landscapes of PfMATE.

Sequence and structural determinants of Na^+- and H^+-dependent conformational transitions

The work presented in previous chapters outlines a transport cycle in which protonation of Glu 163 on IL 4-5 of PfMATE disrupts an interaction of Tyr 224 on IL 6-7, which results in the IF transition. However, Trp fluorescence assays have demonstrated that the N-lobe residues are required for H^+ mediated conformational change. Therefore, proton binding on the extracellular side of the transporter, presumably in the N-lobe cluster, must translocate to the intracellular side to Glu 163 to effect the IF transition. The transduction of signals and energy via protons may be achieved by proton transport through both protonatable residues and buried water molecules due to Grotthuss shuttling (193). The Grotthuss mechanism is a process crucial to a number of fundamental processes in chemistry, physics, and biology. Hydrated excess proton creates a net positive charge defect that is strongly delocalized by altering the covalent bonds and H-bonds of surrounding water molecules. This mechanism facilitates proton translocation between neighboring water molecules via successive hopping events involving the rearrangement of local bonding topologies (194).

While the N-lobe cavity of PfMATE is the likely entry point for protons, a proton translocation pathway to the intracellular side has not been experimentally defined. Examination of the sequence of PfMATE through alignments and sequence analysis (Consurf (156)) identify a putative proton translocation pathway lined by polar and charged sidechains (Fig. 5.2A). The residues that line this pathway are either highly conserved or homologous to residues in NorM-Vc, including Arg 161, which is capable of water mediated proton transfer (195, 196).

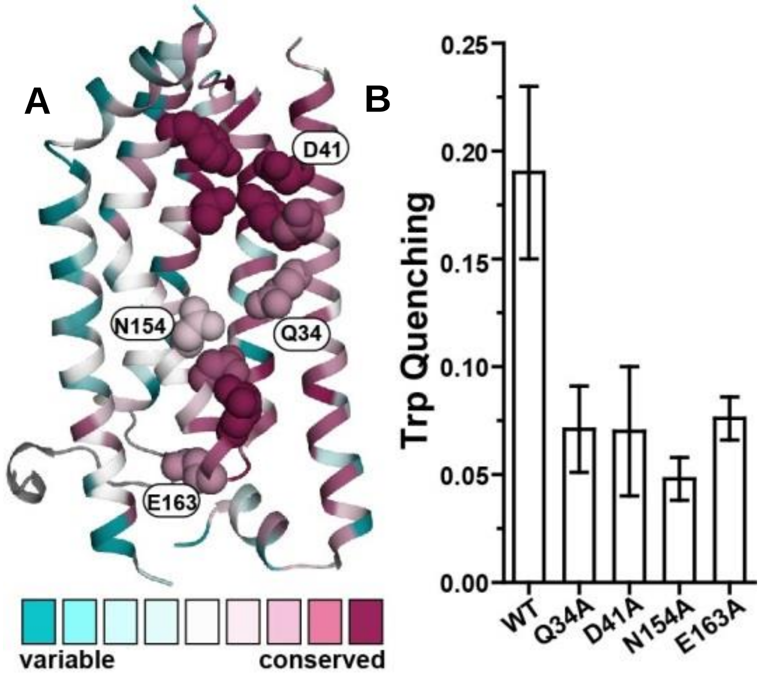

Figure 5.2: **Substitution of conserved residues in a putative proton translocation pathway in PfMATE**. The relative sequence conservation scores were calculated using a Bayesian algorithm and mapped onto the PfMATE crystal structure (PDB 3VVN) using the Consurf server. The conservation scores for each amino acid in the N-lobe of PfMATE (PDB ID: 3VVN) correspond to the discrete color scale (A). Consurf analysis reveals conservation of charged side chains capable of coordinating water molecules (A), which in turn can mediate proton hopping. Mutation of the labeled residues in (**A**) attenuates pH dependent Trp quenching in PfMATE (**B**).

The residues of this putative pathway, Gln 34, Asn 38, Asp 41 (TM1), Tyr 139, Asn 154, Asn 157, and Arg 161 (TM4), Glu 163 (IL4-5), and Thr 202 (TM6) could be individually targeted for mutagenesis to disrupt proton translocation. The consequences of these mutations may be determined by the approach described in Chapter II by size exclusion chromatography to ensure expression of properly folded proteins, binding and cell resistance assays with R6G, and Trp fluorescence measurements to assess the integrity of the proton switch. Preliminary data indicate that alanine substitution mutations of Gln 34 disrupt H+-dependent conformational changes as reported by reduced Trp quenching, in addition to Asp 41, Asn 154, and Glu 163 already reported herein (Fig. 5.2B).

To determine if these residues support H+-dependent isomerization from the OF to IF conformation, the mutations may be incorporated into the background of spin label pairs shown to monitor structural rearrangements by DEER on the intracellular and extracellular sides of PfMATE. The DEER measurements may also be complemented with site-specific NiEDDA, which reports solvent accessibility of single spin labels. Spin labels can be introduced at sites along the translocation pathway in PfMATE to correlate global structural rearrangements with localized changes in hydration of the central cavity. These experiments could reveal how disruption of the translocation pathway affects the H+-dependent conformational equilibrium between OF and IF states.

Substrate binding sites of PfMATE

A structure of PfMATE was determined bound to a molecule of NFX, the density of which was observed deep in the N-lobe cavity. Binding of this molecule was thought to be mediated by side chains of Gln 34, Tyr 37 (TM1), Asn 153 (TM4), Met 173, Ser 177 (TM5), Thr 202, Ser 205, Met 206, Thr 209 and Ile 213 (TM6) (114) (Fig. 5.3A, inset). The binding site identified for PfMATE was incongruous with the crystallographic data from NorM-Ng and DinF-Bh, which were determined bound to R6G, among other substrates (111, 113). The R6G molecule was found in NorM-Ng and DinF-Bh to be coordinated by residues on TMs 1, 2, 7, and 8. However, a structural alignment of these transporters reveal that the corresponding binding sites are nonoverlapping

(Fig. 5.3B), thus complicating the mutagenic approach to determine substrate binding and coupling.

In this work, R6G was shown to bind PfMATE with high affinity. Whereas H$^+$ modestly reduced R6G affinity the presence of Na$^+$ or mutation of conserved residues, including residues implicated in NFX binding by crystallographic data, did not significantly attenuate binding. Therefore, the location of the R6G binding site appears to be non-overlapping with the proposed NFX binding site.

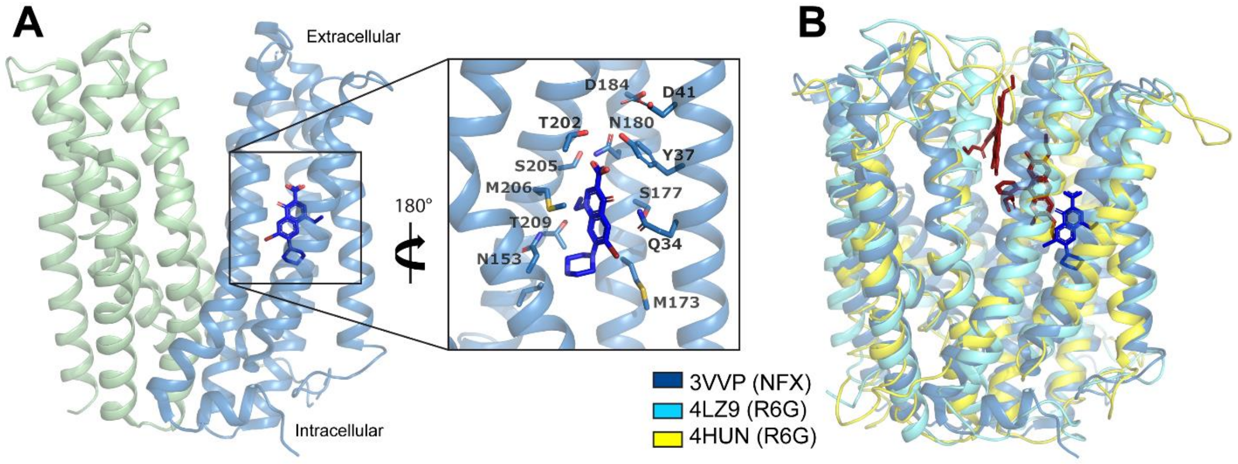

Figure 5.3: **Binding site of NFX in PfMATE does not overlap with R6G binding sites in DinF-Bh and NorM-Vc**. Side view of NFX bound PfMATE structure (PDB ID: 3VVP) (**A**). NFX model is depicted in blue. Residues coordinating NFX binding are highlighted (inset). For clarity TM2 is not shown. A structural alignment of NFX bound PfMATE with R6G bound NorM-Ng (PDB ID: 4HUN) and DinF-Bh (PDB ID: 4LZ9) shows that the binding sites of the molecules are nonoverlapping (**B**).

Using a spin-labeled substrate, binding can be determined using EPR, which can reveal the environment of the label by virtue of its accessibility to solvent, its mobility, and its distance from other spin labels. In a previous study, the binding of spin-labeled verapamil to human P-glycoprotein was determined and active uptake of the substrate into liposome was measured. More recently, the binding of a spin-labeled derivative of daunorubicin, ruboxyl, was determined for NorM-Vc. The location of the ruboxyl binding site in NorM-Vc was triangulated by distance measurements from singly labeled sites on the transporter to the spin-labeled substrate molecule by DEER. The DEER measurements placed the position of the nitroxide moiety of the bound ruboxyl in the periplasmic cleft near TM7 of the transporter. This was consistent with the location occupied by substrates in the crystal structures of NorM-Ng,

A similar approach can be undertaken with PfMATE using a spin-labeled derivative of R6G. Binding of spin-labeled R6G to PfMATE and PfMATE-mediated resistance to the spin-labeled substrate must be established. Changes in the EPR spectrum will also establish binding, since the mobility of the spin label is expected to decrease upon binding. The solvent accessibility of the spin-labeled substrate could also be measured to determine if the binding site is accessible to the buffered milieu. Finally, the distance between single spin label probes on the extracellular and intracellular sides of the transporter and the spin-labeled R6G can be measured by DEER. These experiments should also be done with substitution mutants of residues putatively involved in substrate binding and the translocation pathway. The combined approach would enable the triangulation of the binding site of spin-labeled R6G and may also illuminate the nature of ion and substrate coupling.

PfMATE alternating access and implications for the MATE family of transporters

The DEER analysis of PfMATE presented here provides a molecular blueprint for alternating access of other MATE transporters. Whether the H^+-dependent IF conformation captures a conserved obligatory intermediate in the MATE transport cycle is an outstanding question to be addressed. Indeed, the extent to which MATE transporters from distinct subfamilies share common mechanistic determinants is unclear. Our finding that similar networks of residues within the N-lobe of both PfMATE and NorM-Vc constitute an ion binding site and facilitate conformational changes required for drug resistance indicates that conserved mechanistic features could exist between subfamilies. However, we have also shown that buried carboxylates in the C-lobe of NorM-Vc form part of a mutually exclusive H^+/substrate binding site. These carboxylates are not conserved in PfMATE and therefore indicate that H$^+$/drug binding sites do not overlap.

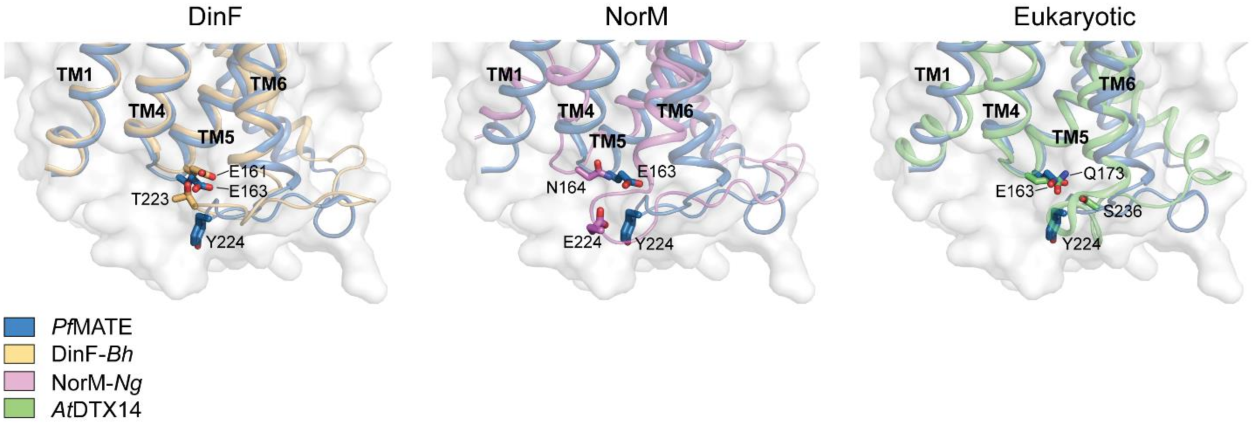

Figure 5.4: **IL4-5 may be implicated in conformational switching across the MATE family of transporters**. Structural alignments of PfMATE with representative MATEs from each subfamily reveal residues on the IL4-5 loop that may have H-bond or electrostatic interactions with residues on the IL6-7 loop of the transporters.

In order to identify common sequence and structural determinants of alternating access in other MATE transporters, structurally equivalent sites can be targeted for site-directed spin labeling guided by the exhaustive dataset of DEER distance distributions of PfMATE presented in Chapter III. We have demonstrated also a model of proton coupling that centers around Glu 163, found on IL4-5, and invokes disruption of interactions with IL6-7, mediated in part by Tyr 224, that destabilizes the OF state resulting in an IF conformation. While these residues are not strictly conserved, a structural alignment shows that charged residues in other MATE transporters are found in these structural elements and may imply mechanistic conservation (Fig. 5.4). Introducing mutations of these residues into reporter pairs in other MATE transporters for DEER experiments would further our understanding of the underlying mechanism of the conformational cycle.

Beyond the current work presented in previous chapters and the future work envisioned here, the results provide a rationale for investigation of the hMATE transporters. As detailed in Chapter I, hMATE paralogues in the kidney represent the site of terminal efflux for drugs and other compounds and is a determinant of drug-drug interactions in the kidney. A 2017 US FDA draft on drug-drug interactions concluded that inhibition of hMATE1 and hMATE2K should be studied for all new investigational drugs. Furthermore, substrate studies are required if 25% of total drug clearance is due to renal secretion (65). Determining the conformational effects of substrates and known inhibitors such as pyrimethamine could allow drug screening using DEER spectroscopy based on the patterns of distance distributions emerging from a reporter pair. The application of DEER to the elucidation of hMATE transport mechanisms would be an exciting next step in the study of MATE transporters. Such studies could delineate the interplay between coupling ions, conserved sidechains and lipid interactions that define differential effects of ligands on the human paralogues. The integration of such results with binding and transport data will lead to a comprehensive model of transport for hMATE and further refine our knowledge of the MATE transporters.

APPENDIX I

SUPPLEMENTAL FIGURES

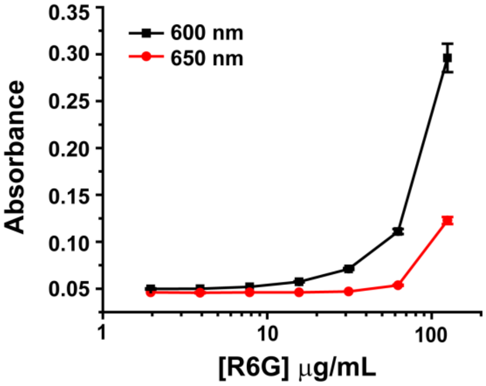

Figure S1: Absolute absorbance of R6G at the given wavelengths as a function of R6G concentration on a 96-well plate. Due to relatively high absorbance of R6G at 600 nm, cell growth on the 96-well plate was monitored at 650 nm. Data are shown as the average and standard deviation of triplicate measurements at each drug concentration.

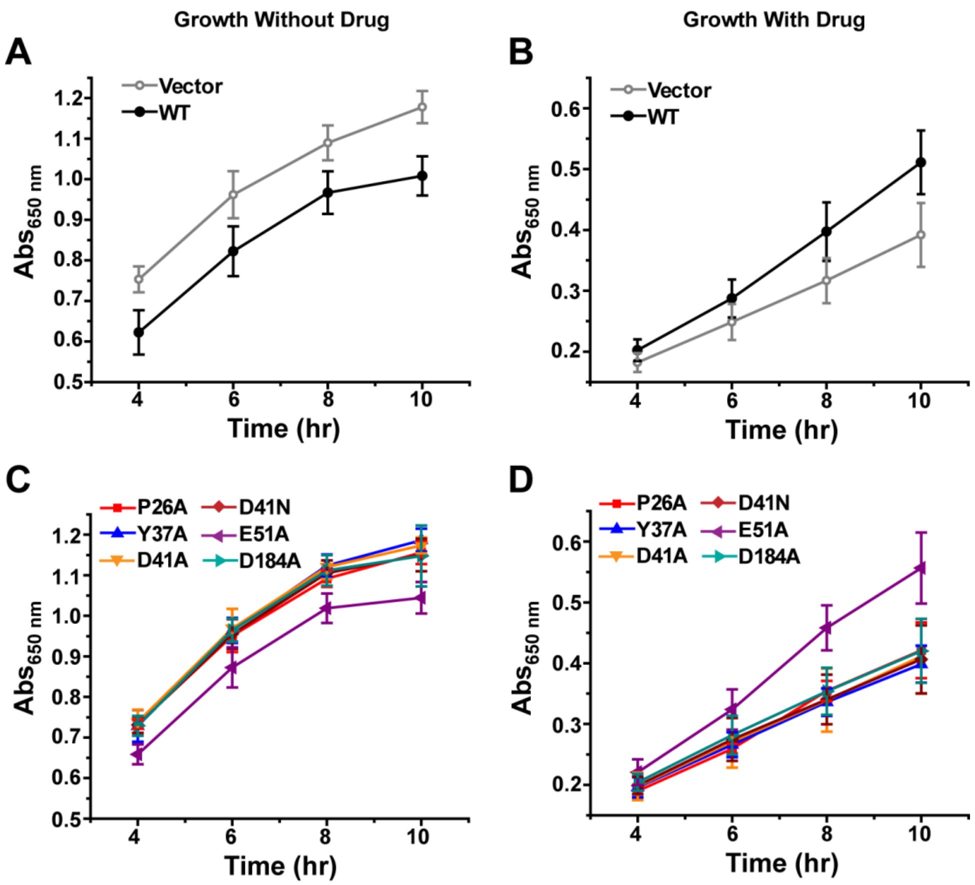

Figure S2: Cell growth curves monitored by absorbance at 650 nm of vector and PfMATE variants in the absence and presence of 75 μg/mL R6G. The growth profiles of cells harboring vector alone and WT PfMATE (panels **A** and **B**) are shown separately from the growth profiles of the variants (panels **C** and **D**) for clarity. The curves were obtained at 37 °C using the 96-well plate format, and the data shown as the average and standard deviation from *n*=3-6 experiments. The x-axis indicates the time of growth following a two hr induction period with 1 μM IPTG and dilution of the cells to identical starting Abs_{600nm} (0.025) according to the **Experimental Procedures**. (**A**) Cells expressing WT PfMATE demonstrated reduced growth relative to the vector control in the absence of drug, consistent with the intrinsic challenge of PfMATE expression to cell growth as shown in **Fig. 2.1A**. (**B**) However, cells that expressed WT PfMATE showed enhanced growth relative to the vector in the presence of drug. (**C** and **D**) Cell growth curves for PfMATE variants in the absence and presence of drug, respectively. The data indicates that functionally-impaired variants (P26A, Y37A, D41A, D41N and D184A) demonstrate similar growth patterns as the vector, whereas E51A is similar to WT. The relative Abs_{650nm} reported in **Fig. 2.1C** and **Fig. 2.2B** was generated by normalizing the growth in panels (**B**) and (**D**) to cell growth in the absence of drug shown in panels (**A**) and (**C**).

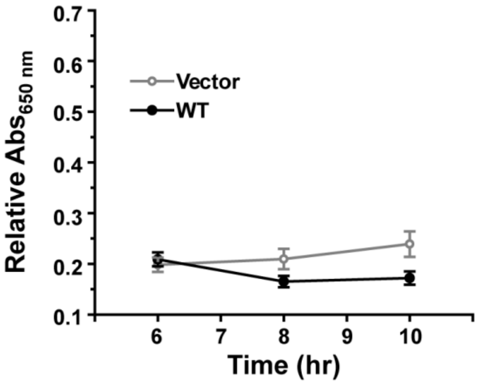

Figure S3: Time course of cell growth following induction with 10 μM IPTG in medium containing 75 μg/mL R6G. Under these conditions, PfMATE-mediated cell survival was not observed relative to the vector control. The y-axis scale is the same as **Fig. 2.1C**. Data are shown as the average and standard deviation from five experiments and each data point measured in triplicate.

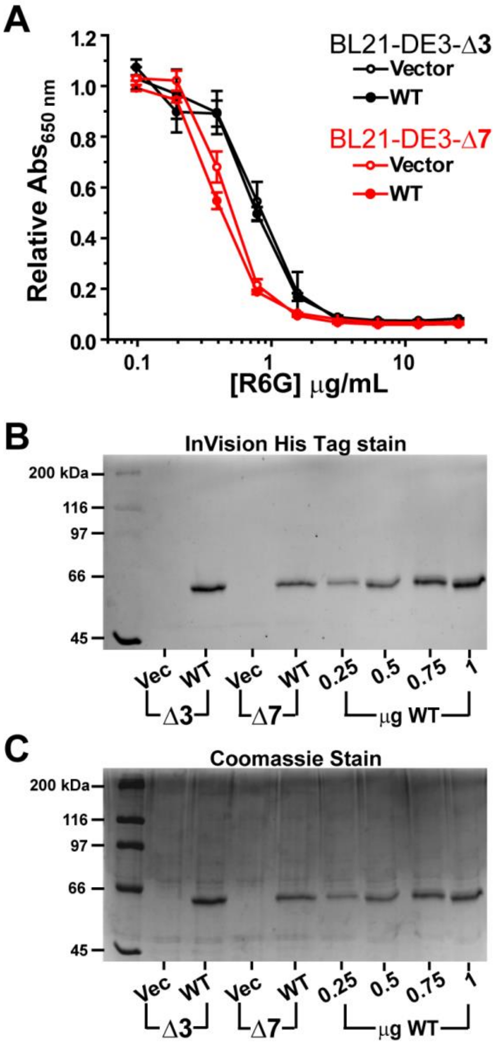

Figure S4: Cell growth curves in hypersensitive *E. coli* strains as a function of R6G concentration. (**A**) These strains are devoid of three (Δ3) and seven (Δ7) endogenous multidrug transporters, as described in the main text. Each data point represents the average of two independent experiments. For each experiment, the data was measured in triplicate from separate wells on the plate after 10 hrs at 37 °C. The standard deviation is shown for each data point. Protein expression was confirmed by SDS-PAGE and staining with either InVision His tag stain (**B**) or Coomassie (**C**). The last four lanes of each gel image is purified PfMATE WT used as a standard.

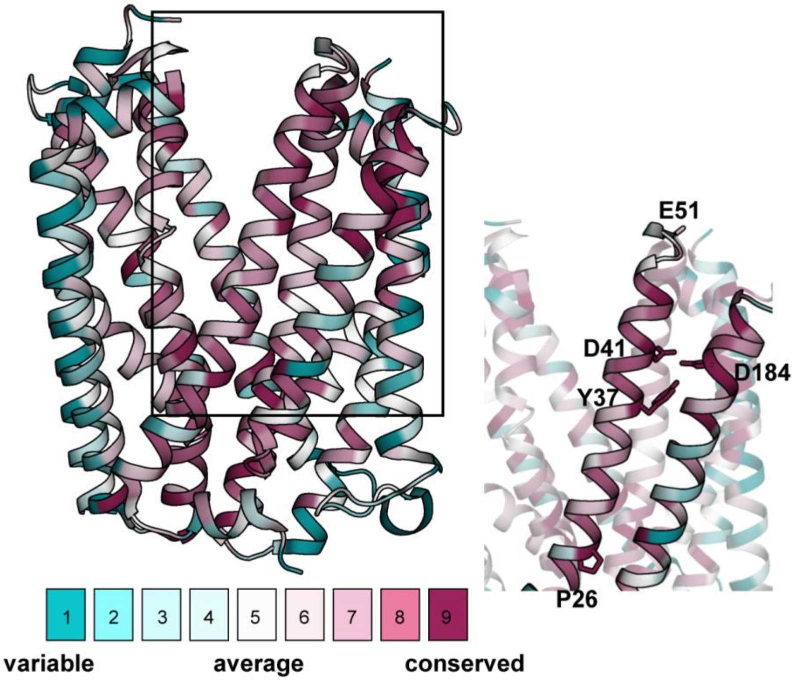

Figure S5: Estimation of PfMATE sequence conservation using the ConSurf server. A phylogenetic tree was built from a CLUSTALW multiple sequence alignment of 500 homologous sequences collected from a filtered UNIPROT database (CLEAN-UNIPROT). The homologs were identified by a hidden Markov model (HMMER) search algorithm with a 0.0001 E-value. The relative amino acid conservation scores were calculated using a Bayesian algorithm and mapped onto the PfMATE crystal structure (PDB 3VVN). The conservation scores for each amino acid correspond to the discrete color scale. This analysis shows that the evolutionary rate of P26, Y37, D41 and D184 is slow, and therefore defined as “conserved”. In contrast, E51 is non-conserved.

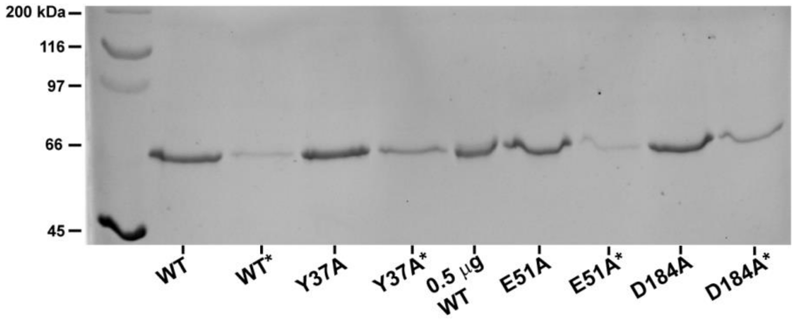

Figure S6: PfMATE expression profile for select variants. The presence of WT and variant PfMATE was visualized via SDS-PAGE followed by staining with InVision His tag stain as described in the **Experimental Procedures**. The amount of purified sample loaded into each well was normalized to the membrane mass acquired during processing of culture. For each construct, the first lane shows the amount of PfMATE isolated from culture following induction with 1 μM IPTG. The second lane (*) shows the amount of PfMATE isolated from culture after diluting a fraction of IPTG-induced cells (~50-60 fold) into a similar volume of medium (50% LB broth, 0.1 mg/mL ampicillin), growing the cells at 37 °C in the absence of R6G and harvesting at $\text{Abs}_{600\text{nm}}$ = 1.0-1.2.

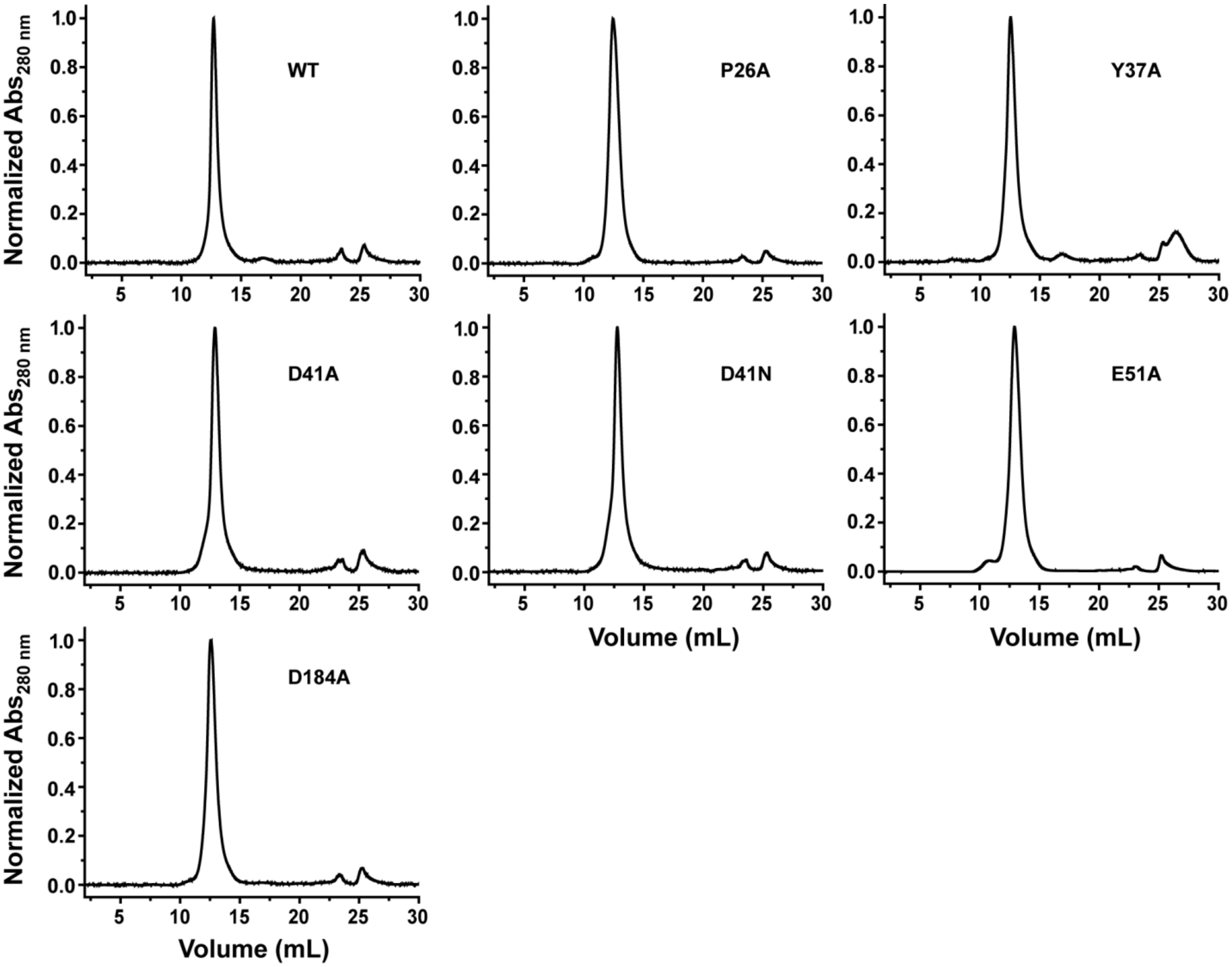

Figure S7: Size exclusion chromatography of purified PfMATE variants in β-DDM buffer. Normalized absorbance at 280 nm is shown as a function of elution volume. The chromatograms were acquired at 23 °C on a Superdex200 Increase 10/300 GL column as described in the **Experimental Procedures**.

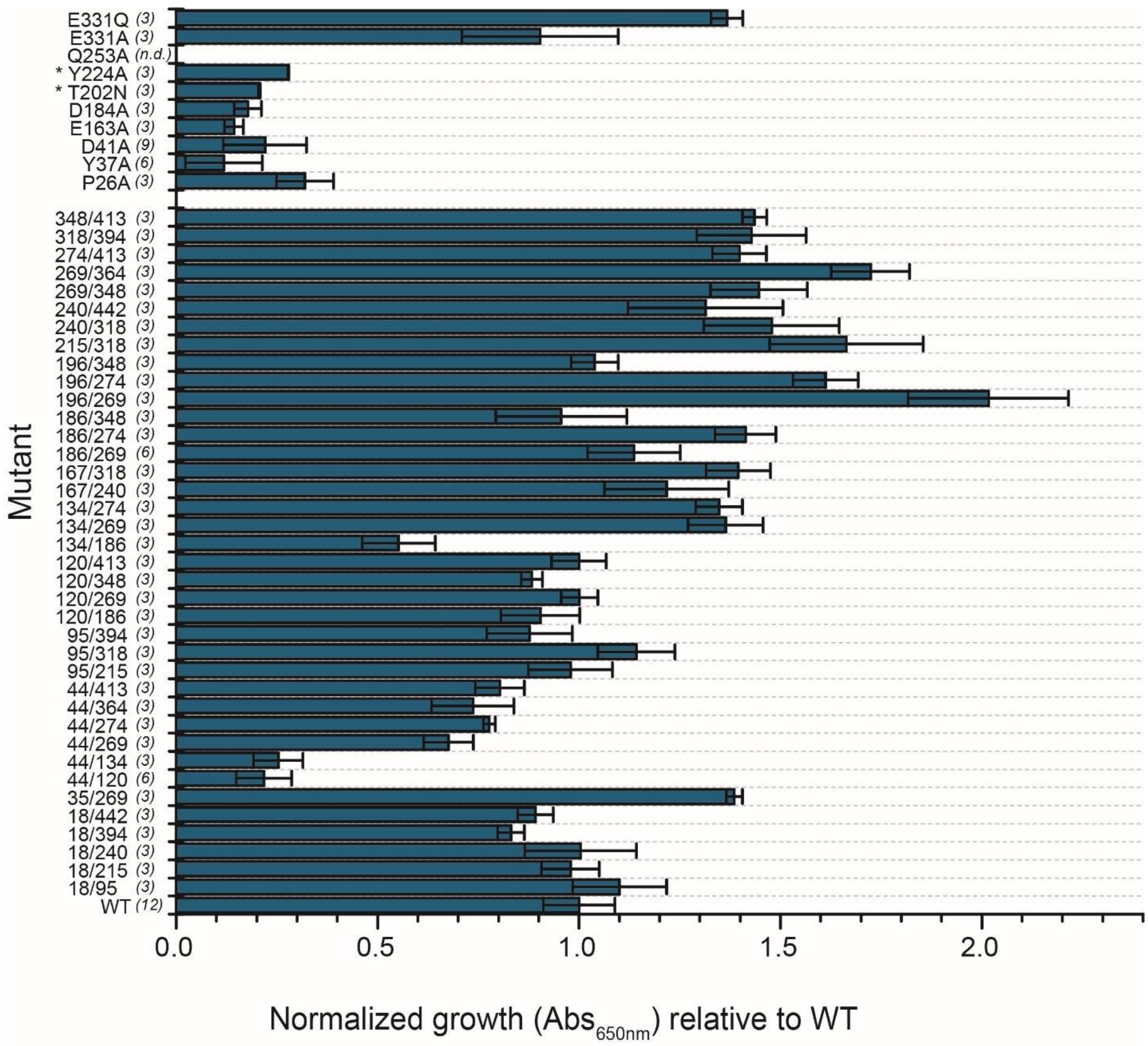

***** Background mutation in 95/318 construct

n.d. not done

Figure S8: R6G resistance profiles of PfMATE mutants used for DEER spectroscopy. Growth profiles of mutants are relative to WT PfMATE after subtracting the contribution of the vector control. The bar plot highlights the average and S.E.M. for at least $n = 3$ replicates. The number of replicates is listed in brackets alongside each construct. A one-way ANOVA indicated that the population means of PfMATE mutants were significantly different at the 0.05 level: F (48, 170) = 19.73., $p < 0.00001$. A Tukey multiple comparison test showed that growth of double cysteine mutants, except 44/120 and 44/134, was not significantly different from WT, indicating that introduction of cysteines into the primary sequence of PfMATE generally has little effect on its ability to confer resistance to R6G. Conversely, growth of background mutants, except E331A/Q, was significantly different from WT, but not significantly different to the impaired mutant, D41A, indicating that these mutants are also functionally impaired.

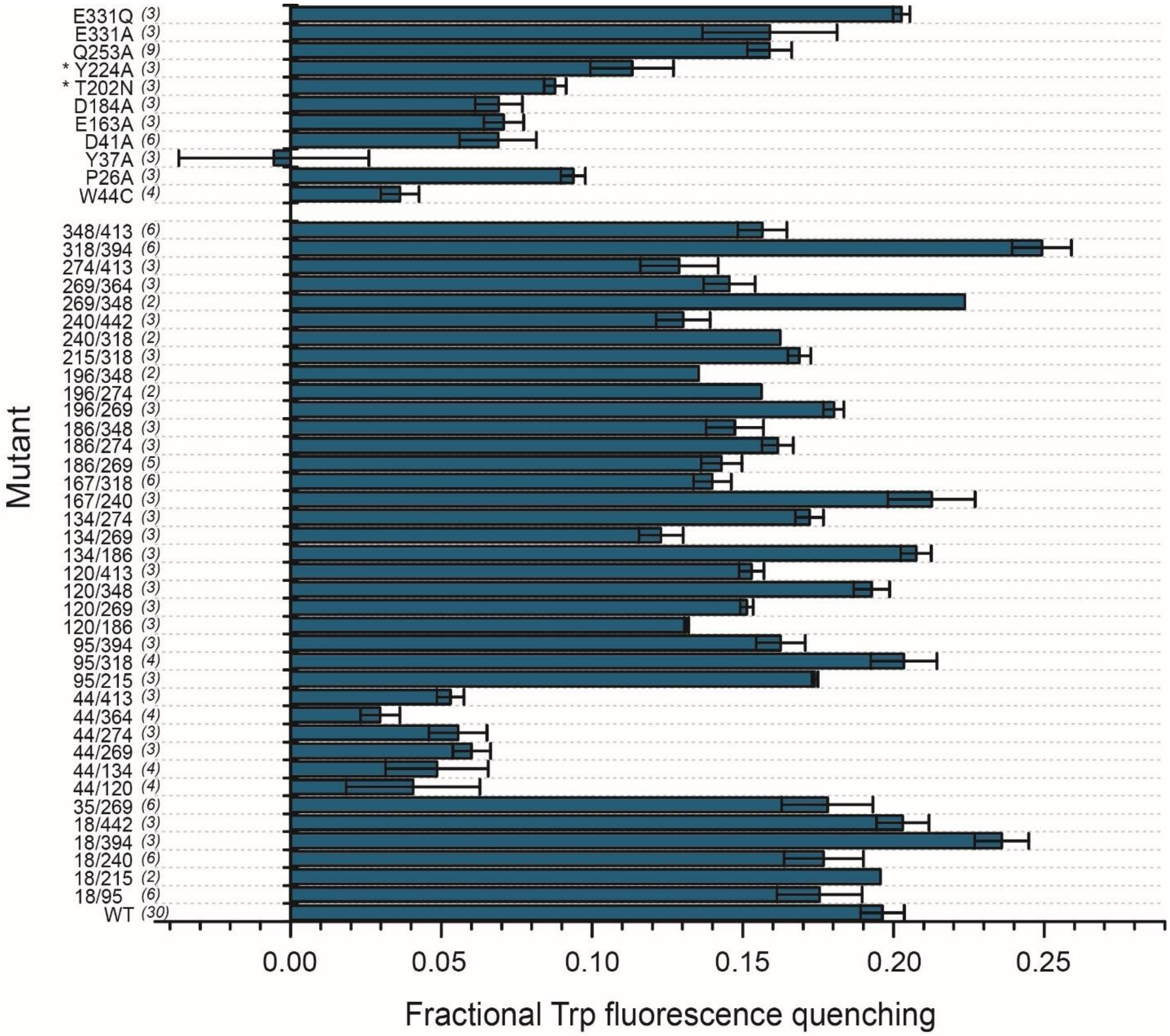

***** Background mutation in 95/318 construct

Figure S9: Fractional fluorescence quenching of PfMATE mutants. Fluorescence quenching at low pH due to W44 was used as a surrogate reporter of conformational changes in spin-labeled PfMATE and background mutants, as detailed in Methods. The number of replicates is listed in brackets alongside each construct. The bar plot highlights the average and S.E.M. for at least n = 3 replicates. Where $n = 2$, the average of 2 replicates are presented. For $n > 3$, data are collected from multiple protein preparations. A one-way ANOVA indicated that the population means of PfMATE mutants were significantly different at the 0.05 level: F (50, 161) = 18.80, $p < 0.00001$. A Tukey multiple comparison test showed, as expected, that double cysteine constructs containing W44C were significantly different from WT and do not demonstrate significant fluorescence quenching at low pH. Double cysteine constructs were significantly different from W44C, indicating that introduction of cysteines into the primary sequence has minimal effects on the pH sensor of PfMATE. For the background mutants (except E331A/Q) Trp quenching was not significantly different from W44C.

Table S1

A. Extracellular cysteine pairs

Mutant	K_D ± S.D.	*n*[†]
PfMATE wt	1.62 ± 0.17	24
35/269[‡]	2.03 ± 0.06	3
44/120[‡]	1.87 ± 0.23	3
44/134[‡]	2.35 ± 0.27	3
44/269[‡]	1.71 ± 0.26	3
44/274[‡]	2.59 ± 0.16	3
44/364[‡]	1.43 ± 0.12	3
44/413[‡]	1.82 ± 0.24	3
120/186[‡]	2.39 ± 0.16	3
120/269[‡]	2.70 ± 0.36	3
120/348[‡]	2.00 ± 0.37	3
120/413[‡]	1.07 ± 0.13	3
134/186[‡]	2.64 ± 0.38	3
134/269[‡]	2.39 ± 0.20	3
134/274[‡]	2.72 ± 0.42	3
186/269[‡]	3.33 ± 0.26	3
186/274[‡]	2.65 ± 0.62	6
186/348[‡]	2.16 ± 0.42	3
196/269[‡]	2.15 ± 0.22	3
196/274[‡]	1.72 ± 0.28	3
196/348[‡]	1.58 ± 0.21	3
269/348[‡]	2.54 ± 0.15	3
269/364[‡]	2.84 ± 0.57	3
274/413[‡]	2.65 ± 0.26	3
348/413[‡]	2.52 ± 0.24	3

For n ≥ 3, average ± S.D.

† Total number of experiments; where n > 3, replicates include multiple protein preparations.

‡ Experiments performed with spin-labeled protein.

B. Intracellular cysteine pairs

Mutant	K_D ± S.D.	*n*[†]
18/95[‡]	2.98 ± 0.24	3
18/215[‡]	1.95 ± 0.40	4
18/240[‡]	2.20 ± 0.24	3
18/394[‡]	2.79 ± 0.08	3
18/442[‡]	1.69 ± 0.03	3
95/215[‡]	2.80 ± 0.21	3
95/318[‡]	1.72 ± 0.18	6
95/394[‡]	2.33 ± 0.18	3
167/240[‡]	1.87 ± 0.21	6
167/318[‡]	3.45 ± 0.07	3
215/318[‡]	2.00 ± 0.28	3
240/318[‡]	2.93 ± 0.25	3
240/442[‡]	2.08 ± 0.45	3
318/394[‡]	4.08 ± 0.18	3

C. Background mutations

Mutant	K_D ± S.D.	*n*[†]
P26A	1.74 ± 0.07	6
Y37A	1.29 ± 0.26	3
D41A	2.06 ± 0.22	3
* E163A[‡]	1.25 ± 0.18	3
D184A	1.98 ± 0.06	3
* T202N[‡]	2.18 ± 0.10	3
* Y224A[‡]	1.87 ± 0.03	3
Q253A	2.98 ± 0.23	3
E331A	2.27 ± 0.42	3
E331Q	3.09 ± 0.31	3

* Background mutation in 95/318 construct

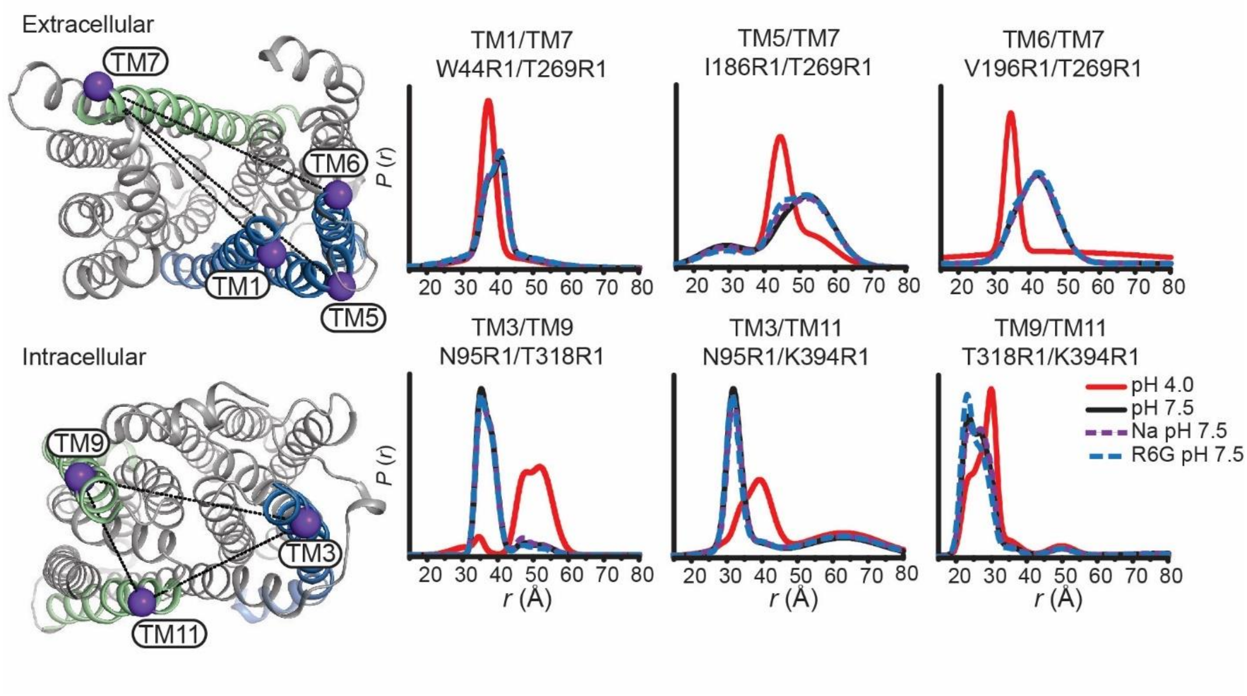

Figure S10: Conformational change is driven by H^+. Sodium (dashed purple traces) and R6G (dashed blue traces) were added to a final concentration of 50 mM and 1 mM, respectively, at pH 7.5. Both ligands demonstrate limited effects on conformational change. The locations of representative spin label pairs on the extracellular (top) and intracellular sides (bottom) are highlighted on the OF structure by purple spheres connected by a line.

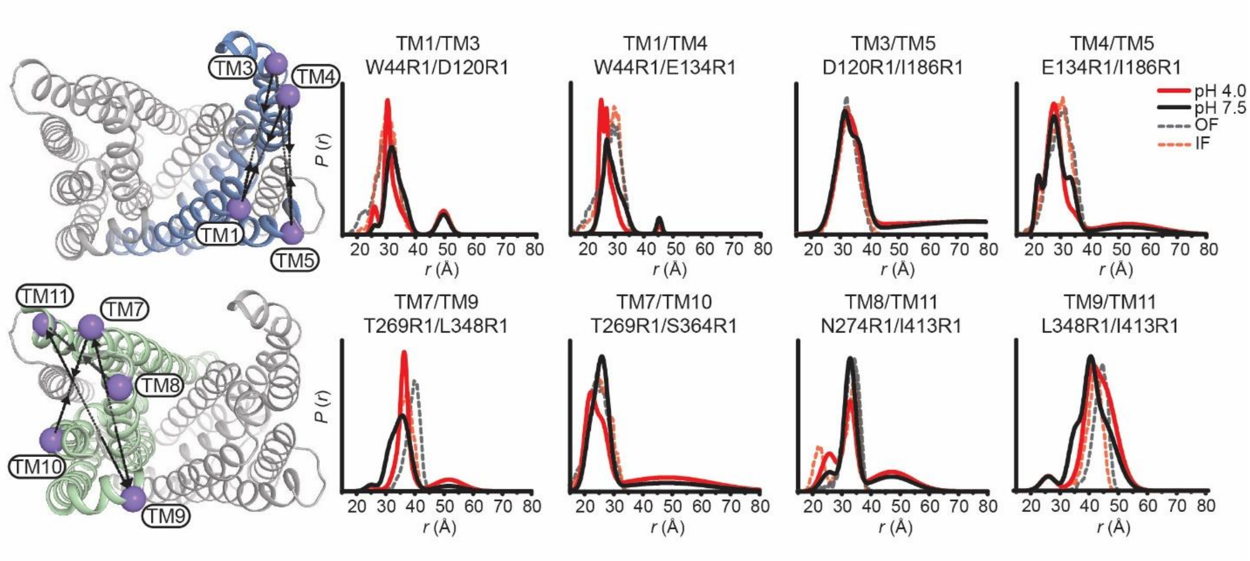

Figure S11: PfMATE intradomain DEER measurements on the extracellular side demonstrate limited conformational changes. Spin-labeled positions on TMs in the N-lobe (top) and C-lobe (bottom) are highlighted on the OF structure by purple spheres. Experimentally-determined distributions (solid lines) are plotted with the predicted distance distributions derived from the OF (black, dashed traces) and the IF (red, dashed traces) crystal structures. Distance changes are denoted on the OF structure by ←--- ---→ (increase) or ---→ ←--- (decrease).

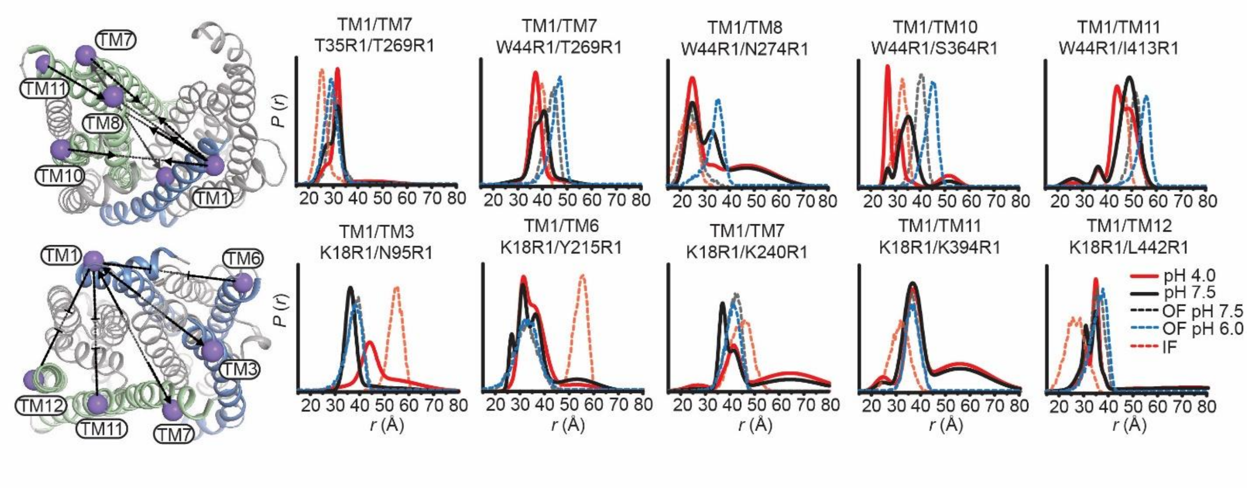

Figure S12: TM1 conformational changes diverge from structural models. Extracellular (top panels) and intracellular (bottom panels) measurements from TM1 are highlighted on the OF structure of PfMATE. Experimentally determined distance changes are denoted on the OF structure by ←--- ---→ (increase), ---→ ←--- (decrease), or ----| |---- (no change). Distance distributions from TM1 are plotted with the predicted distributions derived from the OF crystal structures obtained at pH 8.0 and 6.0 (black and blue dashed traces, respectively) and the IF (red, dashed traces) crystal structure. Conformational changes are observed mainly as population shifts to shorter distances on the extracellular side, which is inconsistent with the longer predicted distances from the OF pH 6.0 structure. On the intracellular side, limited conformational change is observed except between TM1 and TM3, consistent with the conformational changes described in the latter.

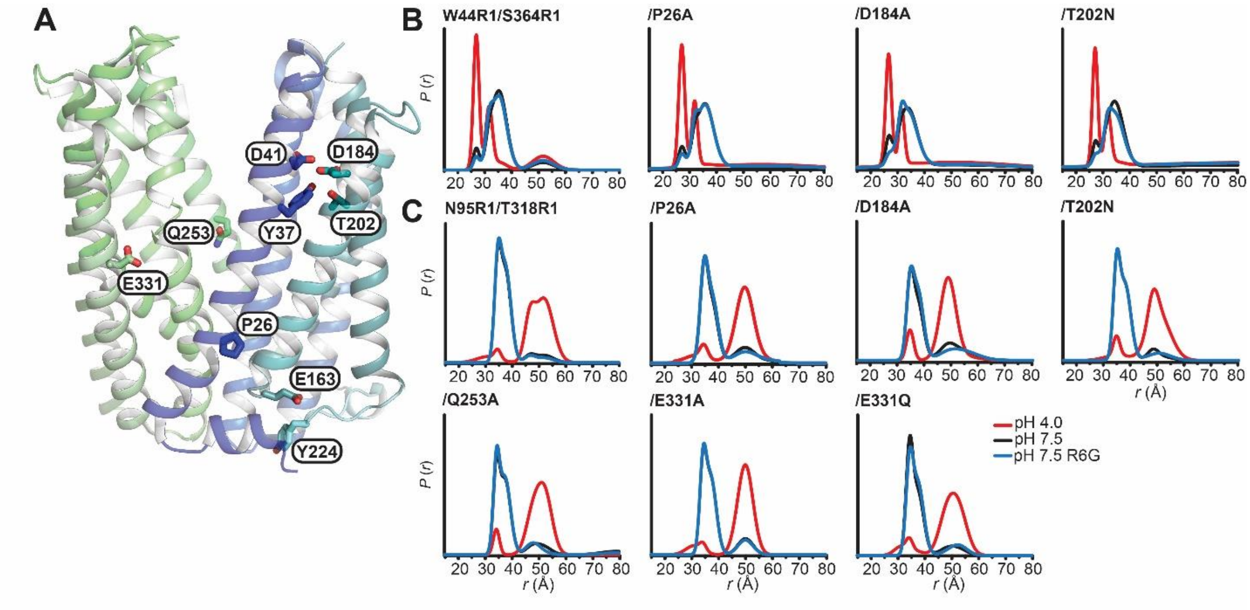

Figure S13: Conformational dynamics of PfMATE N-lobe mutants. (**A**): Sidechains of functionally essential residues in the N-lobe, as well as Q253 and E331, thought to be involved in lipid and proton binding, respectively, are depicted as sticks on the OF PfMATE structure. Mutations of these residues in reporter pairs on the extracellular (**B**) and intracellular (**C**) sides reveal that these residues do not affect the distance changes at low pH.

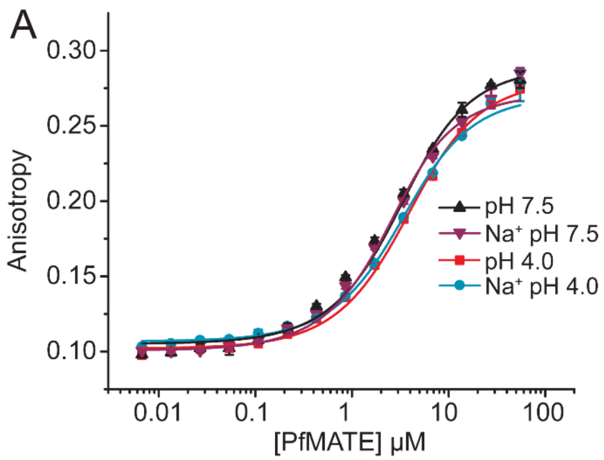

Condition	K_D ± SD	N
pH 7.5	1.62 (0.03)	3
pH 4.0	2.67 (0.17)	3
pH 7.5 Na	1.92 (0.14)	3
pH 4.0 Na	2.64 (0.37)	3

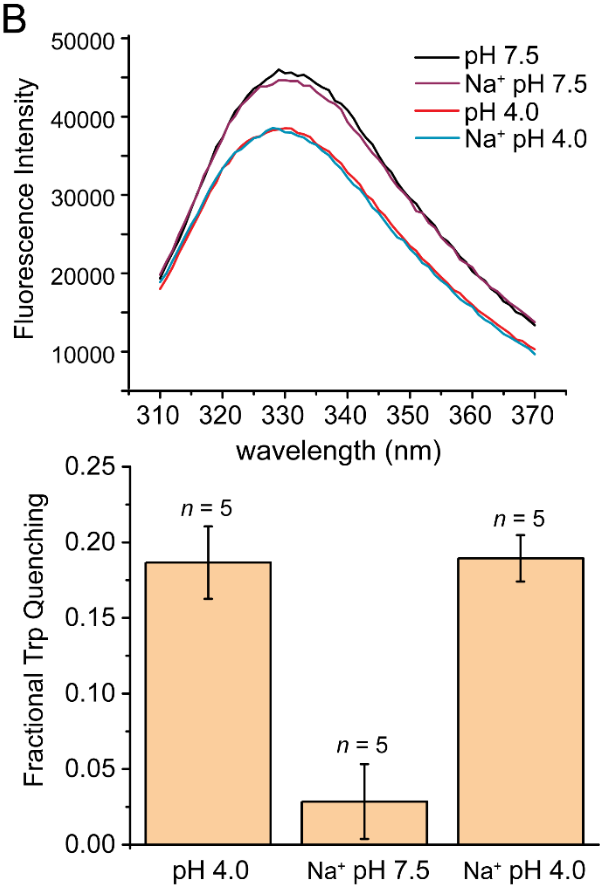

Figure S14: Na$^+$ does not significantly affect R6G binding affinity to PfMATE or Trp fluorescence quenching. Binding curves of R6G to WT PfMATE (**A**) were plotted as a function of protein concentration in β-DDM buffer at the indicated pH, with and without 50 mM NaCl. The data points represent the average ± S.D. of three binding experiments. Average K_D for each condition is indicated in the table. Spectra of Trp quenching for PfMATE WT under different conditions (**B**). Significant quenching (~18%) is observed under low pH conditions. The bar plot highlights the mean ± S.D. for the indicated number of measurements.

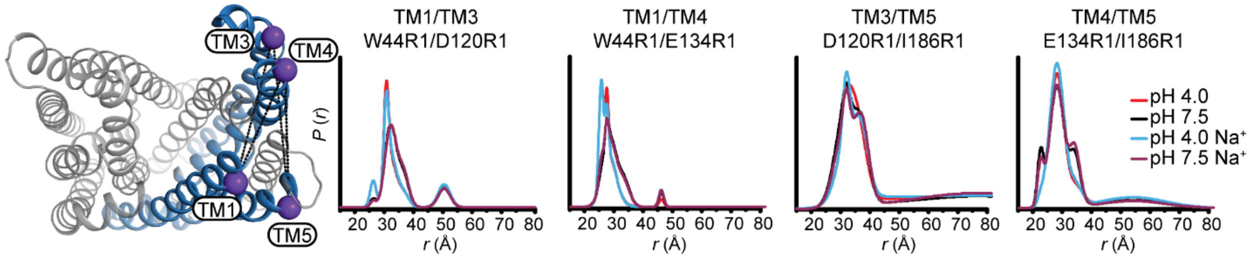

Figure. S15: PfMATE DEER measurements on the extracellular side of the N-lobe demonstrate limited conformational changes. Spin-labeled positions on TMs in the N-lobe (top) and C-lobe (bottom) are highlighted on the OF structure by purple spheres.

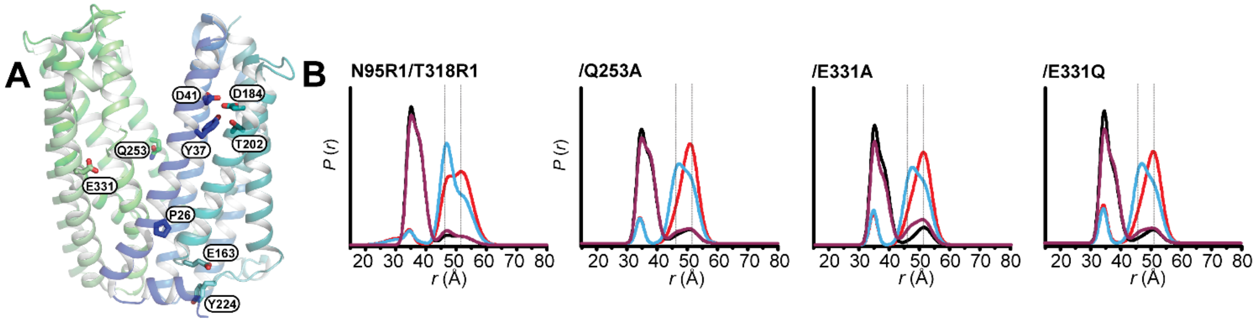

Figure. S16: Conformational dynamics of PfMATE C-lobe mutants. (**A**): Sidechains of C-lobe residues Q253 and E331, thought to be involved in lipid and proton binding, respectively, are depicted as sticks on the OF PfMATE structure. For reference, the side chains of functionally essential residues in the N-lobe are also depicted. Mutations of these residues in the N95R1/T318R1 reporter pair on the intracellular (**B**) side reveal that these residues do not affect the Na$^+$-dependent conformational change (cyan traces) at low pH.

APPENDIX II

Dataset S1 – PfMATE extracellular H⁺/substrate DEER analysis

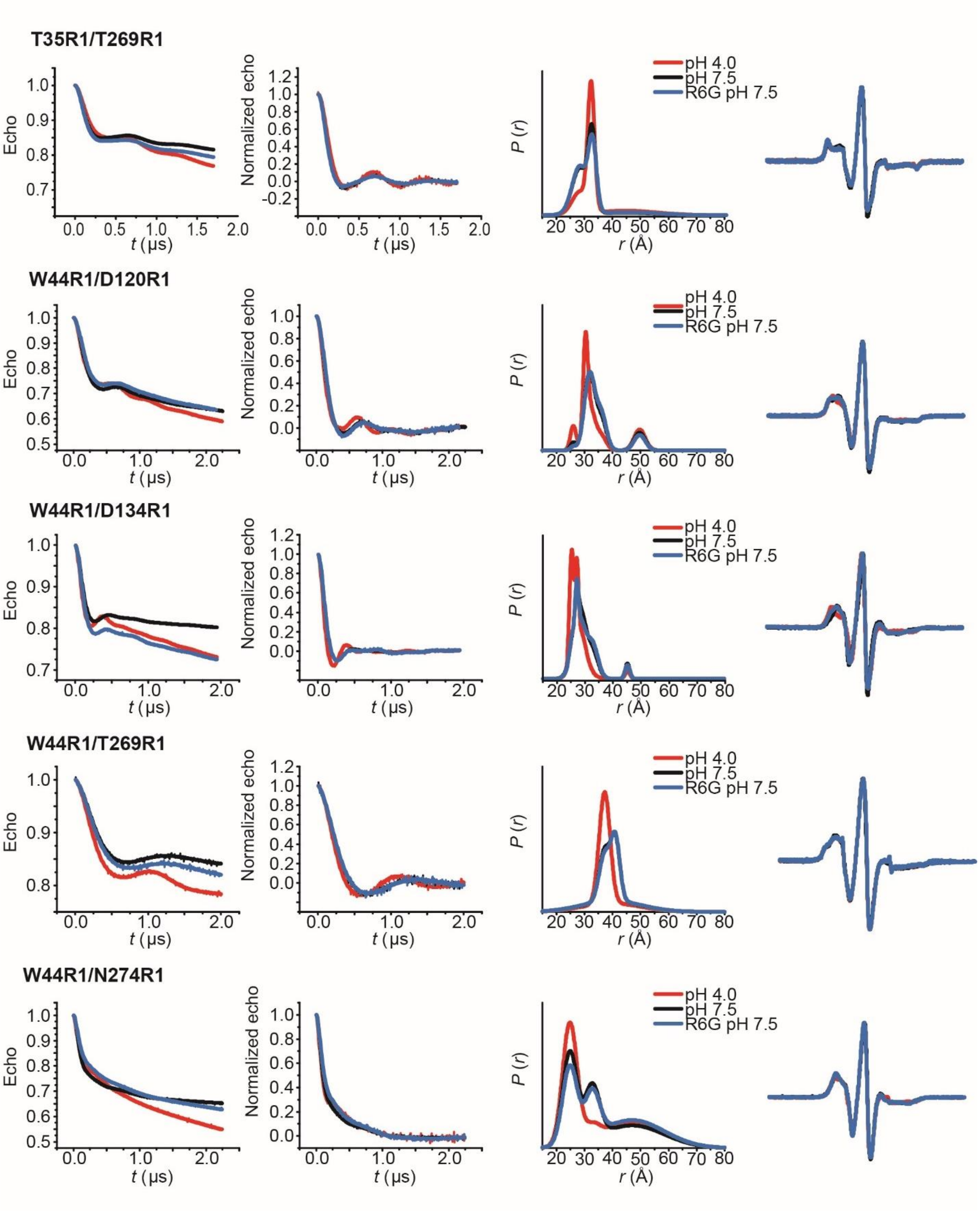

Dataset S1 – PfMATE extracellular H$^+$/substrate DEER analysis

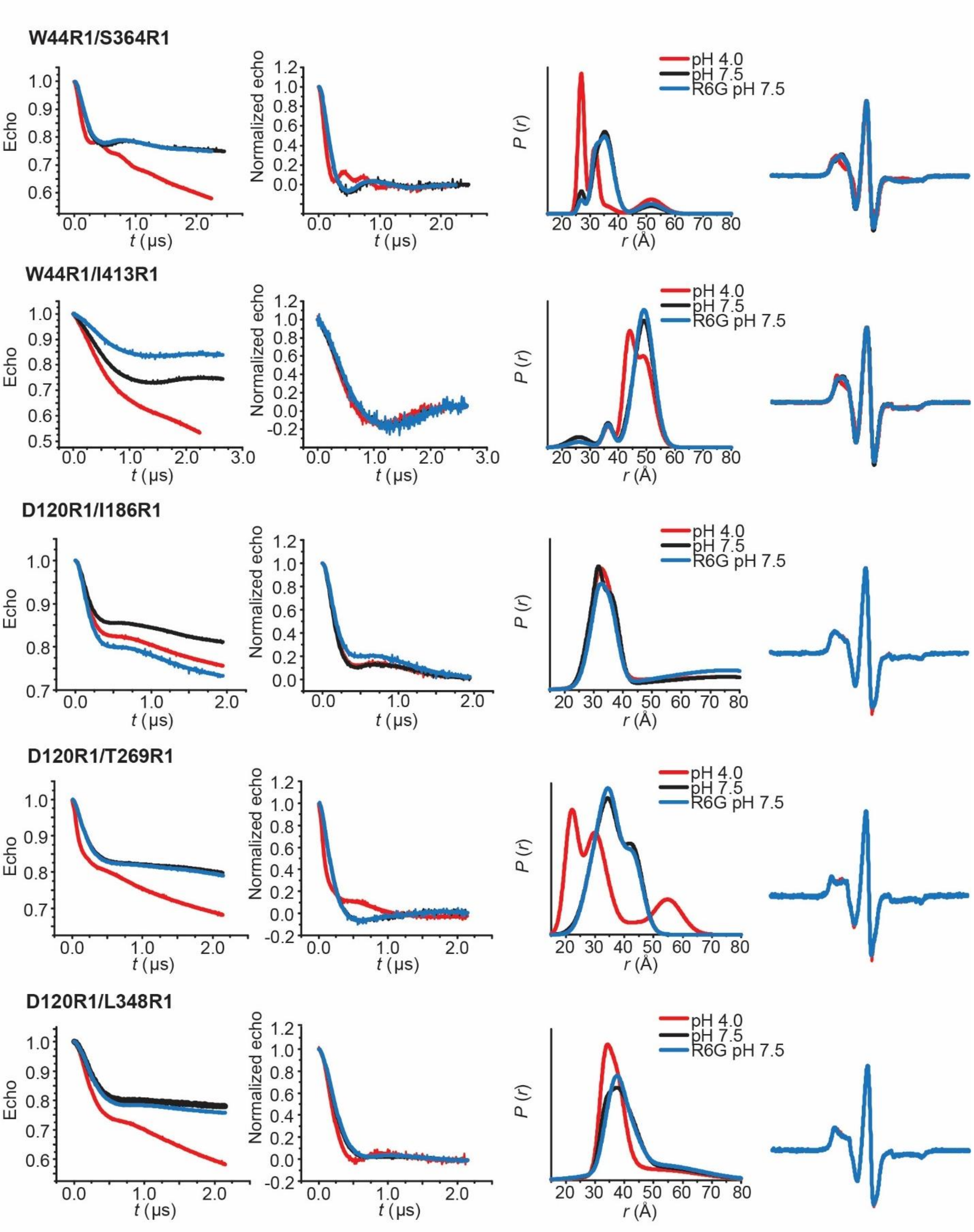

Dataset S1 PfMATE extracellular H$^+$/substrate DEER analysis

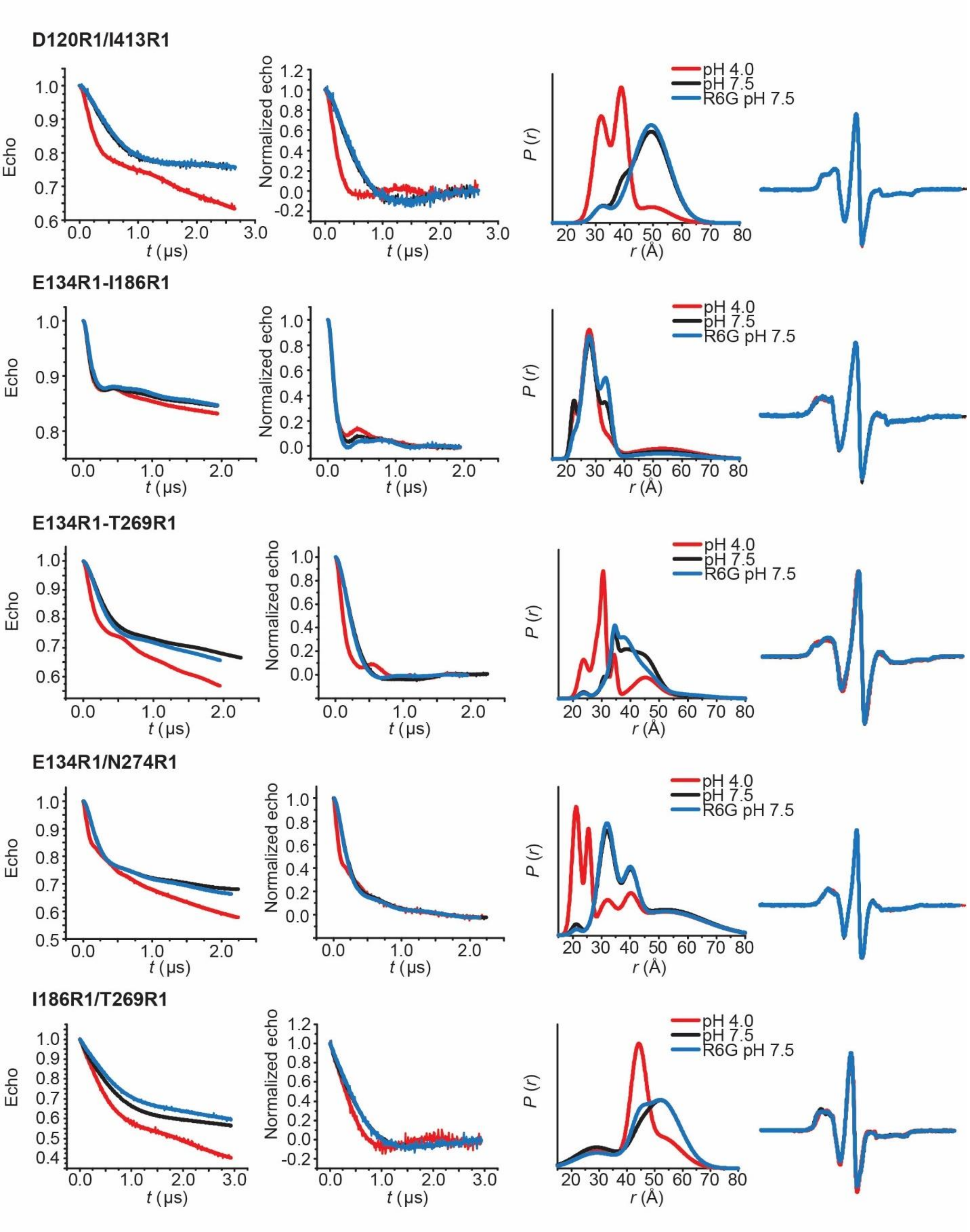

Dataset S1 PfMATE extracellular H$^+$/substrate DEER analysis

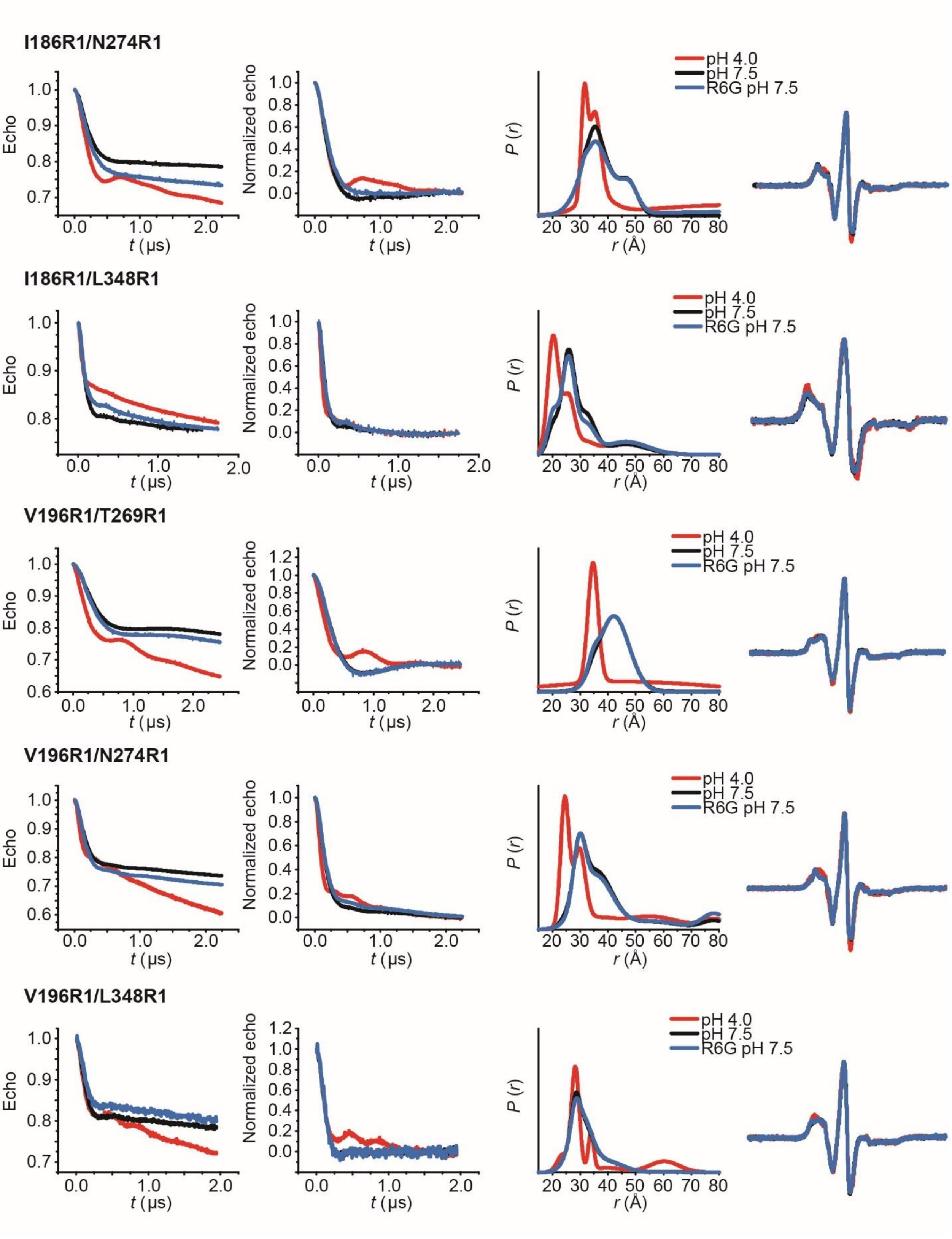

Dataset S1 – PfMATE extracellular H$^+$/substrate DEER analysis

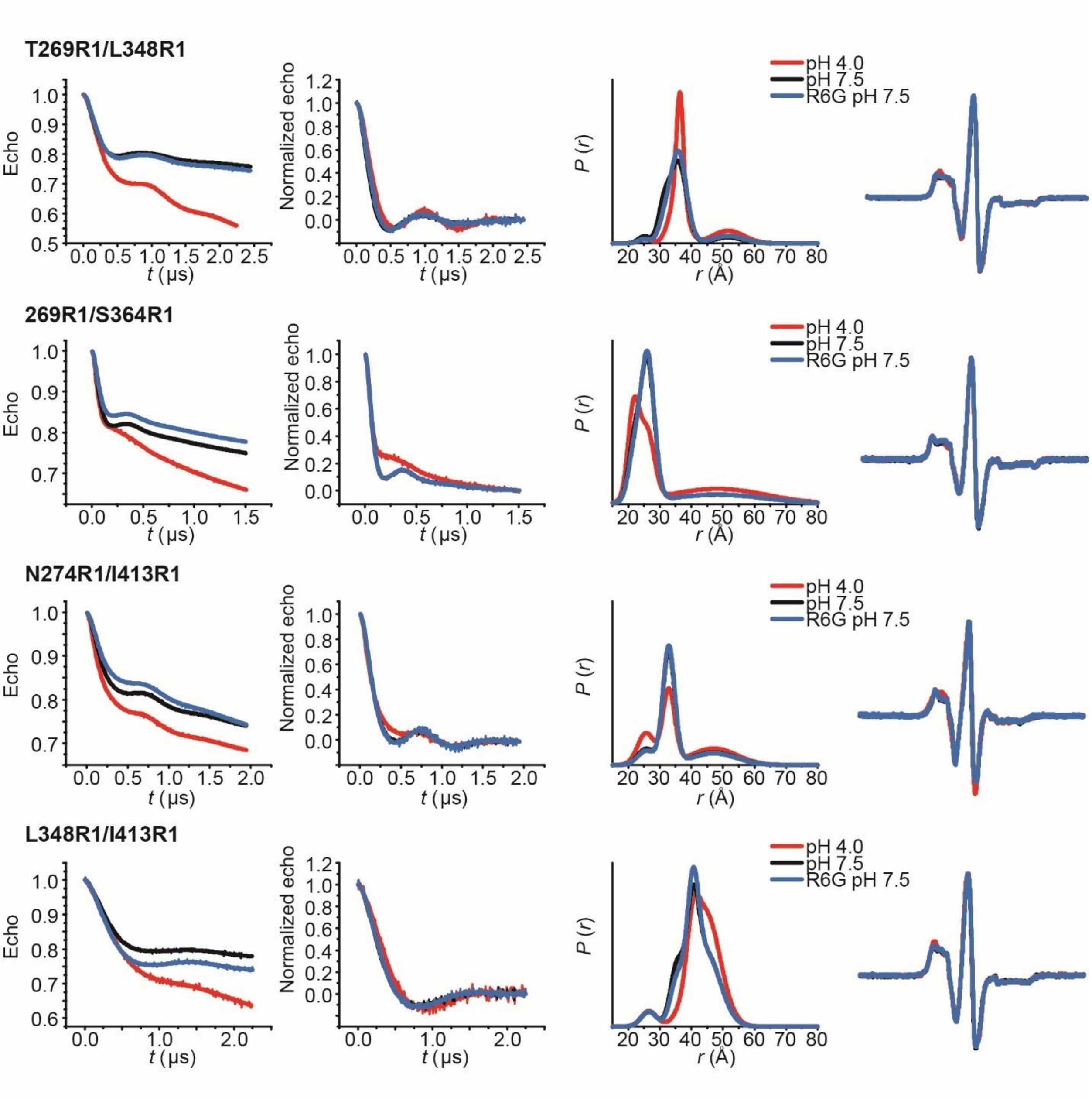

Dataset S2 – PfMATE intracellular H$^+$/substrate DEER analysis

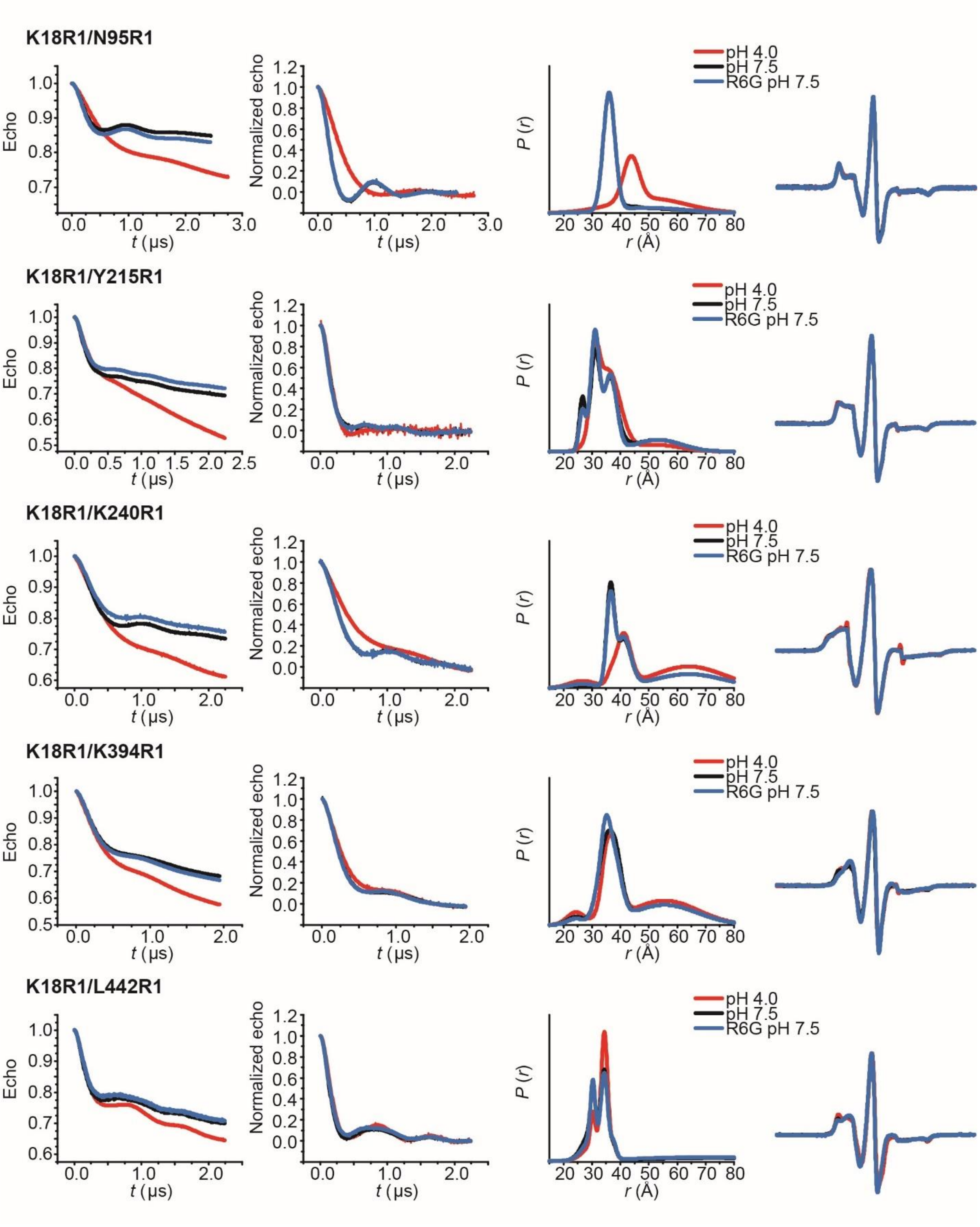

Dataset S2 – PfMATE intracellular H^+/substrate DEER analysis

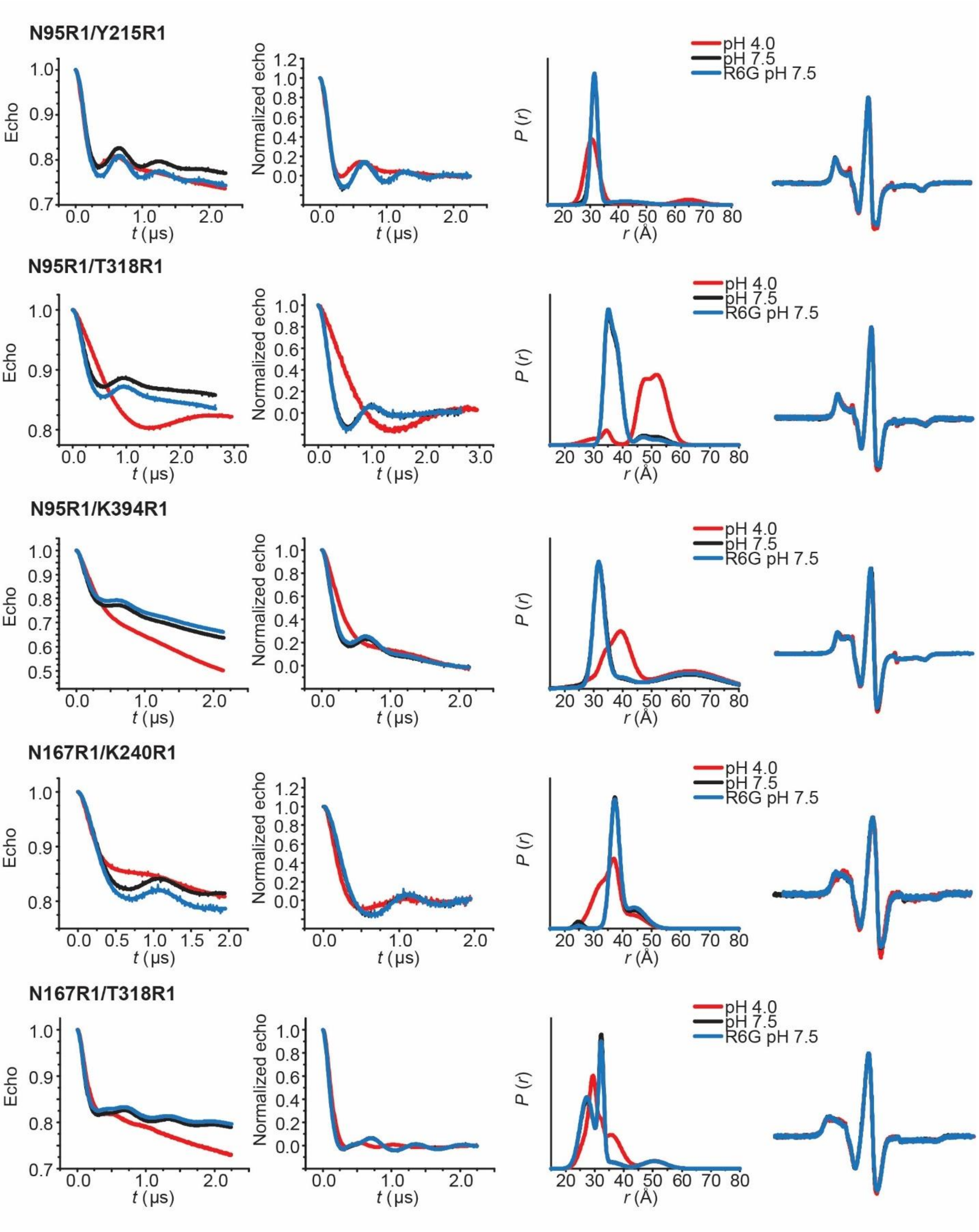

Dataset S2 – PfMATE intracellular H$^+$/substrate DEER analysis

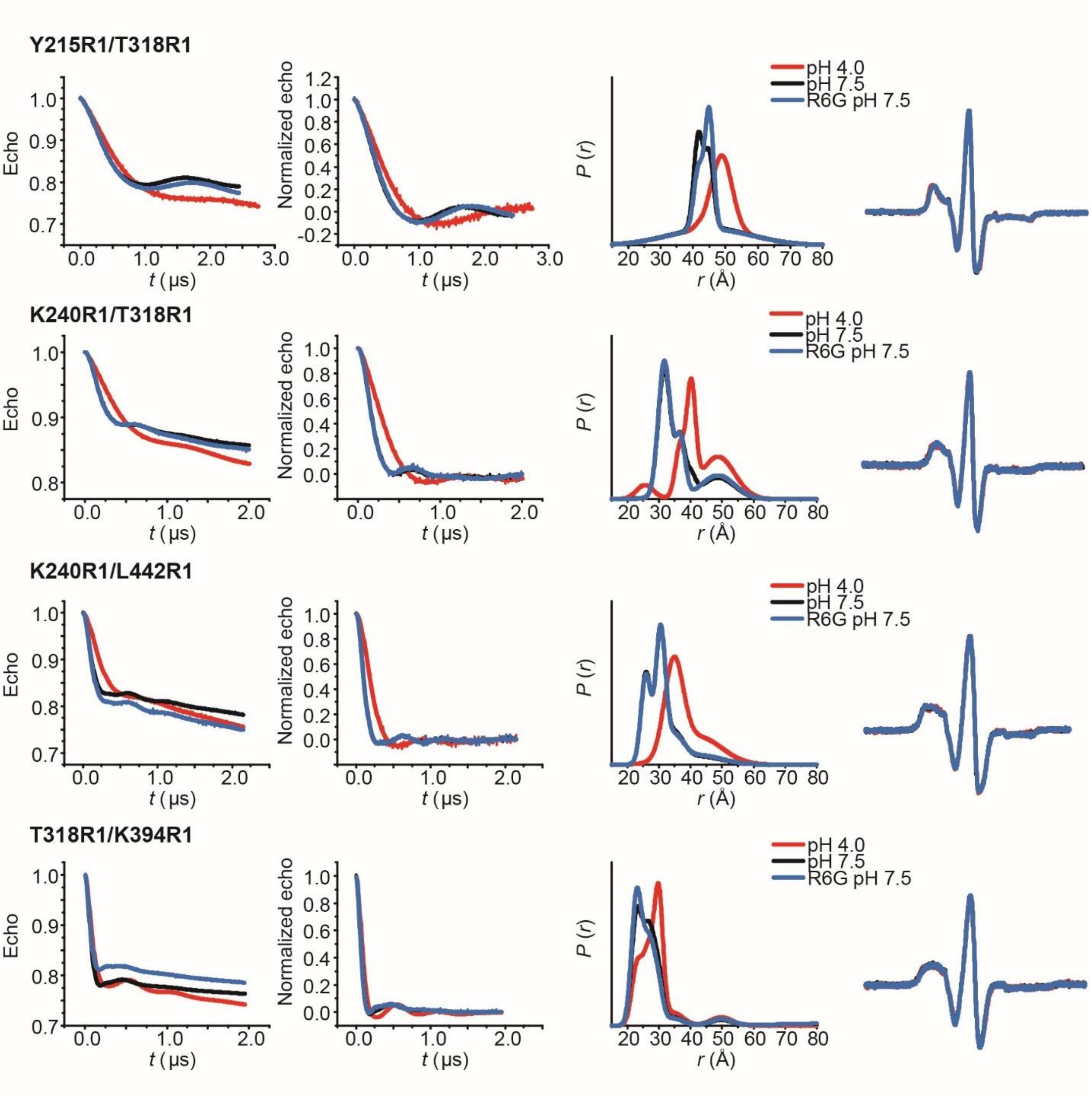

Dataset S3 – PfMATE backgound mutants extracellular H+/substrate DEER analysis

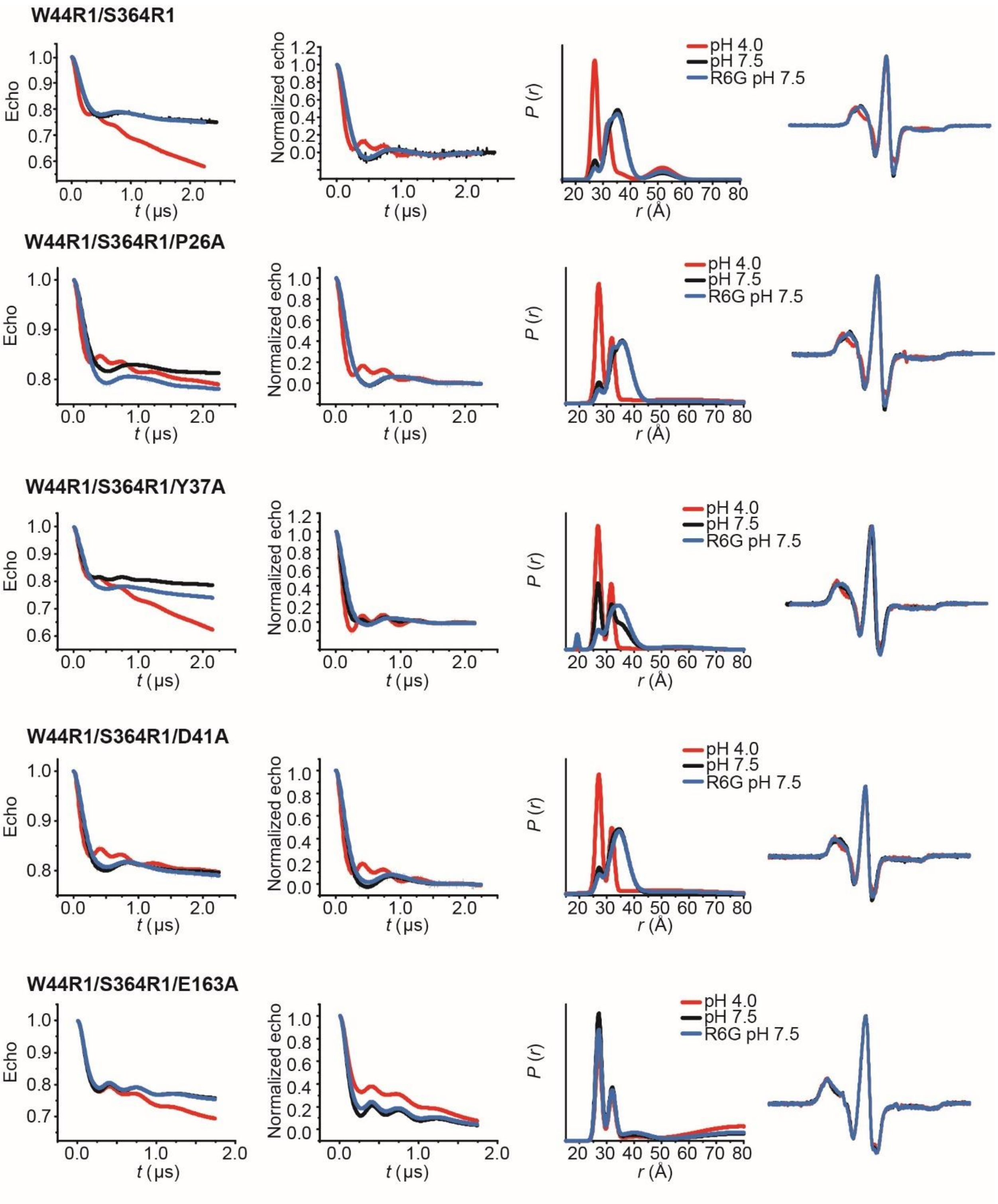

Dataset S3 – PfMATE backgound mutants extracellular H$^+$/substrate DEER analysis

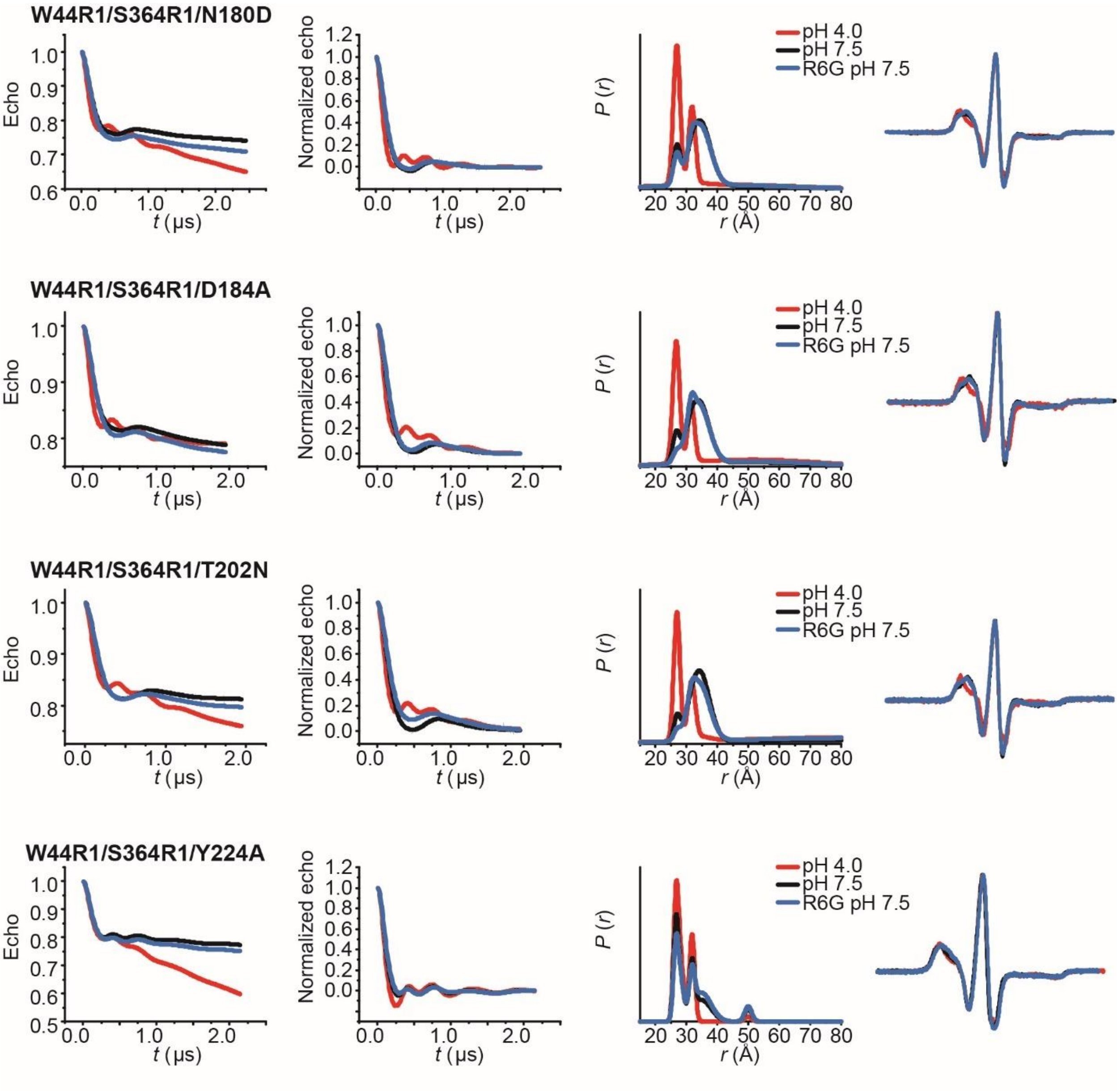

Dataset S4 – PfMATE backgound mutants intracellular H+/substrate DEER analysis

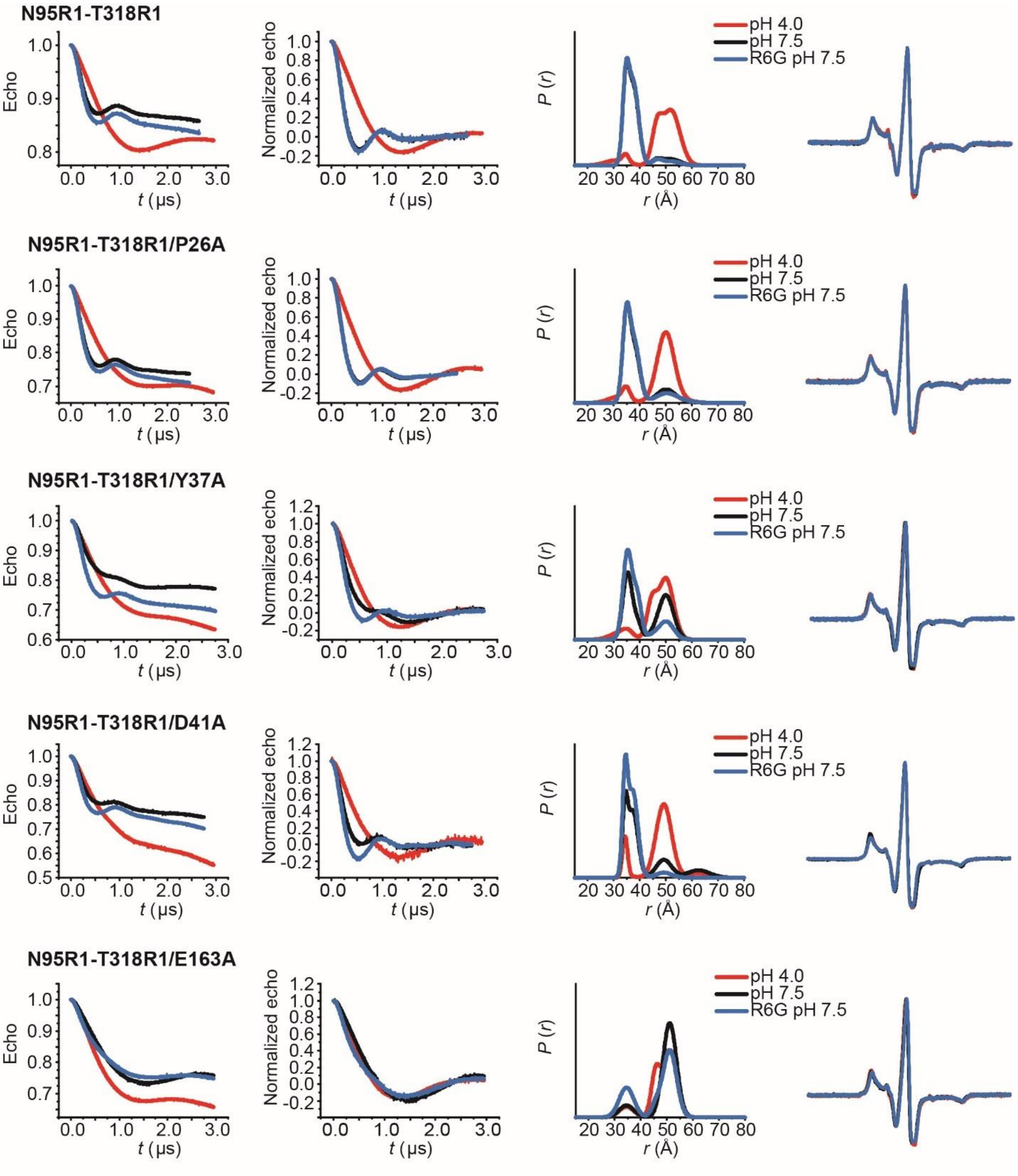

Dataset S4 – PfMATE backgound mutants intracellular H^+/substrate DEER analysis

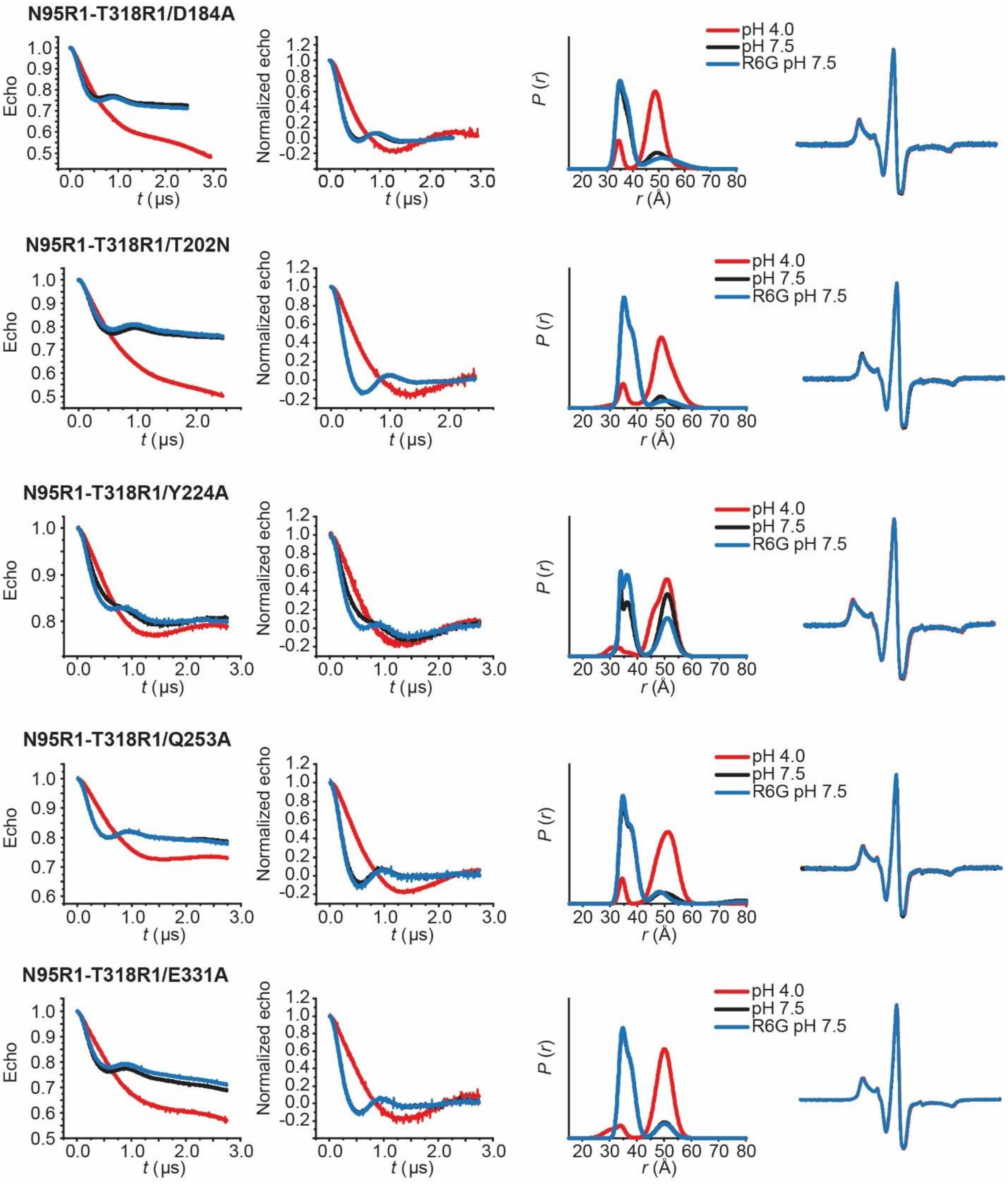

N95R1-T318R1/D184A

N95R1-T318R1/T202N

N95R1-T318R1/Y224A

N95R1-T318R1/Q253A

N95R1-T318R1/E331A

Dataset S4 – PfMATE backgound mutants intracellular H$^+$/substrate DEER analysis

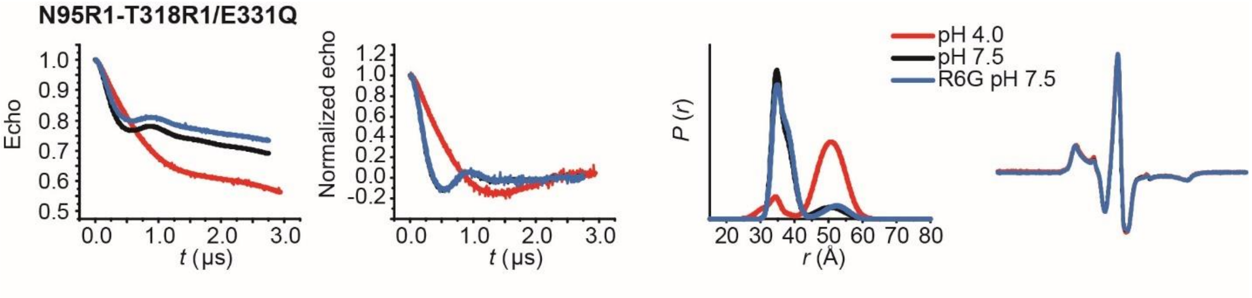

Dataset S5 PfMATE extracellular H$^+$/Na$^+$ DEER analysis

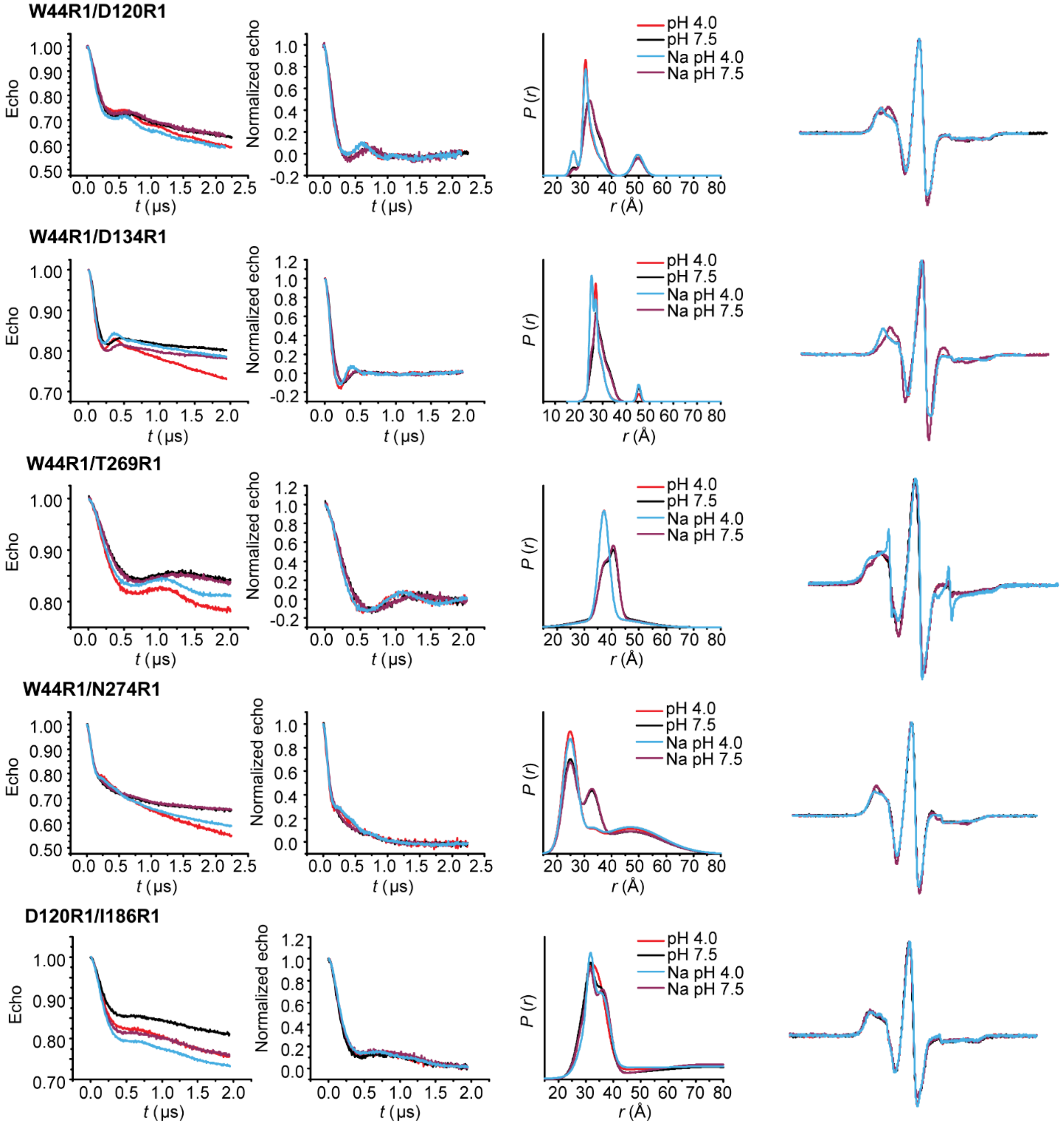

Dataset S5 PfMATE extracellular H$^+$/Na$^+$ DEER analysis

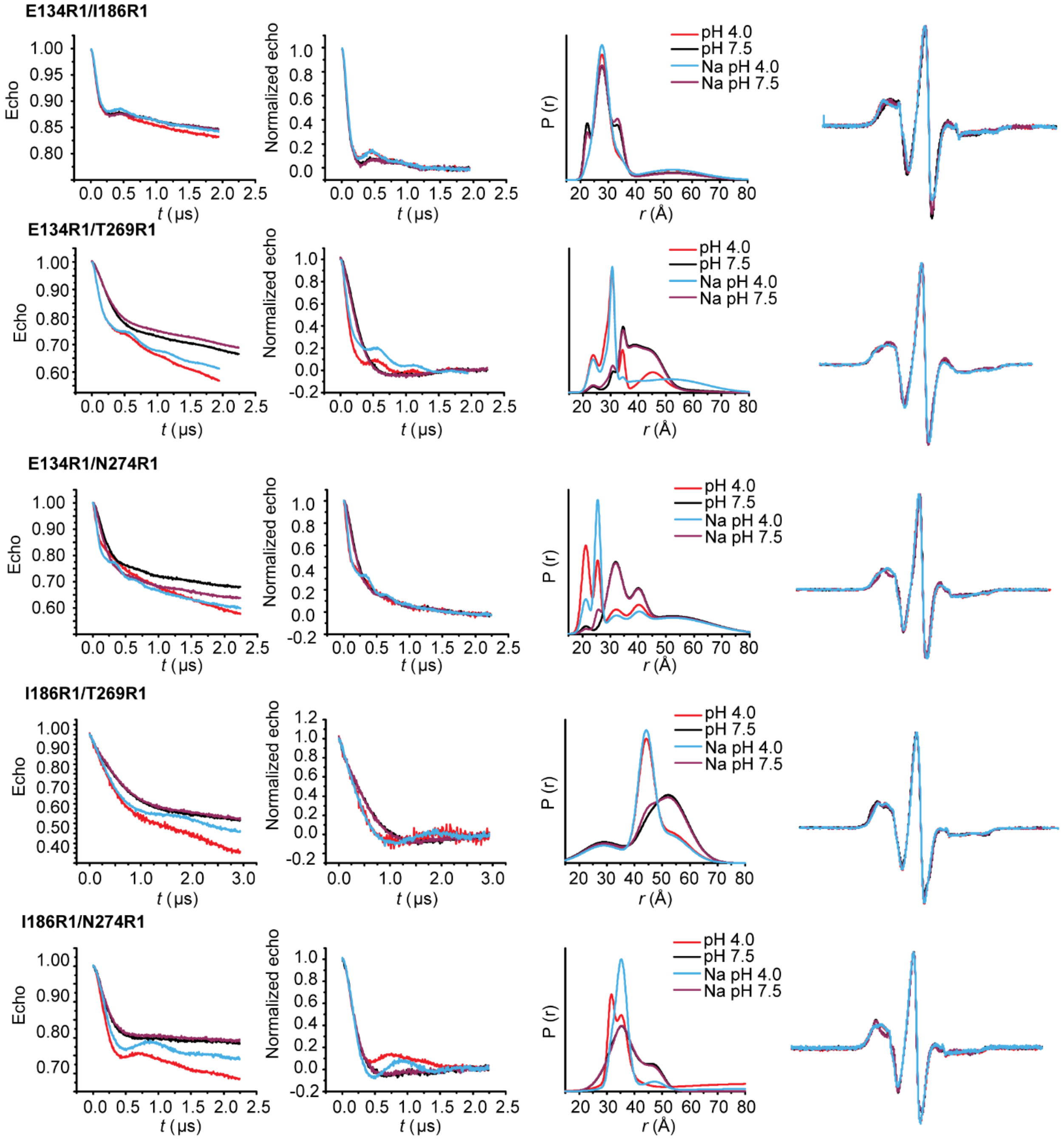

Dataset S5 PfMATE extracellular H$^+$/Na$^+$ DEER analysis

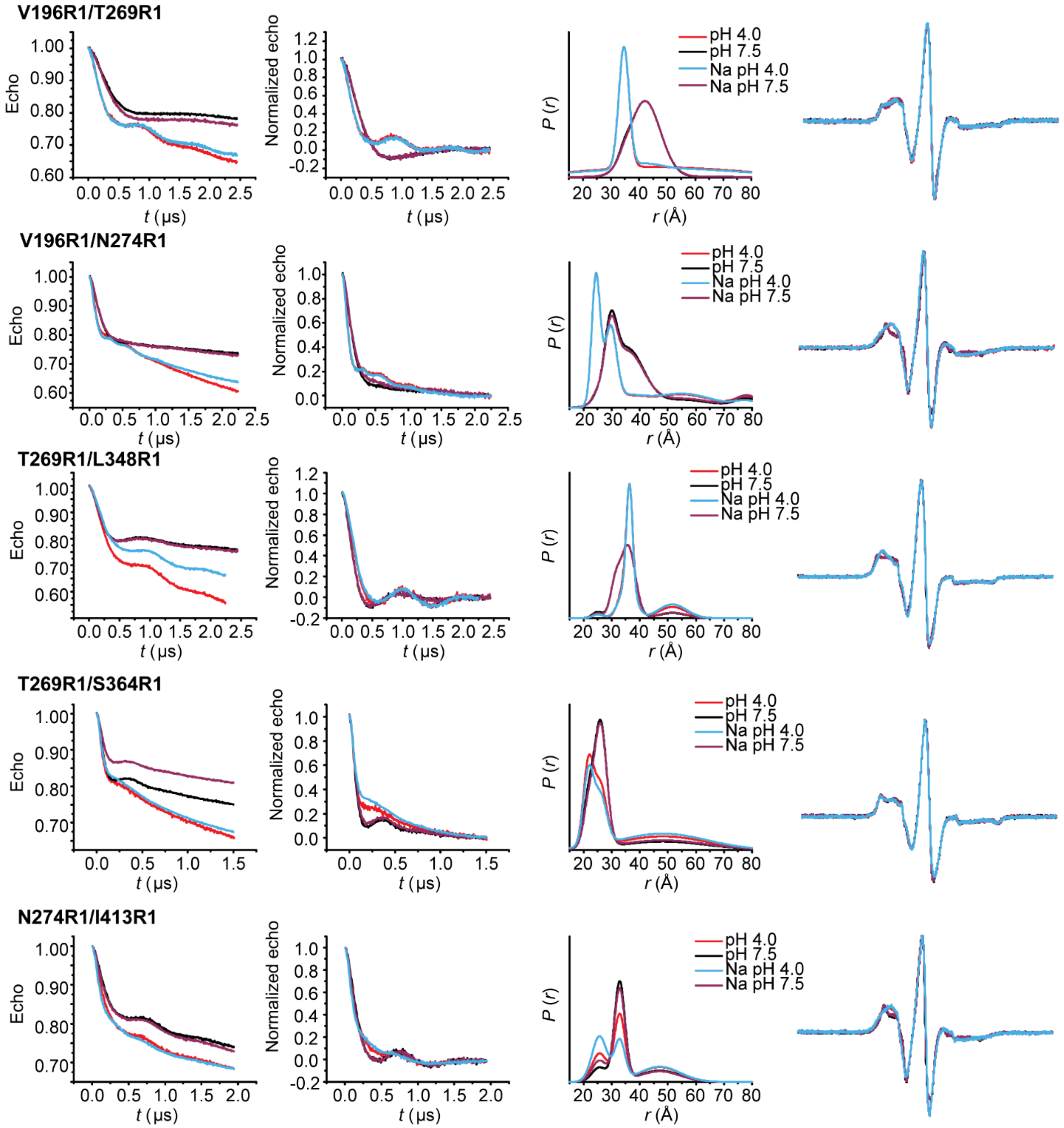

Dataset S6 PfMATE intracellular H^+/Na^+ DEER analysis

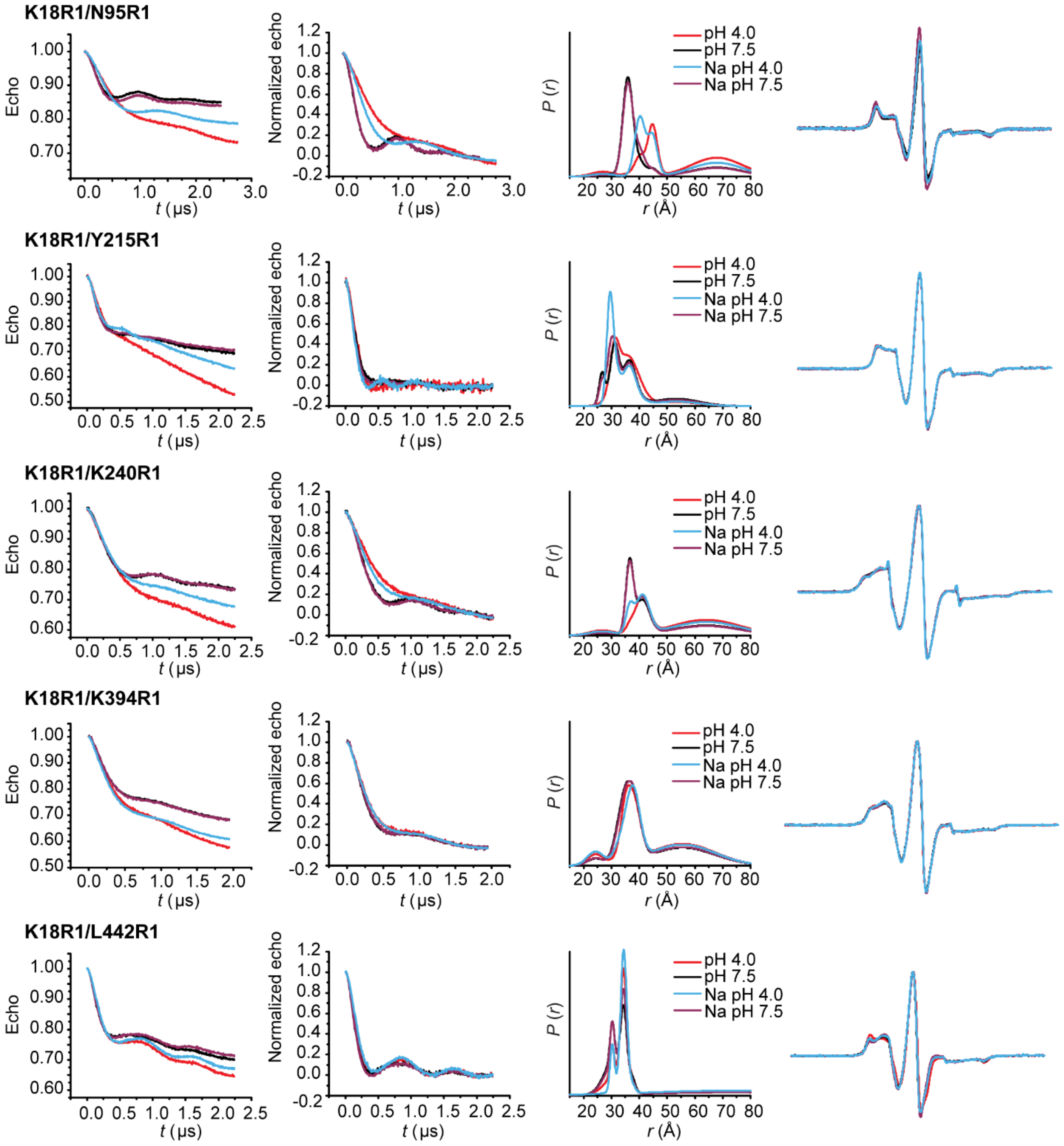

Dataset S6 PfMATE intracellular H$^+$/Na$^+$ DEER analysis

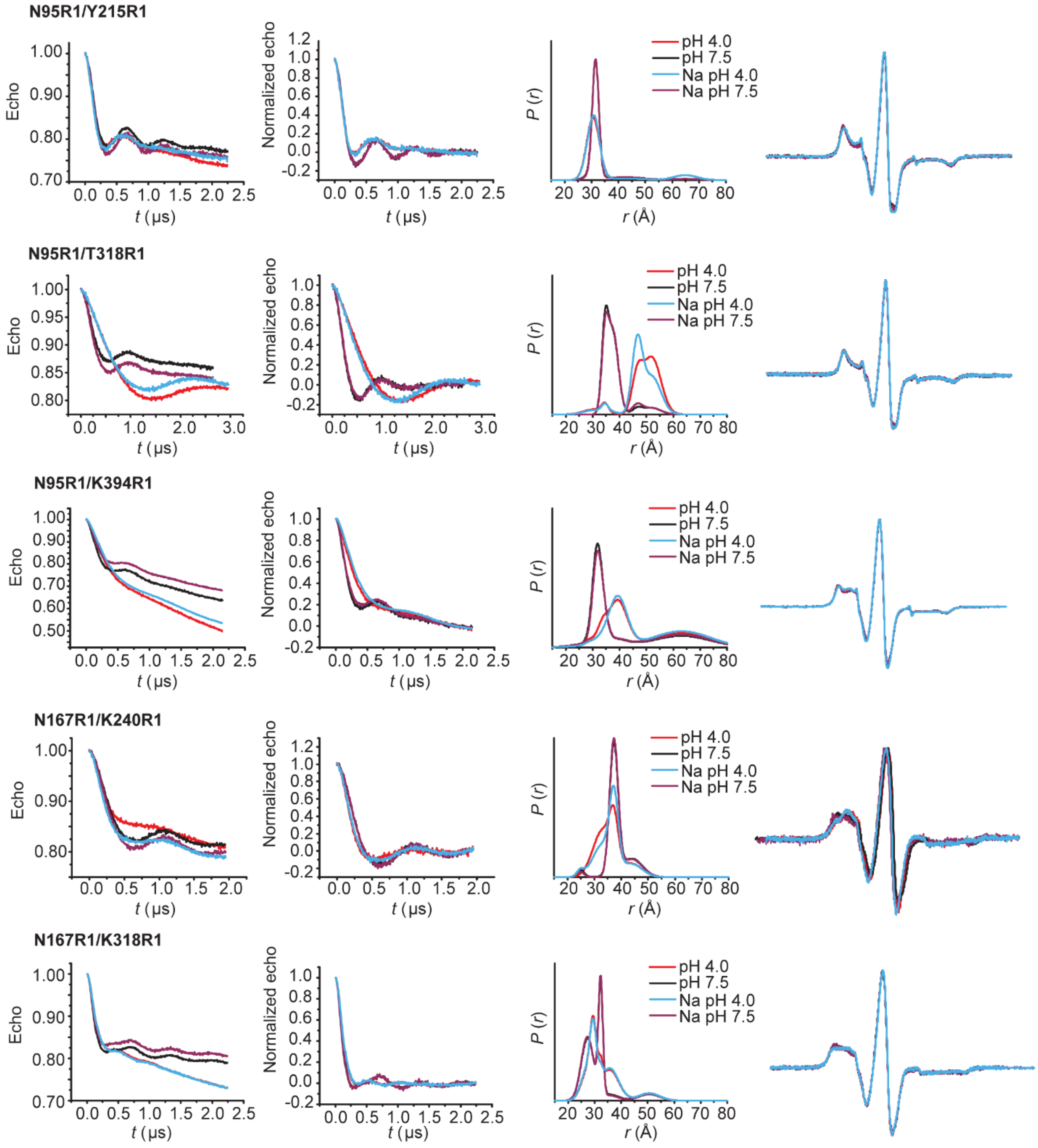

Dataset S6 PfMATE intracellular H^+/Na^+ DEER analysis

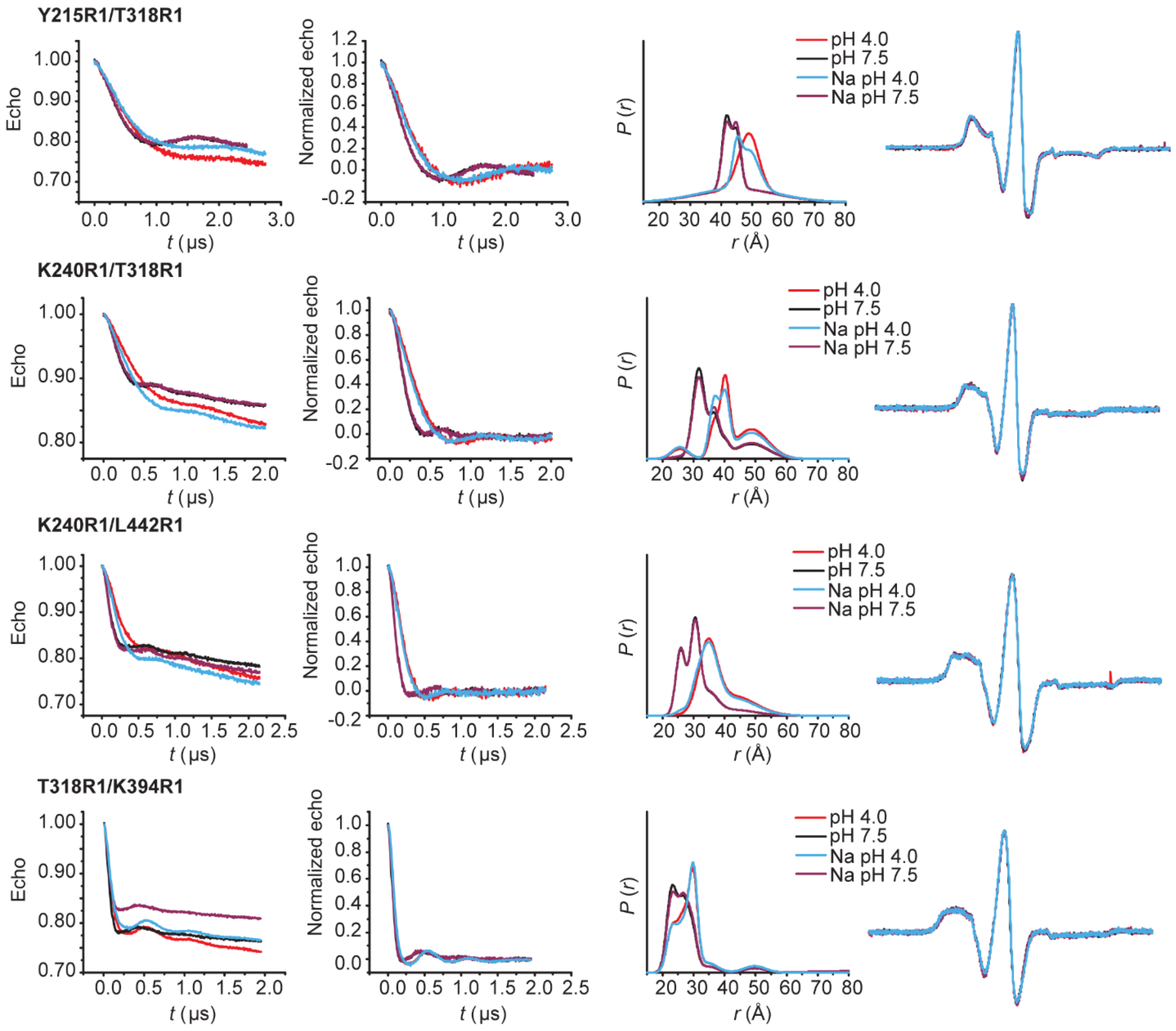

Dataset S7 – PfMATE backgound mutants intracellular H$^+$/Na$^+$ DEER analysis

N95R1/T318R1

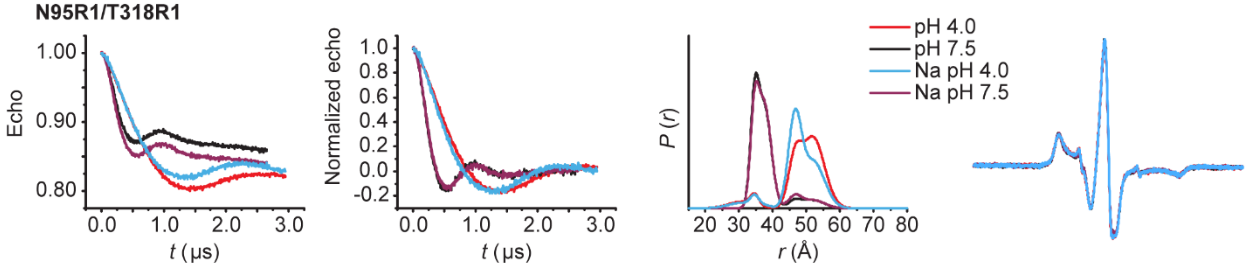

N95R1/T318R1_P26A

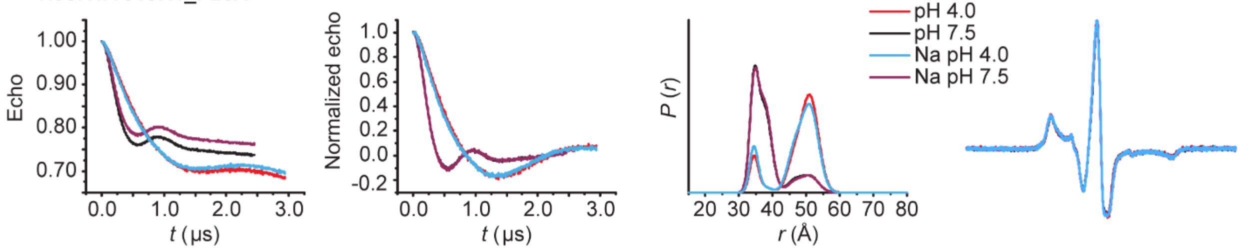

N95R1/T318R1_Y37A

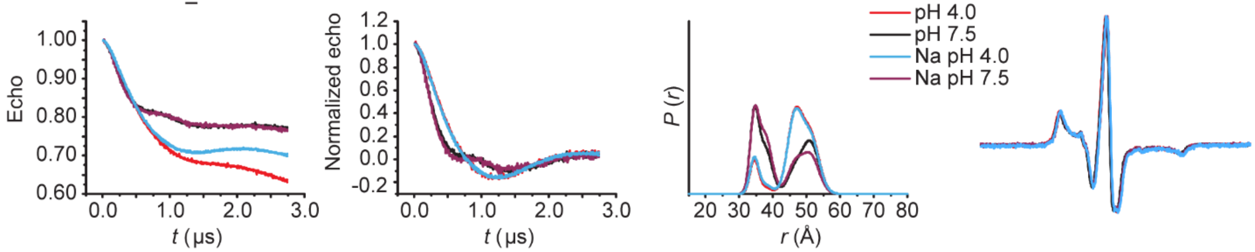

N95R1/T318R1_D41A

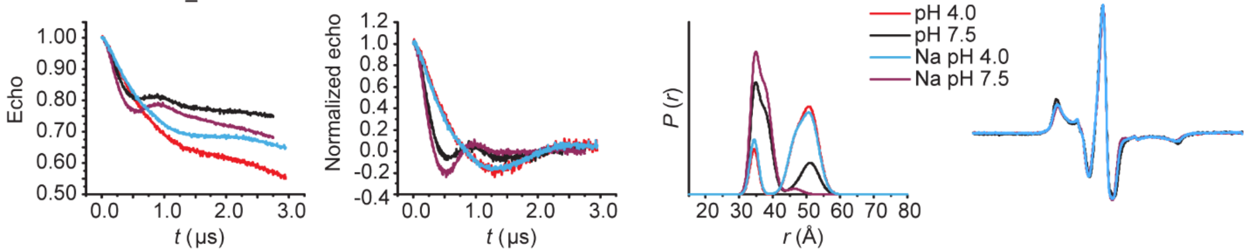

N95R1/T318R1_D41N

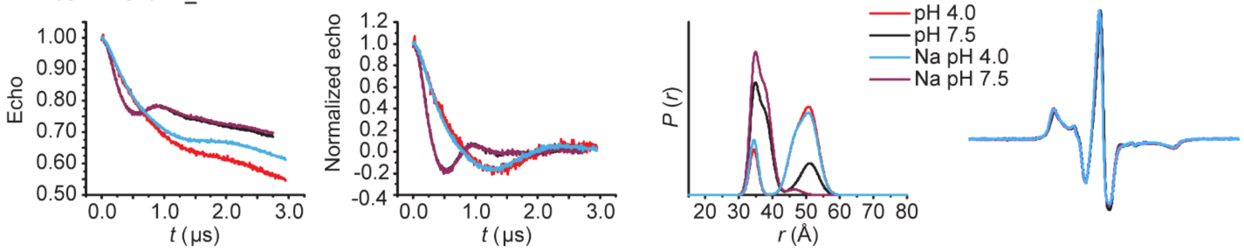

Dataset S7 – PfMATE backgound mutants intracellular H⁺/Na⁺ DEER analysis

N95R1/T318R1_E163A

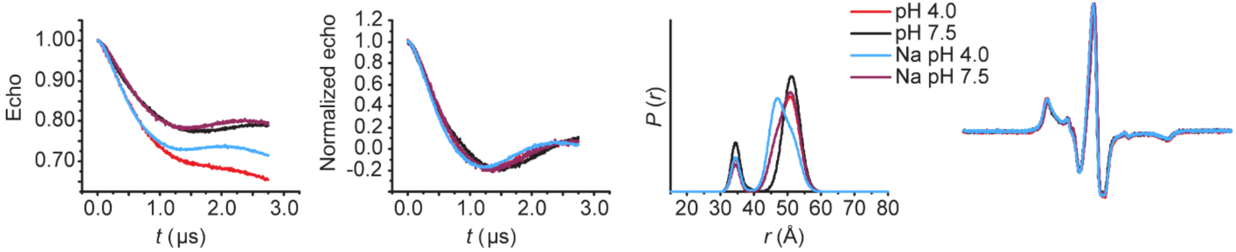

N95R1/T318R1_E163Q

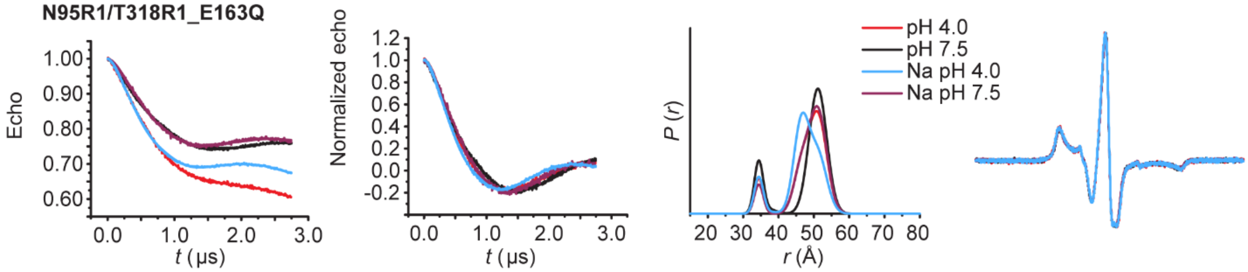

N95R1/T318R1_T202N

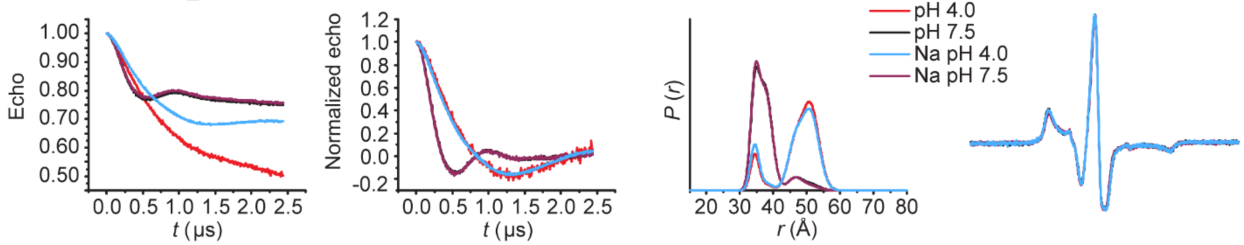

N95R1/T318R1_Y224A

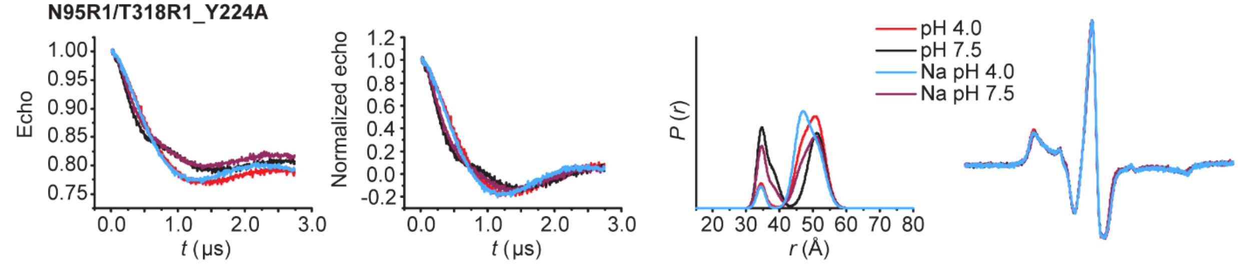

N95R1/T318R1_Q253A

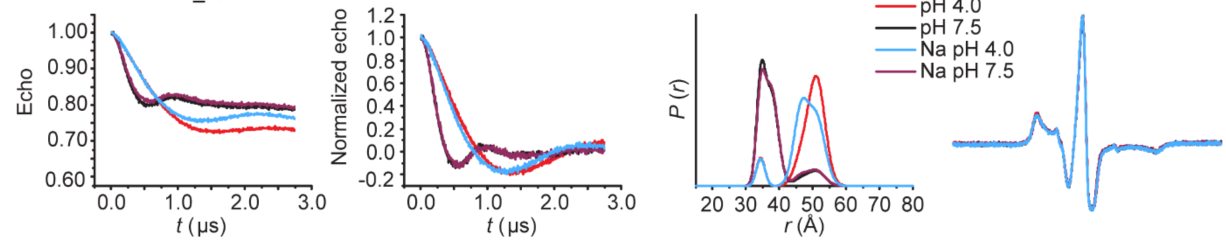

Dataset S7 – PfMATE backgound mutants intracellular H$^+$/Na$^+$ DEER analysis

N95R1/T318R1_E331A

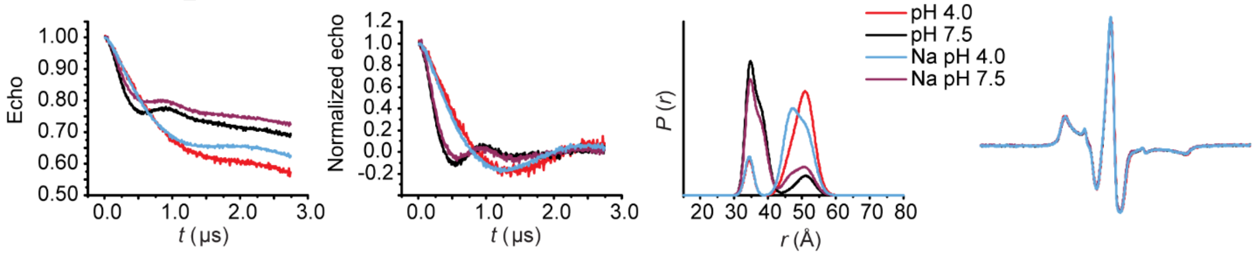

N95R1/T318R1_E331Q

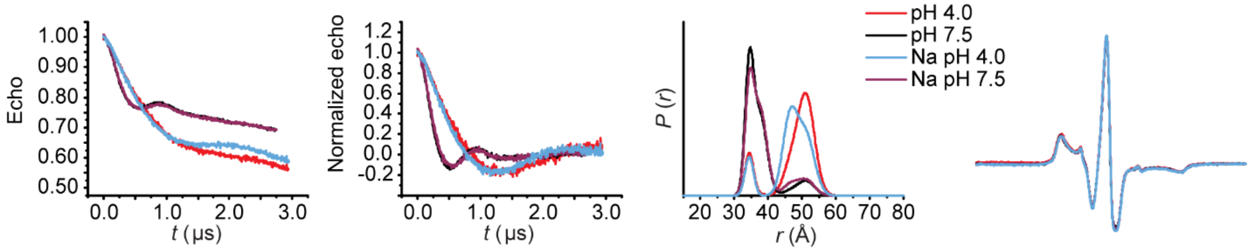

REFERENCES

1. E. Gouaux, R. MacKinnon, Principles of selective ion transport in channels and pumps. *Science (80-.).* (2005) https:/doi.org/10.1126/science.1113666.
2. C. F. Higgins, Multiple molecular mechanisms for multidrug resistance transporters. *Nature* **446**, 749–757 (2007).
3. S. Alibert, *et al.*, Multidrug efflux pumps and their role in antibiotic and antiseptic resistance: a pharmacodynamic perspective. *Expert Opin Drug Metab Toxicol* **13**, 301–309 (2017).
4. M. M. Gottesman, S. V. Ambudkar, Overview: ABC transporters and human disease in *Journal of Bioenergetics and Biomembranes*, (2001) https:/doi.org/10.1023/A:1012866803188.
5. M. M. Gottesman, T. Fojo, S. E. Bates, Multidrug resistance in cancer: Role of ATP-dependent transporters. *Nat. Rev. Cancer* (2002) https:/doi.org/10.1038/nrc706.
6. J. M. A. Blair, M. A. Webber, A. J. Baylay, D. O. Ogbolu, L. J. V. Piddock, Molecular mechanisms of antibiotic resistance. *Nat. Rev. Microbiol.* (2015) https:/doi.org/10.1038/nrmicro3380.
7. S. Kumar, *et al.*, Functional and Structural Roles of the Major Facilitator Superfamily Bacterial Multidrug Efflux Pumps. *Microorganisms* (2020) https:/doi.org/10.3390/microorganisms8020266.
8. S. B. Levy, M. Bonnie, Antibacterial resistance worldwide: Causes, challenges and responses. *Nat. Med.* (2004) https:/doi.org/10.1038/nm1145.
9. D. Du, H. W. van Veen, S. Murakami, K. M. Pos, B. F. Luisi, Structure, mechanism and cooperation of bacterial multidrug transporters. *Curr. Opin. Struct. Biol.* (2015) https:/doi.org/10.1016/j.sbi.2015.07.015.
10. M. H. Saier, I. T. Paulsen, Phylogeny of multidrug transporters. *Semin. Cell Dev. Biol.* **12**, 205–213 (2001).
11. Z. Chen, *et al.*, Mammalian drug efflux transporters of the ATP binding cassette (ABC) family in multidrug resistance: A review of the past decade. *Cancer Lett* **370**, 153–164 (2016).
12. G. W. Kaatz, F. McAleese, S. M. Seo, Multidrug resistance in Staphylococcus aureus due to overexpression of a novel multidrug and toxin extrusion (MATE) transport protein. *Antimicrob. Agents Chemother.* (2005) https:/doi.org/10.1128/AAC.49.5.1857-1864.2005.

13. F. McAleese, *et al.*, A novel MATE family efflux pump contributes to the reduced susceptibility of laboratory-derived Staphylococcus aureus mutants to tigecycline. *Antimicrob. Agents Chemother.* (2005) https:/doi.org/10.1128/AAC.49.5.1865-1871.2005.

14. C. Yilmaz, G. Ozcengiz, Antibiotics: Pharmacokinetics, toxicity, resistance and multidrug efflux pumps. *Biochem Pharmacol* **133**, 43–62 (2017).

15. S. Bin Zaman, *et al.*, A Review on Antibiotic Resistance: Alarm Bells are Ringing. *Cureus* (2017) https:/doi.org/10.7759/cureus.1403.

16. S. Boumahdi, F. J. de Sauvage, The great escape: tumour cell plasticity in resistance to targeted therapy. *Nat. Rev. Drug Discov.* (2020) https:/doi.org/10.1038/s41573-019-0044-1.

17. I. Arozarena, C. Wellbrock, Phenotype plasticity as enabler of melanoma progression and therapy resistance. *Nat. Rev. Cancer* (2019) https:/doi.org/10.1038/s41568-019-0154-4.

18. P. Mitchell, Coupling of phosphorylation to electron and hydrogen transfer by a chemi-osmotic type of mechanism. *Nature* (1961) https:/doi.org/10.1038/191144a0.

19. W. P. Jencks, Utilization of binding energy and coupling rules for active transport and other coupled vectorial processes. *Methods Enzymol.* (1989) https:/doi.org/10.1016/S0076-6879(89)71010-7.

20. I. C. West, Energy coupling in secondary active transport. *Biochim. Biophys. Acta - Rev. Biomembr.* (1980) https:/doi.org/10.1016/0304-4157(80)90005-2.

21. L. R. Forrest, R. Krämer, C. Ziegler, The structural basis of secondary active transport mechanisms. *Biochim. Biophys. Acta - Bioenerg.* (2011) https:/doi.org/10.1016/j.bbabio.2010.10.014.

22. A. Kumar, H. P. Schweizer, Bacterial resistance to antibiotics: Active efflux and reduced uptake. *Adv. Drug Deliv. Rev.* (2005) https:/doi.org/10.1016/j.addr.2005.04.004.

23. T. Kuroda, T. Tsuchiya, Multidrug efflux transporters in the MATE family. *Biochim. Biophys. Acta* **1794**, 763–8 (2009).

24. I. C. West, P. Mitchell, Stoicheiometry of lactose-H+ symport across the plasma membrane of Escherichia coli. *Biochem. J.* (1973) https:/doi.org/10.1042/bj1320587.

25. J. J. Mousa, S. D. Bruner, Structural and mechanistic diversity of multidrug transporters. *Nat.*

Prod. Rep. (2016) https:/doi.org/10.1039/c6np00006a.

26. M. H. Brown, I. T. Paulsen, R. A. Skurray, The multidrug efflux protein NorM is a prototype of a new family of transporters. *Mol Microbiol* **31**, 394–395 (1999).

27. A. B. Chang, R. Lin, W. K. Studley, C. V. Tran, M. H. Saier, Phylogeny as a guide to structure and function of membrane transport proteins. *Mol. Membr. Biol.* (2004) https:/doi.org/10.1080/09687680410001720830.

28. R. N. Hvorup, *et al.*, The multidrug/oligosaccharidyl-lipid/polysaccharide (MOP) exporter superfamily. *Eur. J. Biochem.* (2003) https:/doi.org/10.1046/j.1432-1033.2003.03418.x.

29. Y. Morita, *et al.*, NorM, putative multidrug efflux protein, of Vibrio parahaemolyticus and its homolog in Escherichia coli. *Antimicrob. Agents Chemother.* (1998) https:/doi.org/10.1128/aac.42.7.1778.

30. Y. Morita, A. Kataoka, S. Shiota, T. Mizushima, T. Tsuchiya, NorM of Vibrio parahaemolyticus is an Na+-driven multidrug efflux pump. *J. Bacteriol.* (2000) https:/doi.org/10.1128/JB.182.23.6694-6697.2000.

31. X. Z. Su, J. Chen, T. Mizushima, T. Kuroda, T. Tsuchiya, AbeM, an H+-coupled Acinetobacter baumannii multidrug efflux pump belonging to the MATE family of transporters. *Antimicrob Agents Chemother* **49**, 4362–4364 (2005).

32. M. Braibant, L. Guilloteau, M. S. Zygmunt, Functional characterization of Brucella melitensis NorMI, an efflux pump belonging to the multidrug and toxic compound extrusion family. *Antimicrob. Agents Chemother.* (2002) https:/doi.org/10.1128/AAC.46.9.3050-3053.2002.

33. L. Dridi, J. Tankovic, J. C. Petit, CdeA of Clostridium difficile, a new multidrug efflux transporter of the MATE family. *Microb. Drug Resist.* (2004) https:/doi.org/10.1089/mdr.2004.10.191.

34. X. J. Xu, *et al.*, Molecular Cloning and Characterization of the HmrM Multidrug Efflux Pump from Haemophilus influenzae Rd. *Microbiol. Immunol.* (2003) https:/doi.org/10.1111/j.1348-0421.2003.tb03467.x.

35. C. Rouquette-Loughlin, S. A. Dunham, M. Kuhn, J. T. Balthazar, W. M. Shafer, The NorM efflux pump of Neisseria gonorrhoeae and Neisseria meningitidis recognizes antimicrobial cationic compounds. *J. Bacteriol.* (2003) https:/doi.org/10.1128/JB.185.3.1101-1106.2003.

36. F. Long, C. Rouquette-Loughlin, W. M. Shafer, E. W. Yu, Functional cloning and characterization of the multidrug efflux pumps NorM from Neisseria gonorrhoeae and YdhE from Escherichia coli. *Antimicrob Agents Chemother* **52**, 3052–3060 (2008).

37. G. X. He, *et al.*, An H+-Coupled Multidrug Efflux Pump, PmpM, a Member of the MATE Family of Transporters, from Pseudomonas aeruginosa. *J. Bacteriol.* (2004) https:/doi.org/10.1128/JB.186.1.262-265.2004.

38. G. W. Kaatz, F. McAleese, S. M. Seo, Multidrug resistance in Staphylococcus aureus due to overexpression of a novel multidrug and toxin extrusion (MATE) transport protein. *Antimicrob Agents Chemother* **49**, 1857–1864 (2005).

39. F. McAleese, *et al.*, A novel MATE family efflux pump contributes to the reduced susceptibility of laboratory-derived Staphylococcus aureus mutants to tigecycline. *Antimicrob Agents Chemother* **49**, 1865–1871 (2005).

40. A. K. Singh, R. Haldar, D. Mandal, M. Kundu, Analysis of the topology of Vibrio cholerae NorM and identification of amino acid residues involved in norfloxacin resistance. *Antimicrob. Agents Chemother.* **50**, 3717–23 (2006).

41. A. Begum, *et al.*, Gene cloning and characterization of four MATE family multidrug efflux pumps from Vibrio cholerae non-O1. *Microbiol. Immunol.* (2005) https:/doi.org/10.1111/j.1348-0421.2005.tb03690.x.

42. M. N. Huda, *et al.*, Gene cloning and characterization of VcrM, a Na+-coupled multidrug efflux pump, from Vibrio cholerae non-O1. *Microbiol Immunol* **47**, 419–427 (2003).

43. J. J. Mousa, R. C. Newsome, Y. Yang, C. Jobin, S. D. Bruner, ClbM is a versatile, cation-promiscuous MATE transporter found in the colibactin biosynthetic gene cluster. *Biochem Biophys Res Commun* **482**, 1233–1239 (2016).

44. H. Zhu, *et al.*, Genomewide analysis of MATE-type gene family in maize reveals microsynteny and their expression patterns under aluminum treatment. *J. Genet.* (2016) https:/doi.org/10.1007/s12041-016-0686-2.

45. Y. Li, H. He, L.-F. He, Genome-wide analysis of the MATE gene family in potato. *Mol. Biol. Rep.* **46**, 403–414 (2019).

46. J. Liu, J. V. Magalhaes, J. Shaff, L. V. Kochian, Aluminum-activated citrate and malate transporters from the MATE and ALMT families function independently to confer Arabidopsis aluminum tolerance. *Plant J.* (2009) https:/doi.org/10.1111/j.1365-313X.2008.03696.x.

47. L. G. Maron, *et al.*, Two functionally distinct members of the MATE (multi-drug and toxic compound extrusion) family of transporters potentially underlie two major aluminum tolerance QTLs in maize. *Plant J.* (2010) https:/doi.org/10.1111/j.1365-313X.2009.04103.x.

48. A. C. Diener, R. A. Gaxiola, G. R. Fink, Arabidopsis ALF5, a Multidrug Efflux Transporter Gene Family Member, Confers Resistance to Toxins. *Plant Cell* (2001) https:/doi.org/10.2307/3871390.

49. E. E. Rogers, X. Wu, G. Stacey, H. T. Nguyen, Two MATE proteins play a role in iron efficiency in soybean. *J. Plant Physiol.* (2009) https:/doi.org/10.1016/j.jplph.2009.02.009.

50. T. P. Durrett, W. Gassmann, E. E. Rogers, The FRD3-mediated efflux of citrate into the root vasculature is necessary for efficient iron translocation. *Plant Physiol.* (2007) https:/doi.org/10.1104/pp.107.097162.

51. I. Debeaujon, A. J. M. Peeters, K. M. Leon-Kloosterziel, M. Koornneef, The TRANSPARENT TESTA12 Gene of Arabidopsis Encodes a Multidrug Secondary Transporter-Like Protein Required for Flavonoid Sequestration in Vacuoles of the Seed Coat Endothelium. *Plant Cell* (2001) https:/doi.org/10.2307/3871345.

52. H. Mathews, *et al.*, Activation tagging in tomato identifies a transcriptional regulator of anthocyanin biosynthesis, modification, and transport. *Plant Cell* (2003) https:/doi.org/10.1105/tpc.012963.

53. K. Marinova, *et al.*, The Arabidopsis MATE transporter TT12 acts as a vacuolar flavonoid/H+-antiporter active in proanthocyanidin-accumulating cells of the seed coat. *Plant Cell* (2007) https:/doi.org/10.1105/tpc.106.046029.

54. C. Gomez, *et al.*, Grapevine MATE-type proteins act as vacuolar h + -dependent acylated anthocyanin transporters 1[W][OA]. *Plant Physiol.* (2009) https:/doi.org/10.1104/pp.109.135624.

55. J. Zhao, R. A. Dixon, MATE transporters facilitate vacuolar uptake of epicatechin 3′-O-glucoside for proanthocyanidin biosynthesis in medicago truncatula and arabidopsis. *Plant Cell* (2009) https:/doi.org/10.1105/tpc.109.067819.

56. C. Nawrath, S. Heck, N. Parinthawong, J. P. Métraux, EDS5, an essential component of salicylic

acid-dependent signaling for disease resistance in arabidopsis, is a member of the MATE transporter family. *Plant Cell* (2002) https:/doi.org/10.1105/tpc.010376.

57. P. Lu, *et al.*, Overexpression of cotton a DTX/MATE gene enhances drought, salt, and cold stress tolerance in transgenic arabidopsis. *Front. Plant Sci.* **10** (2019).
58. H. Zhang, *et al.*, A DTX/MATE-type transporter facilitates abscisic acid efflux and modulates ABA sensitivity and drought tolerance in Arabidopsis. *Mol. Plant* (2014) https:/doi.org/10.1093/mp/ssu063.
59. L. Li, Z. He, G. K. Pandey, T. Tsuchiya, S. Luan, Functional cloning and characterization of a plant efflux carrier for multidrug and heavy metal detoxification. *J. Biol. Chem.* (2002) https:/doi.org/10.1074/jbc.M108777200.
60. M. Morita, *et al.*, Vacuolar transport of nicotine is mediated by a multidrug and toxic compound extrusion (MATE) transporter in Nicotiana tabacum. *Proc. Natl. Acad. Sci.* (2009) https:/doi.org/10.1073/pnas.0812512106.
61. T. Shoji, *et al.*, Multidrug and Toxic Compound Extrusion-Type Transporters Implicated in Vacuolar Sequestration of Nicotine in Tobacco Roots. *Plant Physiol.* (2009) https:/doi.org/10.1104/pp.108.132811.
62. J. V. Magalhaes, *et al.*, A gene in the multidrug and toxic compound extrusion (MATE) family confers aluminum tolerance in sorghum. *Nat. Genet.* (2007) https:/doi.org/10.1038/ng2074.
63. P. R. Ryan, H. Raman, S. Gupta, W. J. Horst, E. Delhaize, A second mechanism for aluminum resistance in wheat relies on the constitutive efflux of citrate from roots. *Plant Physiol.* (2009) https:/doi.org/10.1104/pp.108.129155.
64. J. Furukawa, *et al.*, An aluminum-activated citrate transporter in barley. *Plant Cell Physiol.* (2007) https:/doi.org/10.1093/pcp/pcm091.
65. T. Kawasaki, *et al.*, Purification and reconstitution of polyspecific H + /organic cation antiporter human MATE1. *Biochim. Biophys. Acta - Biomembr.* (2018) https:/doi.org/10.1016/j.bbamem.2018.07.005.
66. H. Motohashi, *et al.*, Precise comparison of protein localization among OCT, OAT, and MATE in human kidney. *J. Pharm. Sci.* (2013) https:/doi.org/10.1002/jps.23567.

67. H. Motohashi, *et al.*, Gene expression levels and immunolocalization of organic ion transporters in the human kidney. *J. Am. Soc. Nephrol.* (2002).

68. S. Masuda, *et al.*, Identification and Functional Characterization of a New Human Kidney–Specific H + /Organic Cation Antiporter, Kidney-Specific Multidrug and Toxin Extrusion 2 . *J. Am. Soc. Nephrol.* (2006) https:/doi.org/10.1681/asn.2006030205.

69. Y. Moriyama, M. Hiasa, T. Matsumoto, H. Omote, Multidrug and toxic compound extrusion (MATE)-type proteins as anchor transporters for the excretion of metabolic waste products and xenobiotics. *Xenobiotica* (2008) https:/doi.org/10.1080/00498250701883753.

70. T. Terada, K. ichi Inui, Physiological and pharmacokinetic roles of H+/organic cation antiporters (MATE/SLC47A). *Biochem. Pharmacol.* (2008) https:/doi.org/10.1016/j.bcp.2007.12.008.

71. M. Otsuka, *et al.*, A human transporter protein that mediates the final excretion step for toxic organic cations. *Proc. Natl. Acad. Sci.* (2005) https:/doi.org/10.1073/pnas.0506483102.

72. T. Komatsu, *et al.*, Characterization of the human MATE2 proton-coupled polyspecific organic cation exporter. *Int. J. Biochem. Cell Biol.* (2011) https:/doi.org/10.1016/j.biocel.2011.03.005.

73. S. Gluck, R. Nelson, The role of the V-ATPase in renal epithelial H+ transport. *J. Exp. Biol.* (1992).

74. H. Koepsell, K. Lips, C. Volk, Polyspecific organic cation transporters: Structure, function, physiological roles, and biopharmaceutical implications. *Pharm. Res.* (2007) https:/doi.org/10.1007/s11095-007-9254-z.

75. H. Motohashi, K. I. Inui, Organic cation transporter OCTs (SLC22) and MATEs (SLC47) in the human kidney. *AAPS J.* (2013) https:/doi.org/10.1208/s12248-013-9465-7.

76. J. Yin, H. Duan, Y. Shirasaka, B. Prasad, J. Wang, Atenolol renal secretion is mediated by human organic cation transporter 2 and multidrug and toxin extrusion proteins. *Drug Metab. Dispos.* (2015) https:/doi.org/10.1124/dmd.115.066175.

77. A. T. Nies, K. Damme, E. Schaeffeler, M. Schwab, Multidrug and toxin extrusion proteins as transporters of antimicrobial drugs. *Expert Opin. Drug Metab. Toxicol.* (2012) https:/doi.org/10.1517/17425255.2012.722996.

78. M. Tsuda, *et al.*, Involvement of human multidrug and toxin extrusion 1 in the drug interaction between cimetidine and metformin in renal epithelial cells. *J. Pharmacol. Exp. Ther.* (2009)

https:/doi.org/10.1124/jpet.108.147918.

79. J. Yin, J. Wang, Renal drug transporters and their significance in drug-drug interactions. *Acta Pharm. Sin. B* (2016) https:/doi.org/10.1016/j.apsb.2016.07.013.

80. A. Ivanyuk, F. Livio, J. Biollaz, T. Buclin, Renal Drug Transporters and Drug Interactions. *Clin. Pharmacokinet.* (2017) https:/doi.org/10.1007/s40262-017-0506-8.

81. K. Kato, *et al.*, Involvement of organic cation transporters in the clearance and milk secretion of thiamine in mice. *Pharm. Res.* (2015) https:/doi.org/10.1007/s11095-014-1608-8.

82. S. Ito, *et al.*, Potent and specific inhibition of mMate1-mediated efflux of type I organic cations in the liver and kidney by pyrimethamine. *J. Pharmacol. Exp. Ther.* (2010) https:/doi.org/10.1124/jpet.109.163642.

83. H. Kusuhara, *et al.*, Effects of a MATE protein inhibitor, pyrimethamine, on the renal elimination of metformin at oral microdose and at therapeutic dose in healthy subjects. *Clin. Pharmacol. Ther.* (2011) https:/doi.org/10.1038/clpt.2011.36.

84. A. Yonezawa, K. I. Inui, Importance of the multidrug and toxin extrusion MATE/SLC47A family to pharmacokinetics, pharmacodynamics/toxicodynamics and pharmacogenomics. *Br. J. Pharmacol.* **164**, 1817–1825 (2011).

85. T. Nakamura, A. Yonezawa, S. Hashimoto, T. Katsura, K. I. Inui, Disruption of multidrug and toxin extrusion MATE1 potentiates cisplatin-induced nephrotoxicity. *Biochem. Pharmacol.* (2010) https:/doi.org/10.1016/j.bcp.2010.08.019.

86. A. Somogyi, C. Stockley, J. Keal, P. Rolan, F. Bochner, Reduction of metformin renal tubular secretion by cimetidine in man. *Br. J. Clin. Pharmacol.* (1987) https:/doi.org/10.1111/j.1365-2125.1987.tb03090.x.

87. K. Y. Ohta, *et al.*, Functional characterization of multidrug and toxin extrusion protein 1 as a facilitative transporter for fluoroquinolones. *J. Pharmacol. Exp. Ther.* (2009) https:/doi.org/10.1124/jpet.108.142257.

88. S. Masuda, *et al.*, Identification and functional characterization of a new human kidney-specific H+/organic cation antiporter, kidney-specific multidrug and toxin extrusion 2. *J Am Soc Nephrol* **17**, 2127–2135 (2006).

89. A. Yonezawa, S. Masuda, S. Yokoo, T. Katsura, K. I. Inui, Cisplatin and oxaliplatin, but not carboplatin and nedaplatin, are substrates for human organic cation transporters (SLC22A1-3 and multidrug and toxin extrusion family). *J. Pharmacol. Exp. Ther.* (2006) https:/doi.org/10.1124/jpet.106.110346.

90. Y. Tanihara, *et al.*, Substrate specificity of MATE1 and MATE2-K, human multidrug and toxin extrusions/H+-organic cation antiporters. *Biochem. Pharmacol.* (2007) https:/doi.org/10.1016/j.bcp.2007.04.010.

91. M. Tsuda, *et al.*, Targeted disruption of the multidrug and toxin extrusion 1 (Mate1) gene in mice reduces renal secretion of metformin. *Mol. Pharmacol.* (2009) https:/doi.org/10.1124/mol.109.056242.

92. K. Toyama, *et al.*, Loss of multidrug and toxin extrusion 1 (MATE1) is associated with metformin-induced lactic acidosis. *Br. J. Pharmacol.* (2012) https:/doi.org/10.1111/j.1476-5381.2012.01853.x.

93. W. Q. Qiu, M. F. Folstein, Insulin, insulin-degrading enzyme and amyloid-β peptide in Alzheimer's disease: Review and hypothesis. *Neurobiol. Aging* (2006) https:/doi.org/10.1016/j.neurobiolaging.2005.01.004.

94. M. G. Hong, *et al.*, Evidence that the gene encoding insulin degrading enzyme influences human lifespan. *Hum. Mol. Genet.* (2008) https:/doi.org/10.1093/hmg/ddn137.

95. W. L. Xu, *et al.*, HHEX_23 AA Genotype Exacerbates Effect of Diabetes on Dementia and Alzheimer Disease: A Population-Based Longitudinal Study. *PLoS Med.* (2015) https:/doi.org/10.1371/journal.pmed.1001853.

96. M. L. Becker, *et al.*, Genetic variation in the multidrug and toxin extrusion 1 transporter protein influences the glucose-lowering effect of metformin in patients with diabetes: A preliminary study. *Diabetes* (2009) https:/doi.org/10.2337/db08-1028.

97. I. Tkáč, *et al.*, Pharmacogenomic association between a variant in SLC47A1 gene and therapeutic response to metformin in type 2 diabetes. *Diabetes, Obes. Metab.* (2013) https:/doi.org/10.1111/j.1463-1326.2012.01691.x.

98. J. Oh, *et al.*, Inhibition of the multidrug and toxin extrusion (MATE) transporter by pyrimethamine increases the plasma concentration of metformin but does not increase antihyperglycaemic activity

in humans. *Diabetes, Obes. Metab.* (2016) https:/doi.org/10.1111/dom.12577.

99. M. Goda, K. Oda, A. Oda, N. Kobayashi, M. Otsuka, Involvement of the Multidrug and Toxic Compound Extrusion Transporter in Testosterone Release from Cultured Pig Leydig Cells. *Pharmacology* (2017) https:/doi.org/10.1159/000460822.

100. C. Lechner, *et al.*, Impact of experimental conditions on the evaluation of interactions between multidrug and toxin extrusion proteins and candidate drugs. *Drug Metab. Dispos.* (2016) https:/doi.org/10.1124/dmd.115.068163.

101. E. I. Lepist, *et al.*, Contribution of the organic anion transporter OAT2 to the renal active tubular secretion of creatinine and mechanism for serum creatinine elevations caused by cobicistat. *Kidney Int.* (2014) https:/doi.org/10.1038/ki.2014.66.

102. M. Hiasa, T. Matsumoto, T. Komatsu, Y. Moriyama, Wide variety of locations for rodent MATE1, a transporter protein that mediates the final excretion step for toxic organic cations. *Am. J. Physiol. - Cell Physiol.* (2006) https:/doi.org/10.1152/ajpcell.00090.2006.

103. M. Otsuka, *et al.*, A human transporter protein that mediates the final excretion step for toxic organic cations. *Proc Natl Acad Sci U S A* **102**, 17923–17928 (2005).

104. T. Matsumoto, T. Kanamoto, M. Otsuka, H. Omote, Y. Moriyama, Role of glutamate residues in substrate recognition by human MATE1 polyspecific H + /organic cation exporter . *Am. J. Physiol. Physiol.* (2008) https:/doi.org/10.1152/ajpcell.00504.2007.

105. L. J. Martínez-Guerrero, M. Morales, S. Ekins, S. H. Wright, Lack of influence of substrate on ligand interaction with the human multidrug and toxin extruder, MATE1. *Mol. Pharmacol.* (2016) https:/doi.org/10.1124/mol.116.105056.

106. X. Zhang, N. J. Cherrington, S. H. Wright, Molecular identification and functional characterization of rabbit MATE1 and MATE2-K. *Am. J. Physiol. - Ren. Physiol.* (2007) https:/doi.org/10.1152/ajprenal.00102.2007.

107. P. Mitchell, A general theory of membrane transport from studies of bacteria. *Nature* (1957) https:/doi.org/10.1038/180134a0.

108. O. Jardetzky, Simple allosteric model for membrane pumps. *Nature* **211**, 969–970 (1966).

109. M. Otsuka, *et al.*, Identification of essential amino acid residues of the NorM Na+/multidrug

antiporter in Vibrio parahaemolyticus. *J Bacteriol* **187**, 1552–1558 (2005).

110. X. He, *et al.*, Structure of a cation-bound multidrug and toxic compound extrusion transporter. *Nature* **467**, 991–994 (2010).

111. M. Lu, *et al.*, Structures of a Na+-coupled, substrate-bound MATE multidrug transporter. *Proc. Natl. Acad. Sci. U. S. A.* **110**, 2099–104 (2013).

112. M. Radchenko, J. Symersky, R. Nie, M. Lu, Structural basis for the blockade of MATE multidrug efflux pumps. *Nat Commun* **6**, 7995 (2015).

113. M. Lu, M. Radchenko, J. Symersky, R. Nie, Y. Guo, Structural insights into H+-coupled multidrug extrusion by a MATE transporter. *Nat. Struct. Mol. Biol.* **20**, 1310–7 (2013).

114. Y. Tanaka, *et al.*, Structural basis for the drug extrusion mechanism by a MATE multidrug transporter. *Nature* **496**, 247–51 (2013).

115. T. Kusakizako, Y. Tanaka, C. J. Hipolito, H. Suga, O. Nureki, “Crystallographic analysis of MATE-type multidrug exporter with its inhibitors” in *Methods in Molecular Biology*, (2018) https:/doi.org/10.1007/978-1-4939-7454-2_3.

116. C. J. Hipolito, Y. Tanaka, T. Katoh, O. Nureki, H. Suga, A macrocyclic peptide that serves as a cocrystallization ligand and inhibits the function of a MATE family transporter. *Molecules* **18**, 10514–30 (2013).

117. S. Zakrzewska, *et al.*, Inward-facing conformation of a multidrug resistance MATE family transporter. *Proc Natl Acad Sci U S A* **116**, 12275–12284 (2019).

118. E. Ficici, W. Zhou, S. Castellano, J. D. Faraldo-Gómez, Broadly conserved Na + -binding site in the N-lobe of prokaryotic multidrug MATE transporters . *Proc. Natl. Acad. Sci.* **115**, E6172–E6181 (2018).

119. P. Engel, M. I. Vizcaino, J. M. Crawford, Gut symbionts from distinct hosts exhibit genotoxic activity via divergent colibactin biosynthesis pathways. *Appl. Environ. Microbiol.* (2015) https:/doi.org/10.1128/AEM.03283-14.

120. A. Cougnoux, *et al.*, Bacterial genotoxin colibactin promotes colon tumour growth by inducing a senescence-associated secretory phenotype. *Gut* (2014) https:/doi.org/10.1136/gutjnl-2013-305257.

121. G. Cuevas-Ramos, *et al.*, Escherichia coli induces DNA damage in vivo and triggers genomic instability in mammalian cells. *Proc. Natl. Acad. Sci. U. S. A.* (2010) https:/doi.org/10.1073/pnas.1001261107.

122. J. C. Arthur, *et al.*, Intestinal inflammation targets cancer-inducing activity of the microbiota. *Science (80-.).* (2012) https:/doi.org/10.1126/science.1224820.

123. J. J. Mousa, *et al.*, MATE transport of the E. coli-derived genotoxin colibactin. *Nat Microbiol* **1**, 15009 (2016).

124. T. Kusakizako, *et al.*, LCP crystallization and X-ray diffraction analysis of VcmN, a MATE transporter from Vibrio cholerae. *Acta Crystallogr. Sect. Struct. Biol. Commun.* (2016) https:/doi.org/10.1107/S2053230X16008931.

125. T. Kusakizako, *et al.*, Structural Basis of H + -Dependent Conformational Change in a Bacterial MATE Transporter. *Structure* (2019) https:/doi.org/10.1016/j.str.2018.10.004.

126. B. R. Moser, Biodiesel from alternative oilseed feedstocks: Camelina and field pennycress. *Biofuels* (2012) https:/doi.org/10.4155/BFS.12.6.

127. A. Gehringer, W. Friedt, W. Lühs, R. J. Snowdon, Genetic mapping of agronomic traits in false flax (Camelina sativa subsp. sativa). *Genome* (2006) https:/doi.org/10.1139/G06-117.

128. G. Séguin-Swartz, *et al.*, Diseases of Camelina sativa (false flax). *Can. J. Plant Pathol.* (2009) https:/doi.org/10.1080/07060660909507612.

129. Q. Ma, *et al.*, GsMATE encoding a multidrug and toxic compound extrusion transporter enhances aluminum tolerance in Arabidopsis thaliana. *BMC Plant Biol.* (2018) https:/doi.org/10.1186/s12870-018-1397-z.

130. Y. Tanaka, S. Iwaki, T. Tsukazaki, Crystal Structure of a Plant Multidrug and Toxic Compound Extrusion Family Protein. *Structure* **25**, 1455-1460 e2 (2017).

131. H. Miyauchi, *et al.*, Structural basis for xenobiotic extrusion by eukaryotic MATE transporter. *Nat Commun* **8**, 1633 (2017).

132. V. Cherezov, *et al.*, High-resolution crystal structure of an engineered human β2-adrenergic G protein-coupled receptor. *Science (80-.).* (2007) https:/doi.org/10.1126/science.1150577.

133. E. Y. T. Chien, *et al.*, Structure of the human dopamine D3 receptor in complex with a D2/D3

selective antagonist. *Science (80-.).* (2010) https:/doi.org/10.1126/science.1197410.

134. M. Z. Dawoud, M. Nasr, Comparison of drug release from liquid crystalline monoolein dispersions and solid lipid nanoparticles using a flow cytometric technique. *Acta Pharm. Sin. B* (2016) https:/doi.org/10.1016/j.apsb.2016.01.004.

135. R. Phillips, T. Ursell, P. Wiggins, P. Sens, Emerging roles for lipids in shaping membrane-protein function. *Nature* (2009) https:/doi.org/10.1038/nature08147.

136. G. Khelashvili, *et al.*, Why GPCRs behave differently in cubic and lamellar lipidic mesophases. *J. Am. Chem. Soc.* (2012) https:/doi.org/10.1021/ja3056485.

137. C. Pliotas, *et al.*, The role of lipids in mechanosensation. *Nat. Struct. Mol. Biol.* (2015) https:/doi.org/10.1038/nsmb.3120.

138. M. Landreh, *et al.*, Integrating mass spectrometry with MD simulations reveals the role of lipids in Na+/H+ antiporters. *Nat. Commun.* (2017) https:/doi.org/10.1038/ncomms13993.

139. A. Laganowsky, *et al.*, Membrane proteins bind lipids selectively to modulate their structure and function. *Nature* (2014) https:/doi.org/10.1038/nature13419.

140. E. Pyle, *et al.*, Structural Lipids Enable the Formation of Functional Oligomers of the Eukaryotic Purine Symporter UapA. *Cell Chem. Biol.* (2018) https:/doi.org/10.1016/j.chembiol.2018.03.011.

141. C. Martens, *et al.*, Lipids modulate the conformational dynamics of a secondary multidrug transporter. *Nat. Struct. Mol. Biol.* (2016) https:/doi.org/10.1038/nsmb.3262.

142. M. J. Chalmers, S. A. Busby, B. D. Pascal, G. M. West, P. R. Griffin, Differential hydrogen/deuterium exchange mass spectrometry analysis of protein-ligand interactions. *Expert Rev. Proteomics* (2011) https:/doi.org/10.1586/epr.10.109.

143. A. J. Percy, M. Rey, K. M. Burns, D. C. Schriemer, Probing protein interactions with hydrogen/deuterium exchange and mass spectrometry-A review. *Anal. Chim. Acta* (2012) https:/doi.org/10.1016/j.aca.2012.01.037.

144. M. L. Eisinger, L. Nie, A. R. Dörrbaum, J. D. Langer, H. Michel, The Xenobiotic Extrusion Mechanism of the MATE Transporter NorM_PS from Pseudomonas stutzeri. *J. Mol. Biol.* **430**, 1311–1323 (2018).

145. L. R. Forrest, G. Rudnick, The rocking bundle: A mechanism for ion-coupled solute flux by

symmetrical transporters. *Physiology* (2009) https:/doi.org/10.1152/physiol.00030.2009.

146. L. Nie, *et al.*, Identification of the High-affinity Substrate-binding Site of the Multidrug and Toxic Compound Extrusion (MATE) Family Transporter from Pseudomonas stutzeri. *J Biol Chem* **291**, 15503–15514 (2016).

147. G. Jeschke, DEER distance measurements on proteins. *Annu Rev Phys Chem* **63**, 419–446 (2012).

148. D. P. Claxton, K. Kazmier, S. Mishra, H. S. McHaourab, Navigating Membrane Protein Structure, Dynamics, and Energy Landscapes Using Spin Labeling and EPR Spectroscopy. *Methods Enzym.* **564**, 349–387 (2015).

149. P. R. Steed, R. A. Stein, S. Mishra, M. C. Goodman, H. S. McHaourab, Na(+)-substrate coupling in the multidrug antiporter norm probed with a spin-labeled substrate. *Biochemistry* **52**, 5790–5799 (2013).

150. Y. Jin, A. Nair, H. W. Van Veen, Multidrug transport protein NorM from Vibrio cholerae simultaneously couples to sodium- and proton-motive force. *J. Biol. Chem.* (2014) https:/doi.org/10.1074/jbc.M113.546770.

151. D. P. Claxton, K. L. Jagessar, P. Ryan Steed, R. A. Stein, H. S. Mchaourab, Sodium and proton coupling in the conformational cycle of a MATE antiporter from Vibrio cholerae. *Proc. Natl. Acad. Sci. U. S. A.* **115** (2018).

152. M. Lu, Structures of multidrug and toxic compound extrusion transporters and their mechanistic implications. *Channels (Austin)* **10**, 88–100 (2016).

153. M. Radchenko, R. Nie, M. Lu, Disulfide Cross-linking of a Multidrug and Toxic Compound Extrusion Transporter Impacts Multidrug Efflux. *J Biol Chem* **291**, 9818–9826 (2016).

154. H. Yamanaka, H. Kobayashi, E. Takahashi, K. Okamoto, MacAB is involved in the secretion of Escherichia coli heat-stable enterotoxin II. *J Bacteriol* **190**, 7693–7698 (2008).

155. W. Nishima, *et al.*, Mechanisms for Two-Step Proton Transfer Reactions in the Outward-Facing Form of MATE Transporter. *Biophys J* **110**, 1346–1354 (2016).

156. H. Ashkenazy, *et al.*, ConSurf 2016: an improved methodology to estimate and visualize evolutionary conservation in macromolecules. *Nucleic Acids Res.* (2016)

https:/doi.org/10.1093/nar/gkw408.

157. M. Landau, *et al.*, ConSurf 2005: the projection of evolutionary conservation scores of residues on protein structures. *Nucleic Acids Res* **33**, W299-302 (2005).

158. L. Kozachkov, E. Padan, Site-directed tryptophan fluorescence reveals two essential conformational changes in the Na+/H+ antiporter NhaA. *Proc Natl Acad Sci U S A* **108**, 15769–15774 (2011).

159. I. Smirnova, V. Kasho, J. Sugihara, H. R. Kaback, Probing of the rates of alternating access in LacY with Trp fluorescence. *Proc Natl Acad Sci U S A* **106**, 21561–21566 (2009).

160. Smriti, P. Zou, H. S. McHaourab, Mapping daunorubicin-binding Sites in the ATP-binding cassette transporter MsbA using site-specific quenching by spin labels. *J Biol Chem* **284**, 13904–13913 (2009).

161. N. Tal, S. Schuldiner, A coordinated network of transporters with overlapping specificities provides a robust survival strategy. *Proc Natl Acad Sci U S A* **106**, 9051–9056 (2009).

162. E. W. Yu, J. R. Aires, H. Nikaido, AcrB multidrug efflux pump of Escherichia coli: composite substrate-binding cavity of exceptional flexibility generates its extremely wide substrate specificity. *J Bacteriol* **185**, 5657–5664 (2003).

163. E. W. Yu, G. McDermott, H. I. Zgurskaya, H. Nikaido, D. E. Koshland Jr., Structural basis of multiple drug-binding capacity of the AcrB multidrug efflux pump. *Science (80-.).* **300**, 976–980 (2003).

164. K. L. Jagessar, H. S. Mchaourab, D. P. Claxton, The N-terminal domain of an archaeal multidrug and toxin extrusion (MATE) transporter mediates proton coupling required for prokaryotic drug resistance. *J. Biol. Chem.*, jbc.RA119.009195 (2019).

165. R. Dastvan, S. Mishra, Y. B. Peskova, R. K. Nakamoto, H. S. Mchaourab, Mechanism of allosteric modulation of P-glycoprotein by transport substrates and inhibitors. *Science (80-.).* (2019) https:/doi.org/10.1126/science.aav9406.

166. H. S. Mchaourab, P. R. Steed, K. Kazmier, Toward the fourth dimension of membrane protein structure: insight into dynamics from spin-labeling EPR spectroscopy. *Structure* **19**, 1549–1561 (2011).

167. O. Schiemann, T. F. Prisner, Long-range distance determinations in biomacromolecules by EPR spectroscopy. *Q Rev Biophys* **40**, 1–53 (2007).

168. T. Kusakizako, *et al.*, Structural Basis of H(+)-Dependent Conformational Change in a Bacterial MATE Transporter. *Structure* **27**, 293-301 e3 (2019).

169. S. Jo, T. Kim, V. G. Iyer, W. Im, CHARMM-GUI: a web-based graphical user interface for CHARMM. *J Comput Chem* **29**, 1859–1865 (2008).

170. G. Celniker, *et al.*, ConSurf: Using evolutionary data to raise testable hypotheses about protein function. *Isr. J. Chem.* (2013) https:/doi.org/10.1002/ijch.201200096.

171. A. C. Y. Kuk, A. Hao, Z. Guan, S. Y. Lee, Visualizing conformation transitions of the Lipid II flippase MurJ. *Nat. Commun.* **10** (2019).

172. A. K. Singh, R. Haldar, D. Mandal, M. Kundu, Analysis of the topology of Vibrio cholerae NorM and identification of amino acid residues involved in norfloxacin resistance. *Antimicrob Agents Chemother* **50**, 3717–3723 (2006).

173. J. Song, C. Ji, J. Z. Zhang, Insights on Na(+) binding and conformational dynamics in multidrug and toxic compound extrusion transporter NorM. *Proteins* **82**, 240–249 (2013).

174. M. Masureel, *et al.*, Protonation drives the conformational switch in the multidrug transporter LmrP. *Nat. Chem. Biol.* (2014) https:/doi.org/10.1038/nchembio.1408.

175. S. Vanni, P. Campomanes, M. Marcia, U. Rothlisberger, Ion binding and internal hydration in the multidrug resistance secondary active transporter NorM investigated by molecular dynamics simulations. *Biochemistry* **51**, 1281–1287 (2012).

176. H. Ashkenazy, *et al.*, ConSurf 2016: an improved methodology to estimate and visualize evolutionary conservation in macromolecules. *Nucleic Acids Res* **44**, W344-50 (2016).

177. S. Mishra, *et al.*, Conformational dynamics of the nucleotide binding domains and the power stroke of a heterodimeric ABC transporter. *Elife* **3**, e02740 (2014).

178. P. Zou, H. S. Mchaourab, Increased sensitivity and extended range of distance measurements in Spin-labeled membrane proteins: Q-band double electron-electron resonance and nanoscale bilayers. *Biophys. J.* (2010) https:/doi.org/10.1016/j.bpj.2009.12.4193.

179. R. A. Stein, A. H. Beth, E. J. Hustedt, A Straightforward Approach to the Analysis of Double

Electron-Electron Resonance Data. *Methods Enzym.* **563**, 531–567 (2015).

180. Y. Qi, *et al.*, CHARMM-GUI DEER facilitator for spin-pair distance distribution calculations and preparation of restrained-ensemble molecular dynamics simulations. *J. Comput. Chem.* (2019) https:/doi.org/10.1002/jcc.26032.

181. F. M. Zehentbauer, *et al.*, Fluorescence spectroscopy of Rhodamine 6G: Concentration and solvent effects. *Spectrochim. Acta - Part A Mol. Biomol. Spectrosc.* (2014) https:/doi.org/10.1016/j.saa.2013.10.062.

182. A. Krah, R. G. Huber, U. Zachariae, P. J. Bond, On the ion coupling mechanism of the MATE transporter ClbM. *Biochim. Biophys. Acta - Biomembr.* (2020) https:/doi.org/10.1016/j.bbamem.2019.183137.

183. K. L. Jagessar, D. P. Claxton, R. A. Stein, H. S. Mchaourab, Sequence and structural determinants of ligand-dependent alternating access of a MATE transporter. *Proc. Natl. Acad. Sci.*, 201917139 (2020).

184. H. S. Mchaourab, M. A. Lietzow, K. Hideg, W. L. Hubbell, Motion of spin-labeled side chains in T4 lysozyme. Correlation with protein structure and dynamics. *Biochemistry* **35**, 7692–7704 (1996).

185. K. Gupta, *et al.*, The role of interfacial lipids in stabilizing membrane protein oligomers. *Nature* (2017) https:/doi.org/10.1038/nature20820.

186. N. J. Harris, *et al.*, Comparative stability of Major Facilitator Superfamily transport proteins. *Eur. Biophys. J.* (2017) https:/doi.org/10.1007/s00249-017-1197-7.

187. M. R. Sanders, H. E. Findlay, P. J. Booth, Lipid bilayer composition modulates the unfolding free energy of a knotted α-helical membrane protein. *Proc. Natl. Acad. Sci. U. S. A.* (2018) https:/doi.org/10.1073/pnas.1714668115.

188. C. Koshy, *et al.*, Structural evidence for functional lipid interactions in the betaine transporter BetP. *EMBO J.* (2013) https:/doi.org/10.1038/emboj.2013.226.

189. A. V. Botelho, T. Huber, T. P. Sakmar, M. F. Brown, Curvature and Hydrophobic forces drive oligomerization and modulate activity of rhodopsin in membranes. *Biophys. J.* (2006) https:/doi.org/10.1529/biophysj.106.082776.

190. A. V. Botelho, N. J. Gibson, R. L. Thurmond, Y. Wang, M. F. Brown, Conformational energetics of

rhodopsin modulated by nonlamellar-forming lipids. *Biochemistry* (2002) https:/doi.org/10.1021/bi011995g.

191. O. Soubias, W. E. Teague, K. Gawrisch, Evidence for specificity in lipid-rhodopsin interactions. *J. Biol. Chem.* (2006) https:/doi.org/10.1074/jbc.M603059200.

192. G. Khelashvili, A. Galli, H. Weinstein, Phosphatidylinositol 4,5-biphosphate (PIP2) lipids regulate the phosphorylation of syntaxin N-terminus by modulating both its position and local structure. *Biochemistry* (2012) https:/doi.org/10.1021/bi300833z.

193. T. E. DeCoursey, J. Hosler, Philosophy of voltage-gated proton channels. *J. R. Soc. Interface* (2014) https:/doi.org/10.1098/rsif.2013.0799.

194. Y. Peng, J. M. J. Swanson, S. G. Kang, R. Zhou, G. A. Voth, Hydrated Excess Protons Can Create Their Own Water Wires. *J. Phys. Chem. B* (2015) https:/doi.org/10.1021/jp5095118.

195. J. P. Hosler, S. Ferguson-Miller, D. A. Mills, Energy Transduction: Proton Transfer Through the Respiratory Complexes. *Annu. Rev. Biochem.* (2006) https:/doi.org/10.1146/annurev.biochem.75.062003.101730.

196. M. J. Harms, J. L. Schlessman, G. R. Sue, E. Bertrand García-Moreno, Arginine residues at internal positions in a protein are always charged. *Proc. Natl. Acad. Sci. U. S. A.* (2011) https:/doi.org/10.1073/pnas.1104808108.